UNIVERSITY OF SOUTHAMPTON

FACULTY OF ENGINERRING & THE ENVIRONMENT

Engineering Doctorate – Sponsored by Mott MacDonald

Short-term Behaviour of a Basement Structure in London Clay and Conducting Oedometer, Rowe Cell and Triaxial Tests on Block Samples Obtained from Deep Excavations across Central London

by

Mathew Procter

Thesis for the degree of Doctor of Engineering

January 2020

ABSTRACT

Excavations into overconsolidated clay are becoming increasingly deep around the world to provide functional areas such as transport hubs. These basement structures pose significant engineering challenges since there are often uncertainties relating to ground movements on and around the site.

Field instrumentation was installed at Victoria Station Upgrade (VSU) to measure: ground deformations; earth and water pressures; and slab strains during and after construction. The basement structure is overdesigned as a standalone basement as the future end use of the land above the basement is to develop the site. It was found that the structure limited vertical ground movements (heave) at the approximate centre of the basement to ~10mm (0.1% of excavation depth, H) which is considerably less than the 0.2-0.25%H typically found on similar projects. The conclusion would propose that, contrary to suggestions by Burland and Hancock (1977), small ground movements can be achieved.

Additionally, high quality undisturbed block samples were obtained (with support from industrial sponsor Mott Macdonald) from three sites across Central London. These sites are all deep excavations into overconsolidated clays and never before have block samples been obtained from these depths (>30m). The materials collected were Lambeth Group Upper Mottled Beds and London Clay Units A2 and B2. These high quality block samples have been tested in their intact states using Rowe cell, oedometer and advanced triaxial apparatus.

It was found that the average insitu effective stress, p'_0, was effective at normalising stiffness degradation when plotted against strain. When compared with data obtained by Mott Macdonald on Crossrail sites and previously established bounds, stiffness degradation sits within the expected envelopes.

ACKNOWLEDGEMENTS

I would like to thank my sponsor Mott Macdonald who have provided opportunities to access very sensitive sites across Central London. Additionally there has been unprecedented access to data sets and unpublished material that has been important throughout the research. The second half of this thesis was only possible due to them.

Thank you to Harvey Skinner who dedicated much of his time to repairing, modifying and installing laboratory equipment. Even though everything that could go wrong did, he remained optimistic and always found a way.

I wouldn’t have been able to conduct field work without the endless support of my supervisor Joel Smethurst. There were numerous onsite frustrations and 4am starts to catch the first train into London. Joel provided hands-on solutions to working in and around a congested construction site.

CONTENTS

LIST OF TABLES

LIST OF FIGURES

LIST OF SYMBOLS

$A*$	Function of axial strain
c_u	Undrained shear strength
c_s	Swelling index undisturbed
c_c	Compression index undisturbed
c_r	Recompression index undisturbed
c_s^*	Swelling index Reconstituted
c_c^*	Compression index Reconstituted
c_r^*	Recompression index Reconstituted
C_E	Circumference of the excavation
CF	Clay fraction
D	Depth
D_E	Effective depth
D_c	Depth of concrete poured
e_0	Initial void ratio
e_j	Void ratio at effective stress j
E_u	Isotropic undrained Young's modulus
E'	Isotropic drained Young's modulus
E_h^u	Undrained horizontal Young's modulus
E'_h	Drained horizontal Young's modulus
E_v^u	Undrained vertical Young's modulus
E'_v	Drained vertical Young's modulus
$E_{s\ or\ sec}$	Secant Young's modulus
$E_{t\ or\ tan}$	Tangent Young's modulus

F_h	Horizontal modulus
G	Isotropic shear modulus
$G_{s\ or\ sec}$	Secant shear modulus
$G_{vh}\ and\ G_{hv}$	Shear modulus in the vertical plane
G_{hh}	Shear modulus in the horizontal plane
$G_{t\ or\ tan}$	Tangent shear modulus
H	Depth of excavation
I_v	Void Index
I'_p	Modified plasticity index
I_p	Plasticity index
k_s	Stiffness constant
k_h	Horizontal permeability constant
k_v	Vertical permeability constant
k	Isotropic permeability constant
K0	Ratio between horizontal and vertical effective stress
K	Isotropic bulk modulus
$K_{s\ or\ sec}$	Secant bulk modulus
$K_{t\ or\ tan}$	Tangent bulk modulus
L	Length
L_{BToe}	Length of wall from base of the excavation to wall toe
m_v	Coefficient of volume compressibility
M	Moment
OCR	Over-Consolidation Ratio
p'	Mean effective stress

p_0'	Normalising mean effective stress
p_{pre}	Preconsolidation pressure
q	Deviator stress
u	Pore pressure
u_a	Pore-air pressure
u_w	Pore-water pressure
v	Isotropic drained Poisson's ratio
v_u	Undrained Poisson's ratio
v_{hh}	Poisson's ratio horizontal to horizontal
v_{vh}	Poisson's ratio vertical to horizontal
v_{hv}	Poisson's ratio horizontal to vertical
V_{Sol}	Volume of the solids
V_s	Shear wave velocity
V_T	Total volume
V_V	Volume of the voids
V_x	Volume displaced by the wall
V_{xsToe}	Volume displaced below wall toe
V_{xTss}	Total volume displaced sub-surface by the wall
w	Moisture content
w_n	Natural moisture content
w_p	Plastic limit
w_L	Liquid limit
x_{Toe}	Wall displacement at toe
x_{Max}	Maximum sub-surface horizontal displacement

Y_n	Yield locus number n
z	Depth below surface
Z_T	Total heave
Z_U	Undrained heave
Z_S	Short-term heave
Z_L	Long-term heave
Z_t	Heave after time t
$\mathrm{Z}_{x,U}$	Undrained heave predicted using wall movement
ρ	Density
ρ_B	Bulk density
ρ_w	Water density
ρ_d	Dry density
ϕ	Angle of friction
ϕ_{crit}	Critical angle of friction
ϕ_{peak}	Peak angle of friction
σ'_v	Vertical effective stress
σ'_h	Horizontal effective stress
σ'_a	Effective axial stress
σ'_r	Effective radial stress
σ'_{xx}	Effective stress in the horizontal x axis
σ'_{yy}	Effective stress in the horizontal y axis
σ'_{zz}	Effective stress in the vertical z axis
τ_{xy}	Shear stress in horizontal plane
τ_{yz}	Shear stress in vertical plane

τ_{zx}	Shear stress in vertical plane
σ	Total Stress
ε_v	Vertical Strain
ε_h	Horizontal strain
ε_r	Radial strain
ε_a	Axial strain
ε_p	Volumetric strain
ε_q	Distortional strain
ε_{xx}	Strain in the horizontal x axis
ε_{yy}	Strain in the horizontal y axis
ε_{zz}	Strain in the vertical z axis
Ω_d	Invariant strain
γ_{xy}	Shear strain in horizontal plane
γ_{yz}	Shear strain in vertical plane
γ_{zx}	Shear strain in vertical plane
Prefix Δ	Indicates change of
Prefix δ	Indicates small increment
Subscript 0	Indicates initial or at very small strain
Subscript i	Indicates a layer
Subscript n	Indicates a number

1. GENERAL INTRODUCTION

1.1. Background of the research

Excavations into Overconsolidated Clay (OC) are becoming increasingly deep around the world (Simpson & Tatsuoka, 2008) to provide functional areas such as transport hubs. These basement structures pose significant engineering challenges since there are often uncertainties relating to ground movements on and around the site.

As soil is excavated to form the basement, this reduces the total stress on the expansive soil beneath. The result is the water in the soil pores acts in tension in what is termed an 'undrained' response. In the long-term, pore pressures return to equilibrium values based on surrounding groundwater conditions; this causes the expansive soil to swell. This process can take decades in low permeability materials.

An important measure taken to mitigate ground displacements is a ground-contacting basement slab which is cast at the base of an excavation. Once constructed the basement slab experiences a combination of earth and water pressure that are believed to build over decades. This technique is believed to not only significantly reduce vertical heave but reduce lateral movement of the retaining walls of the excavation. It is worth noting the alternatives to ground-contacting basement slabs which are: to leave a void that the clay can heave into, an example being Lions Yard (Ng, et al., 1998); or the basement slab can be ground-contacting but hinged to allow some heave, an example being Aldershot Road (Carder, et al., 1997).

Although ground-contacting basement slabs have been used on several projects in the past (Burland & Kalra, 1986; Wood 2000), little monitoring of the pressure that builds beneath the slab has been carried out. Current design procedure assumes no dissipation of earth or water pressure prior to slab being cast which may lead to an over-engineered solution.

Also, recent investment in the London Underground (LU) transport network, has brought with it the opportunity, via the industrial sponsor of this thesis Mott Macdonald, to obtain high quality undisturbed block samples from three sites across London. These materials are: London Clay Units B2 and A2; and Lambeth Group Unit Upper Mottled Beds. Although, some testing has been conducted on undisturbed samples of over-consolidated (OC), London Clay, there is no published literature on block samples of over-consolidated clays taken from depths over 30m. Additionally, the Upper Mottled Beds (UMB) have rarely been of

engineering concern until recently and the little testing that does exist is industry focussed. Therefore, there is a real gap in knowledge that surrounds over-consolidated clays at greater depths.

1.2. Aim and objectives

This research set out to better understand earth and water pressures beneath a ground-contacting basement slab and to analyse the effectiveness of ground movement restriction both during and after construction. Additionally, there is a real knowledge gap that surrounds overconsolidated clays at greater depths; therefore, block samples were to be obtained from very deep excavations (>30m) and then engineering properties tested for at the University of Southampton.

To achieve these aims, the objectives are to:

- Review deep basement site monitoring in current/past literature and use this data to draw up relationships describing predicted ground movements over time.
- Install field instrumentation within a basement structure
- Monitor field instrumentation and then compare the results to the literature
- Plan and then obtain block samples from three deep basements across London.
- Rigorously test block samples with all available apparatus at the University of Southampton
- Compare laboratory testing to existing body of literature

1.3. Structure of the thesis

This thesis has seven chapters. Chapter 2 begins with an introduction to overconsolidated clays, characterising and describing behaviour at different strain ranges. The key body of literature is presented and the properties of soils tested are described in detail.

Chapter 3 presents a literature review of site monitored deep basements and relationships between the sites are discussed.

Chapter 4 begins with an introduction to the site instrumentation for monitoring at VSU. Then the installation of the instrumentation is outlined before the results are then presented. Finally, a discussion of the results outlines best practice for designing deep excavations into overconsolidated clays.

After Chapters 3 and 4 provides a comprehensive engineering understanding to current deep basement design, construction and measures to mitigate ground movements, the remainder of the thesis sets out to better understand the clays these engineering structures are built in. Chapter 5 begins by bringing in literature specific to laboratory testing procedure and then, apparatus based at The University of Southampton will be introduced. Finally, preparation methods and procedures used on the described equipment will be detailed from site collection to final placement of soil specimen into apparatus.

A continuation of laboratory-based work is then further presented in Chapter 6 in the form of results to basic forms of testing such as oedometer and X-ray diffraction. This chapter focuses on large strain behaviour, discusses the results and provides insight into the results.

Chapter 7 further explores soil behaviour in a triaxial apparatus and focuses on small strains. Finally, Chapter 8 is conclusions and further work.

2. AN INTRODUCTION TO OVERCONSOLIDATED CLAYS

2.1. Introduction

Overconsolidation occurs when the current stress acting on soil is less than the applied stress in the past. Insitu this typically occurs when a deposition process is followed by erosion at the surface.

This chapter contains an introduction to over-consolidated (OC) clay characteristics and behaviour under strain. Important characteristics such as stiffness degradation over strain and yielding behaviour are described in detail. Finally, the mineralogy and properties of the materials tested later in the thesis are discussed.

2.2. Characteristics and behaviour of over-consolidated clays

2.2.1. Stiffness Degradation

The stiffness of clay is an important parameter when predicting soil swelling. There are many parameters associated with stiffness such as: shear and bulk moduli; drained and undrained elastic moduli; tangent and secant moduli, etc. However, all the stiffness parameters degrade non-linearly with strain; shown in Figure 1 for the elastic Young's modulus.

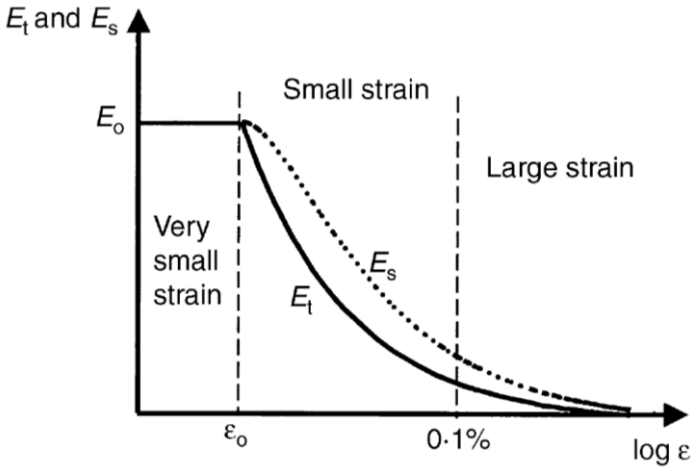

Figure 1: A typical non-linear strain – elastic Young's modulus relationship (Atkinson, 2000)

A summary of soil stiffness non-linearity in design has been provided by Atkinson (2000) and importantly it gives some common behaviour amongst clay soils. However, this may over-simplify the complexity of the stiffness-strain relationship when compared to testing by authors such as Hight et al. (2007) and Yimsiri and Soga (2011). Firstly, Hight et al. (2007) found that for undrained triaxial extension and compression tests on London Clay, modulus decay curves differed between lithological units and were below previous established bounds,

Figure 2. Additionally, Yimsiri and Soga (2011) found differences between horizontally and vertically cut specimens and between London Clay and Gault Clay, Figure 3. Both sets of authors found variation in the decay curve shape.

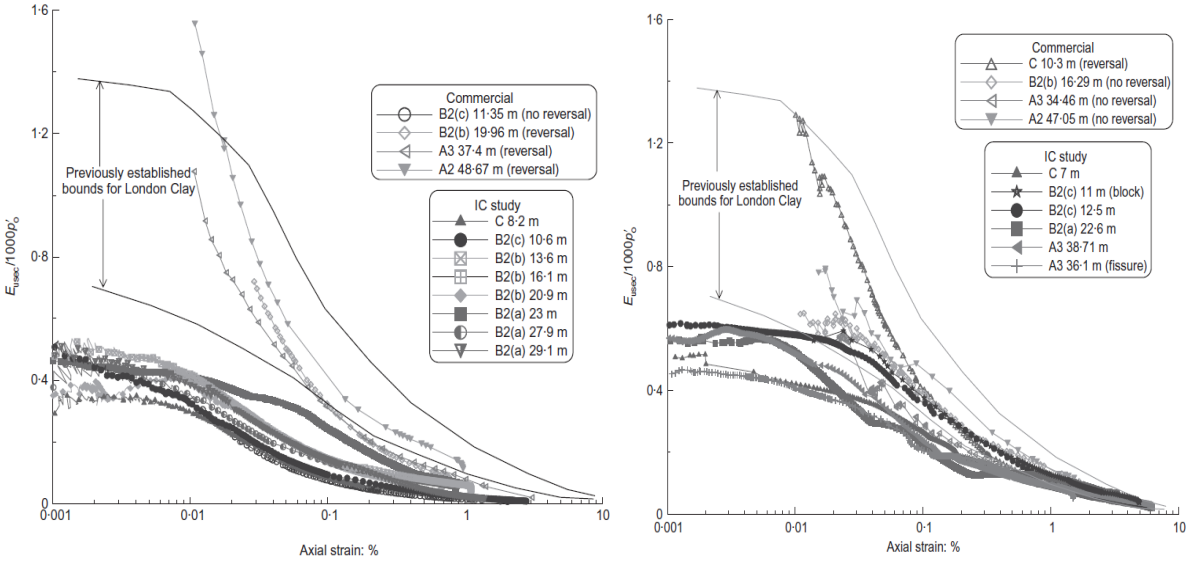

Figure 2: Normalised modulus decay curves for a) undrained triaxial extension and b) undrained triaxial compression of samples of London Clay taken from Terminal 5 Heathrow (Hight, et al., 2007)

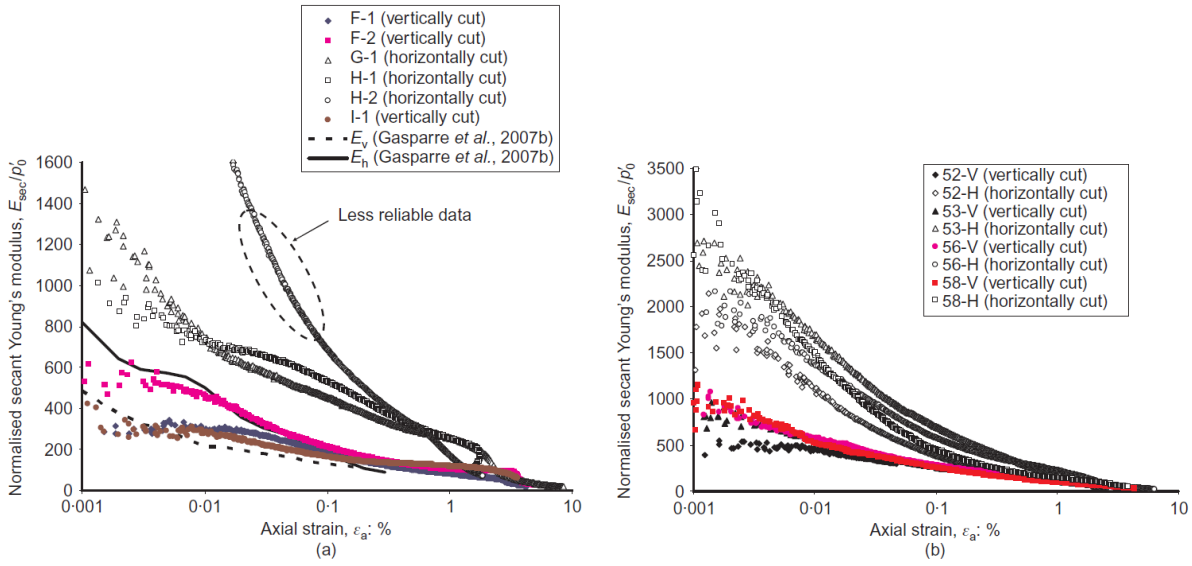

Figure 3: Normalised secant Young's modulus degradation curves a) London Clay b) Gault Clay (Yimsiri & Soga, 2011)

Differences between horizontally and vertically cut specimens can be seen for other materials; Ratananikom et al. (2013) has found that stiffness and stiffness degradation vary in Bangkok Clay for both drained and undrained conditions, Figure 4.

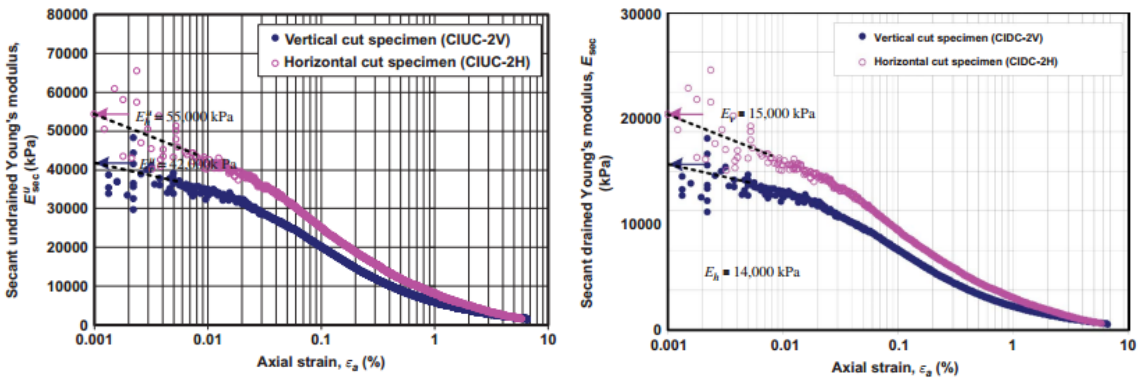

Figure 4: Triaxial compression on Bangkok Clay on vertically and horizontally cut specimens a) Undrained b) Drained. (Ratananikom, et al., 2013)

Very small strain

Very small strains are defined as strains below 0.001% (Atkinson, 2000) and the behaviour of deformation is considered by some to be recoverable and linear elastic. Studies into this region by Jardine (1992) have shown that the linear elastic behaviour only exists for a small range of strains. In addition, Clayton and Heymann (2001) studied this region through triaxial testing on three materials, one of which was London Clay, and they found that the behaviour 'appeared' to act linearly until around 0.002-0.003% strain, Figure 5.

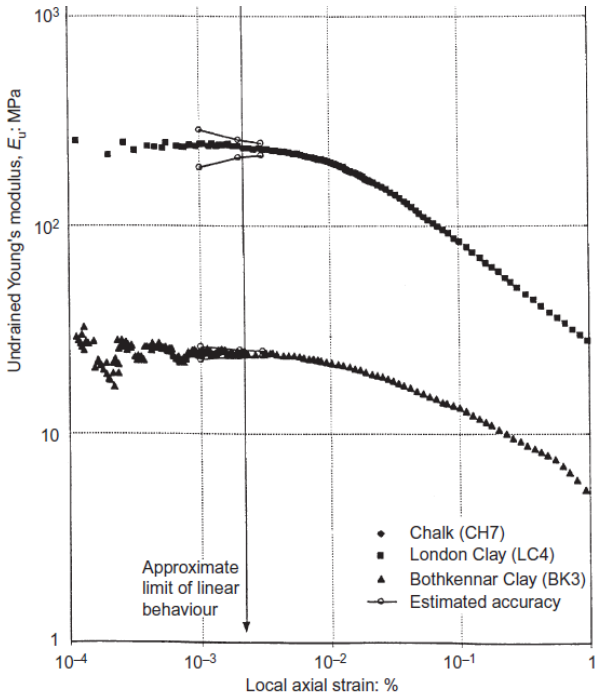

Figure 5: Initial stiffness degradation of London Clay and Bothkennar Clay (Clayton & Heymann, 2001)

On the other hand, due to contact mechanics and micro-yielding it could be argued that this behaviour is not truly linear at all. In fact, Collins (2005) argues that at the micromechanical level 'trapped elastic energy' gained by compression can only be released by plastic

rearrangement strains; therefore, the process is not truly linear or elastic. Whatever the true behaviour, the stiffness is considered a constant for most engineering applications.

Although the very small strain region is small and has little engineering consequence (Simpson, 2010), the initial shear modulus, $G_{0,}$ is an important value. Extensive research into the influence of stress history and over-consolidation has led to a number of proposed relationships, most notably Hardin (1978) and Viggiani & Atkinson (b) (1995), which show initial stiffness to be proportional to the over-consolidation ratio (OCR):

$$G_0 \propto OCR^{\gamma} \tag{2.1}$$

where γ = material constant. However, it is the relationship between the secant shear modulus, G_{sec} and mean effective stress, p' which can be more useful in engineering terms. This equation is given below:

$$G_{sec,0} = A_0^* p'^{0.6} \tag{2.2}$$

Where, A_0^* is the initial value of the function A* which is related to axial strain. The power of 0.6 is based on the work of Viggiani and Atkinson (a) (1995). The benefit of Equation 5.2 is that G_{sec} can be obtained through bender element test data or insitu geophysics data as:

$$G_0 = \rho V_s^2 \tag{2.3}$$

Where V_s is the shear wave velocity through the sample and ρ is the sample density.

The above relationships may be applied to an isotropic understanding of clay but if applied to an anisotropic analysis the relationships would be different. Firstly, $G_{sec,0}$ in Equation 2.2 would be replaced by the initial vertical shear modulus, $G_{vh0,}$ and a relationship between the initial vertical shear modulus and initial horizontal shear modulus G_{hh0} is needed. This relationship is suggested by Nishimura (2005) to be G_{hh}/G_{vh}=1.8-2.2 for London Clay.

Small Strains

Research into the small strain region, which lies between 0.001% and 0.1% strain (Atkinson, 2000), is subject of much debate because of the varied response different soil properties have in relation to strain. Strains found in the field are commonly within the small strain region at 0.01%-0.1% strain; this makes the small strain the most important region to understand.

At the lower end of the small strain region, Jardine (1992) showed that some non-linear strain was fully recoverable for first time loading on Magnus till to around 0.01%, Figure 6. Beyond

this, plastic straining occurs which makes the small strain region particularly difficult to model. It is also shown that the onset of plastic straining varies for each material.

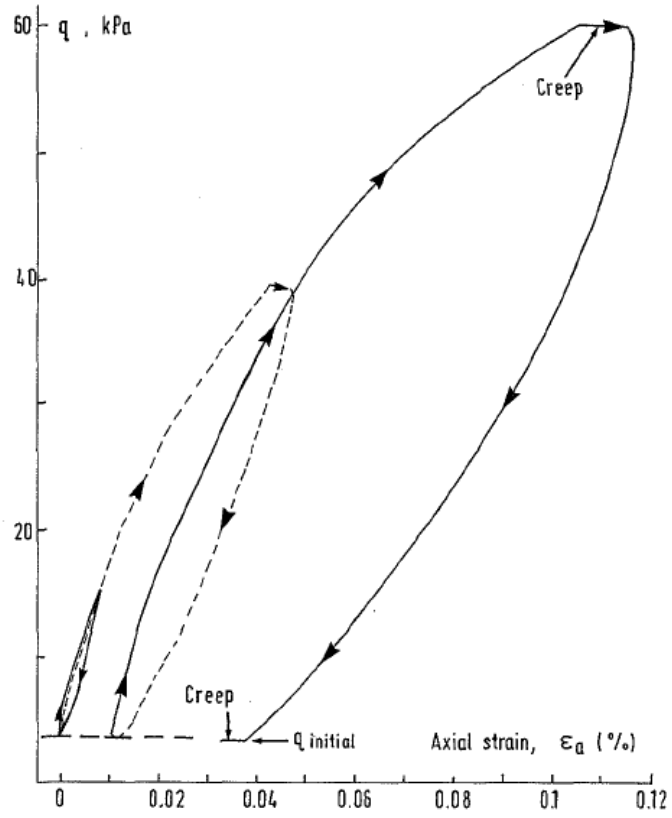

Figure 6: Small-strain load-unload test on Magnus Till (Jardine, 1992)

The stiffness of clays is thought to undergo the largest change in terms of engineering parameters as plastic strains increase. Many models have been designed to represent mathematically this degradation in stiffness (Jardine, et al., 1986; Simpson, 1992; O'Brien & Sharp, 2001a); however, the complexity and variability of clay stiffness degradation means that the balance between a simple model with attainable parameters and a truly representative model which accounts for the many variables that result in strain has been difficult to judge.

The small strain region may be further complicated by a transition from using anisotropic elastic parameters which degrade into isotropic plastic parameters which can be seen in Figure 7.

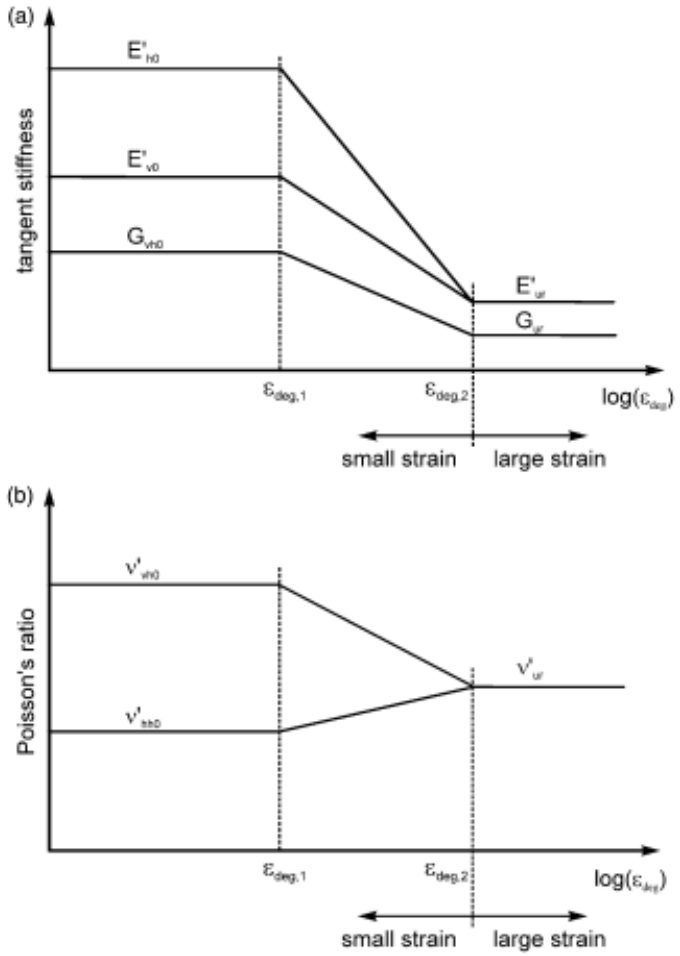

Figure 7: Degradation of anisotropic a) small strain stiffness moduli b) Poisson's ratios (Schadlich & Schweiger, 2013)

Large Strains

Defined as strains above 0.1% (Atkinson, 2000), the large strain region sees a further reduction in stiffness at an inversely proportional rate before a critical minimum stiffness is reached. For very deep construction into unrestrained, swelling clays the critical minimum stiffness is very important as a significant proportion of the heave at the base of an excavation may occur in this 'post-rupture' plastic region. However, Jardine et al. (2004) summarised the main factors for engineering performance of clays as stress history, formative history, microstructure, rate effects and fabric which suggests that performance of clays will be highly variable.

Many authors have published data on over-consolidated clays which have been strained to failure; either to find the peak and critical strengths (Atkinson, 2007), to examine the large strain behaviour (Gasparre, 2005) or to justify a new model (Yao, et al., 2012).

Yao et al., (2012) have proposed a model which neglects the 'true' behaviour of the clay and goes about 'curve fitting' OC clay in triaxial tests. They do this by using an additional yield surface which is called the "reference yield surface". The additional surface accounts for plastic deformations within a classic yield surface creating a region in which the soil can act partially elastic and plastic. Results for heavily OC clays give good agreement, Figure 8, and the model may be of some use to engineers in large strain situations.

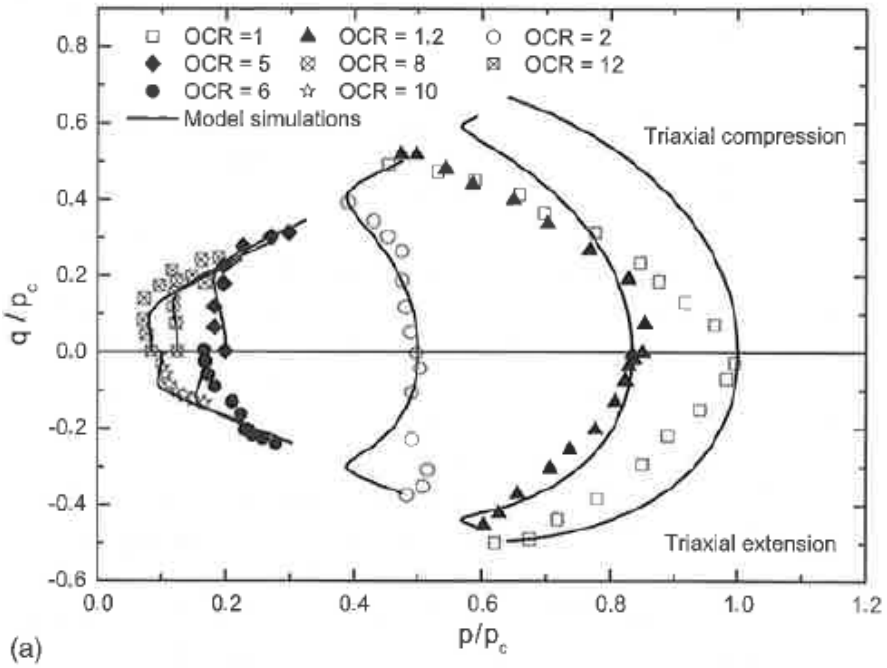

Figure 8: Comparison of test results on Kaolin Clay (Yao, et al., 2012)

2.2.2. Yielding behaviour

The process of yielding for a soil is not instantaneous, shown by the non-linear degradation of stiffness with strain. Models try to simulate this behaviour in different ways but it has become accepted by many that there are many yield points or stages. These are described in the literature as kinematic, yield or 'bubble' surfaces and several models account for this (Al Tabbaa & Muir-Wood, 1989; Jardine, 1992; Simpson, 1992; Stallebrass & Taylor, 1997). However, the most widely accepted framework of clay behaviour is that proposed by Jardine (1992), where there are three yield points, named Y1, Y2 and Y3, and three zones between these yield points. The yield surfaces are explained below and a sketch is provided in Figure 9.

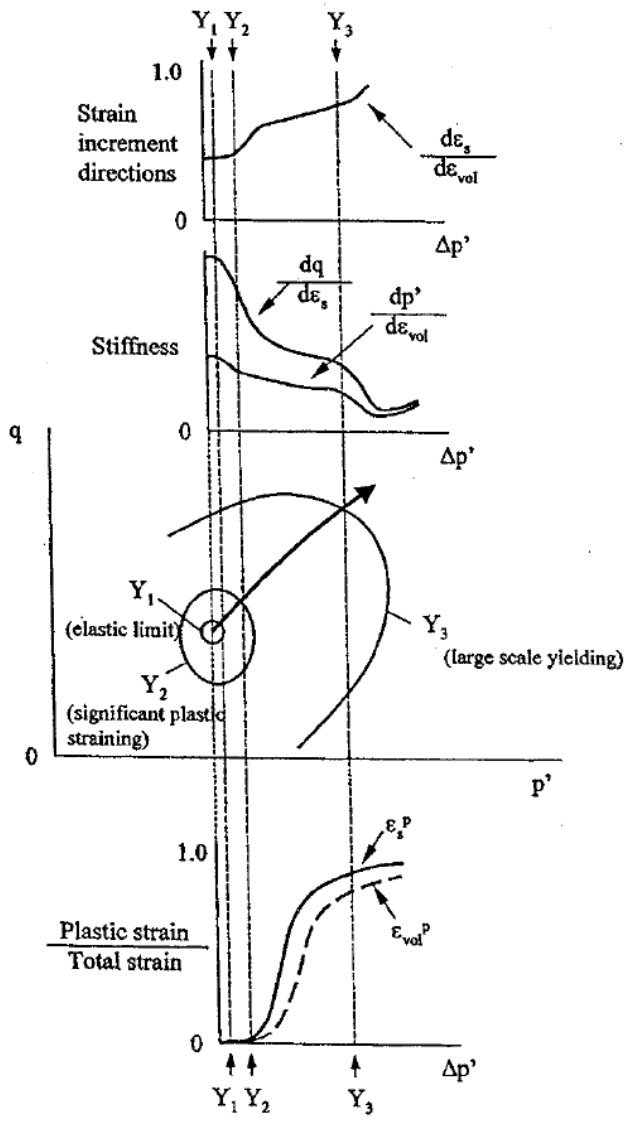

Figure 9: Scheme of multiple yield surfaces (Jardine, 1992)

Y1 yield surface

As strains increase to the limit of the debatably 'linear' elastic region, named zone 1, the clay is thought to reach its' first kinematic yield surface Y1. This, as mentioned in 2.3.2, was found by Clayton and Heymann (2001) to be 0.002-0.003% strain for London Clay. However, Gasparre et al. (2007) found this surface at around 0.0008% axial strain for a unit B2c sample of London Clay. In addition, the authors plotted the Y1 surface as a normalised contour for units A3(2), B2a, B2c and C of London Clay in Figure 10.

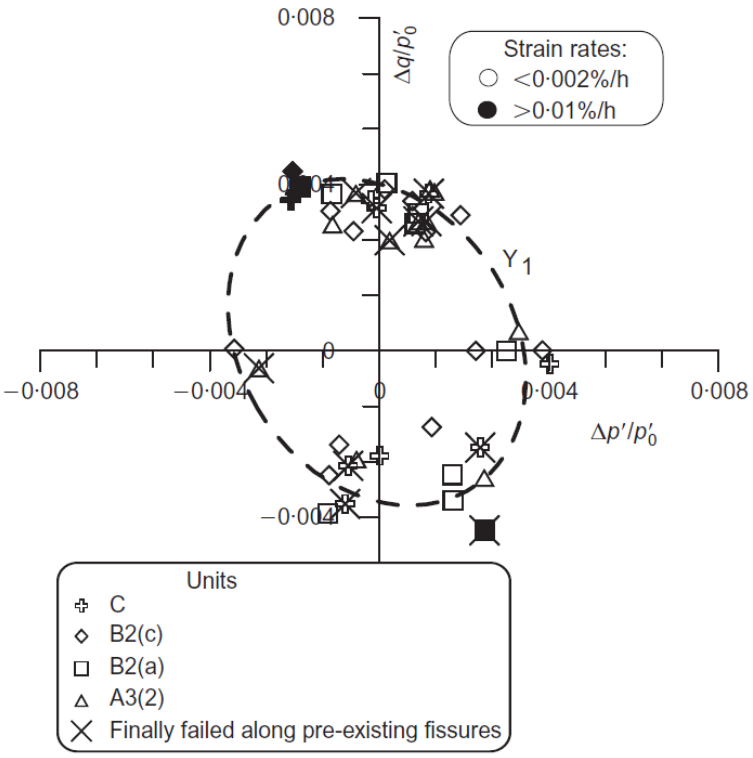

Figure 10: Normalised contour for the Y1 surface (Gasparre, et al., 2007).

Y2 yield surface

Between the Y1 surface and the Y2 surface, the region is termed zone 2 and behaviour is assumed to be non-linear recoverable. As the Y2 yield surface is reached plastic deformation begins meaning the Y2 surface can be seen as the onset of plastic deformation. This is termed the critical strain (Jardine, 1992) and was found to be 0.04% strain for London Clay by Takahashi (1981). Later, Gasparre et al. (2007) showed this to be closer to 0.03% volumetric strain for drained tests on London Clay samples taken from sub unit A3(2) or 0.04%-0.05% strain for undrained triaxial compression tests on London Clay sub units B2c, B2a and A3(2). In addition, the authors plotted a normalised contour for the Y2 surface, seen in Figure 11.

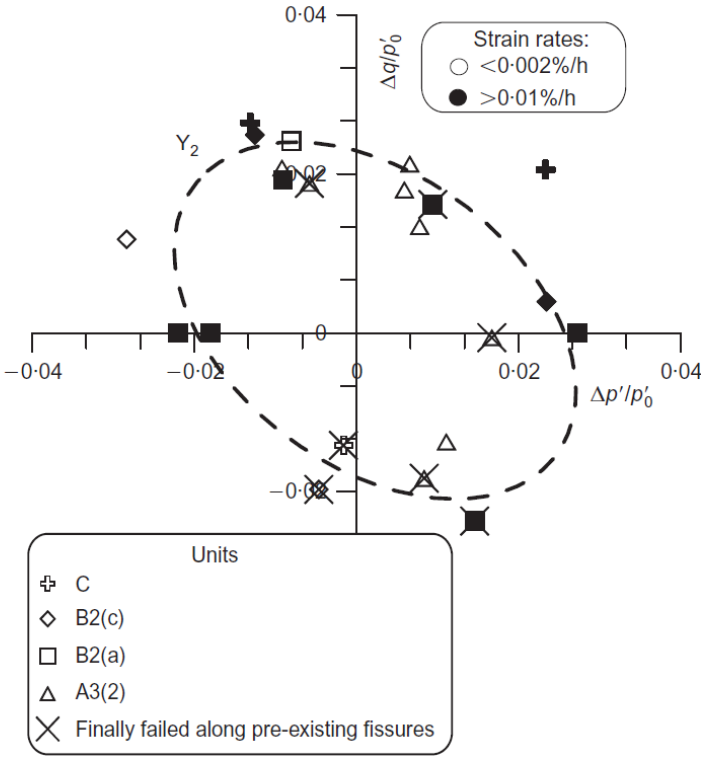

Figure 11: Normalised contour for Y2 surface (Gasparre, et al., 2007).

Y3 yield surface

Beyond the Y2 surface lies zone 3 which becomes progressively more important as the ratio of plastic to total strains increases as shown in Figure 9. Strains will increase until the local boundary surface is reached, known as the Y3 yielding surface. The local boundary surface occurs inside the state boundary surface where the soil will have completely yielded and post rupture behaviour becomes important in understanding the stress path to the critical state. Once reaching the state boundary surface clay will dilate or contract depending on boundary conditions (Jardine 1992). To identify the local boundary surface, changes in tangent stiffness, direction changes of effective stress paths in undrained tests and changes in strain increment direction for drained tests can be used (Gasparre 2005).

2.3. Test Materials

2.3.1. Further background

London Clay has been studied for decades through field observations but the introduction of sophisticated laboratory testing in the late 20th century led to the development of more complex soil models which can be used with finite element software. At first London Clay stiffness was described using a constant value of Young's Modulus (Measor & Williams, 1962), but was soon related with the undrained shear strength; which was found to vary with depth (Burland & Hancock, 1977; Stroud, 1989). At this time London Clay was considered isotropic for analytical purposes but authors begun to realise that properties varied laterally to vertically (Burland & Kalra, 1986).

More recent studies on London Clay (Nishimura, 2005; Gasparre, 2005; Hight et al., 2007; Pantelidou and Simpson, 2007; Yimsiri and Soga, 2011) have shown that over-consolidated, stiff, sedimentary clays are complex, anisotropic and variable over the depth of the formation. Gasparre (2005) found that grading curves, Atterberg limits and water contents varied over the five lithological units tested; Units A2, A3, B1, B2 and C. Also, shearing and compressive behaviour was affected by the structural differences of the units. Other notable findings were: the presence of kinematic yield surface proposed by Jardine (1992); effects of strain rate and pre-existing fissures; and investigation of pre-consolidation pressures. Nishimura (2005) found that high resolution local instrumentation was needed in hollow cylinder experiments to examine pre-failure deformation characteristics. Also, that: void ratio, over-consolidation ratio (OCR), effective stress, shear strain, creep and aging influence small strain stiffness. Anisotropy was the focus of Nishimura's study and the material was found to be highly anisotropic. The importance of shear waves in determining initial shear stiffness was stressed with numerous more recent studies using bender elements on a range of global clays (Ratananikom et al., 2013; Teng et al., 2014; Mitaritonna et al., 2014).

In recent years, another expansive soil, the Upper Mottled Beds (UMB) of the Lambeth Group Formation, has come to the attention of the geotechnical engineering community. This previously, relatively untested stratum was rarely encountered due to its relative depth beneath the London Clay Formation. However, Skipper (1999) realised that although the stratum had begun to be encountered, documentation of the material was sporadic and collation was needed. Skipper (1999) provided the basis for the British Geological Survey who ordered the creation of a report which compiled data from sites which had encountered

The Lambeth Group which was then written by Entwisle et al. (2013). At the time of these major publications, little was known about the Upper Mottled Beds so most engineering behaviour was assumed from earlier work on London Clay.

However, during the period that the research in this thesis was conducted, investment in new underground rail in the form of Crossrail led to a large body of research being conducted on these strata. As this data are unpublished and is the property of Crossrail, permission was gained to use this data as a comparative tool and to improve the analysis produced late in the thesis. What was found from this data are that this stratum is highly variable when compared to London Clay (Black, 2009).

2.3.2. Formation

Lambeth Group – Upper Mottled Beds

Broadly, the Lambeth Group is: highly variable vertically and laterally; underlies much of London and Hampshire; and can be split into three formations. It is generally within 50m of the surface and because of its geographical location, it is of great engineering significance, particularly as excavations are becoming increasingly deep in the centre of London.

The Lambeth Group used to be named the Woolwich and Reading Beds, but it contains three formations which are: Woolwich Formation; Reading Formation; and Upnor Formation. The Woolwich formation contains: Upper Shelly Clay; Laminated Beds; and Lower Shelly Clay. The Reading Formation contains: Upper Mottled Clay and Lower Mottled Clay. The Upper Mottled Clay is referred to in this thesis as the Upper Mottled Beds (UMB) which is the term used in industry practice.

The Lambeth group contains sequences of near-shore, lagoonal, estuarine and alluvial deposits of the Palaeogene. A varying sea level altered the depositional environment several times which caused alternating layers of clays and shelly clays, Figure 12. The UMB was formed after a drop in sea level and/or uplift created a terrestrial environment.

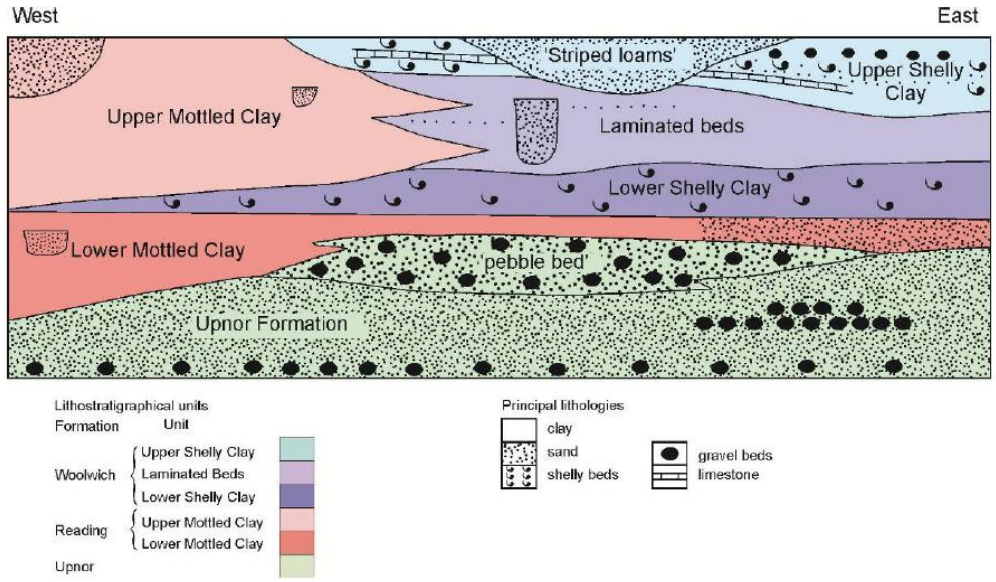

Figure 12: Schematic diagram showing the relationship of the informal lithological units in the Lambeth group in Central London (Entwisle, et al., 2013)

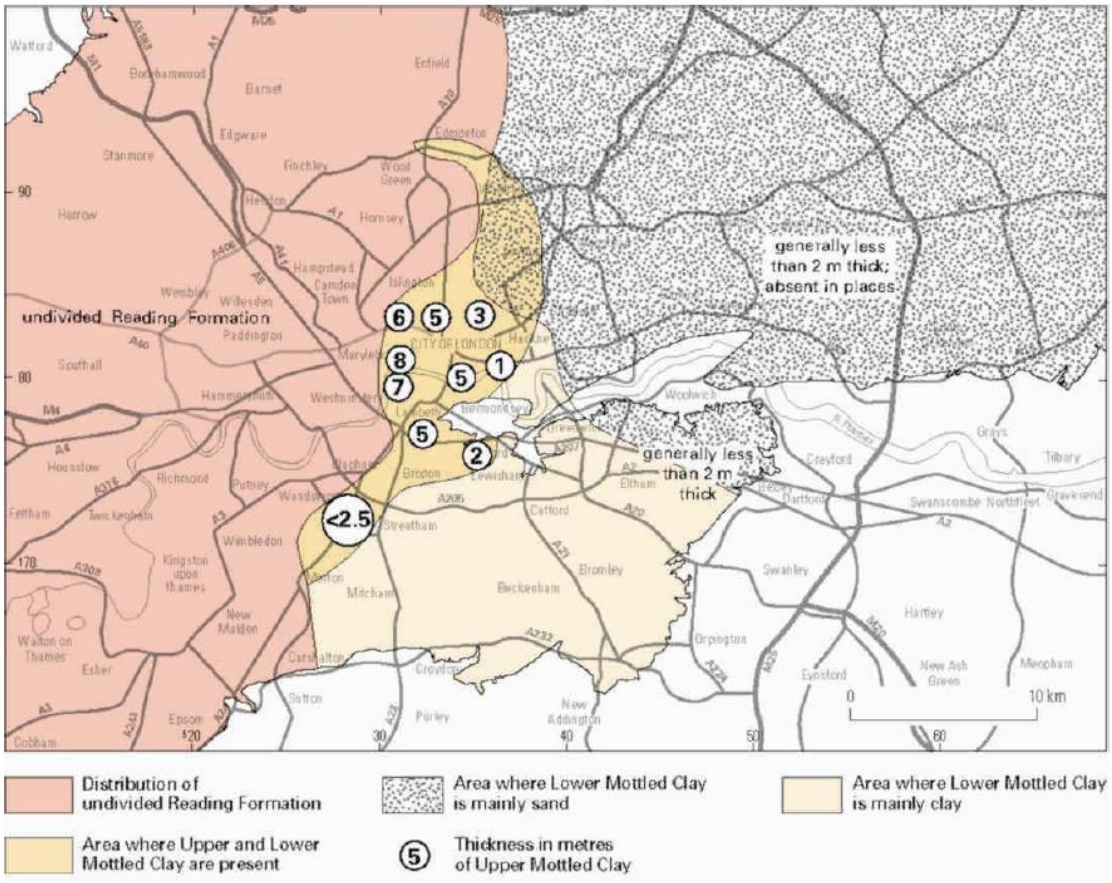

Figure 13: Reading Formation distribution and main lithologies in London (Entwisle, et al., 2013)

At the site where the UMB was taken (described in 5.4.1), there is both Upper and Lower Mottled Clay present and the two clays are separated by Woolwich Formation, Figure 13. However, in areas where this separation does not exist, the differentiation between the two clays is difficult to spot. Both the UMB and LMB are reported to have red mottling in the brown clay which is an iron oxide, the key difference in terms of appearance between the two clays is that the UMB has a carbonaceous grey, blue or black layer near the base while the LMB has a pale or bleached top.

Data for the UMB alone was not commonly separated from the LMB until recent developments in the London Underground. Both for the Jubilee Extension Line (JLE) and now Crossrail, a significantly large dataset now exists showing that UMB can vary widely from a clay fraction of 2-98%, Figure 14. However, it should be noted that the methodology for attaining clay fraction is not always indicated and it is shown by Redshaw (2015) that pipette and hydrometer tests may under-predict clay fraction when compared to X-ray diffraction (XRD); while it is possible XRD over-predicts when compared to the aforementioned methods.

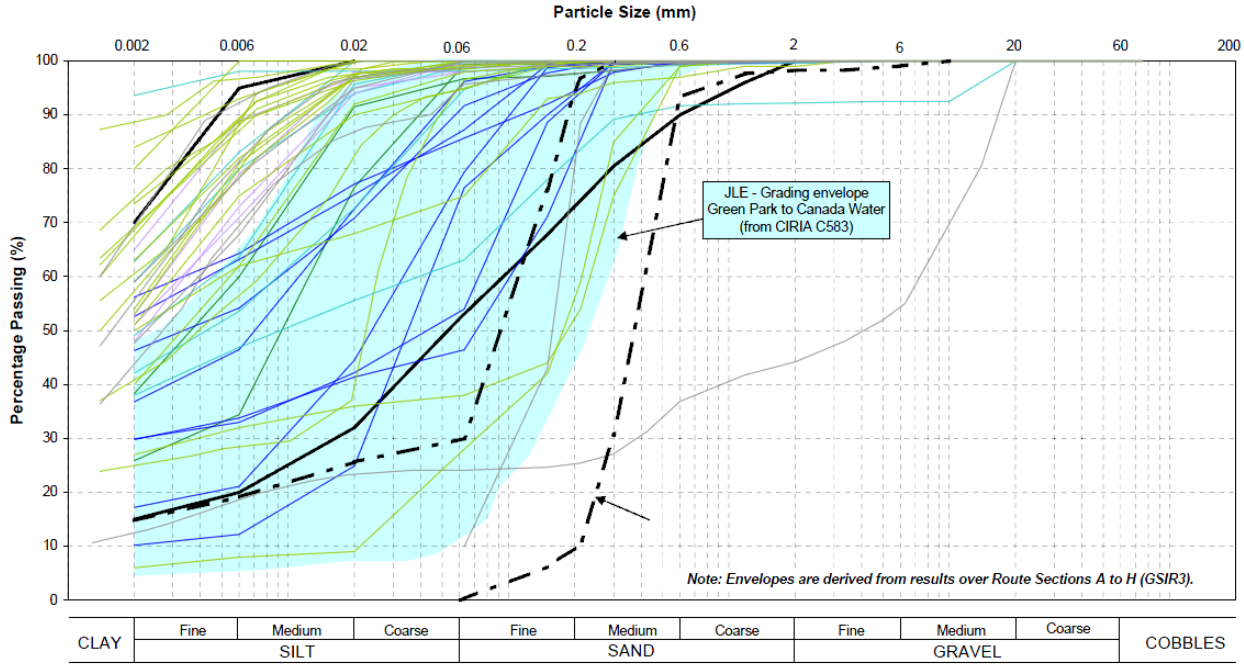

Figure 14: Particle size distribution for UMB (Black, 2009). Data presented compares Crossrail to Jubilee Line Extension (JLE) results

During the Palaeogene period, a sub-tropical climate affected all formations of the Lambeth group. More specifically, oxidation has caused mottling in the clay and clay coatings have devolved on sand grains due to clay enrichment. Additionally, fissuring and laminations have

formed due to desiccation; these can appear polished. Also, fissurings have been reported at several spacings: 4mm spacing; 100mm scale; and 1000mm scale.

Later, the Lambeth Group was buried beneath several hundred metres of sediments; this included the London Clay Formation. Not less than 250m of the sediment was subsequently eroded (Entwisle, et al., 2013), therefore, the material is heavily over-consolidated and has undergone swelling and uplift. A possible consequence is that cementation, the process that sticks particles together when minerals like iron oxides form around soil particles, may have affected clay's stiffness but it is not known whether this would result in a reduction in swelling.

London Clay – Units A-B

London Clay was deposited in the Eocene period between 52 and 55 million years ago (De Freitas & Mannion, 2007). The most common lithology used is that based on King (1981) but further classification of sub-units has continued as London Clay is among the most examined clays in the world. The formation was deposited in marine conditions when sea levels were rising and the London and Hampshire Basins were subsiding. Unlike the Lambeth Group, a single continuous deposition occurred with lithological units indicating sea level changes; this makes London Clay much less variable and 90% consists of clay, silt and silty sands (Nishimura, 2005). However, on close inspection there are clear differences between lithological units and some contain wood fragments, claystones, signs of bioturbation, pyrite and sand layers. The distribution of the London Clay Formation can be seen in Figure 15.

In this thesis, two-three units of London Clay are tested. The first is Unit B2 which may be further sub-classified to Unit B2 (b or c) depending on further analysis. Unit B2 is a relatively homogeneous silty clay with occasional claystones and some thin very silty and sandy beds. The thickness is usually around 25m making it a commonly encountered unit on construction sites around London.

The second is Unit A2 from two depths. This unit is around 12m thick and is very silty clay with sandy clay beds. There are commonly wood fragments found in the upper part of A2 with pyrite nodules visible without close inspection. Near the base of unit A2 there is a sandy glauconitic clay which may be sub- classified as Unit A2(1) while the clay above this is sub-classified as Unit A2(2). Samples were collected from both these sub units for testing described later in this thesis. A detailed description of the lower units of London Clay taken from a borehole is given in Figure 16.

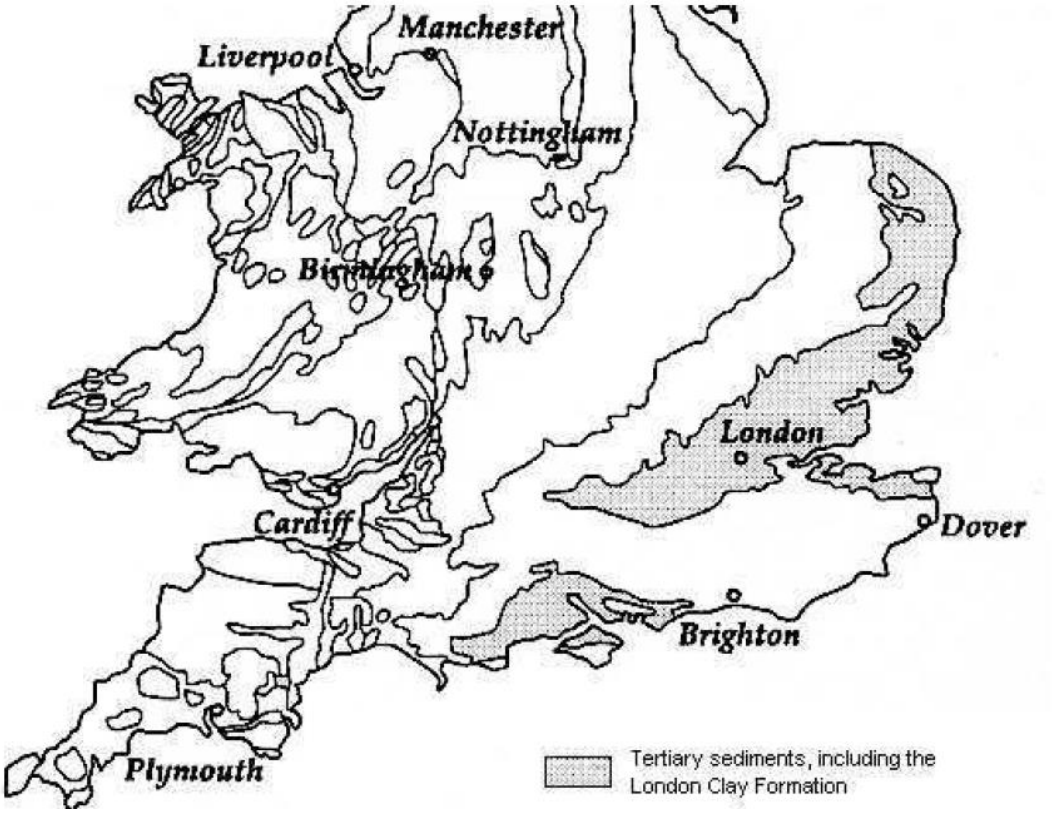

Figure 15: Distribution of the London Clay Formation (Nishimura, 2005)

Data taken from Crossrail shows small differences in the clay contents of each lithological units. For unit B clay fraction is between 40-75% and less than 5% of particles are larger than silt. For unit A2 clay fraction is between 25-65% and up to 50% of particles are larger than silt (Black, 2009). As previously mentioned, Redshaw (2015) found the method for attaining clay fraction has an impact but as a comparison between units and materials it shows that unit A2 is a more variable material than unit B2.

It should be noted that Units A3 and B1 separate Units B2 and A2 and that Unit A3 is subdivided into two sub-classifications A3(1) and A3(2). A3(1) is considered a fairly homogeneous silty clay while A3(2) differs as it has thin sand/silt partings with some calcareous concretions. Unit B1 bears some resemblance to Unit A2(1) as it is a sandy glauconitic clay.

2.3.3. Mineralogy and Fabric

Upper Mottled Beds

Illuviation (deposition of minerals leached from above) and eluviation (transport of that leached minerals) through pedogenesis (process of soil formation) have both contributed to

the colouring of the UMB, seen in Figure 17, as it has become mottled but also wetting and drying cycles may have cemented fissures together with infilling of iron oxides. This may have a significant impact when strength testing in the laboratory.

Non-clay minerals like Quartz, Silica, Feldspar and Iron are all found in the UMB. Quartz can be found throughout the Lambeth group and particles can range from clay to sand size. Silica can be found in the upper part of the UMB in the form of flint gravel and appears black, dark grey or green unless affected by pedogenesis then it is brown or white with a red core. Feldspar is found but as a minor component. Iron or specifically iron-bearing minerals give the UMB its wide colour variations. Minerals include: pyrite, limonite, haematite, magnetite/ilmenite, goethite, jarosite, lepidocrocite and leucocene. It is thought that the oxidation of pyrite is largely responsible for the red mottling. This would have occurred in a sub-tropical weathering process; where during a dry cycle oxidation was deepened though shrinkage cracks (Entwisle, et al., 2013).

The clay mineralogy of UMB, seen in Figure 18, is found to differ in each basin but typically has mixed clay assemblage of smectite, illite, chlorite and kaolinite with a reduction of smectites in the South and West Hampshire Basin. The illite and chlorite is thought to be derived through erosion of rocks and subsequent deposition. The origin of smectite rich sediment is still debated as authors such as Gilkes (1969) believe the erosion and dissolution of chalk in a wet sub-tropical climate creates the smectite while Spinola et al. (2017) believe weathering occurs in a semi-arid climate as it better fits the timeline.

London Clay

Unit B2 has been one of the units tested under X-Ray Diffraction (XRD) and Scanning Electron Microscope (SEM) by Gasparre (2005) and is discussed by Gasparre et al. (2007). It was found that Unit B2, which was sub classified as B2(a), has a homogeneous fabric possibly because of bioturbation and has: an illite content of 21%; smectite content of 63%; chlorite content of 3%; kaolinite content of 11%; and a quartz content of 36.8%.

The clay mineralogy of the lower units A2(1) and A2(2) are similar to the upper B2 units as they consist of a mixture of illite, smectite and kaolinite. Other constituents are quartz, feldspar, calcite, pyrite, and significant amount of fossilised plants, plankton and sea creatures. In general, smectite levels are higher across Unit A2 than Unit B2 as illite levels are reduced. Chlorite only forms a very small part of Unit A2 while quartz quantities are similar to Unit B2 (Figures 19 (a) and (b)).

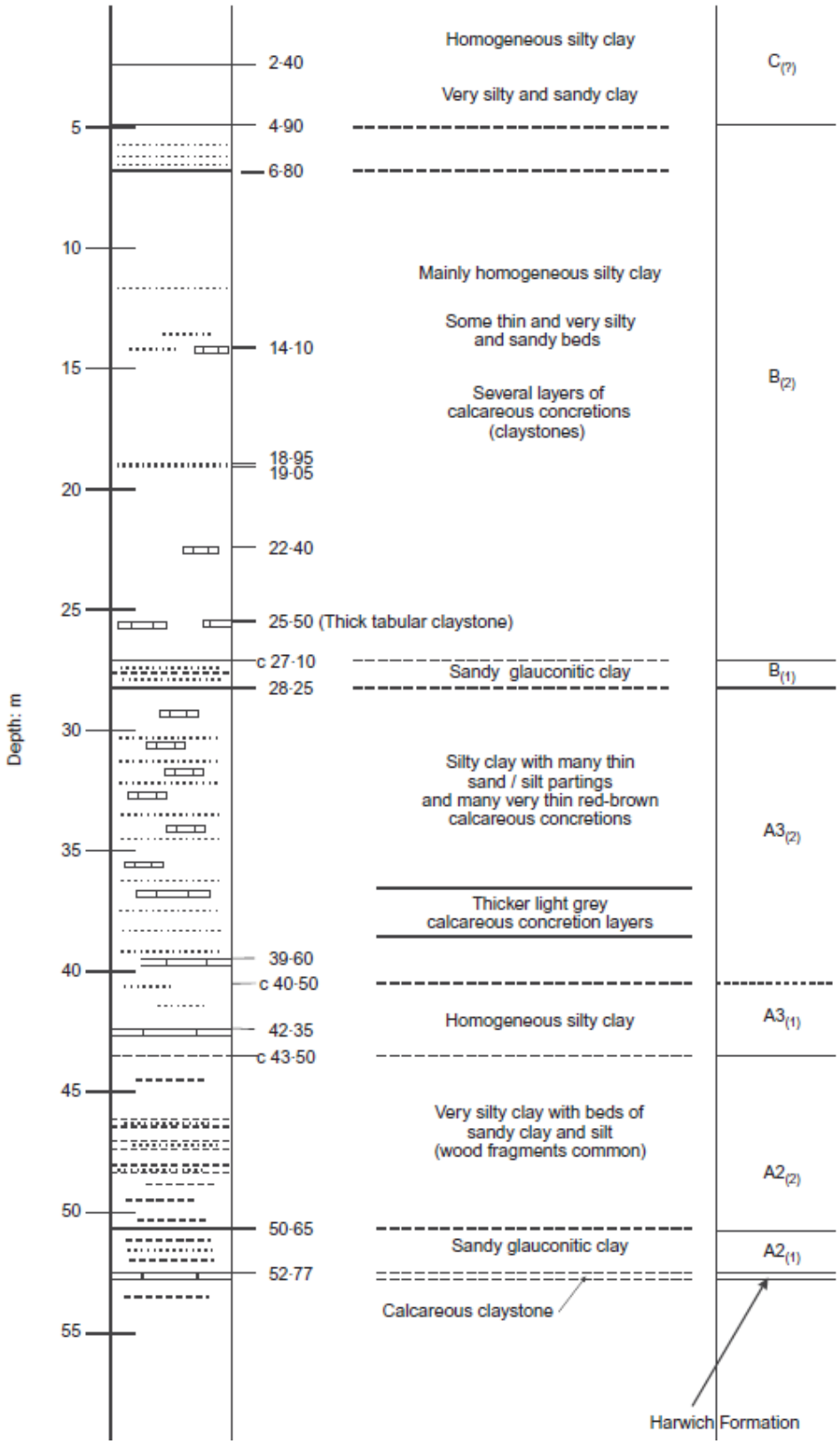

Figure 16: Borehole log for BH 404 prepared by Dr King, identifying lithological units. Taken from Hight et al. (2007)

Figure 17a): Upper Mottled Beds from Moorgate, London (Procter, 2014) b) Reading Formation (LMB) from the Isle of Wight (West, 2013)

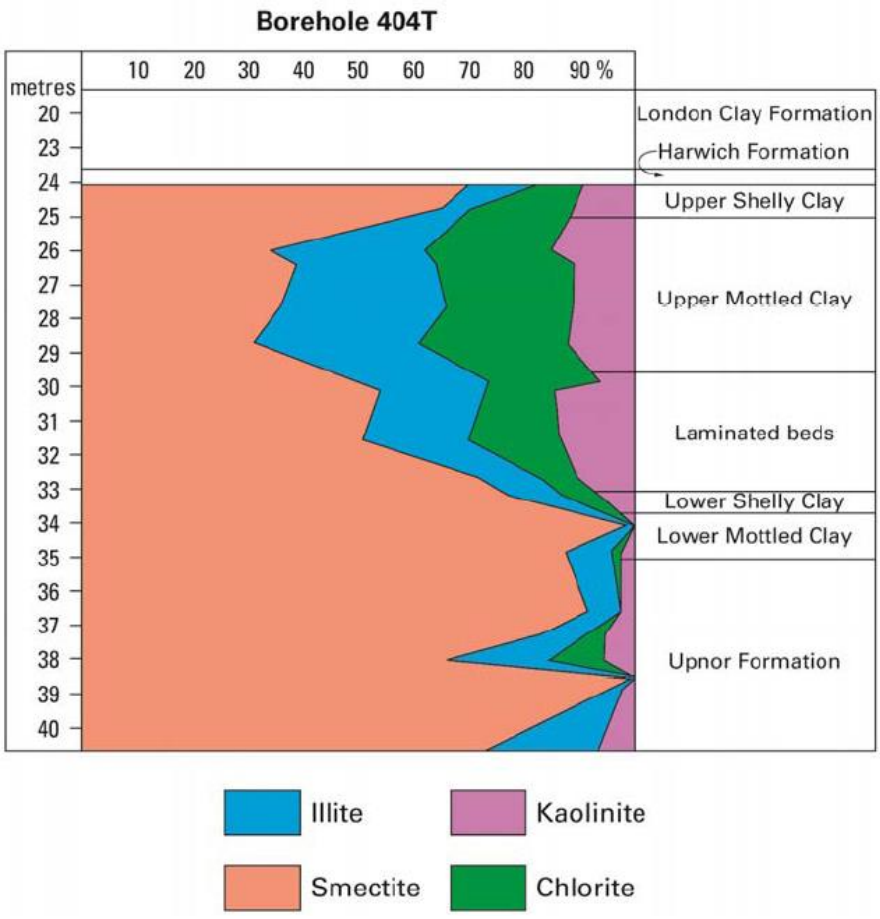

Figure 18: Relative percentages of clay minerals for samples from Jubilee Line Extension borehole 404T. Taken from (Entwisle, et al., 2013)

Middlesex (Gilkes, 1968) and the basal bed at Whitecliff Bay (Fig. 16). The Reading Formation in

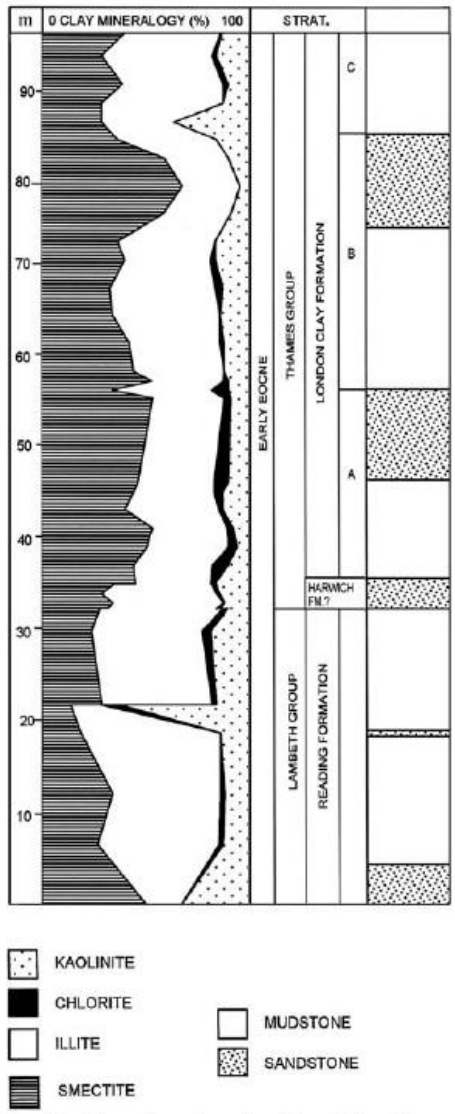

FIG. 15. Clay mineral stratigraphy of the Eocene succession at Alum Bay. A2–C are the stratigraphic

minor smectite, kaolin and chlorite. There is an overall decrease in smectite from the base of the formation to the base of the upper sand.

There is an overall increase in smectite towards the north of the Hampshire Basin and a decrease towards the west (Gilkes, 1966). However, there is a great deal of fine-scale variation in the clay assemblage that may reflect variable pedogenic modification. Gilkes (1968) reported that at Bishops Waltham and Otterbourne in the northeast of the Hampshire Basin the <5 μm fraction is illite- and smectite-dominated, with minor kaolin. By contrast, in the south of the basin (Whitecliff Bay and Alum Bay) he reported it to be illite- and kaolin-dominated with subordinate smectite, which decreased towards the west (Studland Bay, Dorset). New data indicate that the <4 μm fraction of the Reading Beds of the Isle of Wight (Whitecliff Bay and Alum Bay) is generally dominated by illite with moderate amounts of smectite and kaolin, plus rare chlorite (Fig. 10e). Gilkes (1966) and new data for Whitecliff Bay and the Isle of Dogs (east London) show an unusual illite-smectite mineral in the upper part of the Reading Formation. This mineral does not fully collapse on heating at 400°C, possibly due to intercalation of $Al(OH)_3$ or organic compounds. The Alum Bay section includes a bed exceptionally rich in kaolin within the upper mottled beds, immediately below a reworked lignite horizon that is interpreted as pedogenic in origin, possibly a seat-earth. The Isle of Wight data show slightly more smectite at the base than through the rest of the formation. There is also a smectite-rich assemblage at the base of the Reading Formation in the Bunker's Hill and Shamblehurst boreholes (Edwards & Freshney, 1987). The Bunker's Hill borehole assemblage is unusual in containing a narrow zone 3 m above the smectite-rich clay in a narrow zone that possesses a clay assemblage dominated by halloysite with minor mixed-layer vermiculite-chlorite and chlorite-smectite. This assemblage is thought to have formed by *in situ* subaerial weathering of the underlying volcanogenic clay (Edwards & Freshney, 1987). The remainder of the formation is illite-rich as elsewhere in the Hampshire Basin.

The Tower Wood Gravel of Devon was

Figure 19: Relative percentages of clay minerals for samples (a) taken from White Cliff Bay (b) taken from Alum Bay. The London Clay Formation is shown alongside strata from the Eocene period. (Huggett & Knox, 2006)

2.3.4. Engineering properties

Water content and index properties

Due to the relative simplicity of the tests for water content and plasticity, a large data base exists to compare the sampled materials on. The UMB shown on Figure 20 as Upper Mottled Clay has natural water content around 20% with a fairly large deviation which is expected due its' high variability. However, Figure 21 shows that moisture content decreases with

depth above the Mid Lambeth Group Hiatus; this is likely due to the proximity of the groundwater table which sits just below the Lambeth Group.

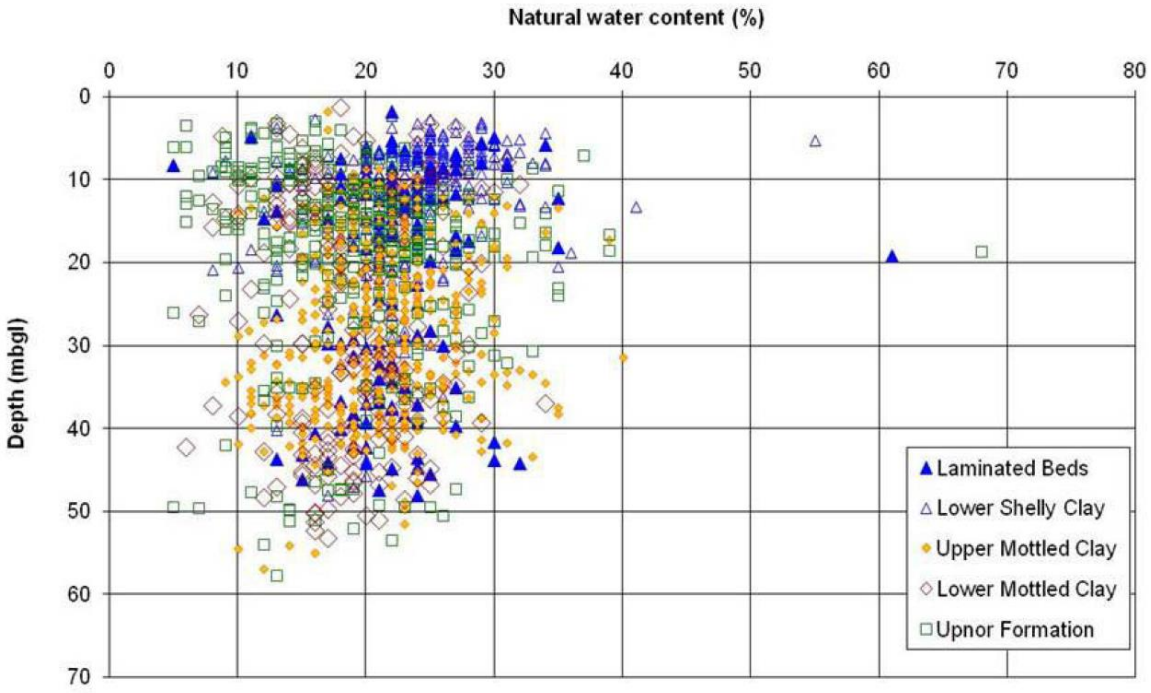

Figure 20: Natural water content of Lambeth group over Central London (Entwisle, et al., 2013)

By contrast, much work has been done on characterising the London Clay divisions using water content itself. Shown in Figure 22, Standing and Burland (2006) demonstrate clear variations in water content across lithological units. In general Unit B2 had the highest water content with Unit A2 having the lowest. Since then Hight et al. (2007), Figure 24a, found small increases and decreases in each sub-unit with a general trend of reducing water content with depth. Although Hight et al. (2007) found water content reduced with depth, much of London is under-drained so water contents are likely to be different in hydrostatic conditions.

Since these early studies, water content has been studied in greater detail and significant data sets now exist. A more recent publication by Standing (2018) presents data across a 5km section across London and uses this data to devise a methodology for identifying the A3 division of London Clay. The paper describes water content as the most effective and cheapest means of identifying the boundaries of lithological units.

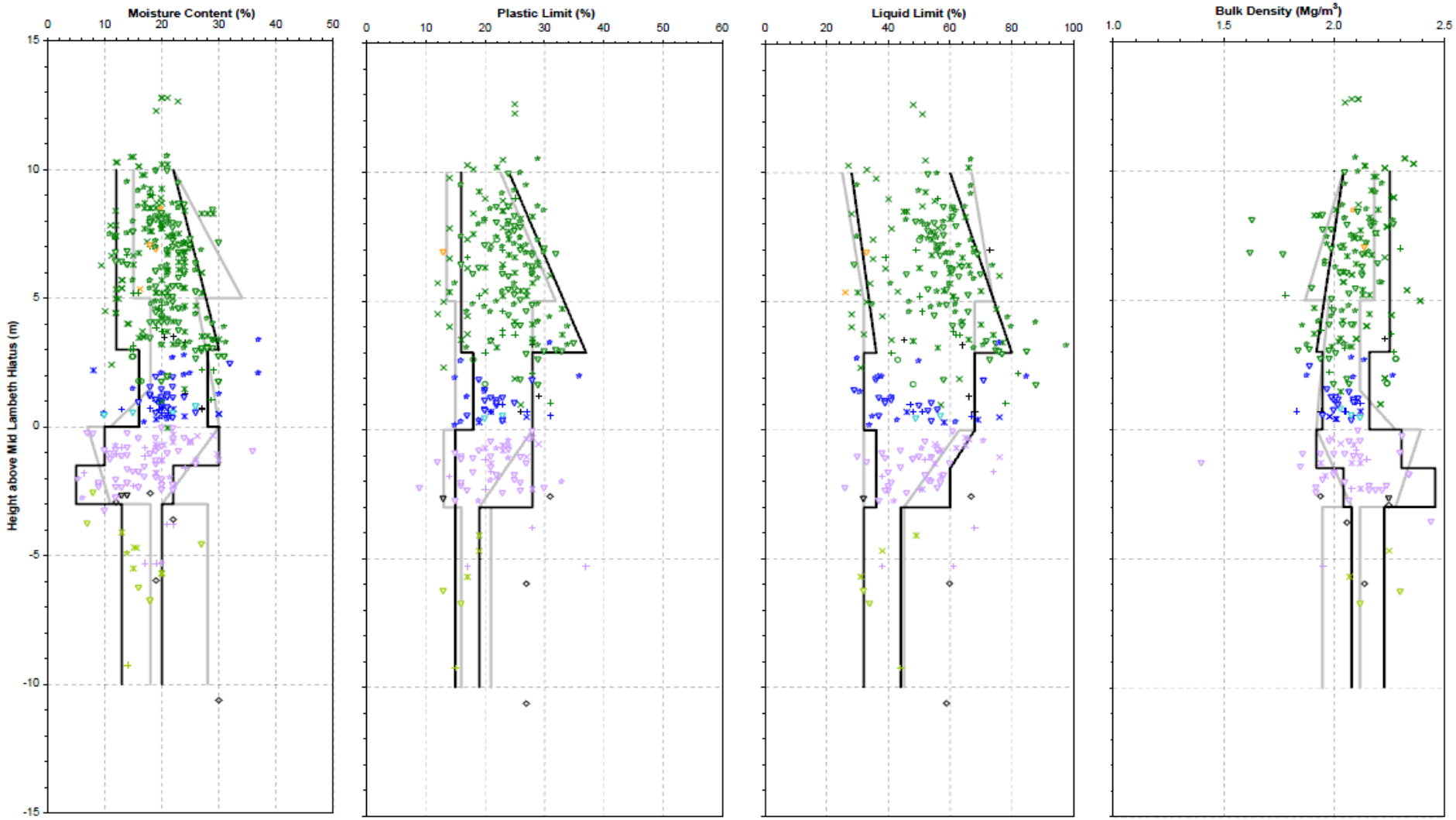

Figure 21: Moisture content %, Plastic limit %, Liquid limit % and Bulk density Mg/m^3 (Black, 2009) (green dots UMB). Data are shown against the mid-Lambeth Group hiatus, which is the when the depositional sequence changes from lower shelly beds clay to lower mottled beds (LMB).

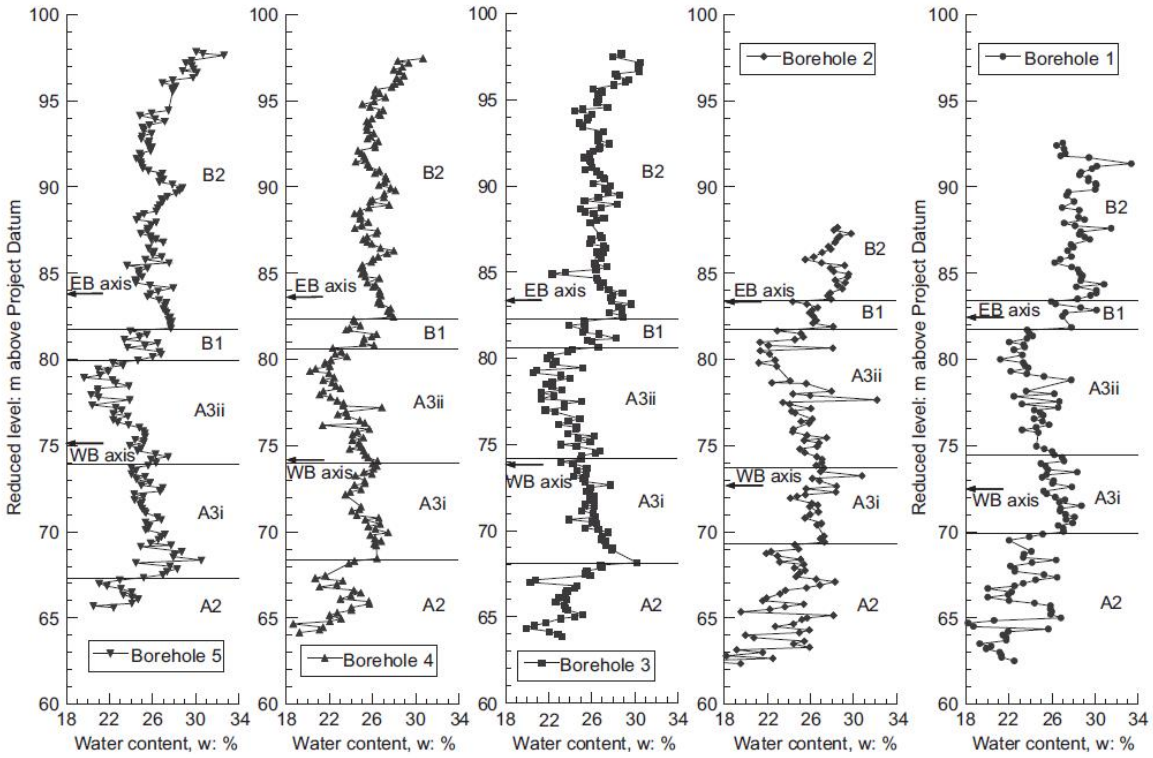

Fig. 6. Water content profiles with depth (in terms of reduced level) for boreholes 1 to 5

Figure 22: Water content profile with lithological unit for five boreholes in the Westminster area (Standing & Burland, 2006)

The Index properties of the UMB, Figures 21 and 23, place it in the high plasticity segment with liquid limit ranging from 20-100% but averaging around 60% and plasticity index ranging from 10-70% with an average between 30-40%. Considering the variability of the UMB and that clay fraction varies between 2-98%, the volume change potential (VCP) (Jones & Terrington, 2011) which uses the modified plasticity index would fall in the low-high category.

A similar set of values exist for the relevant London Clay units B2 and A2, using Jones and Terrington (2011) the VCP is likely to be medium-high for these units. The liquid limit is commonly between 60-80% with an average around 70% for unit B2. Unit A2 appears to average around 60% (Figure 24b). The plasticity index for B2 and A2 are 45 and 40% respectively. However, data from various sites across London show some variation in Atterberg limits.

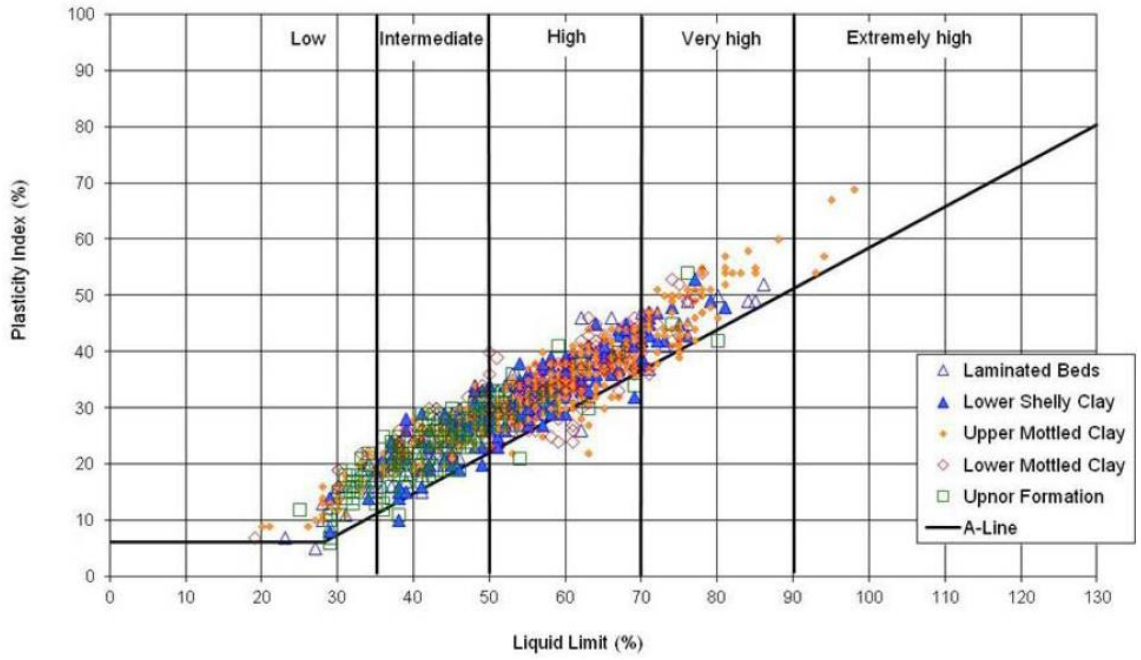

Figure 23: Index properties of Lambeth Group in Central London (Entwisle, et al., 2013)

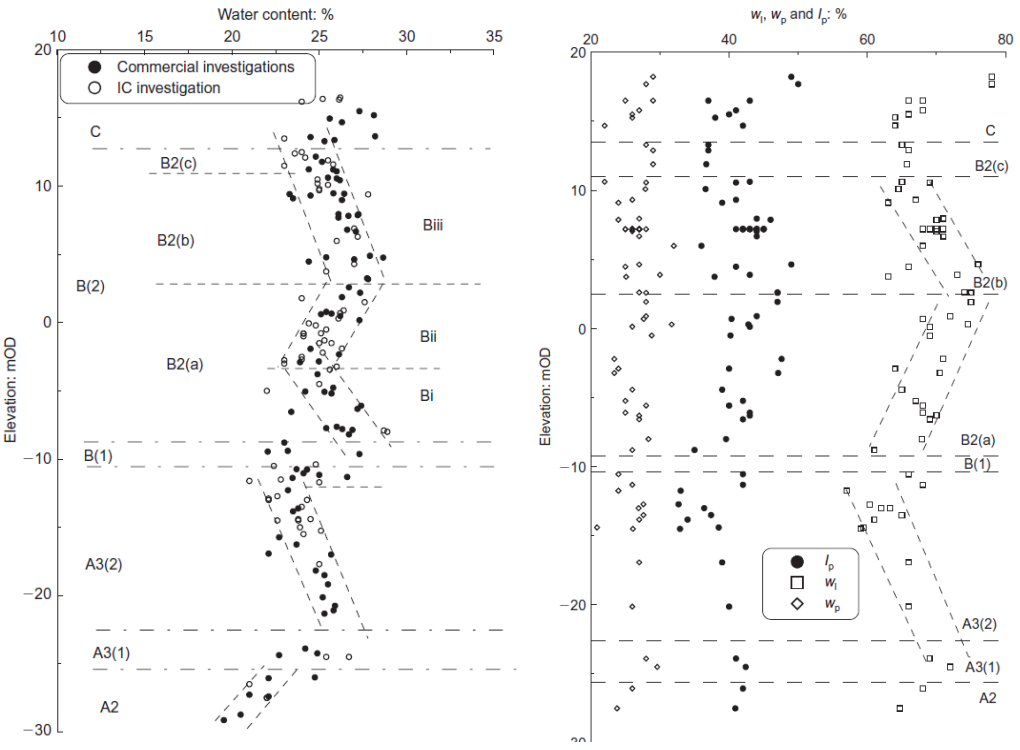

Figure 24: a) Water content profile with lithological unit b) Profile of index properties with lithological unit (Hight, et al., 2007).

Bulk density and undrained shear strength

The bulk density of UMB can be seen in Figures 21 and 25 and averages around 2.1 T/m^3 (Mg/m^3) but decreases slightly with depth above hiatus while London Clay has a bulk density of 2.0 t/m^3 for all units (Black, 2009).

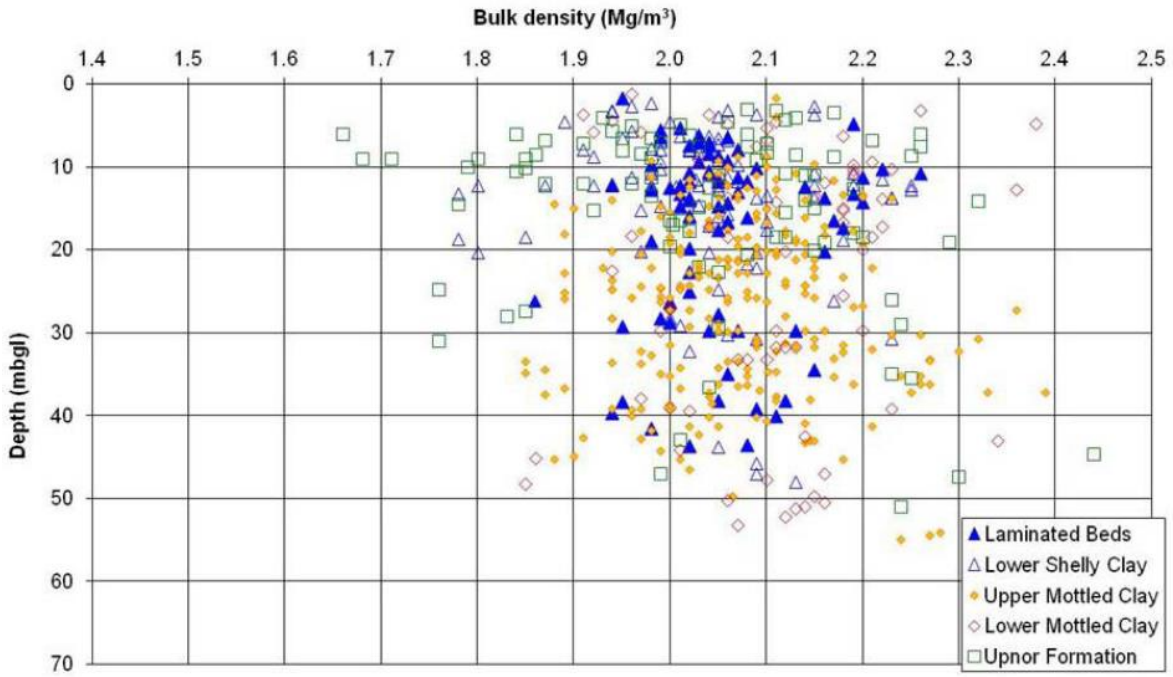

Figure 25: Bulk density of Lambeth group in Central London (Entwisle, et al., 2013)

The undrained shear strength is not as straightforward as bulk density but a relationship of the form: A+Bz where A and B are constants and z = depth below surface of the clay (m), is commonly used. For London Clay the constant A can range from 50-150 and B from 5-11. Whilst UMB is not much different with A ranging from 80-150 and B from 5-10. The simple linear relationship differs from site to site and between lithological units on each site. A typical plot is given in Figure 26 and the range of strengths increases with depth along with the average shear strength. As well as increasing with depth, a stepped increase in undrained shear strength can occur from one unit of London Clay to another and between London Clay and the Lambeth Group (Cragg & Nicol, 2011), this can be seen in Figures 27 and 28.

In summary, the undrained shear strength has been commonly obtained for many sites across London and a reasonable approximation of change with depth can be made. The undrained shear strength does not help to describe complex soil behaviour.

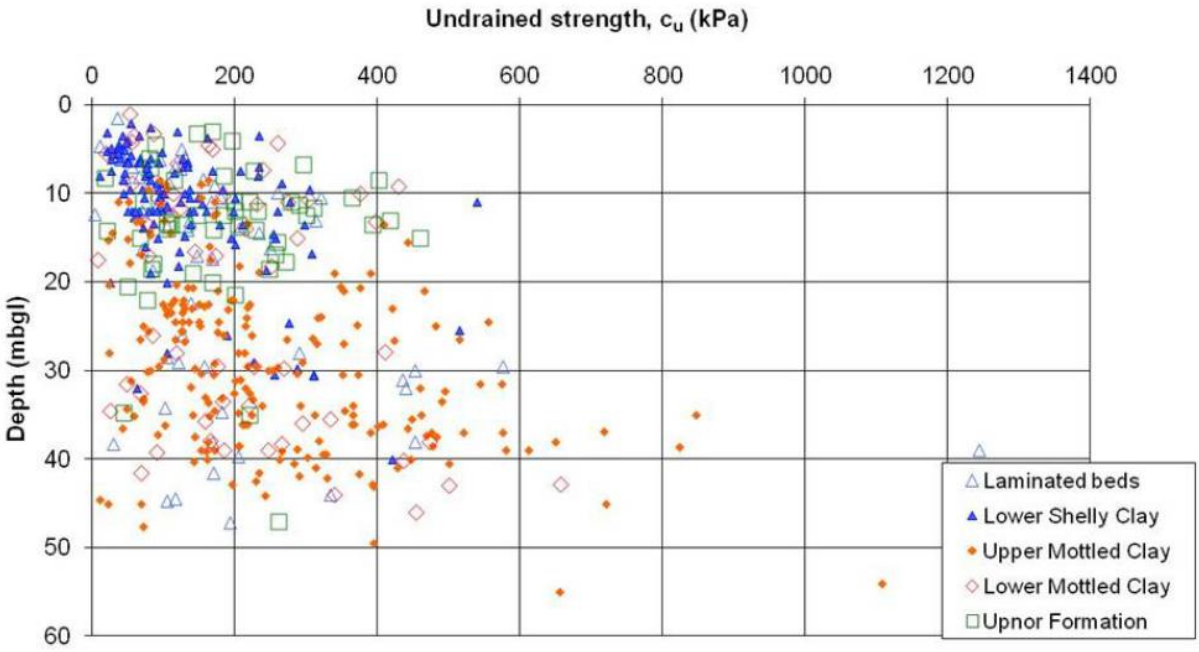

Figure 26: Undrained shear strength of Lambeth Group in Central London (Entwisle, et al., 2013)

Horizontal stresses

Earth pressure at rest (K_0) is the ratio of horizontal to vertical effective stress. In over-consolidated (OC) clays the value of K_0 becomes difficult to estimate because of a complex stress history which involves unload, reload and changes in pore water pressures. One method to estimate K_0 at the maximum over-consolidated state is to use Equation 2.4 which is a modified version of Schmidt (1966) suggested by Mayne and Kulhawy (1982).

$$K_{0,OC} = K_0 OCR^{sin\phi} \tag{2.4}$$

Where: $K_0 = 1 - sin\phi$, which is Jaky's (1944) formula. This formula works when it is possible to reliably estimate the preconsolidation pressure to get the over-consolidation ratio (OCR) and assuming water pressures are hydrostatic for London Clay and Lambeth Group estimates. It is accepted in industry practice that the pre-consolidation pressure can be reliably estimated by plotting insitu values of the void index Iv and the intrinsic compression line (ICL) against log (σ'_v). The point where the void index values cross the ICL is defined as the pre-consolidation pressure (Terzaghi, et al., 1996).

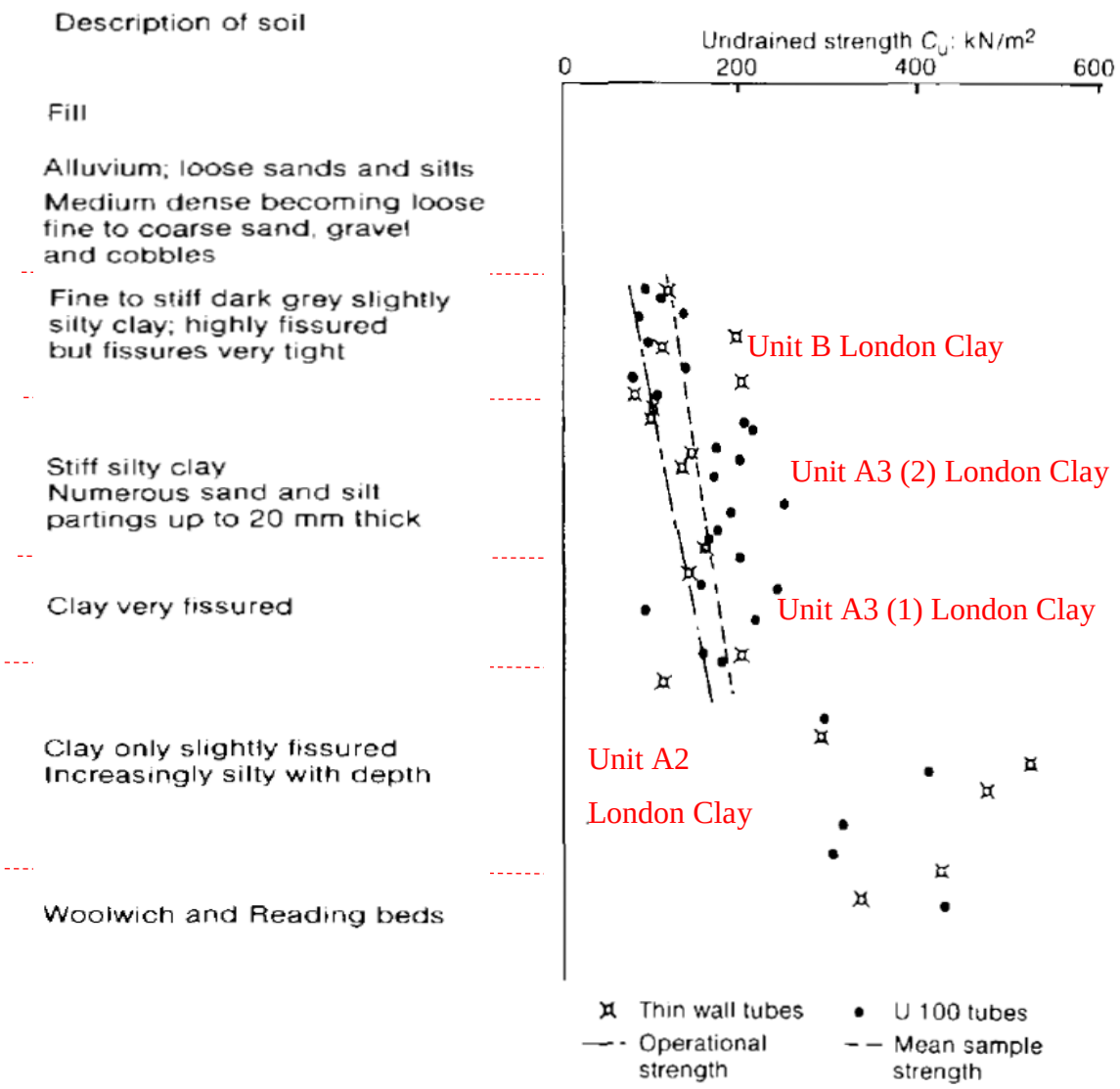

Figure 27: Undrained shear strength profile, taken from QE2 conference centre (Burland & Kalra, 1986)

To obtain a value of K_0 at current stress conditions, the reload (typically of gravel, etc.) is accounted for using Equation 2.5. This is because the horizontal effective stress increases on reload at a lower rate to vertical effective stress due to the anisotropic structure of the clay.

$$\frac{\Delta\sigma'_v}{\Delta\sigma'_h} = \frac{v'}{1 - v'} \qquad (2.5)$$

Where v'=drained Poisson's ratio. Graphically, the value of K_0 can be seen in Figure 29 based on these Equations (Burland, et al., 1979). The upper and lower limits are the active and passive pressure limits 0.5 and 3.5 respectively. Using this theory and applying it to the materials later tested in this thesis, London Clay Unit B2 can be found at a variety of depths meaning that K_0 is highly variable and will have to be taken on a site by site basis; however, the value is likely to be between 1 and 1.5.

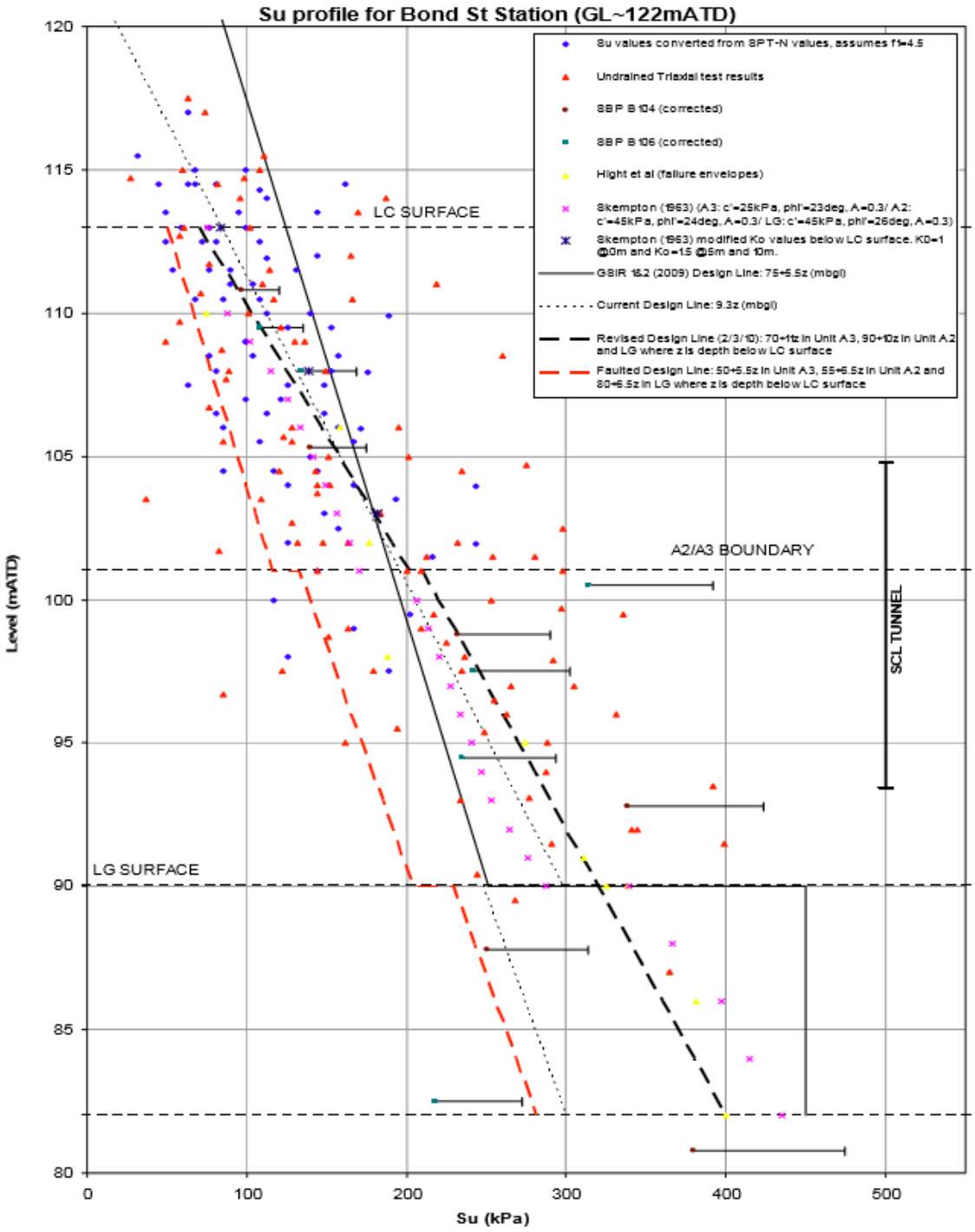

Figure 28: Variation of undrained shear strength with depth (Cragg & Nicol, 2011)

For London Clay Unit A2 and UMB the likelihood is that it has been taken from greater depth and so K_0 is going to be less effected by reload and the OCR is not going to be as large. In this case the value of K_0 is going to be closer to 1 but will again vary from site to site.

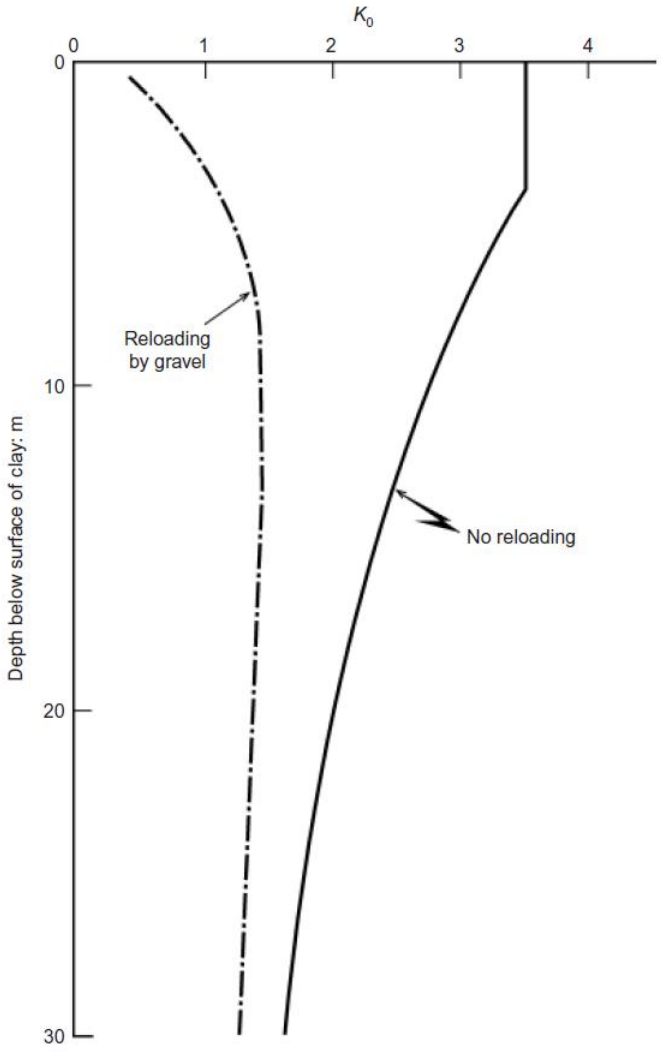

Figure 29: K_0 profiles postulated by Burland et al. (1979)

Elastic parameters

Historically, elastic parameters were estimated as uniform isotropic values of stiffness, as relatively quick estimates could be achieved and it does not require much field data or testing. Early work by Serota and Jennings (1959) estimated the Young's modulus of London Clay at 1200tons/sqft (115MPa) which was later reduced to an estimated 945 tsf (90.5MPa) by Measor and Williams (1962) for London Clay at the Shell Centre. However, the results of the undrained heave put the value significantly higher than this and Ward (1962) pointed out that this would be a further underestimate due to the Bakerloo tunnels beneath the excavation unloading and disturbing the London Clay further.

As time progressed, estimates deduced from field tests at various sites across London involving different depths were used. Burland and Hancock (1977) used 60MPa at the surface of the London Clay, while below 20m they used 220MPa. It was noted by the authors that

these values were 3-5 times larger than the results from lab tests to find swelling and compression cycles. Later similar values were used by Hubbard et al. (1984) at E = 64 +4.8z MPa where z = depth below clay surface. Figure 30 shows a comparison of the undrained Young's modulus estimates obtained from field data by Burland and Kalra (1986).

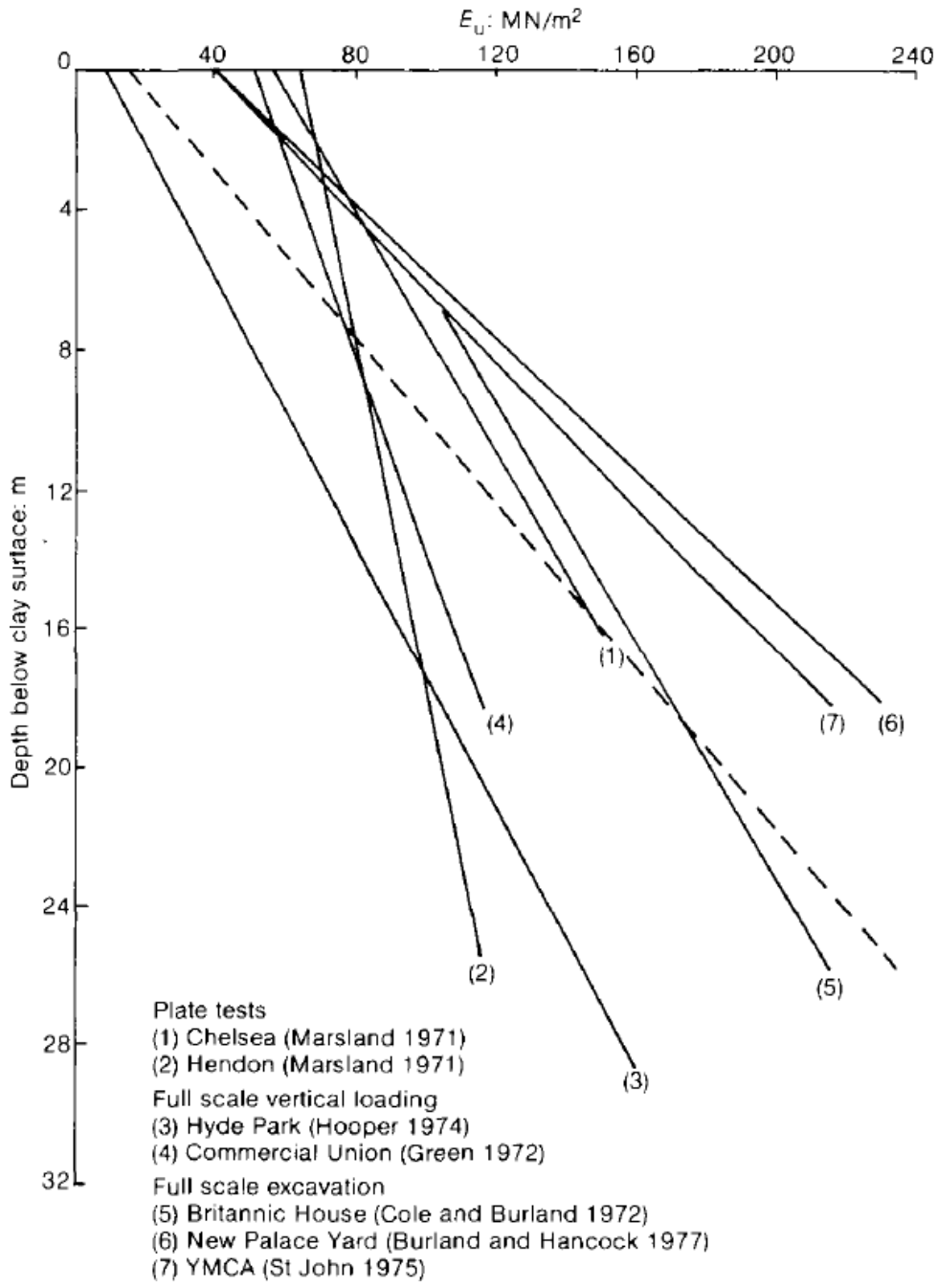

Figure 30: Value of undrained Young's modulus deduced from various sites in London (Burland & Kalra, 1986).

The drained Young's modulus, for isotropic conditions, can be obtained using Equation 2.6, where G = shear modulus, v' = drained Poisson ratio, v_u = undrained Poisson ratio and E' = drained Young's modulus. This means that the drained Young's modulus is somewhat

dependent on the drained Poisson's ratio because the undrained Poisson's ratio is taken as 0.5 or 0.499 for modelling purposes. The variation in the drained Poisson ratio is generally between 0.125-0.2 with the values used by authors, often in numerical models or calculations, given in Table 1. Gasparre et al. (2007) finds the value to be averaged at 0.1 for triaxial tests on unit B2c of London Clay and Yimsiri and Soga (2011) find the value to be 0.07 for Unit A2 of London Clay. Therefore, for the test materials unit B2 and A2 it is likely that the drained Poisson's ratio can be taken as 0.1. For UMB it is difficult to estimate this parameter as it has not been tested but following the same logic as authors who modelled London Clay before it was widely tested, a value of 0.2 could be used for modelling purposes.

$$\frac{E_u}{1+v_u} = 2G = \frac{E'}{1+v'} \tag{2.6}$$

Site	Clay	Drained Poisson's Ratio (v')	Reference
Queen Elizabeth Centre	London	0.06-0.17 (mean 0.125) (testing)	(Burland & Kalra, 1986)
Bell Common	London	0.2 (modelling)	(Hubbard, et al., 1984)
House of Commons	London	0.15 (modelling)	(Burland & Hancock, 1977)
Horseferry Road	London	0.2 (modelling)	(Clarke & Hird, 2013)
St James's park	Lambeth Group	0.2 (modelling)	(Clarke & Hird, 2013)
Lions Yard	Gault	0.2 (modelling)	(Ng, et al., 1998)
Sedgewick Centre	London	0.15 (modelling)	(Wood, 2000)

Table 1: Comparison of drained Poisson ratios used in the literature

When considering the soil stiffness, it is important to note the differences between the vertical and horizontal parameters. In some cases, they will be completely different so isotropic modelling does not truly represent the soil. Studies of anisotropic stiffness in stiff OC clays began with Bishop (1966) using inclined test specimens in a triaxial apparatus to prove anisotropy in a qualitative sense. However, beyond observing a greater lateral stiffness

on site (Burland & Kalra, 1986) few laboratory studies complemented these findings until the late 1990's when authors Jovicic and Coop (1998) begun studies into this.

Lings et al. (2001) provided a comparison of anisotropic formulations developed by various authors and explores the relationships between anisotropic parameters. The derivation in the paper gives a full description of a cross-anisotropic elastic material using five independent parameters which are: the vertical Young's modulus, E_v, horizontal Young's modulus, E_h, Poisson's ratio for horizontal strain due to vertical strain, v_{vh}, Poisson's ratio for horizontal strain due to horizontal strain at right angles, v_{hh} and shear modulus in the vertical plane, G_{hv}. Cross-anisotropy is the most common type of anisotropy and is represented by the matrix in Equation 2.7.

$$\begin{bmatrix} \delta\varepsilon_{xx} \\ \delta\varepsilon_{yy} \\ \delta\varepsilon_{zz} \\ \delta\gamma_{yz} \\ \delta\gamma_{zx} \\ \delta\gamma_{xy} \end{bmatrix} = \begin{bmatrix} \frac{1}{E_h} & \frac{-v_{hh}}{E_h} & \frac{-v_{vh}}{E_v} & 0 & 0 & 0 \\ \frac{-v_{hh}}{E_h} & \frac{1}{E_h} & \frac{-v_{vh}}{E_v} & 0 & 0 & 0 \\ \frac{-v_{vh}}{E_v} & \frac{-v_{vh}}{E_v} & \frac{1}{E_v} & 0 & 0 & 0 \\ 0 & 0 & 0 & \frac{1}{G_{hv}} & 0 & 0 \\ 0 & 0 & 0 & 0 & \frac{1}{G_{hv}} & 0 \\ 0 & 0 & 0 & 0 & 0 & \frac{2(1+v_{hh})}{E_h} \end{bmatrix} \begin{bmatrix} \delta\sigma'_{xx} \\ \delta\sigma'_{yy} \\ \delta\sigma_{,zz} \\ \delta\tau_{yz} \\ \delta\tau_{zx} \\ \delta\tau_{xy} \end{bmatrix} \quad (2.7)$$

It should also be noted that G_{hv} is considered the same as G_{vh} in this model and can be seen to be written as both by some authors.

There is now a complete set of parameters for London Clay and Gault Clay but there is some disparity between some of these variables. Typically, values of the drained Poisson ratios vary the most. Gasparre et al. (2007) found for London Clay that v'_{vh} averaged at 0.1 +/-0.14 for triaxial tests and 0.25+/-0.05 for static Hollow Cylinder Apparatus (HCA) tests. Also, v'_{hv} had a mean of 0.71 and 0.49 for triaxial and HCA tests respectively; while there is a standard deviation of 0.15 for both tests. This variation is quite large, and the tests were only carried out for unit B2c which suggests there could be even greater disparity if the other units were included. However, the stiffness measurements have much less variability where E_{uv}/E'_v = 1.5 and E'_h/E'_v=2 with K0 around 1.2.

Lings (2001) and Lings et al. (2000) have also documented the anisotropic parameters for Gault Clay finding that the material has greater differences between its horizontal and vertical elastic parameters. E_{uv}/E'_v was found to be 2.91 and E'_h/E'_v to be 4. The drained Poisson's ratio, v'_{vh} value was found to be 0 which is much lower than the previous estimates of 0.2 used by Ng (2004) in isotropic analysis.

Yimsiri & Soga (2011) have conducted isotropic consolidation stress tests on both clays, London and Gault, and have found different values for all of the elastic properties. The largest difference was E'_h/E'_v =2.32 for Gault which is nearly half the value found by Lings (2001). This most likely is due to the differences in experimental procedure and the natural variability of the material, but this does raise concerns to the reliability of the values quoted and makes it difficult to establish suitable values for analysis.

On the other hand, there is some consistency with parameters over depth. Modulus ratios and moduli increase with depth. This is interesting as K_0 decreases with depth when there is no reloading and decreases after a peak at around 10m depth for reloading cases. No research into elastic parameters for UMB has been conducted so far.

Modulus decay curves

Although the ratios between elastic parameters are useful, it is often that stiffness with strain is more valuable in practice. A normalising factor of mean effective stress p' is often used as the Young's modulus itself is influenced by insitu stresses. It should be noted that nearly all tests are undrained due to the cost and speed when compared to drained tests.

In Figures 31-35 there is a clear difference in behaviour when each material strains. Using Hight et al. (2007), who states a decay curve for London Clay across the units, as a reference point on each, unit B generally sits just below the stiffness found by Hight et al. (2007) while unit A2 sits on average just above the normalised stiffness found by Hight et al. (2007). There are the same differences when comparing unit B and A2 for extension tests.

UMB is similar to unit A2 as it initially responded to shearing by acting very stiff, followed by the stiffness quickly degrading. However, in general the stiffness sits above the envelope for London Clay by Hight et al. (2007).

Overall there is a clear difference between triaxial compression and triaxial extension; specimens in triaxial extension act stiffer than sample in triaxial compression at small strains. At larger strains the normalised stiffnesses of compression and extension appear to merge.

When comparing the London Clay Unit B data taken from across Crossrail sites with the previously established envelope it is clear there is a trend in compression that sits below the lower envelope boundary, Figure 31. In fact the average decay curve sits around the current lower envelope boundary.

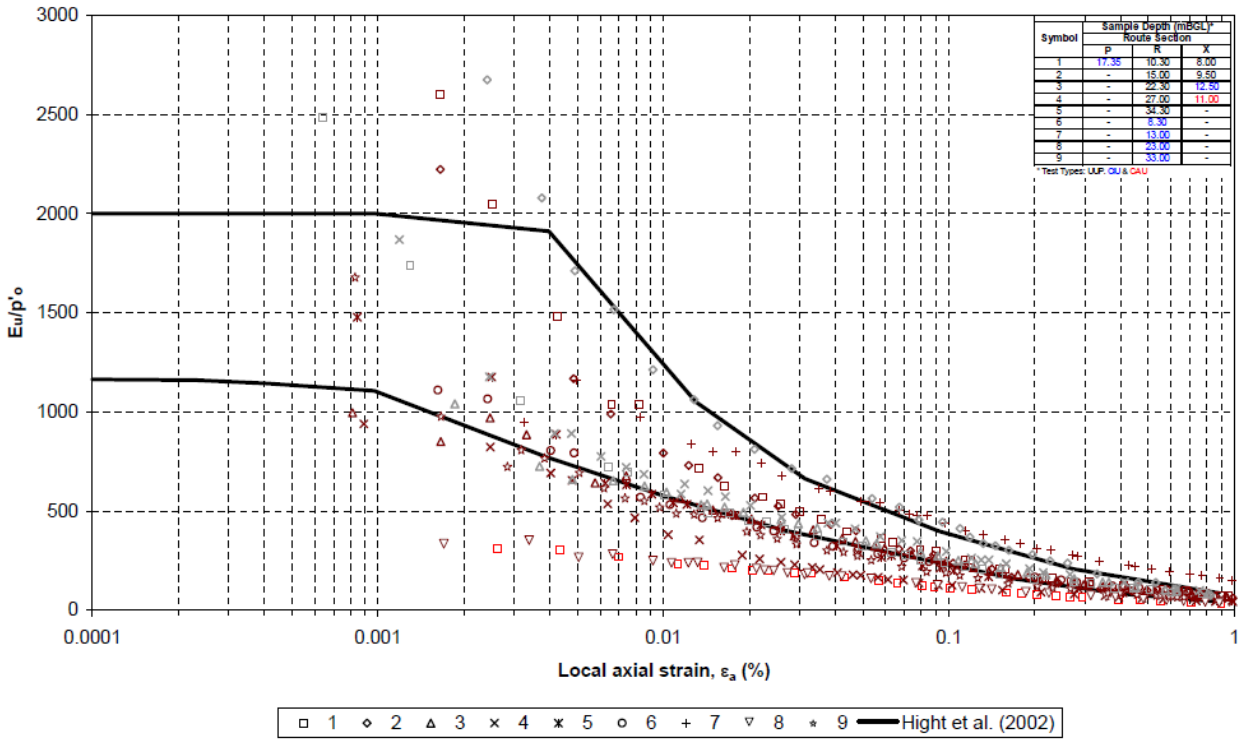

Figure 31: Modulus decay in compression for unit B London Clay (Black, 2009). Data are taken across Crossrail sites.

When comparing specimens in extension for London Clay Unit B, Figure 32, with the envelope, a similar trend of averaging around the lower envelope boundary exists. This could suggest that the samples tested by Hight et al (2007) were unusually stiff as there are greater sample variances in the Crossrail dataset. However, it is possible that Hight et al. (2007) took greater care to minimise sample disturbance.

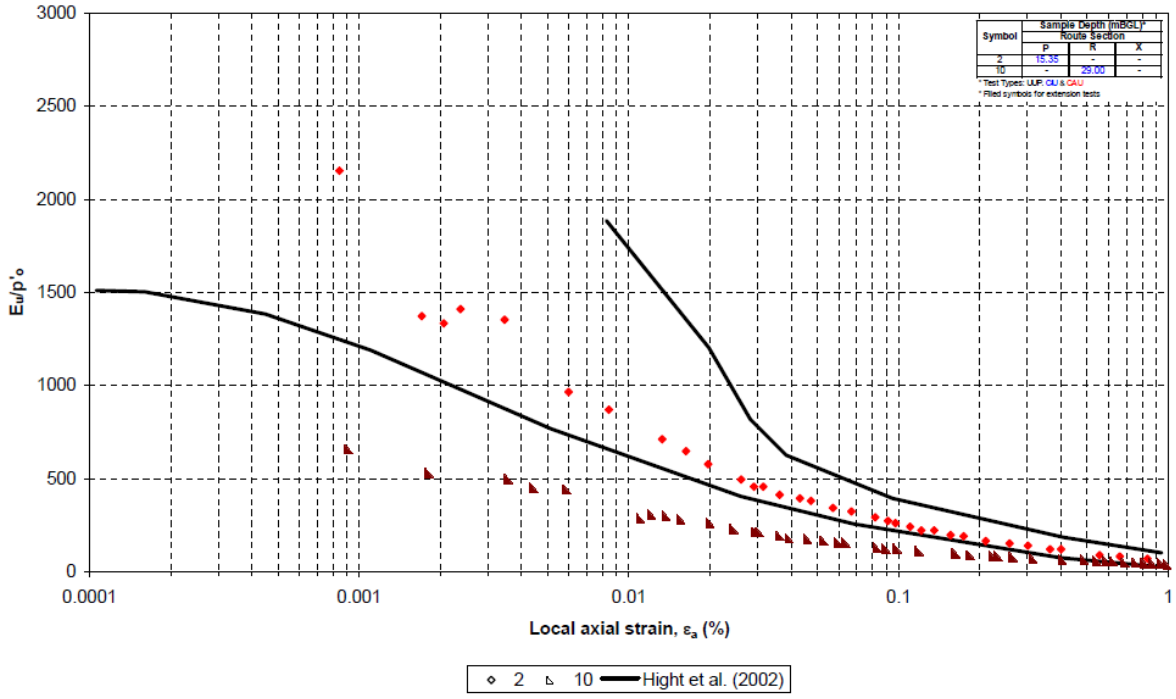

Figure 32: Modulus decay curve in extension for unit B London Clay (Black, 2009). Data are taken across Crossrail sites.

When comparing the London Clay Unit A2 data taken from across Crossrail sites with the previously established envelope it would appear that the datasets are comparable. The Crossrail data sits both within and just outside the current envelope suggesting the current envelope is accurate. At smaller strains the Crossrail dataset becomes stiffer than the High et al. (2007) envelope allows and it may be the case that no upper bound envelope should exist at smaller strains similar to the extension envelope.

For specimens in extension for London Clay Unit A2, there is a trend in the Crossrail dataset toward the lower London envelope but as with Unit B this could suggest the samples tested by Hight et al. (2007) were unusually stiff.

Overall, it is clear that the envelope by Hight et al. (2007) is a good indicator but the envelope fits the data for Unit A2 better than for Unit B where the lower boundary of the envelope should be adjusted.

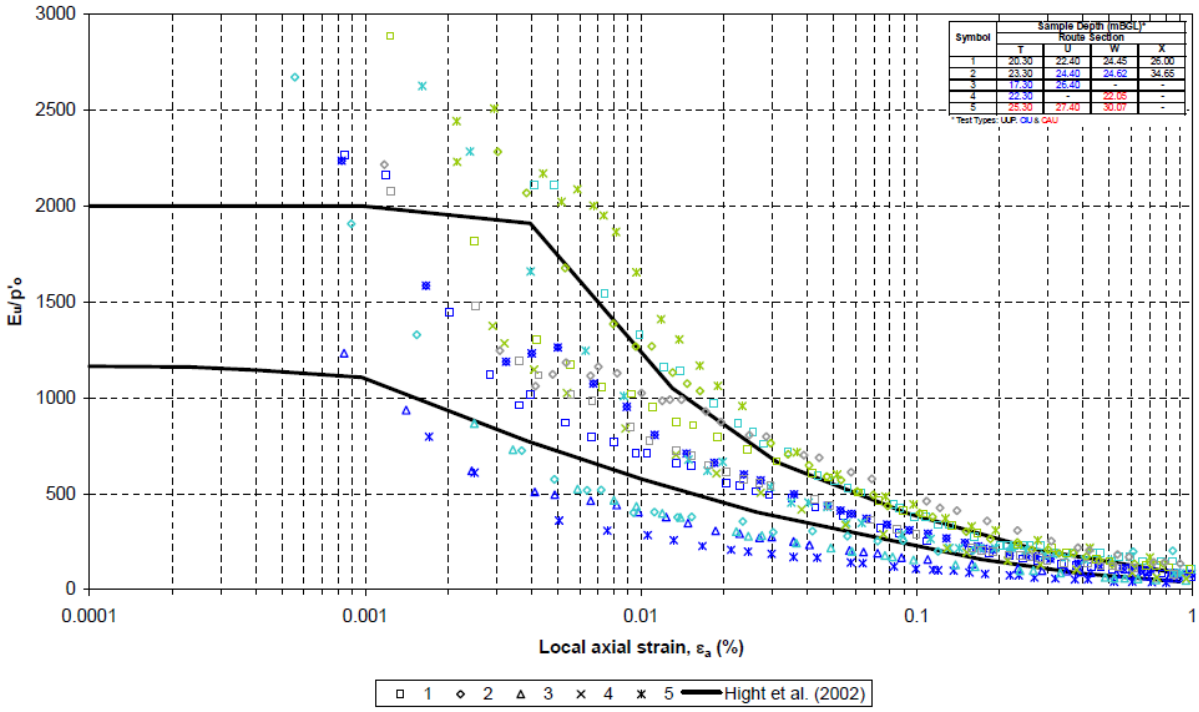

Figure 33: Modulus decay curve in compression for unit A2 London Clay (Black, 2009). Data are taken across Crossrail sites.

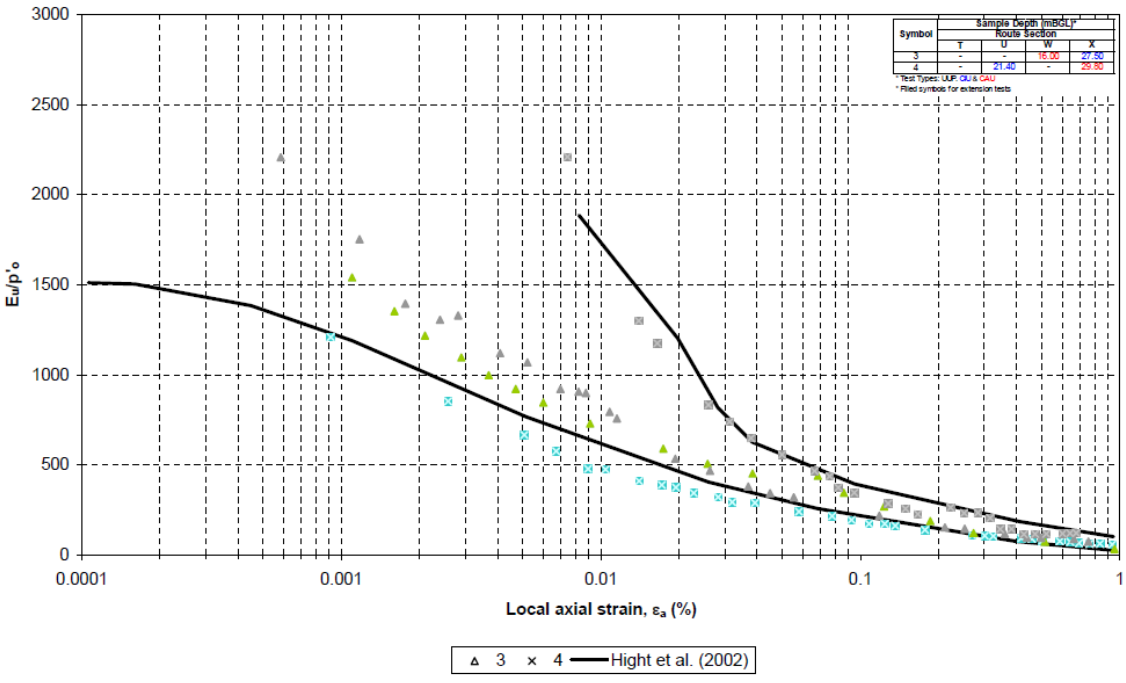

Figure 34: Modulus decay curve in extension for unit A2 London Clay (Black, 2009). Data are taken across Crossrail sites.

When comparing decay curves for UMB with the envelope for London Clay, Figure 35, it is clear that UMB behaves stiffer in triaxial compression than London Clay. At smaller strains the stiffnesses are considerably more than London Clay.

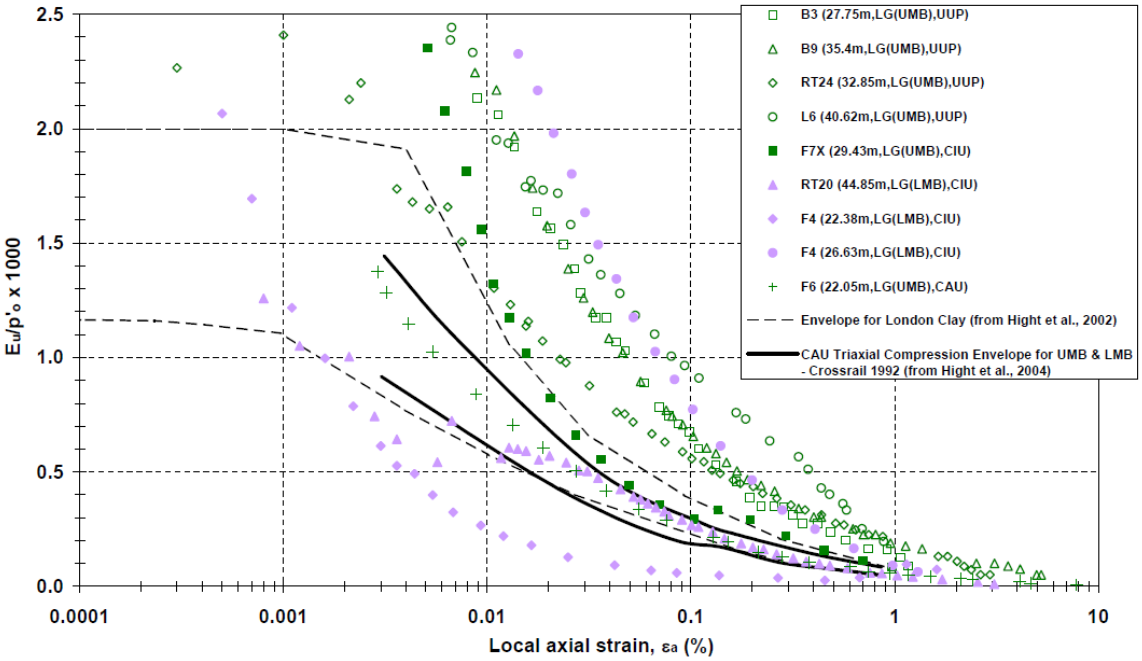

Figure 35: Modulus decay curves for UMB and LMB (Black, 2009). Data are taken across Crossrail sites.

3. OBSERVED GROUND MOVEMENTS DURING AND AFTER CONSTRUCTION OF DEEP BASEMENTS

3.1. Introduction

From the observations made over the past 60 years and extensive testing on stiff sedimentary clays such as London Clay (Gasparre, 2005), a greater understanding of non-linear soil stiffness (Atkinson, 2000) under a range of stress changes has increased the accuracy of predicted strains (Gasparre, et al., 2007; Hight, et al., 2007; Pantelidou & Simpson, 2007). However, remembering the "engineering significance" of stiffness is to note the relevant strain ranges (Simpson, 2010), and so this chapter investigates field data and observations of strain and displacements from deep basement case histories

3.2. Timescale

The amount of heave resulting from excavation processes has been monitored at several sites; some for decades. The most famous case is The Shell Centre (SC) where 27 years of heave was reported for the Bakerloo tunnels below the basement excavation (Burford, 1988), with the heave showing little sign of slowing when monitoring stopped. Another case where heave is shown to continue for decades is at Horseferry Road (HR); here, heave was slowing down but after 21 years (Chapman, 1999). Both cases show that the process of heave can take decades but despite both excavations being in London Clay the swelling behaviour over time is quite different.

Generally heave slows with time and can often be seen plotted against the square root of time (Chapman, 1999) or against time on a semi-logarithmic scale (Mesri, et al., 1978) but at SC heave was still increasing approximately linearly with time (Burford, 1988).

3.3. Short-term heave and wall movements

There are three types of heave referred to when considering unloading OC clays. The first is the immediate, 'elastic', undrained heave which occurs without volume change of the soil before any pore pressure equalisation occurs. This is difficult to quantify as the speed of excavation dictates that pore pressures will have time to begin equalisation between excavation stages and so 'during excavation' heave is often referred to as 'short-term' heave. During this first stage of heave, the velocity of the swell is most commonly greatest and occurs due to shear effects. Considerable lateral movement of the boundary walls into the excavation has been recorded with widely differing deflected shapes in relatively uniform

ground conditions (Burland & Hancock, 1977). This swell is often excavated away during the excavation period but is still important when considering final swell pressure.

The inward deflection profile and short-term heave has been monitored at five case studies. These are Aldershot Road (AR), Lions Yard (LY), House of Commons (HC), British Library (BL) and Bell Common (BC). The key results are in Table 1 with: wall toe displacement at the end of excavation as a percentage of excavation depth (%H); maximum sub-surface horizontal wall displacement at the end of excavation as a percentage of excavation depth x_{Max} (%H); wall displacement at toe x_{Toe} (mm); length of wall from the base of excavation to the wall toe L_{BToe} (m); volume displaced below the excavation surface by wall movement per m of wall V_{xss} (m^3/m); volume displaced below wall toe per m assuming wall toe has 5m influence (unless otherwise stated) V_{xsToe} (m^3/m); circumference of excavation C_E (m); total sub-surface volume change from wall movement into the excavation assuming a consistent wall deflection profile V_{xTss} (m^3); and heave calculated from wall deflections assuming: undrained volume conservation and a pyramid distribution of heave over the excavation $Z_{x,U}$ (mm). Parameters are shown in Figure 36.

The assumptions made are: that the wall deflection profile in the section measured extends around the perimeter of the excavation and that a linear relationship exists between measured datum points. It should be noted that the section with the maximum lateral wall displacement was chosen and so the limitations of this assumption is that it may over-predict the undrained ground movement. However, the opposite is true for the other assumption which may under-predict undrained ground movements. A limitation is that the time (or construction stage) at which the wall and heave measurements are taken is not always explicitly stated in the references, making them difficult to match. Therefore, a best estimate to the closest construction stage is used. A measure of time after construction begins was not used as each case varies in its construction time sequence.

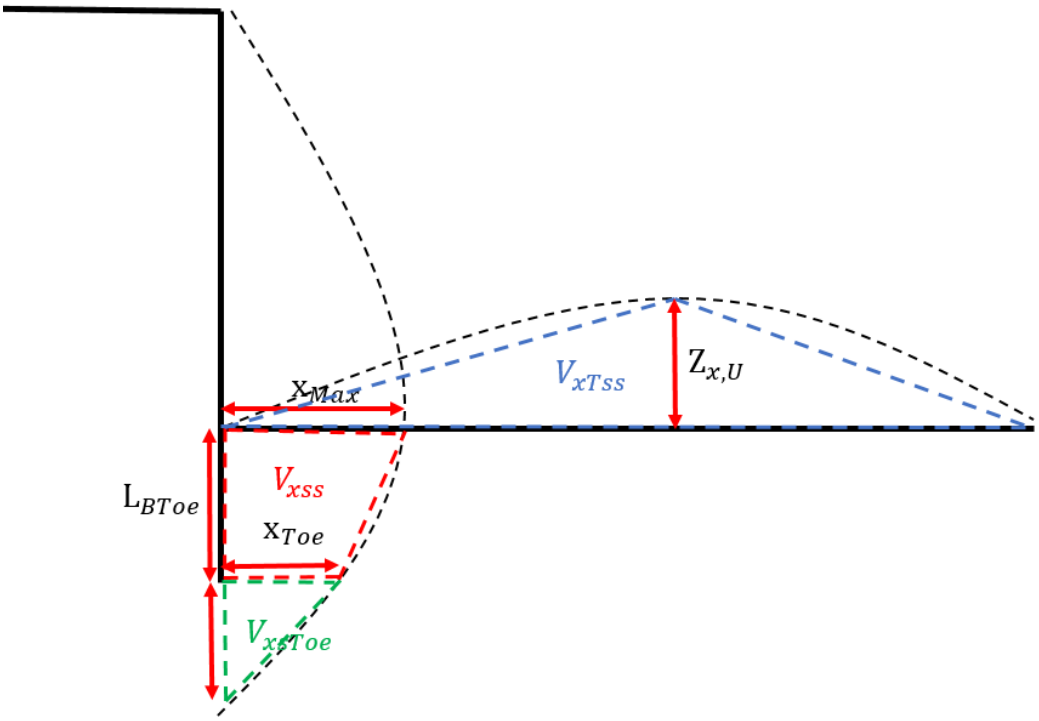

Figure 36: Parameters visually represented

The results in Table 2 demonstrate that an increase in wall movement results in a larger amount of maximum heave in the short-term; however, the amount of heave calculated assuming undrained volume conservation is less than the measured field values in all but one case. This suggests that there are other mechanisms causing short-term heave; for example, some pore pressure equalisation could have occurred during excavation. It could simply be that the ground cannot be considered undrained for very long and some pore pressure equalisation begins to occur as unloading takes place. There is only one case where heave related to pore pressure equalisation can be subtracted from the short-term heave and this is Lion Yard where 21mm of the 26mm heave at AM9 are considered "elastic" and undrained (Ng, 2004). This further suggests that there may be another mechanism causing heave while the ground is considered 'undrained' as wall movement alone does not account for this. This significantly complicates our understanding of the mechanics during this process and this is discussed further later in this chapter.

Case and Reference	Stage measurements are taken	Wall and foundation pile arrangement	Equipment used to compare data	Measured max. heave at time stage stated (mm)	x_{Max} (mm)	x_{Toe} (mm)	L_{BToe} (m)	V_{xss} (m^3/m)	V_{xsToe}(m^3/m)	C_E (m)	V_{xTss} (m^3)	$Z_{x,U}$ (mm)
Aldershot Road (AR) (Carder, et al., 1997)	Shortly after temporary prop release	1.2m thick retaining wall	Inclinometer E6 and magnetic rings MR9	~30 (0.28%H)	7.5 (0.07%H)	6 (0.06%H)	8	0.054	0.009 (3m influence)	N/A	0.126 per m along cutting	8.4 (0.08%H)
Bell Common (BC) (Tedd, et al., 1984)	After Stage V(b)	1.18m dia. secant pile wall	Inclinometer tube I_w and levelling station 'S'	35 (0.39%H)	11 (0.12%H)	0	9	0.0495	0	N/A	0.099 per m along tunnel	4.5 (0.06%H)
British Library (BL) (Simpson & Vardanega, 2014)	After Final Excavation	Propped retaining walls; 1.8m dia. under-reamed bored piles;	Extensometer 118 and Inclinometer F75	60 (0.24%H)	24 (0.10%H)	13 (0.05%H)	5	0.0925	0.0325	350 (deepest section only)	32.375	11 (0.04%H)
House of Commons (HC) (Burland & Hancock, 1977)	After excavation Stage 5	1m thick propped diaphragm wall; 2.3m dia. under-reamed bored piles	Inclinometer 3 and ME at final excavation level	45 (0.25%H)	29 (0.16%H)	11 (0.06%H)	12	0.24	0.0275	232	55.68	56 (0.30%H)
Lions Yard (LY) (Ng, 2004)	Stage XIII	0.6m thick propped diaphragm wall; under-reamed bored piles	Panel 22 and ME AM9 (-1.71m OD)	26 (0.25%H)	14 (0.14%H)	5 (0.05%H)	7	0.0665	0.0175	220	14.63	15 (0.15%H)

Table 2: Short-term Heave and Wall Displacement of Case Histories

Other cases where short-term heave has been measured without information on wall deflection are given in Table 3. The cases are: Charing Cross Road (CC), Shell Centre (SC), Cromwell Road (CR), The British Library shallow side of the excavation (BLS) and the Queen Elizabeth Conference Centre (QE2).

Case	Short-Term Heave (mm)	Reinforcements	Reference
CC	35 (0.29%H)	0.8m thick propped diaphragm wall	(Wood, 2000)
SC	21 (0.18%H)	Cantilever retaining wall; under-reamed bored piles	(Burford, 1988)
CR	18 (0.2%H)	Propped retaining wall; under-reamed piles	(Owsianka, 1988)
BLS	25-40 (0.17-0.27%H)	Propped retaining walls; under-reamed bored piles	(Simpson & Vardanega, 2014)
QE2	18 (4.5m depth) (0.13%H)	0.8m thick propped diaphragm wall; under-reamed bored piles	(Burland & Kalra, 1986)

Table 3: Short-term Heave of Remaining Case Histories

Based on the case histories in Tables 2 & 3, the maximum short-term horizontal sub-surface deflection (δ_{hs}) of the retaining wall and maximum short-term measured on-site vertical displacement (δ_{vs}) of the base of excavation can be estimated using 0.15%H for the wall deflection and 0.25%H for the ground. However, if broken down into categories with and without foundation piles in the base of excavations, the values can be altered to 0.21%H and 0.32%H respectively. This does suggest that foundation piles in the base of excavation as-measured act to restrain the short-term heave and it is noteworthy that the construction method used for the majority of piled case histories is top-down with the piles installed pre-excavation, while a variety of basement construction methods are used for the un-piled case histories.

Another way of considering wall inward deflection in relation to the base heave is to use ground surface deflection profiles from behind the wall; which should follow the same volume conservation rules while the soil is undrained. Osman and Bolton (2006) and later Lam (2010) show that modelling the behind wall surface deflection as a trigonometric wave

allows it to be equated to heave at the base of the excavation. This is shown in Figure 37 and it is noteworthy that in Osman and Bolton's approach, a considerable proportion of the sub-surface lateral movement for free end fixity condition occurs below the wall toe. From the case histories in stiff clay, this is not the case. It may be that Osman and Bolton's approach is better suited to softer clays and a modified set of equations would suit stiffer clays. On the other hand, sub-surface lateral movements may continue below the base of the inclinometers in the case histories as the base of the inclinometer may have been used as a reference point where zero lateral movement is assumed. If this were the case, the peak of sub-surface lateral movement would be positioned closer to the wall toe (as shown in Figure 37) and from the case histories this is not the case. In conclusion, if Osman and Bolton's constant alpha was calculated from the values s and l in Figure 37, then alpha would be around 1.5 for the case histories. This suggests that stiff clay and possibly the embedment depths used, act to restrain the end of the wall toe.

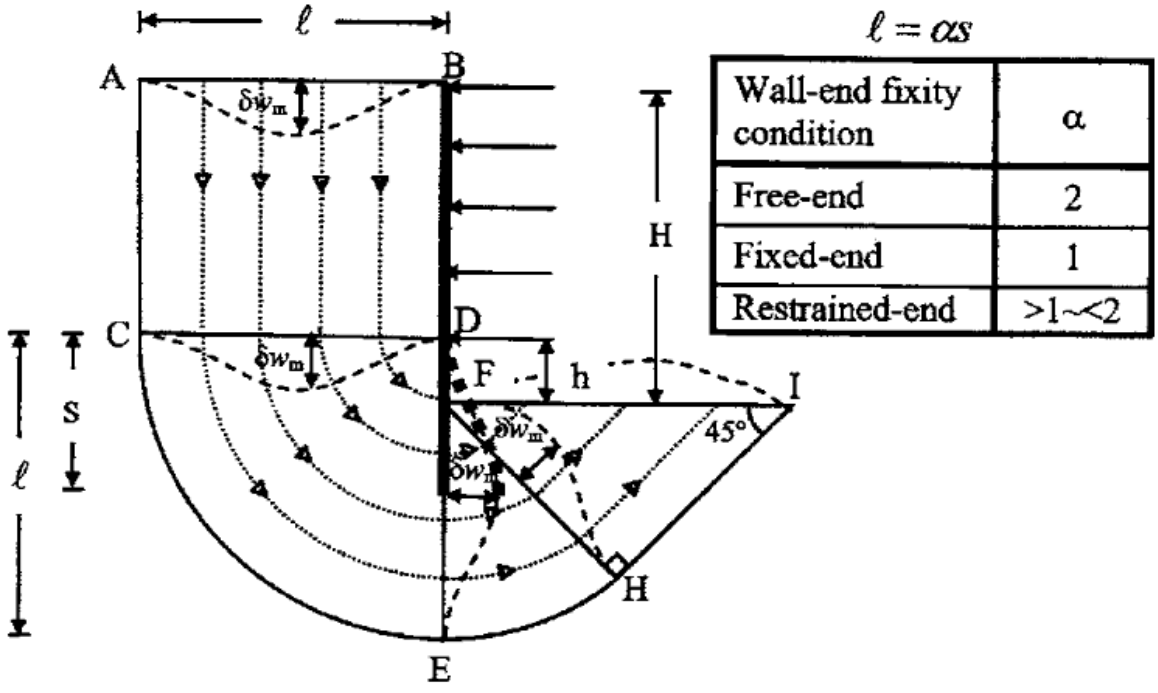

Wall-end fixity condition	α
Free-end	2
Fixed-end	1
Restrained-end	>1~<2

Figure 37: Behind the wall deflection propagating through the ground as a trigonometric wave (Osman and Bolton, 2006)

Long (2001) has studied maximum behind-the-wall vertical soil displacement and the horizontal distance over which it occurs. Long found that maximum vertical displacement behind the wall was between 0.1-0.2%H and horizontal range of deflections was 4H (Long, 2001). Applied to Osman and Bolton's approach, this would make the distance from bottom prop in the excavation to the wall toe 2H, which is not the case for the majority of the case

histories. Long has recorded field data from hundreds of sites so the conclusion would have to be that the range of behind the wall deflection does not equate to the maximum depth of sub-surface lateral movement and so that Osman and Bolton's approach may be limited in this regard.

A simple modification to the equations suggested by Osman and Bolton would make their approach more applicable to stiff clays. This would be to change O'Rourke's (1993) formula from Equation 3.1:

$$\delta x = \left(\frac{\delta x_{max}}{2}\right)\left[1 - cos\left(\frac{2\pi z}{l}\right)\right] \tag{3.1}$$

To Equation 3.2:

$$\delta x = \left(\frac{\delta x_{max}}{2}\right)\left[1 - cos\left(\frac{2\pi z}{X_1 L_{B,toe}} - X_2 x\right)\right] \tag{3.2}$$

Where, X_1 and X_2 are constants which act to skew the curve.); L_{BToe} (m) is the length of wall from the base of excavation to the wall toe, z (m) is the depth of the excavation, x_{max} is the maximum horizontal displacement, x is horizontal displacement. This would appear to better represent lateral movement in stiff clays. Using volume conservation, undrained heave could be accurately calculated from this.

Combining the findings of Long (2001) and the case histories in this thesis, it is possible to give an estimate of 'short-term' ground movements for generalised site geometry, given in Figure 38. The ground movement profiles are not to scale and are just a guide for a basement structure in stiff clay; similar to Figure 37 (although for soft clay). The base of the excavation in Figure 38 only shows heave to the centre of the excavation which will be influenced by wall movements on all boundaries not just the wall shown. The dashed directional lines demonstrate that the offsite behind wall compression translates as wall movements and then heave at the base of the excavation and should not be taken literally.

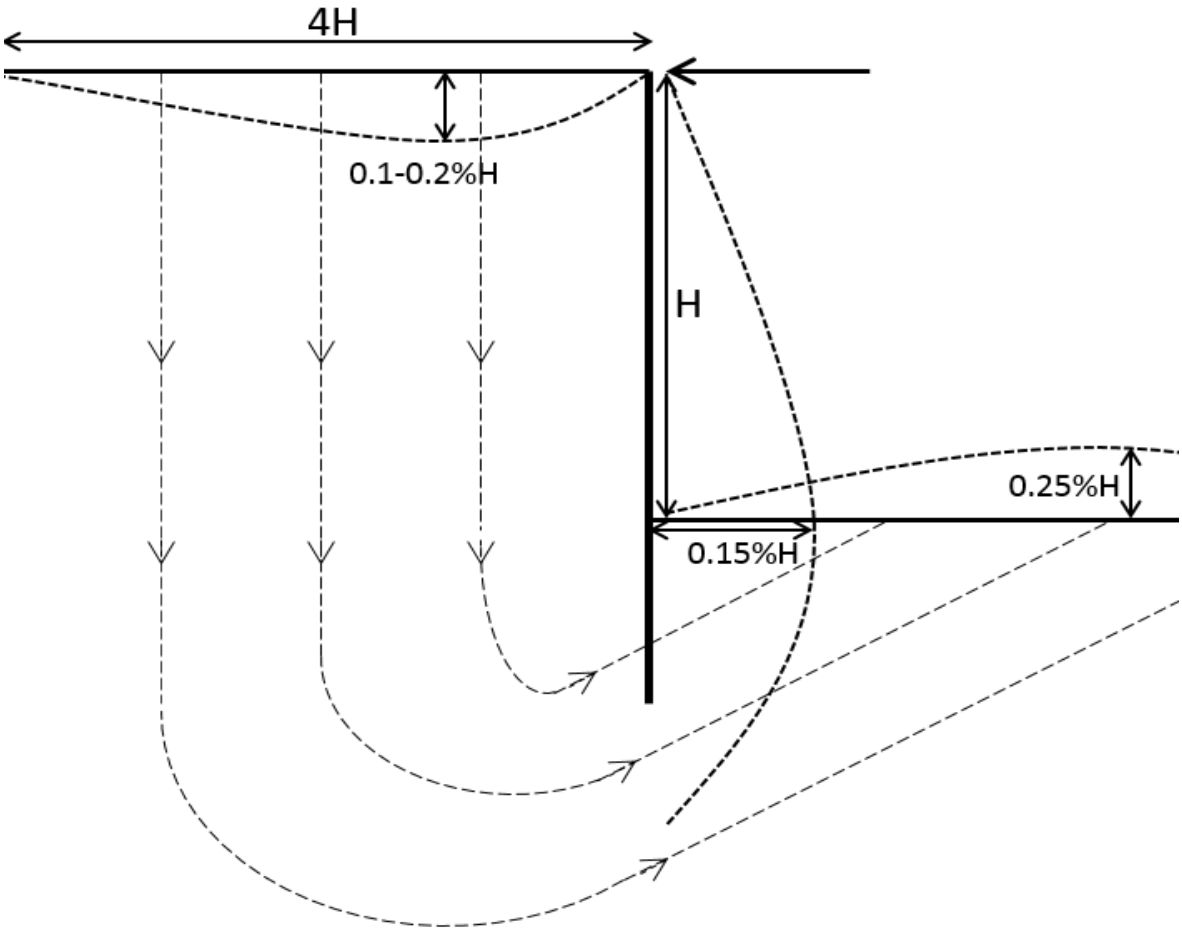

Figure 38: Undrained ground movement averages (indicative)

Another comparison is shown in Figure 39, which gives the excavated plan area with the measured short-term heave as a percentage of excavation depth. It is clear there is a general trend of the larger the excavated area, the larger the short-term heave but it is difficult to draw too many conclusions. The majority of the results sit between 0.2-0.3%H with a slight increase with area. The two points outside this zone are: at Bell Common, where the 35mm of short-term heave may incorporate more pore pressure equalisation than other sites due to the unique construction sequence (44x470m long tunnel); and QE2 where the heave was taken at 4.5m depth and is likely to have been higher at the surface.

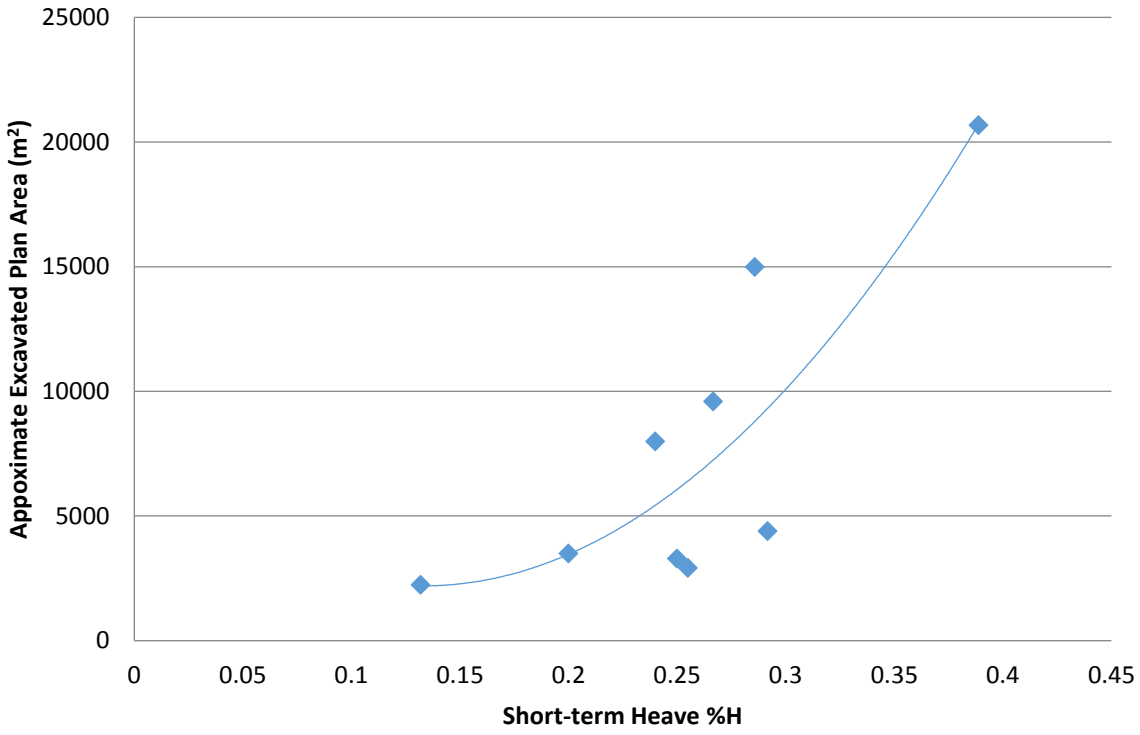

Figure 39: Measured short-term heave against area of excavation

3.4. Long-term heave and wall movements

The influence of lateral wall displacement continues throughout the heave process but as volume is not conserved, the drained Poisson ratio (0.0-0.2) is much lower than the undrained Poisson ratio (0.5). This could mean that instead of lateral wall and ground movement directly translating into vertical heave movement, some lateral compression of the soil between adjacent walls could be expected. Long (2001) has recorded retaining wall and offsite movements for 300 case histories. The findings were that in stiff clays, the maximum total long-term horizontal displacement would be between 0.125%H and 0.4%H depending on support system; the average should be taken around 0.2%H. Base heave measurements are not given for these cases. For the case histories considered in Tables 2 and 3, considerably less wall movement occurs after excavation is complete when compared to during construction wall movements.

The majority of heave that occurs after an undrained response is caused by pore pressure equalisation and is known as primary heave. The remainder of heave occurs due to secondary effects (Mesri, et al., 1978). The effects of primary and secondary swelling cannot be separated readily and so the two types of heave are known as ‘Long-Term’ heave.

There are several cases where heave has been monitored over periods long enough to record some long-term heave but few cases have a record longer than two years after construction. The measurements associated with heave are given in Table 4.

From the long-term heave data, it is difficult to make a connection between sites as they differ significantly in the depth and time of measurements. Site geometry is very important too and there is little that is similar. Part of the reason for differences is the differences in effective stress states. For example, for HR pre-excavation pore pressures are high at the depth of the base of the excavation and the heave is unrestrained while at AR there is a hinged slab adding total stress and a pump reducing pore pressures beneath the slab. In both cases the change in effective stress differs while the depth of excavation is similar.

Case	Long-Term Heave (mm)	Piled (Y/N)	Time Taken after Excavation (years)	Reference
AR	30 (0.29%H)	N	7 (At 3m depth)	(Carder, et al., 2004)
BC	50 (0.56%H)	N	11 (At 1.5m depth)	(Carder & Darley, 1998)
CC	25 (0.21%H)	Y	0.5	(Wood, 2000)
HR	105 (1.05%H)	N	21	(Chapman, 1999)
LY	42 (0.41%H)	Y	2 (At 1.91m depth)	(Ng, 2004)
SC	50 (0.42%H)	Y	27 (At 1.75m depth)	(Burford, 1988)

Table 4: Long-term heave data

Another consideration to long term heave is the effect known as ‘deep-seated’ heave. At Aldershot Road where the London Clay is very stiff at shallow depths, there is evidence of ‘deep-seated’ heave (Carder, et al., 2004). The data from two locations, MR10 and MR11, show the heave at shallower depths has increased at a slower pace and has caused apparent compression in the upper clay layers (Figure 40). This can be seen at MR10 where the heave in mid-June 1997 was recorded at around 42mm for M13 and 21mm for M10 with a difference of 21mm. Then in 2002 M13 became 52mm and M10 became 39mm with a difference of 13mm. This closing of the differences is compression between M10 and M13 at MR10 (albeit M10 and M13 are still further apart than before construction activities).

Additionally at MR11, M17 sits above M15 and is heaving at a quicker rate supporting the deep seated heave theory.

It could be argued that the artesian pressure below the base of the clay and the drainage layer beneath the slab created a vertical flow that kept pore pressures above hydrostatic and encouraged heave from the base up. In addition, the slab cast over the clay surface may have provided restraint to shallow movements. On the other hand, it is possible that this is a reading or instrument error as it might be expected that any heave at depth would translate to at least a similar heave closer to the surface.

Long-term heave is shown to extend to considerable depths at other sites. At BC it was measured to 13.65m (Symons & Tedd, 1989); at BL to 21.5m (Simpson & Vardanega, 2014) and at LY to 20m (Ng, 2004).

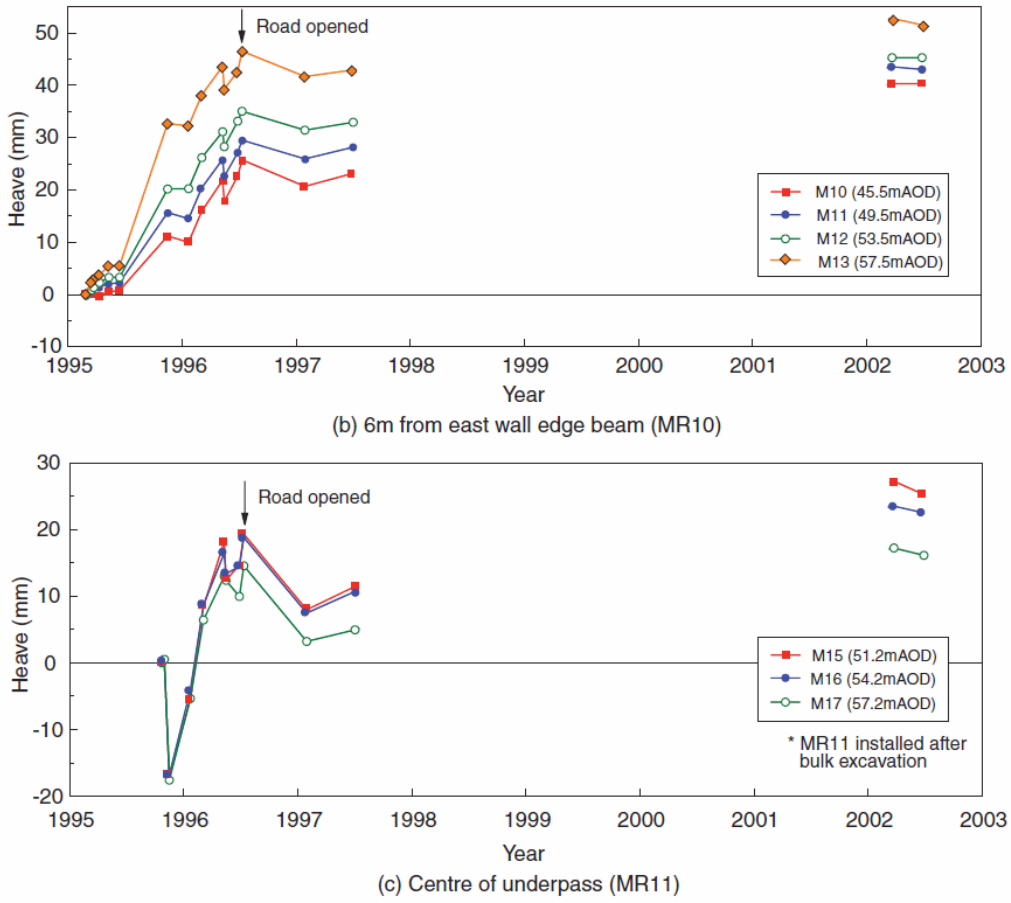

Figure 40: Heave at MR10 and MR11, Aldershot Road (Carder, et al., 2004)

3.5. Pore Pressures

The length of time associated with heave is in part due to the low permeability of the clay. Pore pressure equalisation should therefore take significant time and occur from the drainage

boundaries first (Ng, 2004). However, as shown when the pore pressures were measured at, Lions Yard, Figure 41 and Aldershot Road, Figure 42, that the majority of pore pressure equalisation occurs 'relatively' quickly which is suggestive of two-phase behaviour (Ng, 2004). This is where the initial 'rapid' rise in pore pressures occurs through the exploitation of the fissure system and then a lag of swelling behaviour follows from the water permeating slowly into 'soil lumps'.

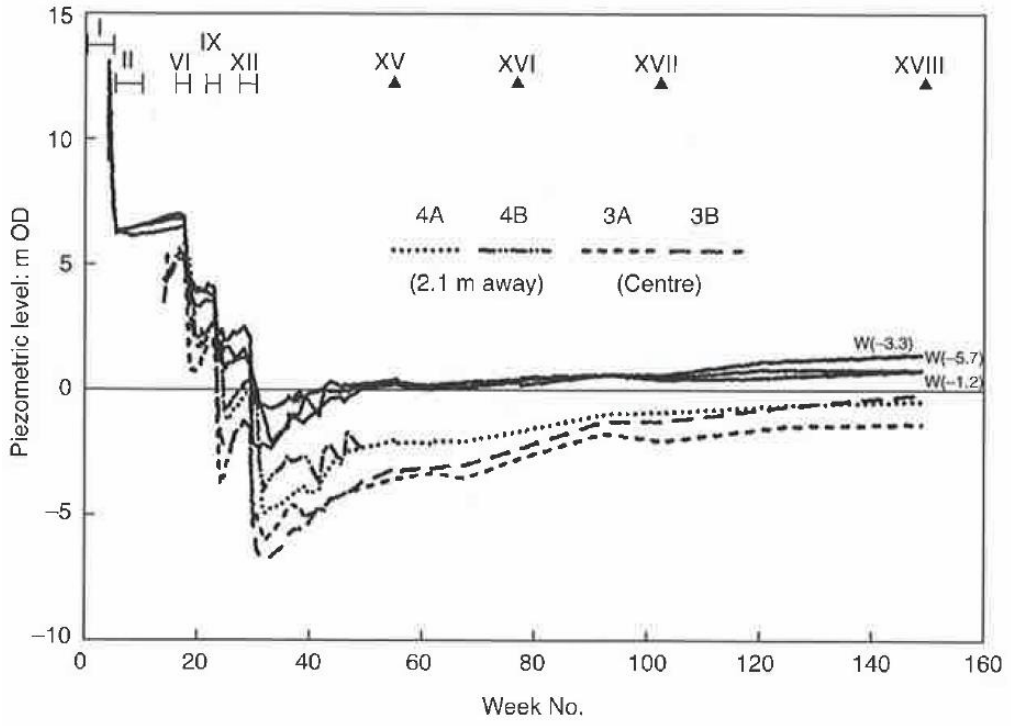

Figure 41: Piezometric levels at Lions Yard (Ng, 2004). Initially quick pore pressure equalisation.

The effect of this two-phase behaviour would lead to more heave occurring in the short-term in the upper layers. It may be inferred from this that predicting rate of heave is a function of the bulk permeability as well as the permeability of 'soil lumps'.

Another factor to consider when looking at two-phase behaviour is climatic influence as it is common for excavations to be left exposed to the elements and rainfall can quickly equalise pore pressures in the upper layers of an excavation.

Looking at the data from the case histories, it could be argued that the recorded short-term heave values consist of both undrained behaviour and the first phase of pore pressure equalisation. Bulk permeability is often much higher than permeabilities measured in the laboratory and in the case of the House of Commons, a large water source in the form of the Thames could have provided a significant proportion of this first phase.

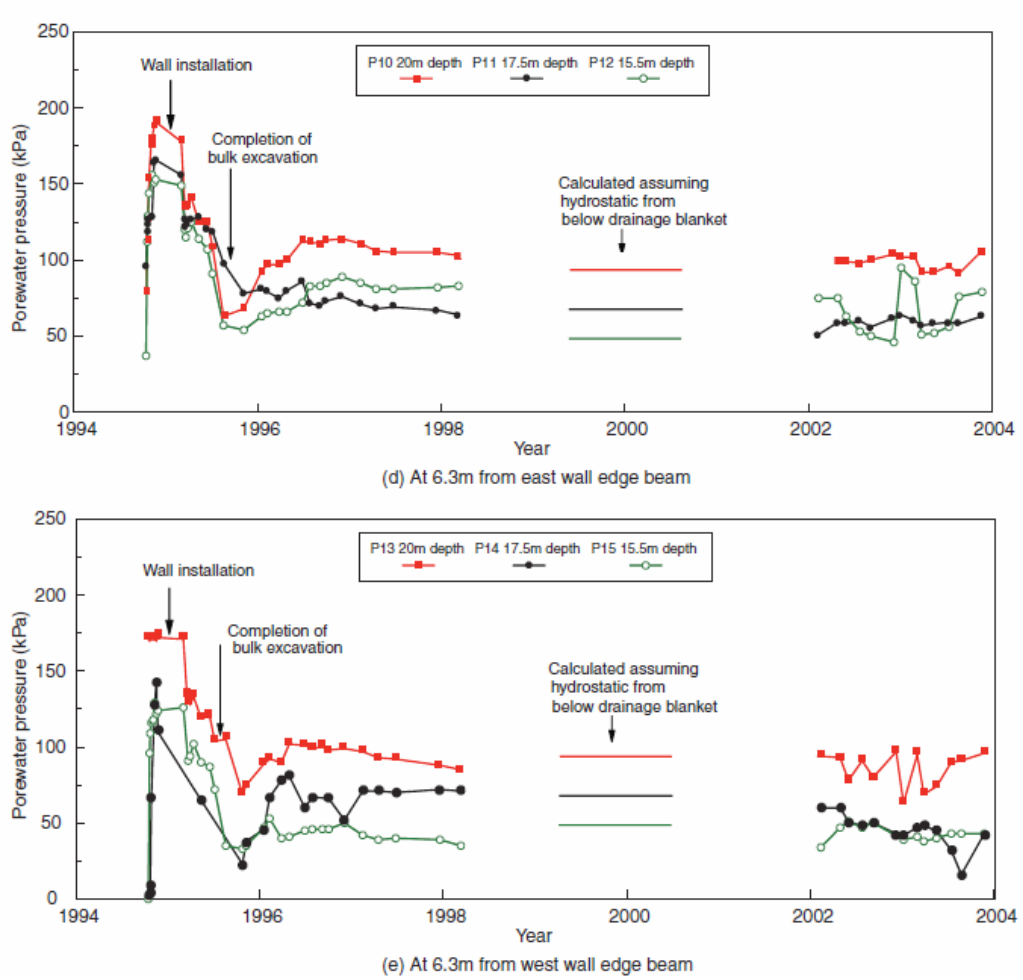

Figure 42: Porewater pressures at Aldershot Road (Carder, et al., 2004). Deeper piezometers record quickest recovery.

When considering the effect of undrained unloading, pore pressures are likely to become negative and therefore, suctions are created in the upper clay layers. These suctions may reach high levels; however, they should not be high enough to form 'cavitation' (Fredlund, et al., 2012). Cavitation is the 'unstable' expansion of vapour-filled cavities within the pore-fluid air and could potentially lead to the fracture of soil.

Fracture of the clay weakens it and may contribute some heave in the short-term. This is thought to be responsible for "a fraction" of the short-term heave that occurred at the British Library (Raison, 1988) but it seems unlikely that cavitation would have caused the fracture as sufficient suctions would not have been reached.

3.6. Difficulties in calculating and predicting heave relative to field observed values

The difference in heave between field observations and that calculated from laboratory experiments is usually subject to some interpretation but nonetheless it has generally been particularly difficult to use laboratory results to correctly predict heave.

In the 1950's, observed ground movements could be over 1000% below the predicted values (Vargas, 1955), such inaccuracies in estimates would be unacceptable today. However, differences between laboratory and field values of parameters such as the swelling index, which is single value given to the change in void ratio per logarithmic cycle of effective stress when unloading, are still relatively large with a good example being for London Clay. The swelling index was found to be 0.15 in the laboratory (Gasparre, 2005); however, most field observations place this value at around 0.03 (Isik, 2009). This is the case for Gault Clay too, as at Lions Yard the swelling indices deduced from oedometer tests on undisturbed samples are two to three times larger than back analysed field measurements, Figure 43 (Ng, 2004). This is in large part due to sample disturbance which is discussed in Chapter 5.

The insitu stiffness is very difficult to quantify and the extent it 'softens' through straining is a complex non-linear relationship (Atkinson, 2000). SPT N-values, and more recently CPT, are sometimes the only insitu test available with Stroud's method used to convert into usable parameters (Stroud, 1989). However, using SPT values is crude and if soil investigation cost is an issue self-boring pressuremeter tests are preferable assuming expertise are available for correctly calibrating the test equipment and interpreting the disturbance of dataset (O'Brien & Newman, 1990).

Strains in the field are rarely of practical engineering significance until 0.01-0.1% (Simpson, 2010) and can typically be over 1% in the upper clay layers (Figure 43) at the base of an excavation (Simpson & Vardanega, 2014). This stiffness degradation has not been analysed in the field to an extent where predictions can be made and few simple methods exist to deal with this.

Also, despite soil swell predictions becoming more accurate with better understanding from field observations and laboratory experiments, ground-contacting slabs have generally been avoided. This is over concern about large earth and water pressures that could develop beneath the slab. Instead, a void is often left beneath (Burland & Hancock, 1977; Ng, 2004) or a drainage layer is provided (Carder, et al., 1997; Wood, 1990).

The cases where a slab is cast ground-contacting (Burland & Kalra, 1986; Wood, 2000), the weight of the slab and building acted to reload the ground beneath the excavation and left a small net unload which did not incur significant long-term heave. The contact pressure was measured at CC but only shows that the stiffer sides of the basement slab have higher contact pressures than the more flexible centre (Wood, 1990). The spade cells used have an installation effect which needs to be compensated for (Richards, et al., 2007) and the installation of the cells and any correction is not explained by Wood (1990).

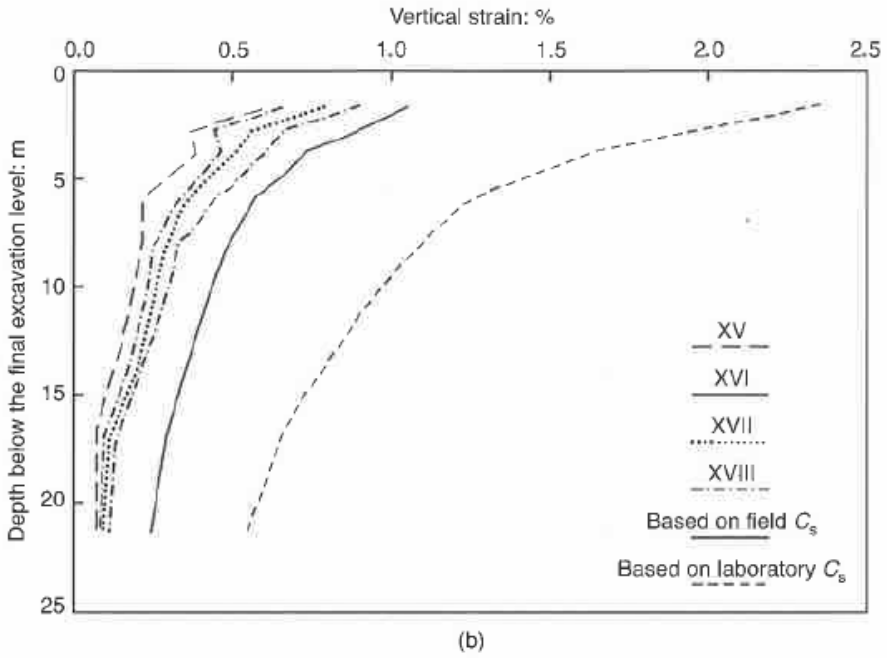

Figure 43: Strain in the field at Lions Yard. Difference between laboratory and field measured swelling index (Ng, 2004)

To establish a true representation of ground-contacting slab behaviour, observation of the contact pressure on a basement slab following a large net unload of the ground is needed. However, minimising slab deflection through increasing its thickness or by stiffening the joints with the retaining wall is common practice in order to: reduce behind the wall and internal ground movements; maintain structural stability; and to remain within serviceability limits. Therefore, there is little deflection to compare with 'swelling pressure'. Some would argue that prevention of soil swelling prevents the soil 'softening' which prevents stiffness degradation and more heave.

The swelling pressure is defined in this thesis as the earth pressure that occurs on the base of ground-contacting basement slab. If measuring the total (or contact) pressure using a cell on the underside of the slab, both the water pressure and the self-weight of the slab must be

accounted for. Water pressure can simply be subtracted from total pressure while slab weight acts to restrain heave and may cause initial compression of ground. Therefore, the self-weight of the basement slab should be subtracted from both the contact pressure and potential swell pressure. The relationship between the 'swelling pressure' of the soil and heave is not fully understood and there is a significant 'region of uncertainty'. This has been graphically represented in Figure 44 but does not account for uncertainty in both quantity and proportion of total or undrained heave prior to the basement slab being cast. Neither does it show the case of a perfectly stiff slab where the final swell pressure would be where total heave (horizontal) line crosses the soil heave vs swelling pressure line.

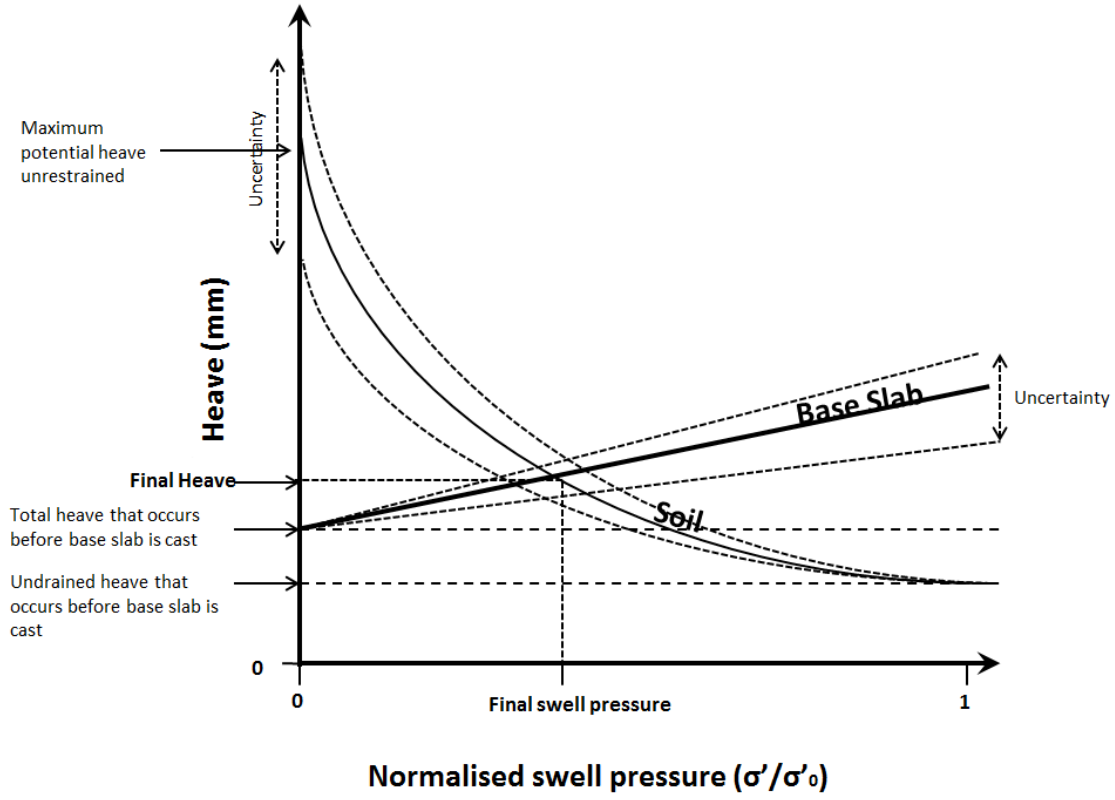

Figure 44: Sketch showing normalised swelling pressure on the base of a ground-contacting slab

Another factor to consider when modelling swelling pressure is the use of piles, which is a well-established method of heave reduction, and may also act below the column to reduce settlement due to applied loads e.g. from a superstructure. The extent this reduces the swelling pressure through heave mitigation is not fully understood. It is thought that reducing heave locally around a pile will decrease the potential swelling pressure on the basement slab but increase the uplift pressure experienced by the pile.

In conclusion to the literature on case histories, considerable uncertainty exists over heave and swelling pressures when basements are constructed into overconsolidated clays. The following uncertainties are examined through installation of instrumentation at Victoria Station Upgrade (VSU):

1. Short -medium term ground movements - both during excavation and shortly after a ground-contacting basement slab was cast. Heave at the centre of the site was measured using magnet extensometers and wall inclinometers, installed by a third party, show during excavation sub-surface lateral movement.
2. Pore pressures – both deep and shallow piezometers are installed to measure the response of pore water pressures during and after excavation.
3. Swelling pressure – contact pressure is measured beneath the ground-contacting basement slab in multiple locations. The pressure is measured at the centre of the slab to examine how the relationship between swell and swell pressure; and both next to and between tension piles to examine the effect the piles have on swell pressure.
4. Slab rigidity – strain gauges are installed to compare ground swell to strain in the slab.

The VSU case history is described in the next Chapter while laboratory testing has been conducted to examine the difference in field measured soil stiffness and laboratory tested soil stiffness. This research is discussed and presented in Chapters 5, 6 and 7.

4. VICTORIA STATION UPGRADE (VSU) NORTHERN TICKET HALL (NTH)

4.1. Introduction

Vicotria Station Upgrade is located in Central London next to the infamous Victoria Station. The Northern Ticket Hall is part of VSU and consists of a 9-12m deep basement into London Clay. The basement was constructed over three years using a top-down methodology. The land above the basement is intended to be sold to a developer and so the basement itself is designed to withstand a large structure above. This has led to the basement being heavily reinforced and as a standalone structure it would be overdesigned.

This has presented a unique opportunity to monitor a basement structure which wasn't predicted to move much. Therefore, measurements were taken to examine ground movements in the short-medium term using magnet extensometers; pore pressures at shallow and deep depths using piezometers; swelling pressure beneath a ground-contacting basement slab using pressure cells; and slab rigidity using strain gauges in the slab.

The first part of this Chapter describes Victoria Station Upgrade and the instrumentation that has been installed at the site. The second section gives the results of the instrumentation and places them into context.

4.2. Description of Victoria Station Upgrade

Instrumentation has been installed at the Victoria Station Upgrade (VSU) North Ticket Hall which is located in Central London, England (Easting 529088, Northing 179217, Latitude 51.49716, and Longitude -0.14177553), Figure 45. VSU North Ticket Hall is part of the larger VSU project which involves constructing two new underground ticket halls, connecting passageways to alleviate overcrowding, platform extension and facilitate step free access to Victoria Station underground station. In addition, the wider Victoria Transport Interchange project coincides with redevelopment of the Victoria area of Central London. The Northern Ticket Hall has been designed with particular consideration to the surrounding buildings and a ground-contacting basement slab has been used in conjunction with a secant piled wall to minimise off-site ground movements.

The geological sequence of the site consists of Made Ground overlying Alluvium and River Terrace Deposits; these are underlain by the London Clay Formation and then the Lambeth Group. The phreatic surface lies in the Terrace Deposits and groundwater is assumed to be

hydrostatic in London Clay Unit B while in London Clay Units A2 and A3 underdrainage causes pore pressures to drop below hydrostatic conditions.

The installed instrumentation was intended to reduce uncertainties typical of deep excavations into OC clays. Firstly, vertical extensometers were installed in late 2013 (details later in Section 4.2.4 Figure 54) to provide insight into the short-term heave below the site. In addition, pore pressures were monitored to capture reductions in water pressures on unloading and the pore pressure equalisation. Strain gauges were attached to the reinforcement in the 'upper' base slab (Figure 46) to measure deflections and pressure cells are laid below the 'upper' base slab to measure swelling pressure.

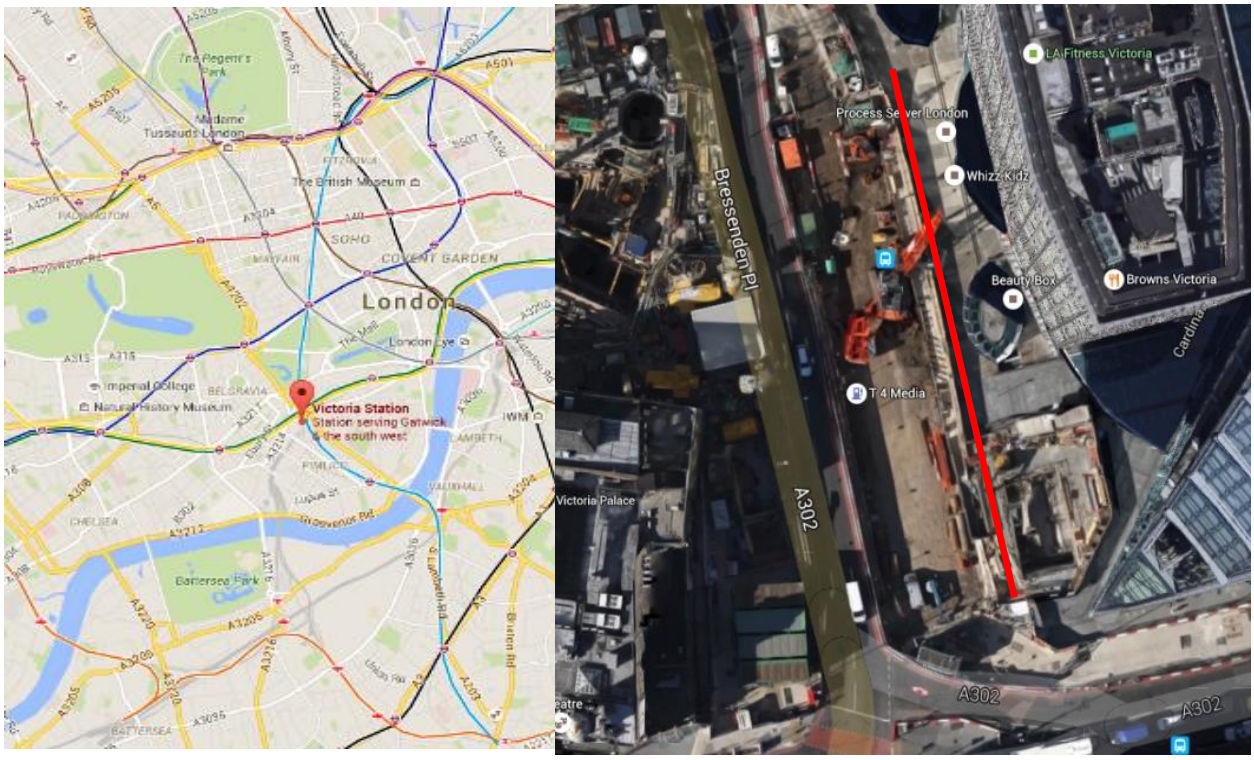

Figure 45: Location of Victoria Station Upgrade (Google, 2015)

4.2.1. Description of site

VSU Northern ticket hall, seen in Figure 46, is 75m in length and up to 32.5m wide, but the width reduces to around 20m for 50m of the length. The depth of excavation varies between 9-12m and includes the use of ground-contacting basement slabs to minimise on and off-site ground movements.

The ticket hall has a 1.2m dia. secant piled wall and is propped by roof and floor slabs. The roof slab is 1m thick and is cast between roof beams which were precast off-site spanning 18m in length across the width of the majority of the basement. There is a 0.5m thick floor

slab cast at 5mbgl while the 1.2m thick upper base slab is cast at 9mbgl. Also, there is a 1.5m thick lower base slab cast at 12mbgl. There are 1.8-2.1m diameter, 39-42m long (from base slab), bored piles at 6-7m spacing below the base slab (shown on Figures 54 and 57). The majority of piles contain plunge columns and each of the slabs are connected to the columns and piles.

4.2.2. Construction sequence

The Northern Ticket Hall was constructed using a top-down methodology, see Figure 47 and Table 5. This begun in the autumn of 2013 with the construction of a secant piled wall around the perimeter of the ticket hall. This was followed by construction of the piles below the base slab which consisted of boring and pouring concrete into a single pile a day (50-51m long pile from the surface). The reason for such slow pile construction was the volume of the pile; a large number of trucks are needed to transport muck away and bring in concrete while the site sits in a heavily congested area of Central London. This meant large diameter bored piles, which were uncased below River Terrace Gravels, were left standing open for up to 8 hours at some depths. The effects of this are discussed in 4.3.5.

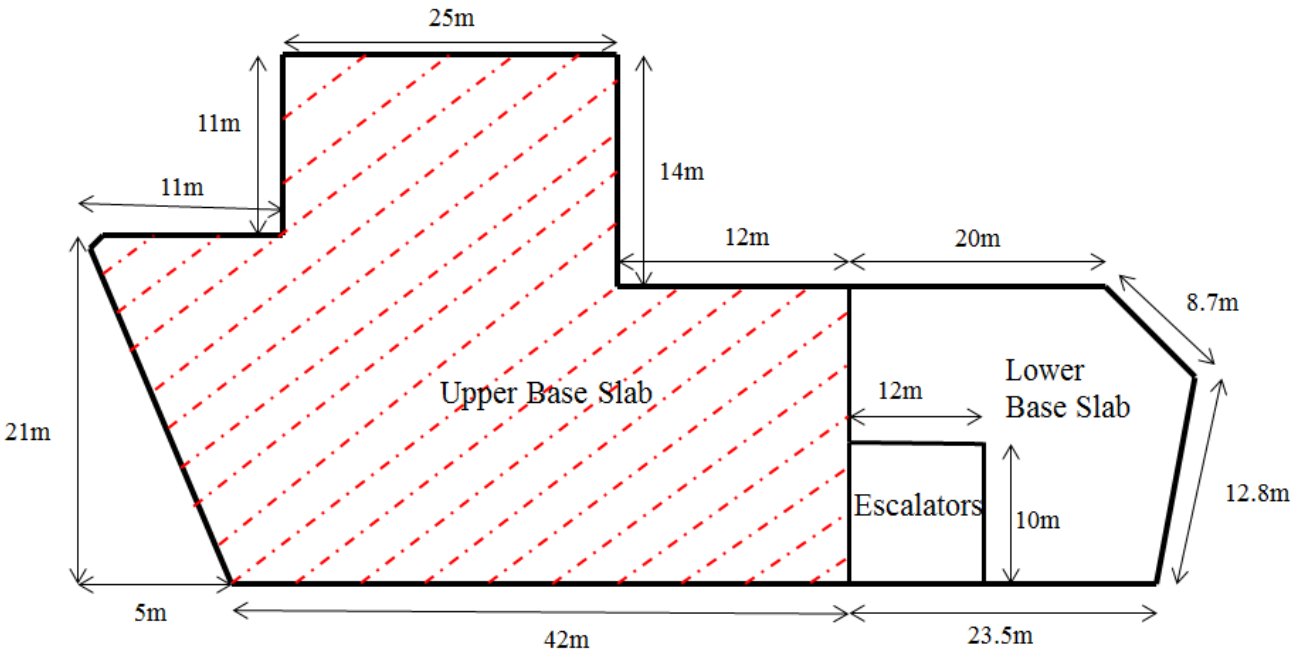

Figure 46: Plan view of VSU Northern ticket hall

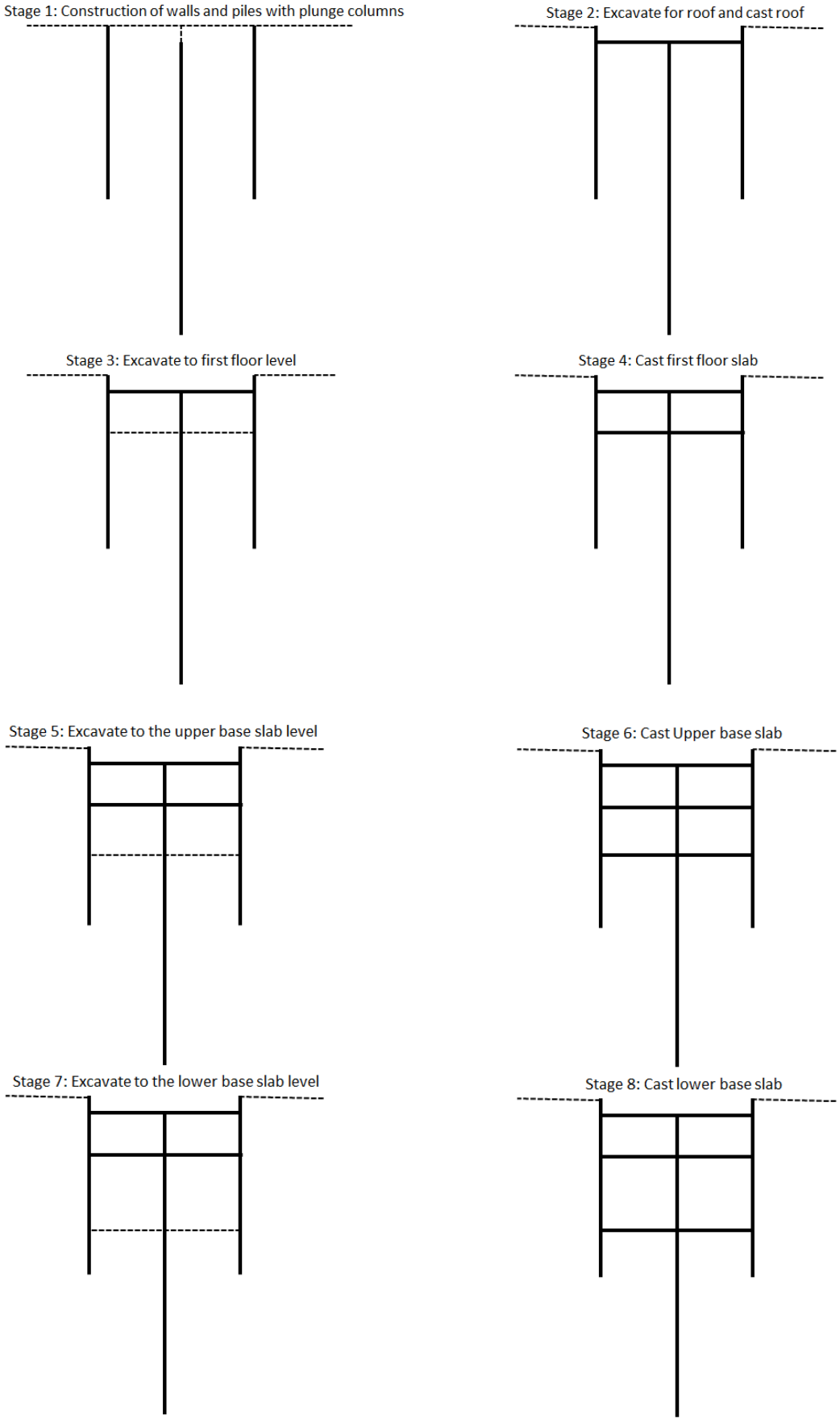

Figure 47: Stages of top-down construction (not to scale). This is indicative only

Table 5: A summary of the construction sequence at VSU Northern ticket hall

Stage	Timescale
1 – Secant piled wall and bored piles with lunge columns constructed	September-November 2013
2 – Excavate to roof level and cast roof slab	December 2013
3 – Excavate to first floor level	February-April 2014
4 – Cast first floor slab	May 2014
5 – Excavate to the upper base slab level	June – July 2014
6 – Cast upper base slab	September 2014
7 – Excavate to lower base slab level	October - November 2014
8 – Cast lower base slab	December 2014
9 – Fit out	January 2015-December 2016

Then, in December 2013, further excavation to the base of the roof slab level was achieved and pre-cast roof beams spanning the full excavation width were craned into place, see Figure 48. The sculpted pre-cast units were intended to create an attractive finish to the ceiling of the ticket hall below. Concrete was then cast between and above the precast roof beams to form the roof slab with a gap left in the slab for plant to begin excavation underneath the roof slab. Once concrete in the roof slab had set sufficiently for it to support its own weight, excavation could begin underneath the slab, Figure 49, until the first-floor level was reached, in April 2014. At this point, Figure 50, the first-floor level slab could be poured with the same gap left in the slab to enable further excavation.

Further excavation to the upper base slab level then occurred in July and August 2014 with an additional 30cm of excavation occurring to reach the top of the London Clay layer (see 3.3.3). Blinding was then cast to the height of the original base of the upper base slab and the upper base slab was cast over two thirds of the site, Figure 51, in September 2014. The other third was left with blinding over it to reduce water mitigation into the soil and clay heave.

Once the upper base slab had set, further excavation could begin to reach lower base slab level. A slope was created between the two levels which would eventually support an escalator. Before the lower basement slab was cast, a considerable foundation was cast on the slope to support the escalator. Once the lower base slab was cast, winter 2014/15, work to fit out the basement begun. At the time of originally writing this section of the thesis, this work was ongoing.

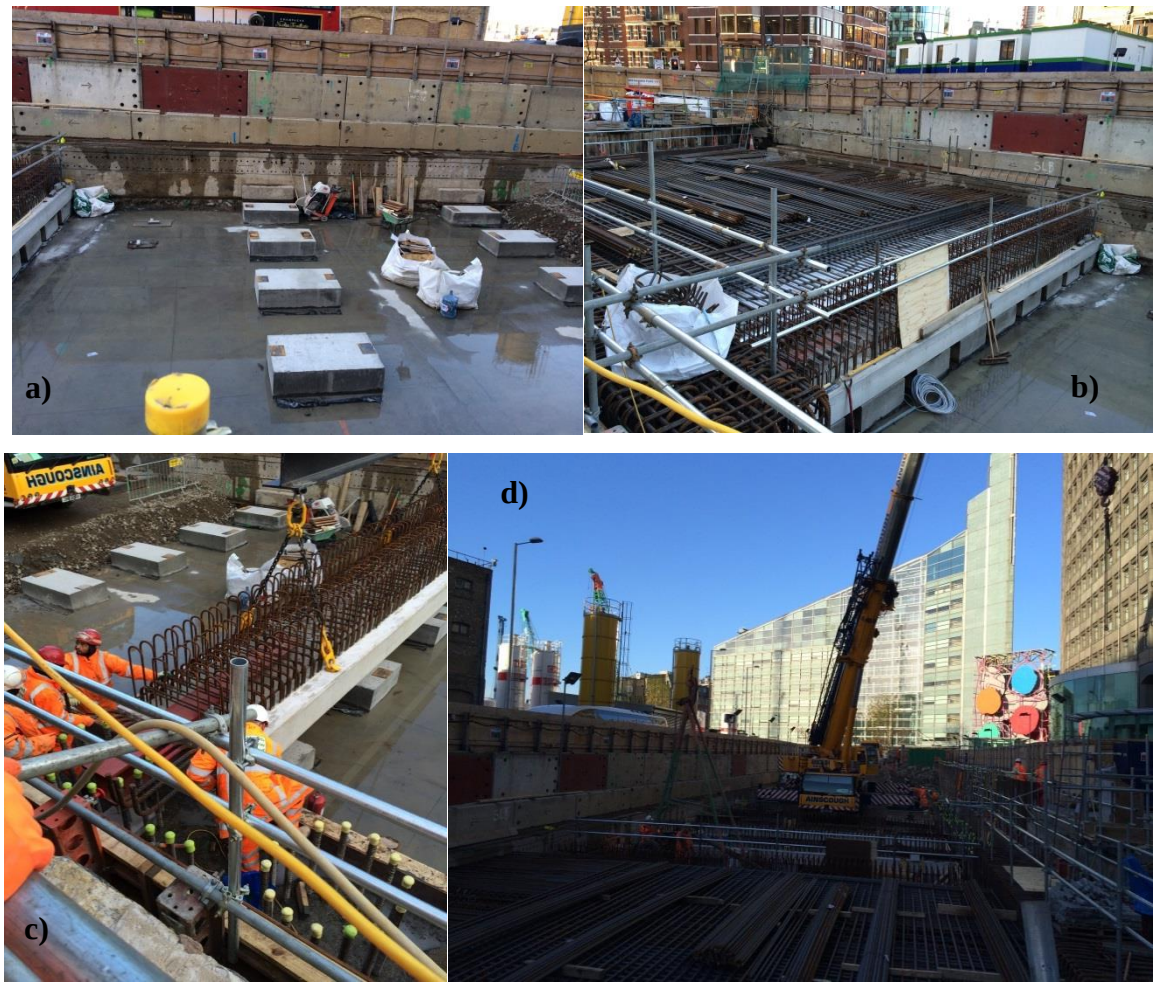

Figure 48 a), Top left is the footings for the roof beams; b) top right is the steel reinforcement being laid for the roof slab; c) bottom left is a roof beam being lowered by a crane into position with workers assisting; d) bottom right is the view down the length of the site in December 2013.

Figure 49: Roof slab once strength gained and an excavator beginning the excavation in the gap left in the roof slab

Figure 50: View of the first-floor level excavated area and the metal casings around the instrumentation boreholes, which were subsequently removed

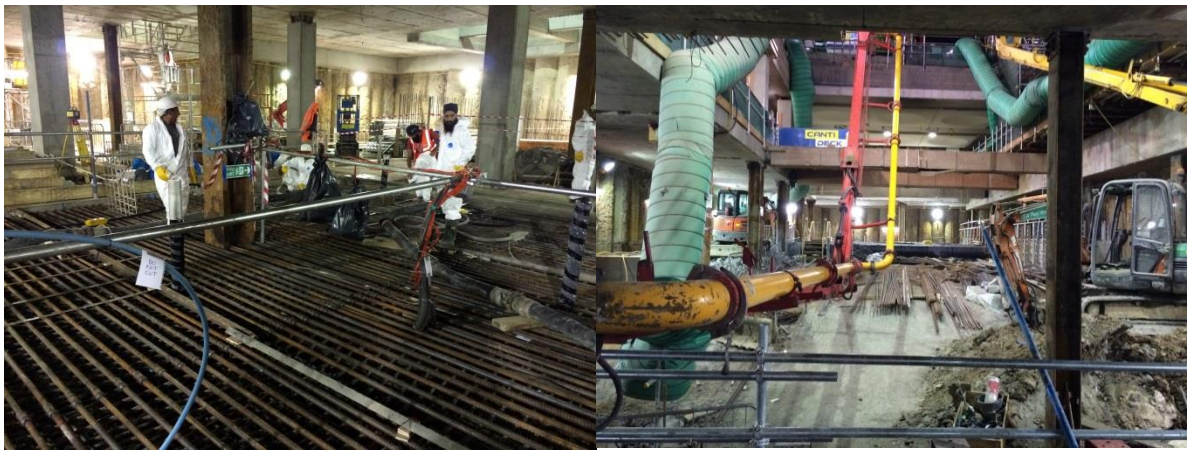

Figure 51: The upper base slab level as concrete was poured into the slab

4.2.3. Geotechnical Interpretation

The following interpretation is formed using extensive preconstruction site investigation provided by Mott Macdonald. The site had numerous usages throughout its history with the presence of historic construction rubble and even an old Victorian entrance to Victoria station uncovered during excavation so unsurprisingly the first soil encountered is Made Ground which varied in thickness between 0.4 and 5.4m. Initially a hard surface of paving slabs, asphalt and concrete overlaid very heterogeneous soil. It has been described as grey, brown, black or yellow sandy Gravel, gravelly sometimes silty Sand and soft to firm brown, grey, sometimes sandy gravelly organic rich Clay that contain brick, sandstone, flint, wood, pipe, leather, etc. More generally, the Made Ground was coarser at the surface and fine towards the base.

Below the Made Ground, a stratum of Alluvium was encountered with a thickness between 0.5-7m. It has been described as grey, black, brown, green, blue or mottled clay. There are 'slight' to 'very' proportions of sand and occasional peaty layers. It was generally soft-firm.

Beneath the Alluvium, River Terrace Deposits were of thickness between 1.5-7.7m but more generally between 5-7m. The base of the River Terrace Deposits would generally lie around 11mbgl. The River Terrace Deposits were both unmodified and/or modified in parts with the description ranging from brown or yellow Sand or sandy Gravel.

The London Clay Formation underlies River Terrace Deposits and has a thickness of 44.2-46m. Using the sub-divisions proposed by King (1981), Units B1 and B2 are closest to the surface and Units A2 and A3 overlie the Lambeth group Formation. The London Clay is described as stiff to very stiff fissured, thinly, very thinly laminated, dark brown mottled grey/dark grey slightly sandy clay. The sand is fine grained and present in partings. Fissures are random and usually horizontal.

The Lambeth Group Formation has a thickness of 10.3-11.3m and comprises at the site Reading Formation mottled silty clay and Upnor Sands Formation slightly silty, gravelly, fine to medium sand. More detailed geology for this formation is not available for this site. Underlying the Lambeth Group is the Thanet Sand Formation and the Upper Chalk Formation.

Groundwater conditions are greatly influenced by the relatively impermeable clays. A perched aquifer exists as a phreatic surface lies in the River Terrace Deposits between 7-8mbgl. Hydrostatic conditions can be assumed until 19mbgl but then the London Clay and Lambeth Group Formations experience underdrainage which equates to sub-hydrostatic variation of pore-water pressures (Mott MacDonald , 2008). A further phreatic surface level lies in the lower aquifer at depth in the Upper Chalk Formation.

4.2.4. Description and installation of monitoring equipment

Magnetic Extensometers

The magnet extensometers used are Geo-Observations magnetic probe extensometers, similar to the equipment shown in Figure 53. A series of 3 leaf spider magnets are placed at the required depths embedded into the walls of a borehole. Then, a probe is dropped down through an access pipe until a beep is heard. Using the tape on a reel, a measurement can be taken which indicates the current position of the magnet, relative to the top of the access pipe,

see Figure 53. As measurements are manually read using a tape, resolution is +/- 0.5mm and accuracy of 1mm.

Two boreholes were drilled, termed E1 and E2, to approximately 50m below the base of the roof slab and installed before the roof slab was completed, each approximately 6m apart; the base of the roof slab itself is cast 1-2mbgl. Both boreholes are positioned as close to the centre of the site as possible but careful attention was needed in order to position the boreholes to allow for monitoring into the long-term. The boreholes were drilled in December 2013 using a shell and auger rig seen in Figure 52. The positioning of the boreholes can be seen in Figure 54. The initial part of drilling was slow due to some unexpected concrete being found from an old subway which ran underneath Bressenden Place. This caused considerable delay but once the London Clay was reached, drilling moved quickly. Some collapse of the boreholes was evident from the final depth of the equipment and from the quantity of grout used to backfill.

The grout used was made from cement-bentonite mix at 3:1 ratio with 50 litres of water to one 20kg bag of cement. This was mixed on-site with a hand-mixer in small, frequent batches.

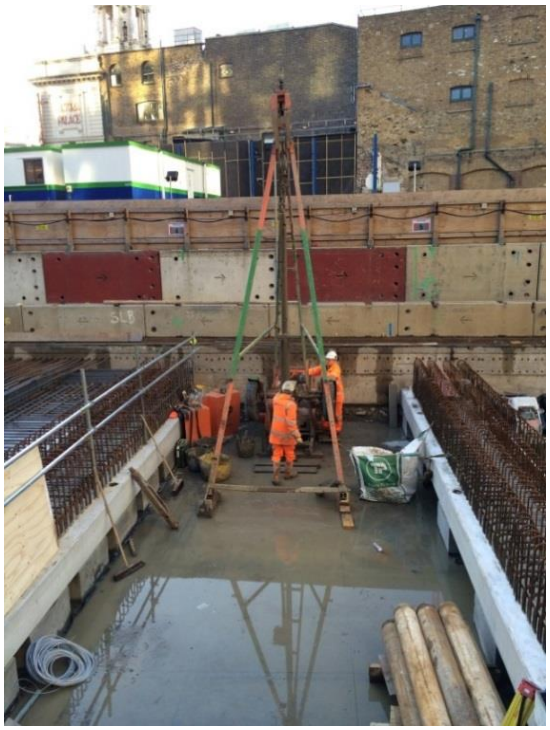

Figure 52: Shell and auger rig drilling the first borehole.

Magnets were installed at base of each borehole for use as a reference point. In borehole A, magnets were installed at depths below the top of the roof slab of: 12m, 14m, 16m, 18m,

20m, 25m, 31m and 36m but the magnet at 16m slipped down during installation to merge with the magnet at 18m. In borehole B, magnets were installed at depths below ground level (bgl) of: 11m, 12m, 14m, 16m, 18m, 20m, 25m, 31m and 38m were installed. The geotechnical assessment (given in detail in 4.3.3) of the site places the start of the London Clay at around 11m below initial ground level so this should leave the magnets at depths beneath the London Clay surface: 2m, 4m, 8m, 10m, 15m, 21m and 26m for borehole A and 1m, 2m, 4m, 6m, 8m, 10m, 15m, 21m and 28m for borehole B.

These locations were chosen near the centre of the excavation, Figures 54 and 55, as this is where the most heave was expected. The base magnet was placed as deep as possible as even at great depth, some heave is predicted. The alternatives to this system would either to use a reference point at ground level or to use an automated measurement system; both these options were technically challenging due to the construction sequence which involved excavation around the metal cased instrumentation.

The first step to installation is the borehole construction which was 150mm diameter and 50m depth from the roof slab. The first 12m was lined by steel casing as this was just over the predicted depth of the River Terrace Deposits.

After overcoming the difficulties of site constraints, installation of the probe access tubes began. This involved connecting 3m long plastic tubes as they are fed to the bottom of the borehole. Once the access tubes were secure, the spider magnets are lowered into position around the access tube using an installation tube that passes around the central access tube. The magnets are secured by pulling them upwards into the walls of the borehole to secure them into the London Clay. Once secured the installation tube can be unscrewed from the magnet and pulled out with the process repeated.

A check was performed at the end of installations using the probe to check the final positions of the magnets. It was noticed that a magnet installed at 16m in borehole A had slipped to meet the magnet below at 18m. Finally, the holes can be filled around the access tube with grout; this secures the magnets and protects them from inaccurate reading. As the magnet extensometers were installed prior to bulk excavation, the plastic tubing which the 3 leaf spider magnets surrounded was cut down during each excavation stage. At one point the pipe was extended to ensure it was readable from an unrestricted area.

The locations of the extensometers were chosen to be as close to the centre of the site as possible and in the middle of a group of piles as this was thought to be the location which would experience the most heave.

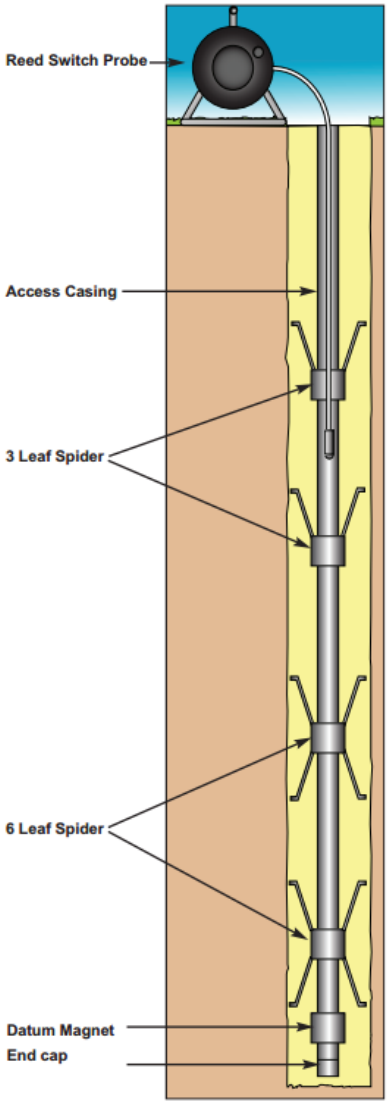

Figure 53: Typical magnet extensometer set up Invalid source specified.

Deep Piezometers

Deep piezometers are installed into a further borehole at the same time as the magnet extensometers. The deep piezometers used are ITM soil W4 vibrating wire, Table 6, with instrument ranges 0-300kPa and capable of measuring negative pore pressure of -50kPa. They have a resolution of +/- 0.025% full scale, accuracy of 0.1% full scale and operate up to a temperature of 80 degrees Celsius. In addition, thermistors are fitted to monitor temperature

in four out of the five piezometers. A single, multi-channel data-logger (RST DT2055) was used to collect the piezometer readings at 15-minute intervals initially, before being replaced by a Campbell Scientific CR1000.

The five piezometers were installed at different depths down the same borehole, as close to the centre of the site as practically possible, Figures 54 and 56. The depths are: 27m, 24m, 19m, 15m and 12m below the roof slab which positions the piezometers at depths: 18m, 15m, 10m, 6m, 3m below the base of the basement slab at this point. However, it should be noted that only the bottom two piezometers were correctly grouted due to complications with grouting onsite.

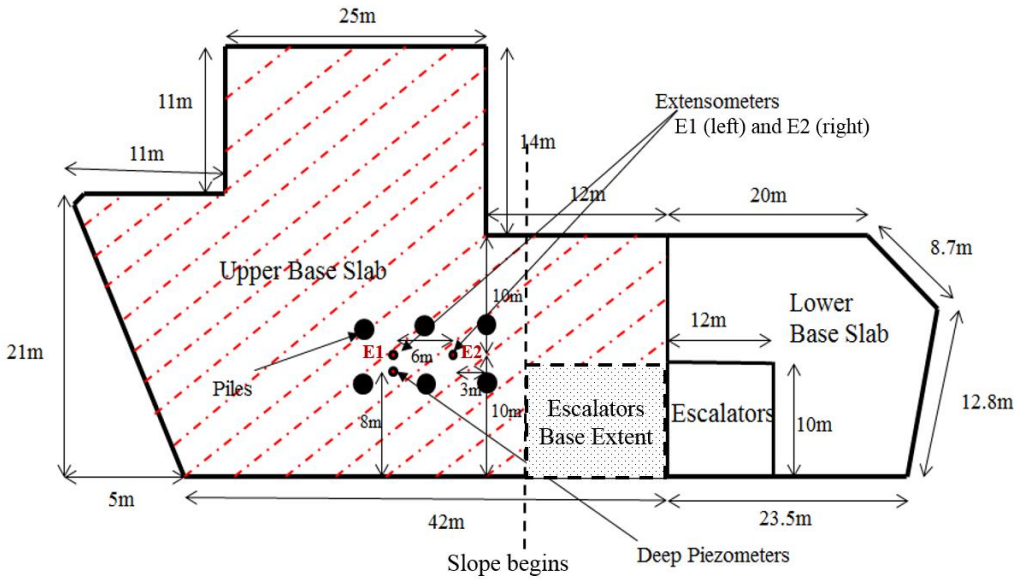

Figure 54: Positioning of boreholes – indicative only (only local base slab piles shown – not to scale)

Before arrival onsite, zero values were determined by taking values at atmospheric pressure multiple times. Using the manufacturer's calibration sheets some piezometers consistently under/over predicted the pressure by +/-0.5kPa compared to that stated by the Meteorological Office but the zero values taken in the laboratory were used and a potential error of +/-0.5kPa was accepted as reasonable considering the pressure range that was going to be measured.

To install the piezometers into the borehole, they were lowered on a plastic installation tube. The tube needed to be constructed as the piezometers were lowered and the tube is left in the borehole to keep the piezometers at the required depth. The piezometers were fixed to the tube using extra strong and large cable ties and then the cables that came from the piezometer head were also tied to the tube. The installation process was difficult due to the weight of the

entire installation. Once all piezometers were lowered into the borehole, the data-logger could be attached to the cable ends and the borehole could be filled with grout.

The piezometers were located at the centre of the site, and the borehole was as close to the extensometer borehole as possible without causing borehole wall instability.

Shallow piezometers, total pressure cells and wall inclinometers

Shallow piezometers were installed in hand augured boreholes (~50-100mm wide) immediately (~ 0.1m deep to the measurement head of the piezometer) below the basement slab. These were Geosense VWP-3000 vibrating wire piezometers, Table 6, which are their standard model; with high air entry air filters. The piezometers are connected to a Campbell Scientific CR1000 datalogger. These piezometers have a range of 350kPa, have a resolution of +/- 0.025% full scale, accuracy of 0.1% full scale and operate up to a temperature of 80 degrees Celsius.

The total pressure cells installed below the blinding were from two suppliers, Geosense (Table 6) and Soil Instruments Ltd. The pressure cells were connected to the Campbell Scientific CR1000 datalogger. Geosense cells provide a range of 350kPa, have a resolution of +/- 0.025% full scale, accuracy of 0.1% full scale and operate up to a temperature of 80 degrees Celsius. Soil Instruments Ltd cells provide a range of 500kPa, have a resolution of +/- 0.025% full scale, accuracy of 0.1% full scale and operate up to a temperature of 80 degrees Celsius.

In addition to equipment installed by the author, the contractor chose to monitor wall movements through a third party. These in-place inclinometers were installed at multiple locations and depths in the secant piled wall; however, only a single set of wall inclinometers are presented in this thesis. As for the depths in the wall pile, they are 11, 12, 13, 14, 15, 16, 17, 18 and 19m below original ground level. Permission has been gained to use the relevant data and this is presented in Section 4.4.1.

The location of the shallow piezometers, wall inclinometers and pressure cells can be seen in Figure 56. These are shown as green dots for the pressure cells, blue dots for the shallow piezometers, the black dots are the surrounding piles and a red dot with blue ring is the wall inclinometers location.

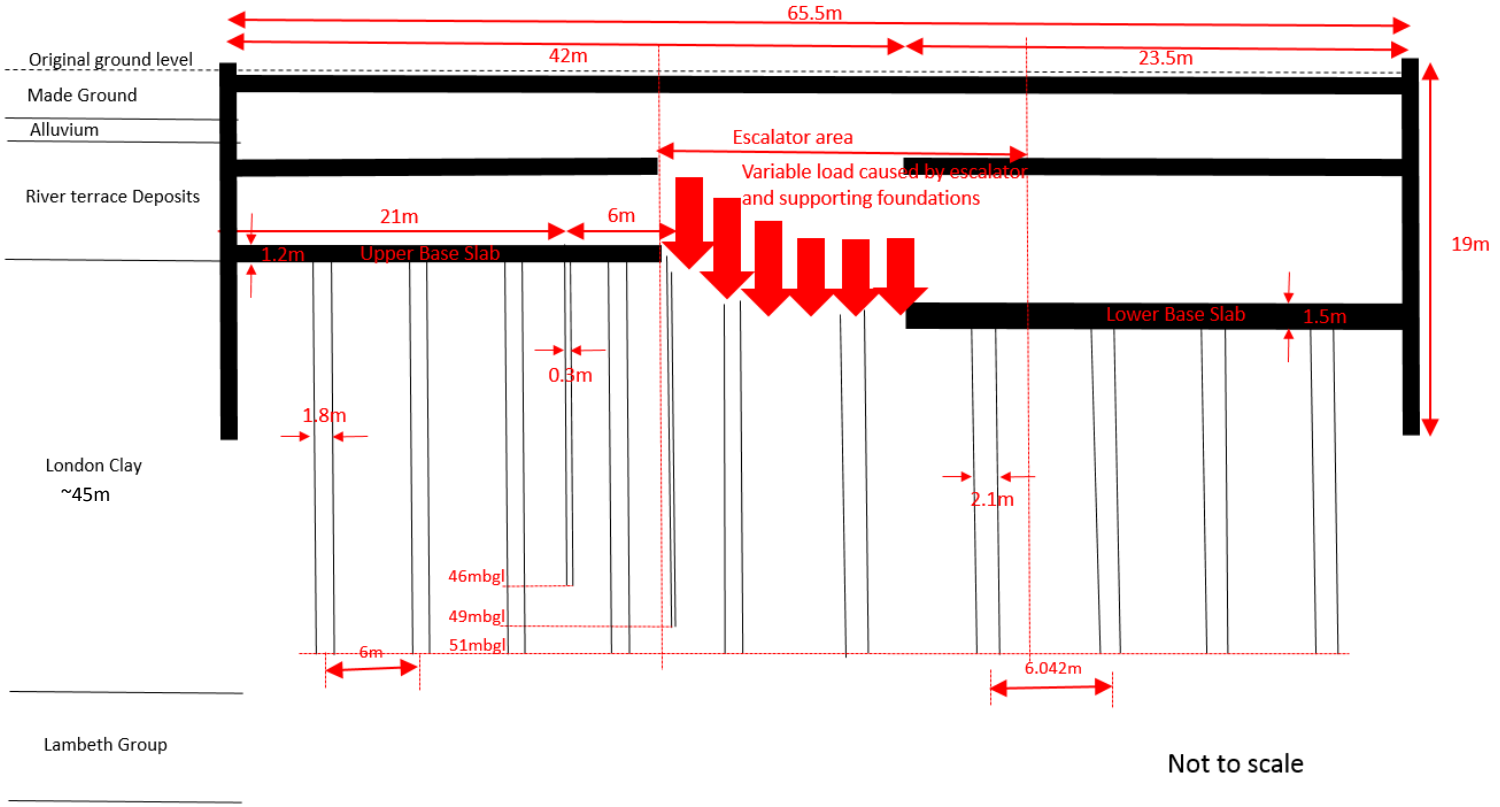

Figure 55: Cross section of VSU North Ticket Hall

The shallow piezometers were placed between each four-pile configuration to understand the effective stresses beneath the base slab. The pressure cells were installed at various locations: firstly, at the centre of two different 4 pile configurations which were both roughly at the centre of the upper basement slab; second, in the middle of two piles; and finally, next to a single pile (~ 300mm). This configuration was to demonstrate the difference in pressures that build beneath the basement slab. It is thought that flexibility in the slab should reduce the swelling pressure while piles can act to prevent swell. Both cases were to be examined. Wall inclinometers were installed by a third party out of concern of the surrounding buildings and so were strategically spaced around the perimeter of the excavation.

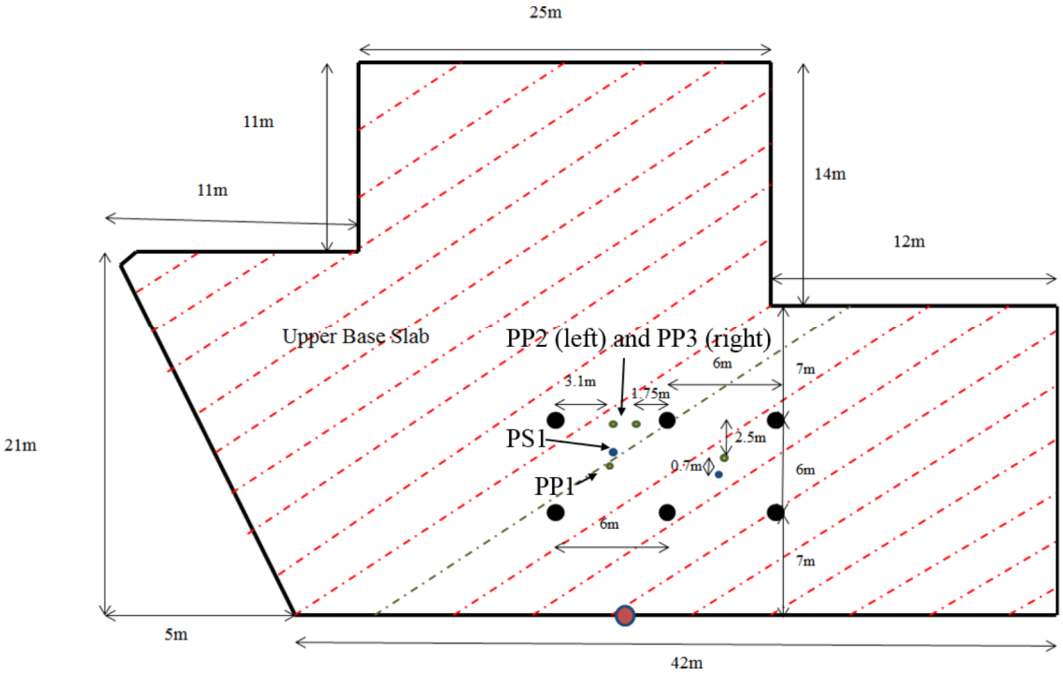

Figure 56: Location of shallow piezometers and total pressure cells (not to scale)

Zero values for all but the inclinometers were determined on-site due to time restrictions so the necessary adjustments to the data were made with the aid of the calibration sheets.

The installation of the shallow piezometers began by boring a small hole using a hand auger. The borehole was around 40cm deep in order for the full length of the piezometer to sit inside with an additional 10cm to be backfilled using silica flour mixed with water. To install the piezometers, a thick paste of silica flour and water was placed into the borehole. The piezometer was then pushed into the paste which remains unset, but ensures that suctions can be transmitted from the soil to the ceramic of the piezometer. The wires leading from the piezometer were then taken carefully to datalogger.

For the total pressure cells, a domed surface needed to be created to ensure good contact with the pressure cells and to obtain reliable data. This was achieved by cutting the surface of the clay with a spade and then using silica paste to act as a filler material. Once a relatively smooth and domed shaped surface was created, a paste of silica flour was applied to the clay and the pressure cell bedded into it. The silica paste was intended to fill any remaining imperfections in the clay surface and ensure a solid and even contact exists between the ground and the cell. The cells were placed on the ground with the long, thin, stems (shown in Table 6) containing vibrating wire pressure readers pointing towards the dataloggers. The stems were then held in place with tent pegs to ensure no movement when the blinding was poured over the cells.

As both the shallow piezometers and total pressure cells were installed just beneath the ground-contacting base slab, formwork was made to provide a working space while the blinding was poured over the remainder of the excavated surface. This can be seen in Figure 57. The wooden formwork was later removed and the internal void around the instruments was filled with concrete blinding. This was done with care as not to disturb the instrumentation. As for the wall inclinometers, these were installed by a third party during the secant piled wall construction and it is likely that they would have been attached to the steel reinforcement cages and lower into a pile bore before pouring concrete into the bore.

Figure 57: Formwork for the piezometers and total pressure cells

During construction, a slight design change to the basement resulted in a single pressure cell and a shallow piezometer becoming exposed on what was to become the escalator slope. The shallow piezometer was not damaged but was exposed to the air while the pressure cell was no longer functional, see Figure 58 for slope. The orange wires disappear beneath the timber formwork and upper basement slab at the top of the slope. At the base of the slope a datalogger is held in a bucket while data was extracted to keep out of the surface water seen.

Figure 58: Exposed instrumentation on slope. The spade (green) is placed within the photograph as a reference point. Photo shows a pressure cell partially destroyed at the top of the slope with a shallow piezometer connected to a datalogger (held in a bucket).

Strain gauges

There are twenty vibrating wire sister bar strain gauges supplied by Geosense, Table 6. They are 16mm in diameter and consist of a sister bar which is tied to reinforcing bars within the floor slab. They are installed in pairs either side of the neutral axis to provide bending moments and axial loads. They comprise two lengths of ribbed rebar welded to a central gauge section. The strain gauge consists of a steel wire tensioned between two end blocks. A thermistor is installed in each strain gauge to analyse the effect of slab cooling. The strain gauges provide a range of 2500με, have a resolution of +/- 0.6 με, accuracy of 0.25% full scale, gauge length 50mm, De-bonded length 175mm, overall length 1.39m and the bars have a coefficient of thermal expansion of 12ppm/°C.

The installation of the strain gauges involved working within the reinforcement cage, shown in Figure 59. Using the steel rebar, metal wire was used to tie the strain gauge to the correct steel rebar. The steel rebar chosen was used due to its geometry in line with the columns.

Each strain gauge was located on the inside of the cage so that it was not too close to the surface of the concrete when poured.

Table 6: Instrumentation used at VSU

 **Magnetic extensometers and probe on a reel with tape, Geosense image not available (itmsoil, 2014)**	 **Vibrating wire piezometer (itmsoil, 2014)**
 **VWP-3000 (Geosense, 2015)**	 **Vibrating wire strain gauge (Geosense, 2015)**
 **Geosense total pressure cell (Geosense, 2015)**	

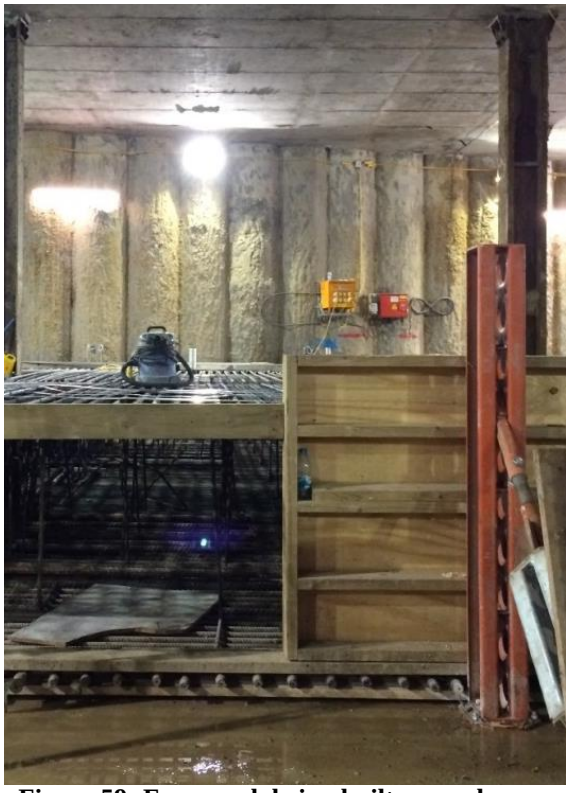

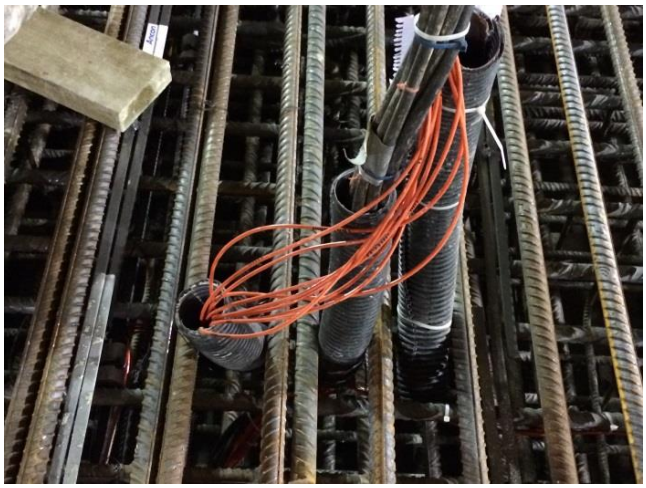

Figure 59: Formwork being built around one section of the ground-contacting basement slab reinforcement cage and the cables shown to be brought up through the reinforcement

Five strain gauges were placed on the upper and lower steel cage in the North-South direction and East-West direction and the locations can be seen in Figure 60. The idea was to have five measurement points to be able to describe approximate bending of the slab. This location was chosen as it was as close to the centre of the excavation as possible and there were restrictions on access so the datalogger needed to be in a corridor within 5m of the strain gauges.

Once fixed, zero readings were taken using a vibrating wire reader and then each strain gauge was wired into the datalogger which was located above S10. The wiring would follow the steel cage and was fixed using ties.

There was a period of a few days before the pouring of the basement slab. During this time, wooden panels were placed above the strain gauges to protect them from the workers above. When the pouring of the slab commenced, supervision to ensure the gauges remained fixed was undertaken and direct pouring of the concrete onto the gauges was avoided.

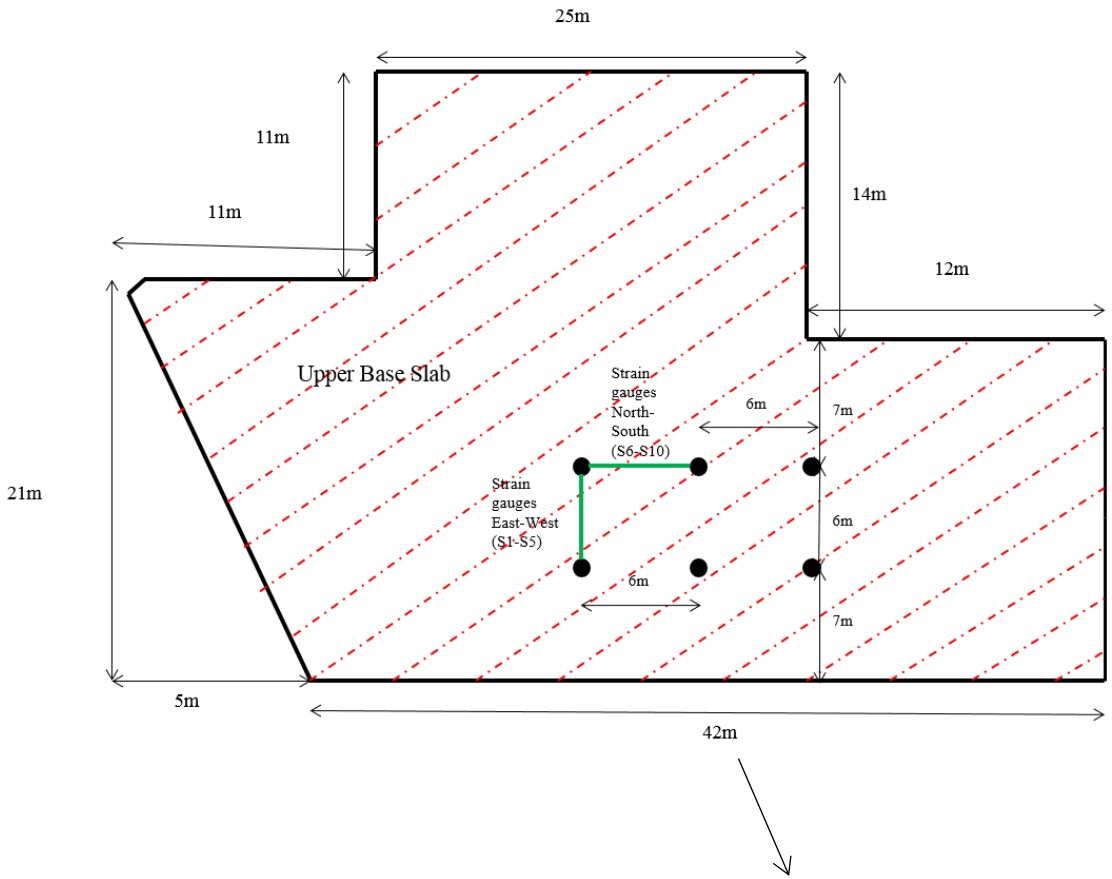

Pairs	Reference
G4, B8	S1
G5, B4	S2
G8, B10	S3
G1, B3	S4
G9, B1	S5
G10, B5	S6
G2, B2	S7
G7, B6	S8
G3, B7	S9
G6, B9	S10

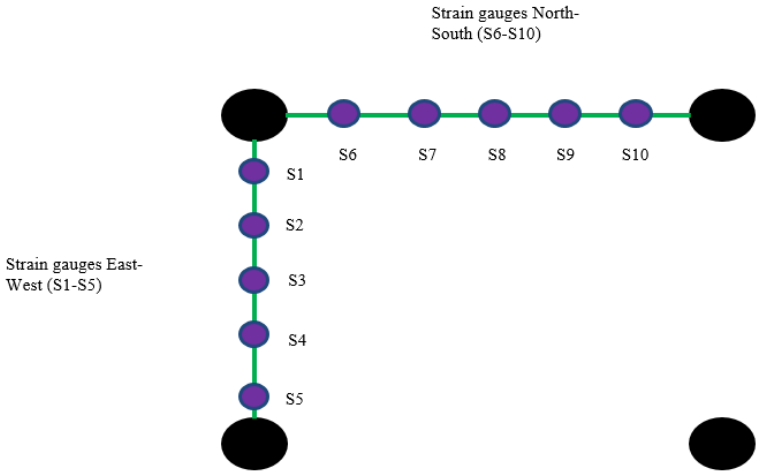

Figure 60: Location of strain gauges between plunge columns (not to scale)

4.3. Field results and discussion

4.3.1. Heave and wall movements

Multiple sets of zero readings for both magnet extensometers were made shortly after installation and then averages taken. The results are given in Table 22 in Appendix. Each time they are measured at least two sets of readings are taken for each magnet, and the magnets are designed to beep as the probe passes through two points and so both values are recorded giving four readings for each magnet. The average of the magnet movement was calculated and is given in Table. The repeatability of measurement is typically +/- 1mm; however particular attention was needed to achieve this due to the flexibility and potential movement of the top of the access tube. This unsupported section of the access tube varied in length depending on the stage of excavation.

Results for heave are given in Figures 61 and 62; overall, there has been less heave than expected when compared to the design of the structure. There has been no more than 10mm of measured heave which is around 0.1%H and heave is significantly less than for the case histories considered in Chapter 3. For the first set of readings on the 8th April 2014, E1 shows the remainder of magnets in compression with the top magnet heaving while for E2 all magnets heave relative to the base magnet. It is possible E1 magnets were swelling from a state of further compression prior to the readings; possibly due to casting of the roof slab. For the second set of readings in the final week of April 2014, both E1 and E2 have all magnets heaving relative to the base magnet.

For the set of readings in the first week of August 2014, there is some compression when compared to the previous reading in April 2014 at both E1 and E2 with some magnets at E2 recording compression relative to the zero reading. This is possibly due to the casting of the first floor basement slab. The second set of readings in August 2014 continue the trend towards compression; particularly at depth despite excavation to the upper basement slab level in July 2014. Following on from this period there is a distinct difference in behaviour at E1 and E2. At E1 there is a period of heave up until the final readings in August 2016. At E2, the magnets continue to record settlement.

Looking at E1 and E2 against the site timeline, Figures 64 and 65, it is shown that the ground heaves in total by 6-7mm (~0.13%H) and 2-4mm (~0.06%H) for the first and second excavations, respectively. Considering that after the first excavation that there was around 5-6m of overburden overlaying the top magnet, this suggests the heave at the excavated surface

could have been closer to the expected 0.25%H found in the prior case histories if the majority of overburden consisted of OC clay and not river terrace gravels.

Some wall movement would be expected after the first excavation; however, inclinometers started recording after the first excavation. Between the first excavation and the second excavation there was less than 1mm of wall movement in Figure 63 while over 10mm might have been expected at this point from the case histories.

For the second excavation, wall movements were approximately 1-1.5mm towards the excavation, while the heave was very small. It is likely that the construction and applied load of the first-floor slab has had the effect of compressing the ground prior to excavation beginning. This may have been the reason for the small wall movements too. The first-floor slab is connected to the plunge columns and cast on the excavated surface meaning the slab reloads the ground through both contact points. Considering the 4-5m of excavated soil from the first excavation was a mix of unsaturated river terrace gravels, alluvium and made ground with a bulk unit weight around 18-20kN/m^3 and the 1.2m of wet concrete has bulk unit weight of 25kN/m^3, the 'effective depth' excavated drops to below 3m by the end of the first floor slab construction and a further drop in effective depth of excavation if the weight of the roof slab loading through the walls and columns is considered to influence the soil located around each extensometer.

Doing the same calculation for the second excavation, the effective depth of the excavation is around 7m (making predicted heave 14mm using the 0.2%H rule from case histories), and 10mm of heave becomes 0.14%H (effective). This figure is still low and this may be due to the large piles installed below the basement slab, which have diameters 1.8-2.1m with 6m spacing and to depth 50m below original ground level. Additionally, a 19m deep, 1.2m thick secant piled wall which used a hard-hard methodology has minimised lateral wall movement. This means the 'undrained' aspect of heave has been reduced through volume conservation, see Figure 63. Since the end of excavation, wall movements have continued to reach a peak of approximately 3mm before beginning to stabilise at approximately 2.5mm peak lateral movement.

Examining the pattern of displacement at E1, it is clear that heave values are highest near the surface while at E2 both the settlement and heave is highest at the surface. The reason for the different responses at E1 and E2 is the location of the boreholes. At E1, the ground clearly settles after the installation of the upper basement slab and has slowly heaved since. While at

E2, settlement has continued post slab construction due to an additional weight being added in the form of foundations for the escalators. The foundations of the escalators consist of a large block of reinforced concrete of variable height which at its greatest is over 4m tall. The block aims to support the base of the escalators which span from the first-floor slab to the lower base slab; this creates a variable load on the excavated sloping section running from the upper to the lower base slab. Analysis of this load case is tricky as the stress changes become a complex 3D problem, but just taking the weight directly above E2, there should be a slight net unload during the overall construction process. The reason for the settlement might be due to a localised effect of roof slab loading, first floor slab loading and escalator foundations acting on the slope between the upper and lower base slab. Alternatively, it is not impossible that the base magnet could have heaved while the top magnets settled slightly. All the results use the base magnet as a reference point but it is worth noting that this base magnet should heave around 1-2mm based on the assumptions that: Young's modulus is at least 1GPa below the base magnet; the stress change at depth is calculated using a Poulos and Davis stress distribution (Poulos & Davis, 1974); and the relative position to the base of the piles is ignored.

A further complication might be the alterations of the extensometer read-tube. Due to site construction processes this tube was shortened and then lengthened with a bend put into E2 near the surface. This does not move the magnets but has decreased the repeatability and frequency of the results obtained at E2. During the final lengthening of the read tube, a bend was placed in the tube to allow reading to take place in more convenient location post-construction. This bend has made it difficult to get the magnet reader down the tube and on at least one occasion damage to the magnet reader occurred.

Finally, looking at the total strain after 2 and a half years of heave, the average strain between the magnets is just 0.03%, with a maximum strain between the top two magnets of 0.2%. This is of significant interest as the 0.03% is in the small strain degradation of stiffness region and at 0.2% is only just in the large strain region. If deep basements are to be constructed with such emphasis on ground movement restriction, the small strain region becomes much more important to understand. This could be described as an over-engineered solution for the prevention of ground movements; but on the other hand, the site sits in a sensitive area of central London and any off-site ground movements could damage adjacent buildings and cost millions of pounds in compensation. Furthermore, this may be the direction the industry prefers to go as it minimises risk and opens up potential use of the space above the site.

In summary, small ground movements can be achieved behind and in front of the wall, contrary to Burland & Hancock (1977). The construction sequence, design of the structure to prop the walls and use of plunge columns has been very effective at mitigating ground movements.

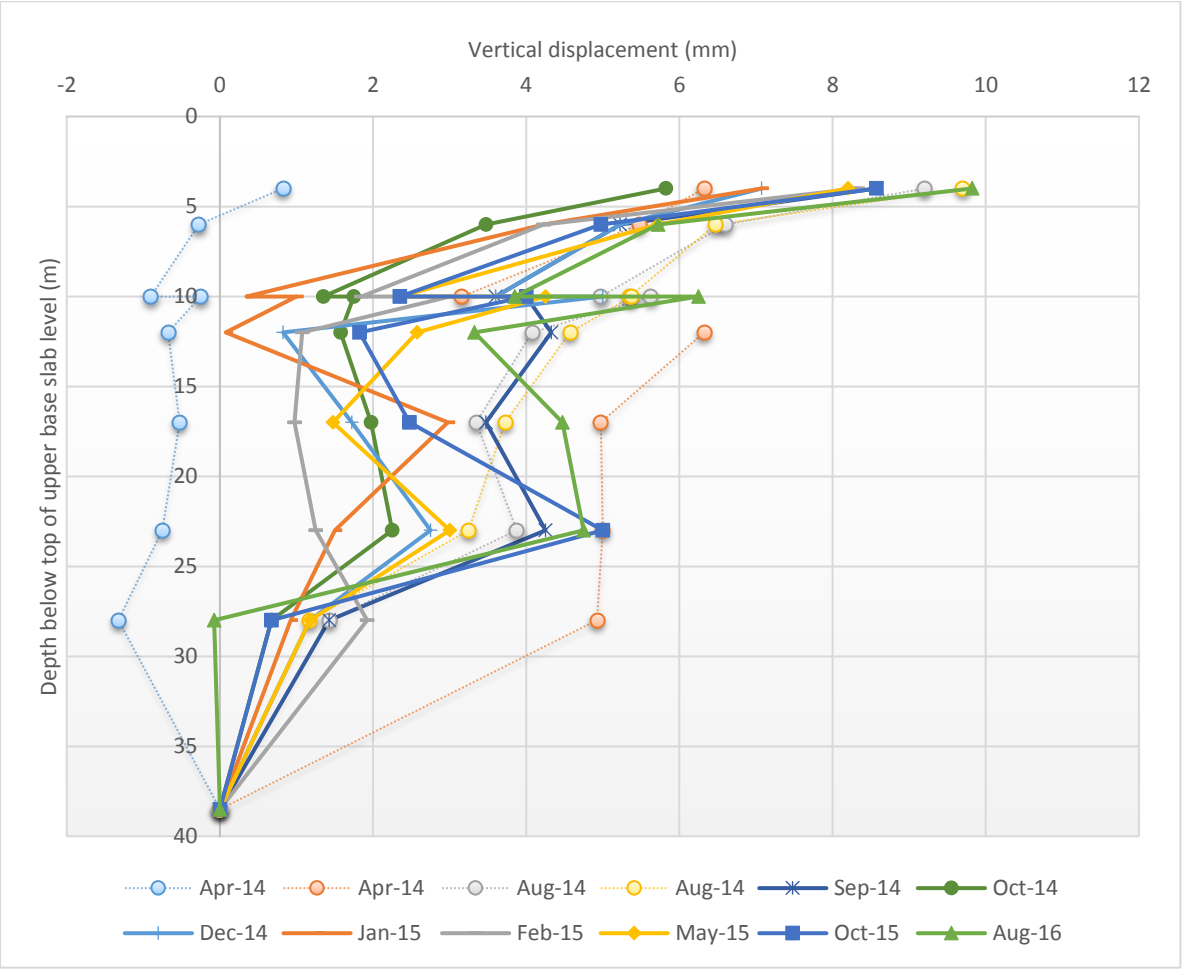

Figure 61: Vertical displacement from E1; readings shown in chronological order

4.3.2. Pore pressures

The results for shallow piezometer PS1 are shown in Figure 66. After installation, readings begin just after the blinding for the basement slab was poured; therefore, the first readings show a steady increase in suction as excess pore pressures, caused by undrained loading from the weight of the blinding, dissipate. It appears that the soil was in suction to around 40kPa before the basement slab was cast. Casting of the basement slab increases the pore pressures due to undrained loading of the soil. It is not clear whether the shallow piezometer measured the full dissipation of excess pore pressures caused by pouring of the blinding before being further loaded by the basement slab. The expected suctions resulting from unloading are theoretically much higher than measured before each concrete pouring, but it is possible that

some suction has been lost through absorption of moisture from concrete and because the site was (in part) open to the elements.

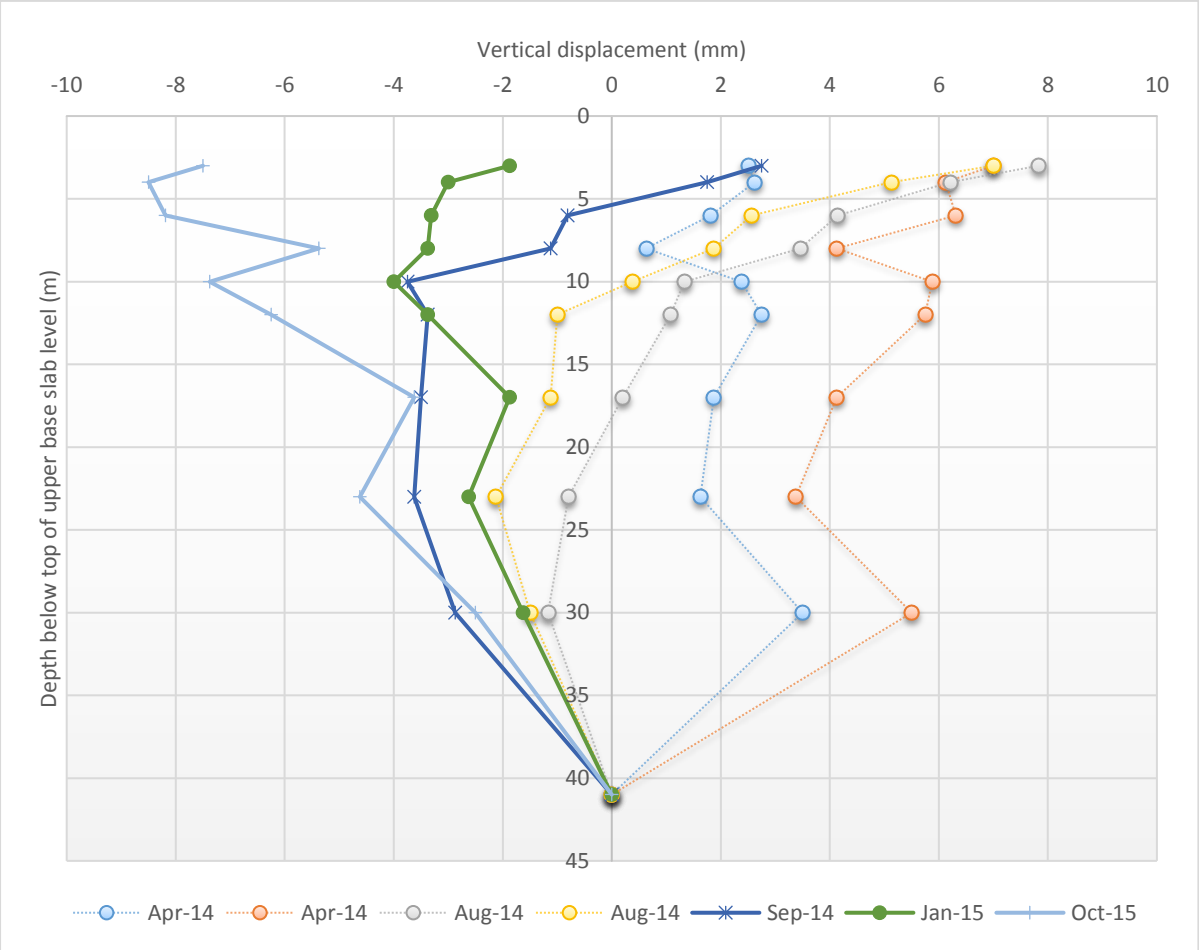

Figure 62: Vertical displacement from E2; readings shown in chronological order

After casting of the base slab, suctions reduced non-linearly with a gap in the data accounted for in rewiring of the data-loggers (marked in Figure 66). The small 'jumps' in the data around January and February 2015 are not fully explained but further excavation activities continue onsite and storage of equipment on the base slab, etc. may explain a jump in the suction value. The final measured value of pore pressure is a positive value of 12kPa which appears to be steady with the small variation in pressure explainable through seasonal temperature variation. It should be noted that the design predicted final water pressures are far greater than this and a gradual rise is expected in the long term.

.

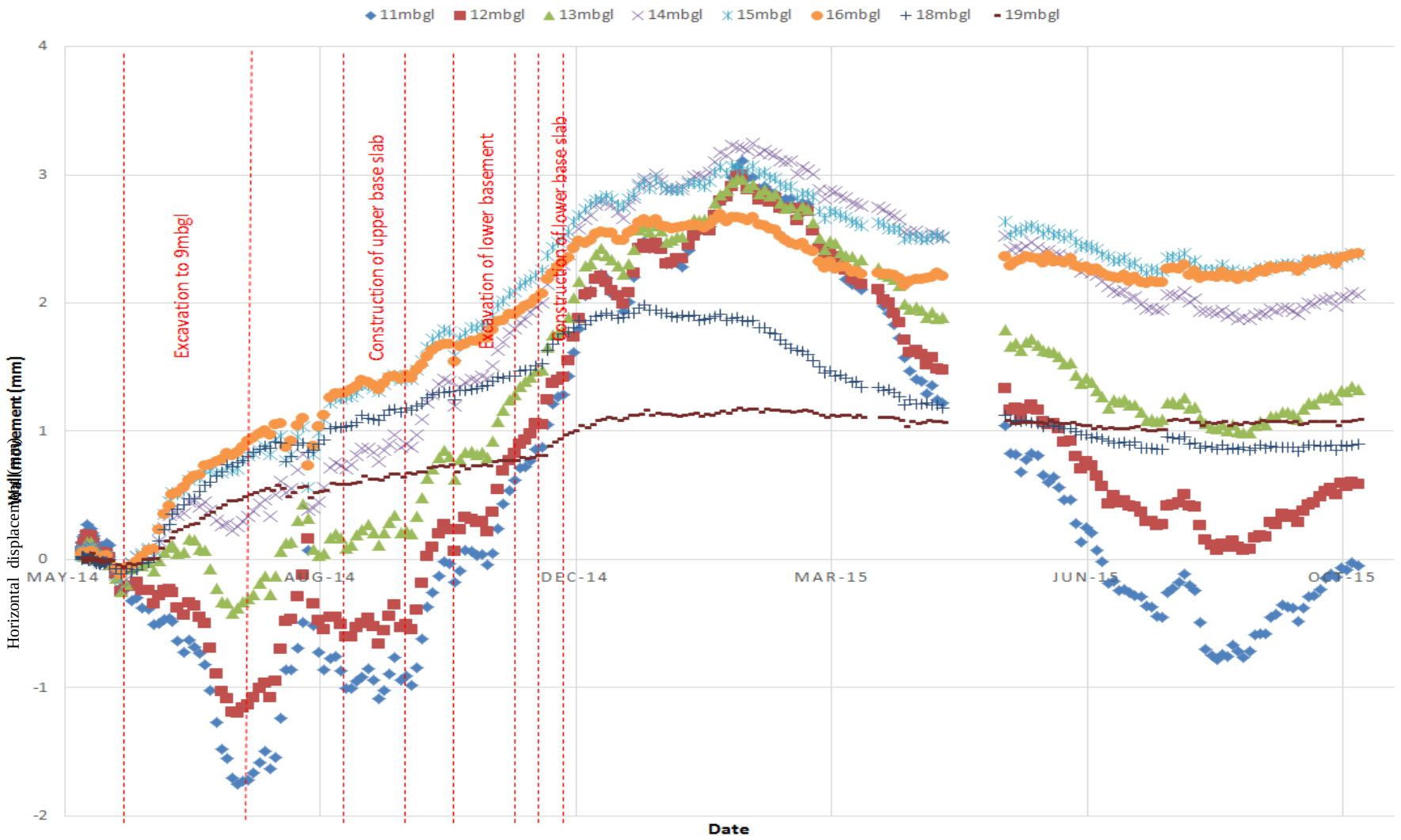

Figure 63: Wall inclinometers (metre below ground level) - wall movement (+ve towards excavation) vs. site timeline. Note inclinometers start recording after first excavation phase

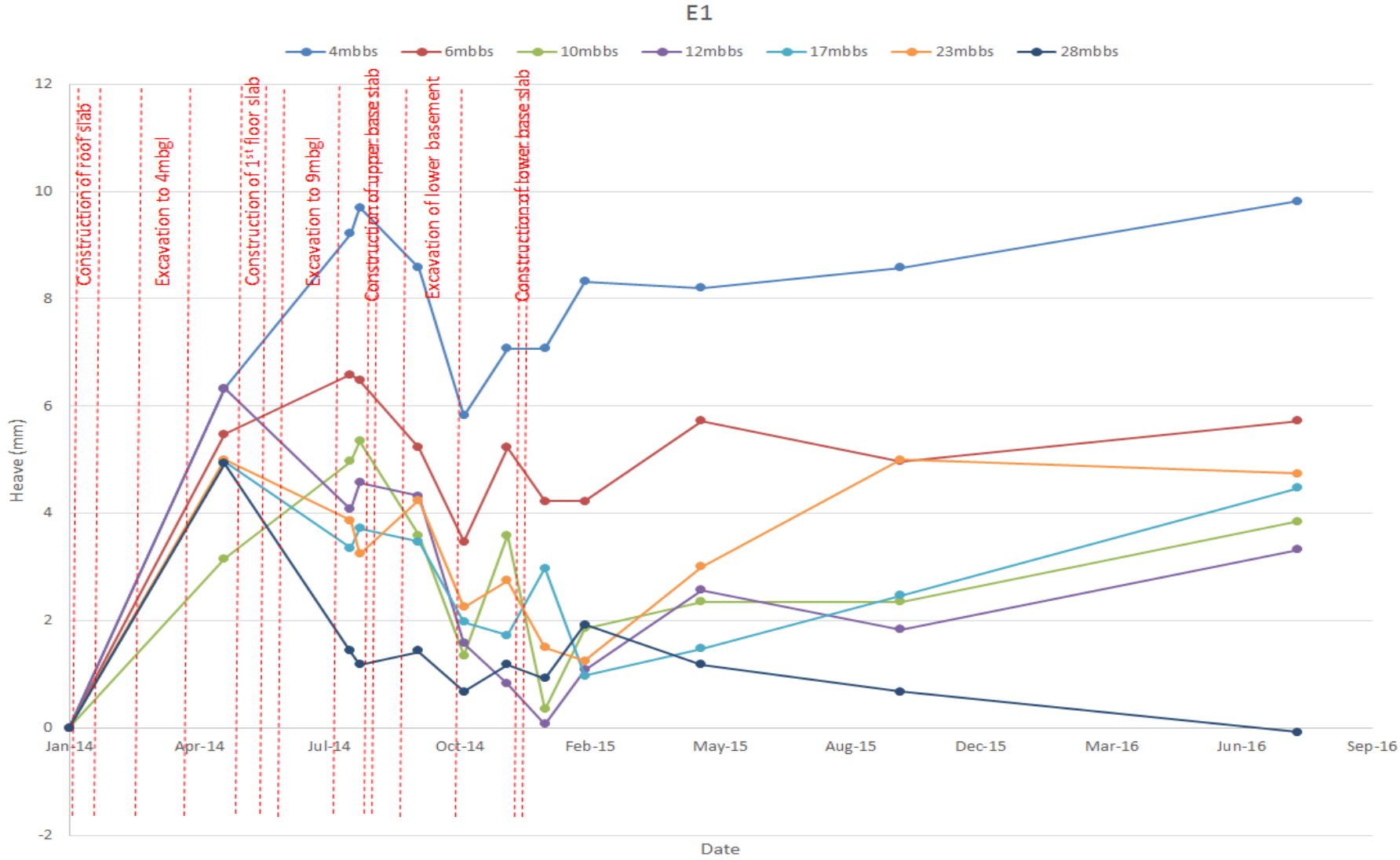

Figure 64: Vertical displacement at E1 for each magnet (metres below the base slab) against site timeline. Note that excavation beyond the upper base slab is adjacent to the extensometers

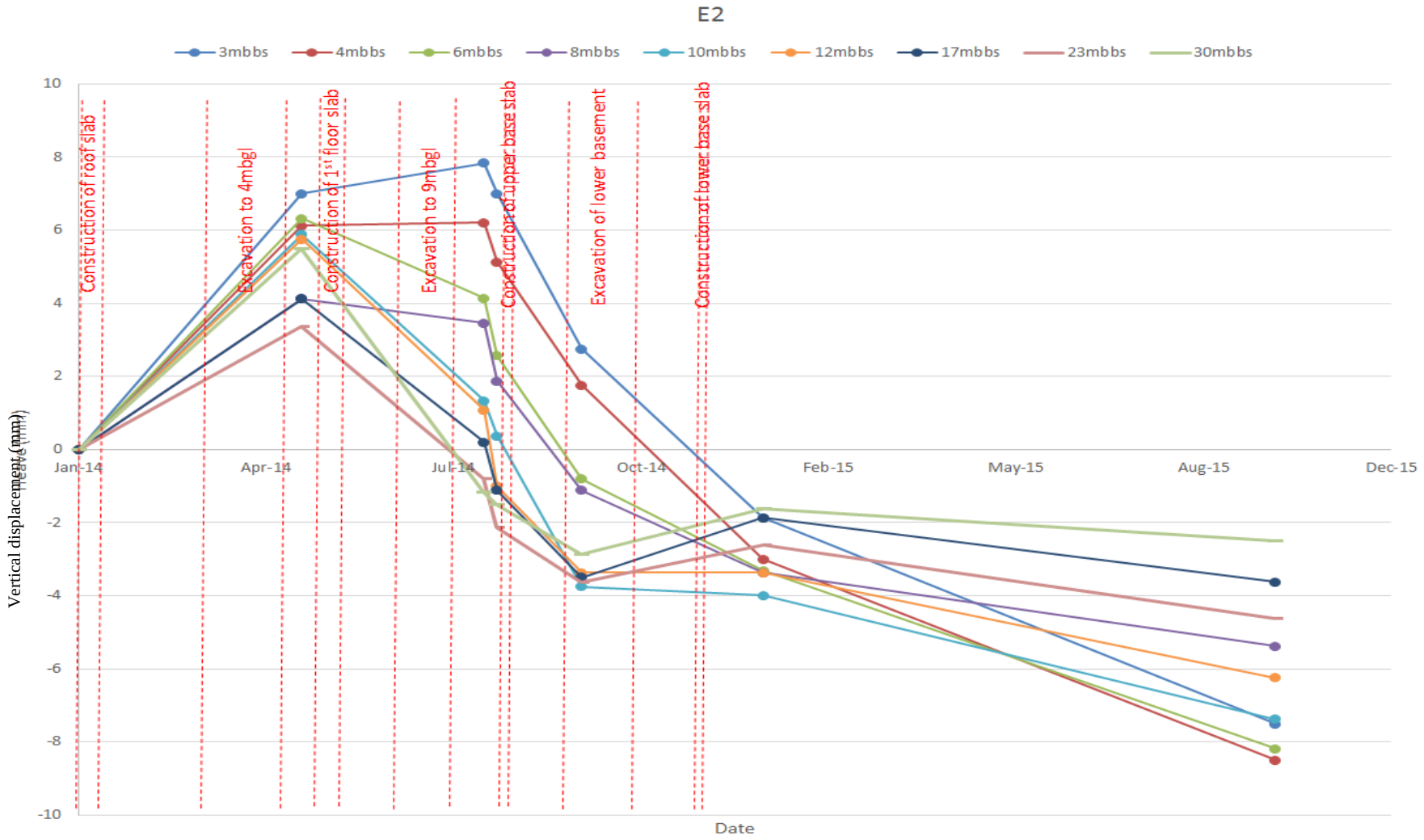

Figure 65: : Vertical displacement at E2 for each magnet (metres below the base slab) against site timeline. Note that excavation beyond the upper base slab is adjacent to the extensometers

Pore pressure measured in the deepest piezometer P1, Figure 67, which is situated 27mbgl has recorded a rise in pore pressures from around 50kPa at the beginning of 2014 to over 140kPa in August 2016; the reason for this steady rise is discussed in 3.4.5. Examined closely with the site timeline overlaid, the behaviour of the ground to loading and unloading can be seen with rises and slight falls in the pore pressures, overlying a trend of generally rising water pressures. The construction of the roof slab is seen with a small bump up in pore pressures; this reaction is less than may be predicted if the dead weight of the roof slab is applied uniformly to the ground. However, the roof slab is constructed to spread the load with bias to the secant piled wall either side of the excavation and therefore, the loading effect maybe localised to the walls.

Moving along the timeline, both the excavations to 4mbgl and 9mbgl are followed with either an expected drop in pore pressures or a reduction in the positive gradient; however, this may not be due to just unload of the ground and might be due to the dissipation of increased pore pressures from the undrained loading that results from the casting of the first-floor slab and upper base slab. The depth and position of the piezometers relative to the pile bases may mean that loading through the plunge columns to the piles, as is certainly the case for the first-floor slab, causes a localised rise in pore pressures greater than the effect of excavation nearly 20m above P1. Furthermore, if there were a case for this, it would be the fact that the first-floor slab, which is the lightest of the slabs, is the only slab to focus the majority of its' dead weight through the piles and it is the first-floor slab that causes a significant rise in pore water pressures.

Comparing the behaviour of P2 (24mbgl) with P1, the initial site construction processes are less noticeable in the readings of P2 until the first-floor slab is constructed, and even at this point the rise in pressures is nearly 10kPa less. From this point, the opposite is true. First, there is a sharper rise in pore pressures when the upper base slab is constructed; this is expected as the slab was laid on the ground and P2 is closer to the surface. Then as a period of data loss is experienced, P2 rises considerably. During this time, both the construction of the lower base slab and the foundations for the escalators take place. Both load the ground directly and through piles immediately adjacent to the piezometers.

After major construction activities that alter the loading of the ground end, a seasonal pattern in the pore pressures begins. It appears that P1 will begin to rise at the end of the summer months, followed by P2 in Autumn/Winter. This simply may be explained through the

position of P1 and P2 to the water table as P2 is the shallow probe. What this tells us is that the bulk permeability of the ground is of the order of 10^{-7}-10^{-8}m/s which is much greater the predicted by laboratory tests. This calculation is based on the following assumptions: that the time taken for P2 to reach a measured pressure on P1 is 4-12 months ($1x10^8$ - $3x10^8$ seconds), for example, when P1 measures 50kPa, it takes P2 4 months to reach 50kPa and when P1 measures 90kPa it takes P2 12 months to reach the same value. The other assumptions are that the piezometers are exactly 3m apart and the pressures measured by P1 and P2 extend laterally so the water source comes from beneath the piezometers. These assumptions only provide a crude estimate as a constant head is not maintained but $3m/3x10^8$ seconds = $1x10^8$m/s.

In addition to pore pressures being plotted against time, pore pressures are plotted with depth in Figure 68. The Figure shows the before construction pore pressure design line which is based on numerous standpipe measurements, boreholes, trial pits and data from a comprehensive desk study of the area. The site is under-drained and pore pressures increase with depth at approximately 70% hydrostatic pressures between 83m above the datum (ATD – datum reference point not known) - 65mATD and 50% hydrostatic pressures below that. Data from P1, P2 and PS1 show that pore pressure equalisation occurs at a similar speed over time with an exception being January 2015 where a rise in P2 occurred without it occurring at P1. Note: The boundaries between London Clay Units A2, A3 and Unit B are not in agreement with the literature and the Figure has been overlaid with suggested changes.

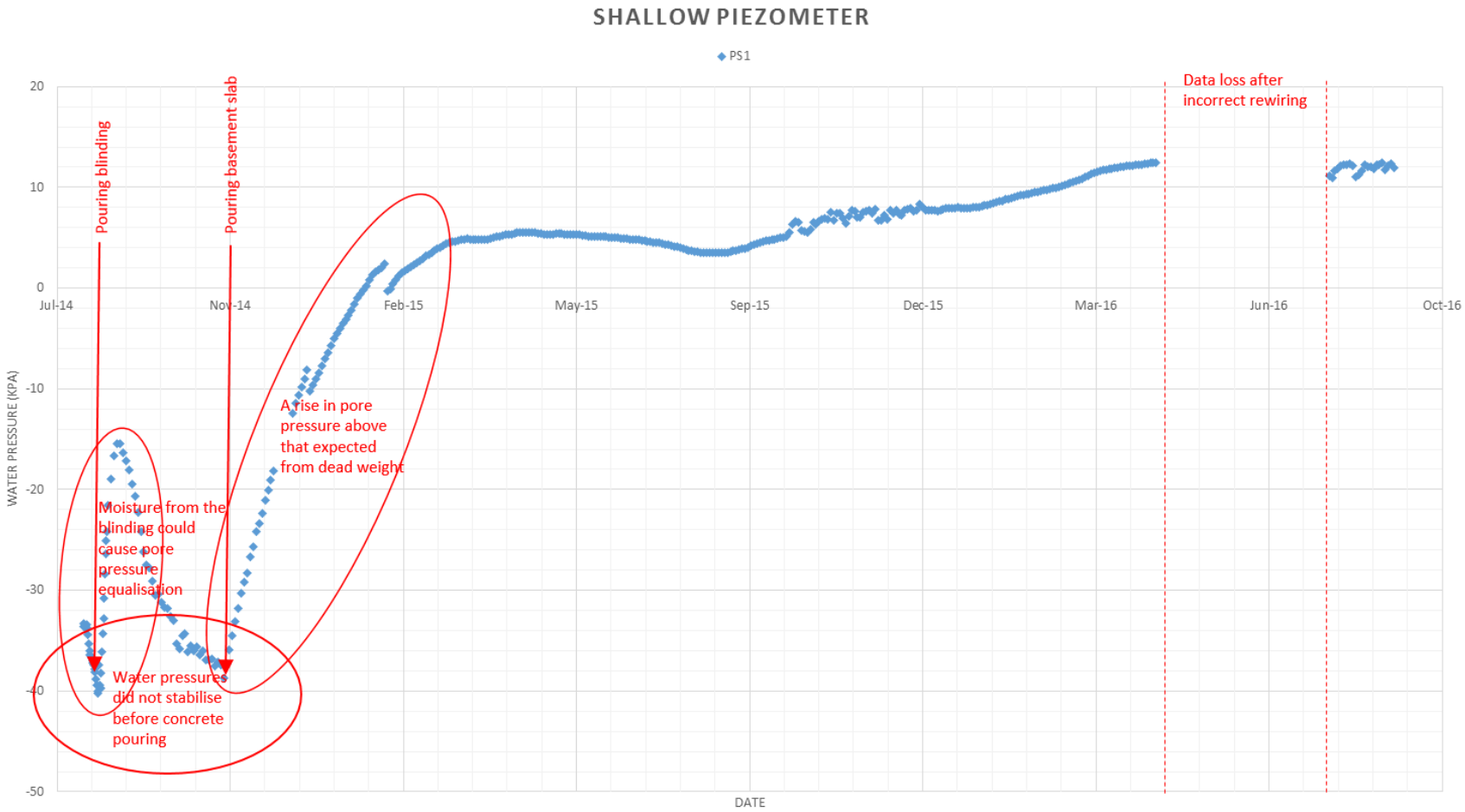

Figure 66: Shallow piezometer PS1, plotted water pressure vs. site timeline with annotated notes

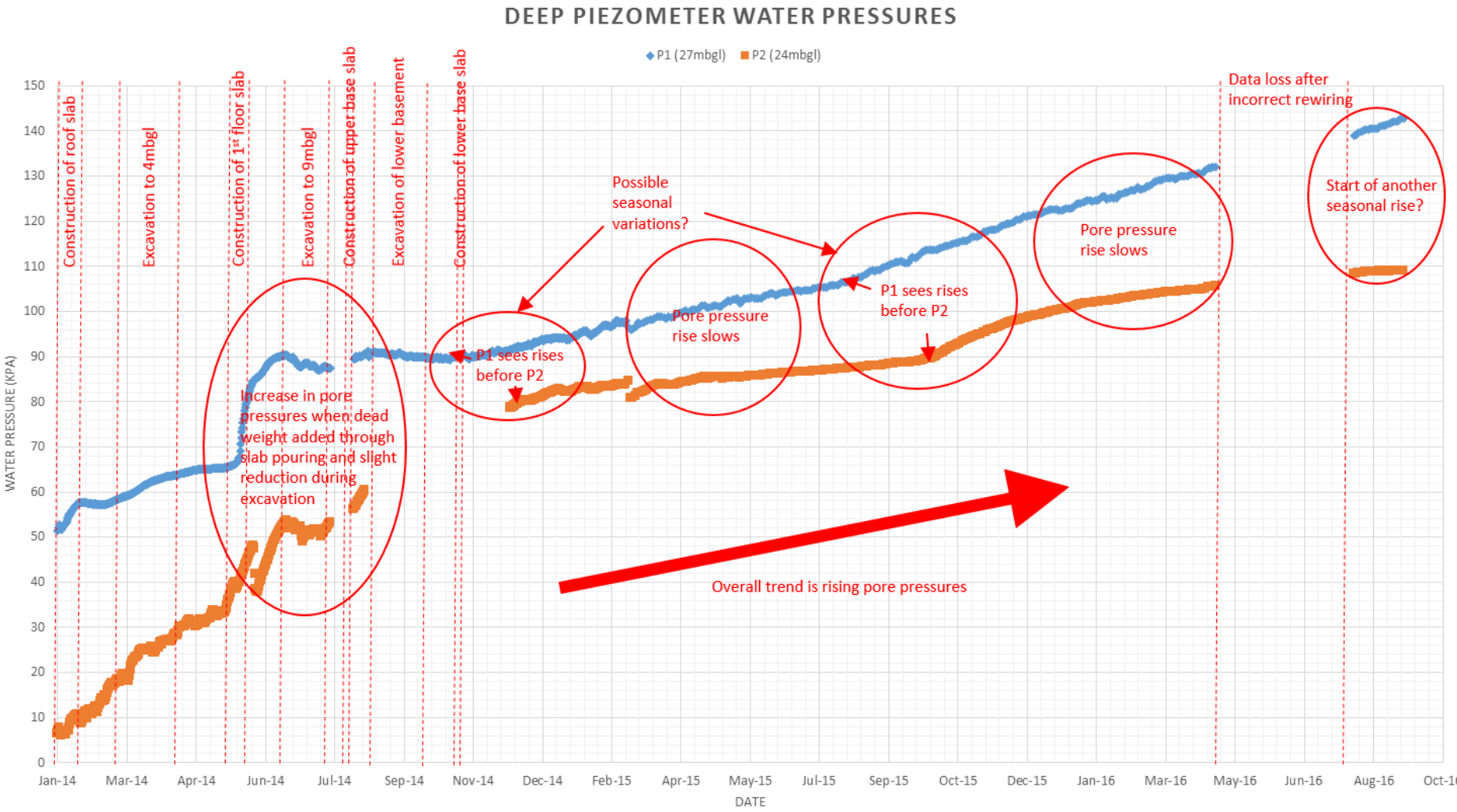

Figure 67: Piezometer P1 and P2, plotted water pressure vs. site timeline with annotated notes

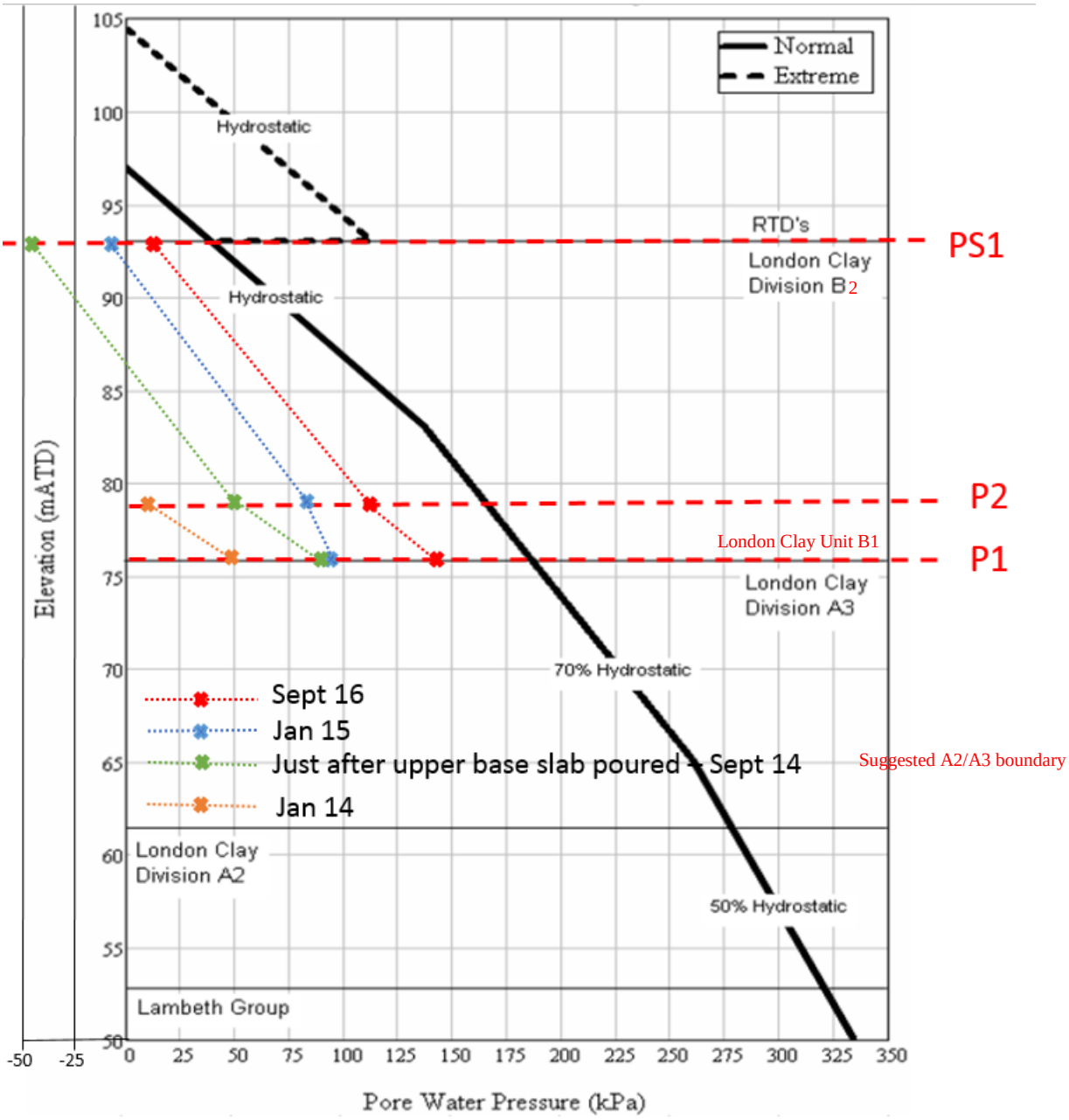

Figure 68: Pore pressures in time with depth taken from Mott Macdonald, 2008 and overlaid with data

4.3.3. Pressure cells

Firstly, examining the behaviour across all three pressure cells it is clear that temperature (measured by the pressure cells) has had an effect on the initial values of the load measured (Figure 69). Discounting the actual values, the trend is that PP1 reads the lowest increase from dead load caused by blinding, followed by PP2, and PP3 has not got data until the main slab is poured. The author was onsite during the pouring of both the blinding and the base slab and the site team took the decision to increase the depth of the blinding around the location of the cells. This was because the base level of the river terrace gravels was considered closely with the blinding level and the river terrace gravels were removed to

ensure the slab sat on clay. At the location of PP1, there was no additional gravel to remove so the blinding was of a standard depth 100mm. At PP2 and PP3, this was not the case, and although not measured, the blinding was waist deep (650-800mm) close to the piles (next to PP3). The dead weight, at PP1, after pouring of the uniform slab is given by: unit weight of wet slab = 25kN/m^3, depth of slab = 1.2m, depth of blinding ~ 0.1m; therefore, total pressure = 25*1.3 = 32.5kPa. Using the same calculation to estimate the thickness of the blinding over PP2 and PP3; the depth of the blinding was 200mm and 680mm, respectively.

After the initial response of the pressure cells to the pouring of the slab, the slab cools and the pressures recede slightly which is only evident towards February 2015. Before this, a rise is experienced, most likely because moisture from the concrete is reducing negative pore pressures in the clay surface and causing swelling; this can be seen at PS1.

As a normal temperature variation is established in the slab, pressure readings at PP2 and PP3 vary with temperature and do not rise more than 5kPa in one year. These pressure cells appear to be more susceptible to temperature than PP1 and it is noteworthy that they are not from the same supplier. As for PP1, there has been a steady rise until recently in 2016 where it has slowed considerably. No attempt has been made to correct for temperature fluctuations as the focus of these readings is to assess pressure rises annually and not seasonally.

A comparison of all the pressure changes experienced by the piezometers and the pressure cells is given in Figure 70. What this shows is that the total pressure measured by the cells rises most at the cell PP1 furthest from the piles, and is comparable with pore pressure equalisation at depth. This means that as pore pressures climb from the initial low pore pressures at the start of monitoring, they may be causing pressure build up below the slab. The piles may be acting to prevent as much swell pressure acting on PP2 and PP3 through preventing heave. A similar comment on the performance of the piles in reducing heave is made by Burland & Hancock (1977).

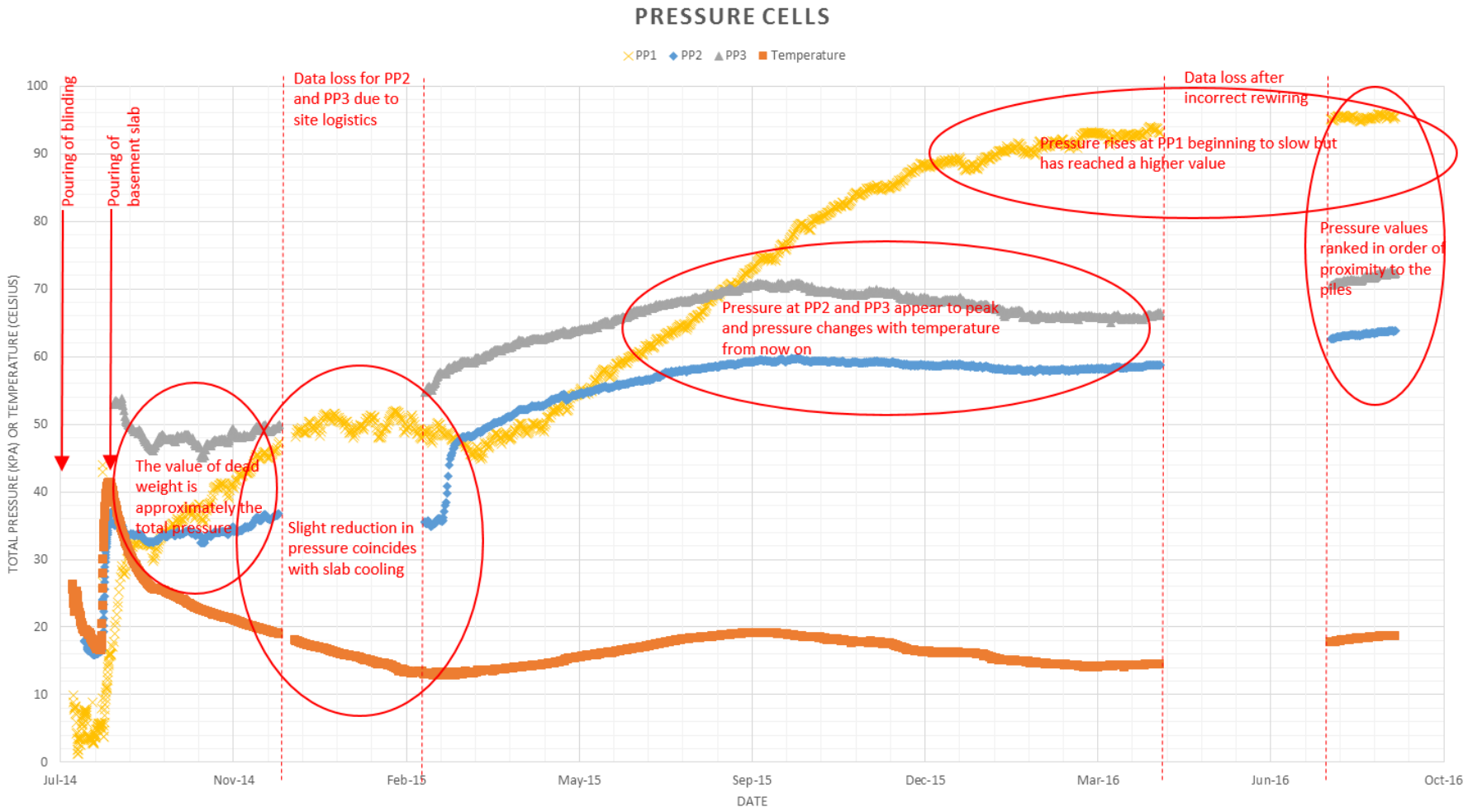

Figure 69: Pressure pads PP1 (centre of slab), PP2 (centre of 2 piles) and PP3 (next to pile), plotted water pressure and temperature vs. site timeline with annotated notes

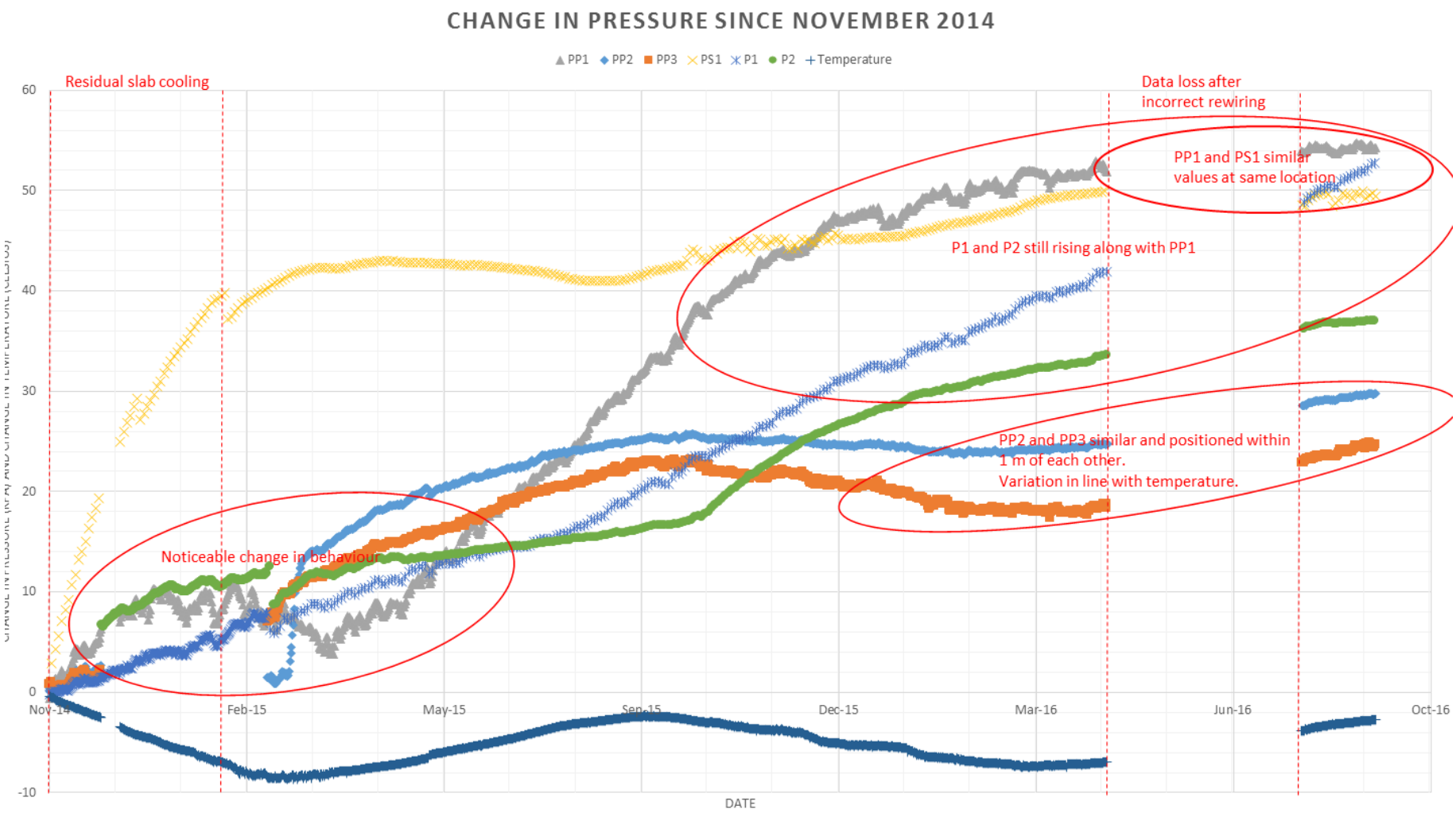

Figure 70: Changes in pressure at all pressure cells and piezometers since Novemeber 2014

4.3.4. Strain Gauges

The data from the strain gauges and their thermistors are given in Figures 71 and 72. Positive readings are compression and negative readings are tension. Data are shown from the 1st October 2014 as this is when the slab had cooled to a temperature that could be experienced during the summer months; however, this point could have been taken later as effects of slab cooling are visible till February 2015. The 1st October 2014 was six weeks since the slab was poured. The datum for strain readings is often taken several weeks after concrete pouring as the initial effects of temperature and concrete shrinkage makes interpreting strains from the strain gauges (which are sensitive to both of these things) generally difficult (Smethurst & Powrie, 2007). Additionally, there is reasonable evidence from the pressure cells that the slab is not be carrying any load over that period.

Both sets of strain gauges in the top and bottom of the slab show a positively trending microstrain reading from October 2014 until February 2015. After a short period of data loss due to site activities, the trend of the top and bottom gauges changes. In the top of the slab, change in strain slows and/or slightly reverses. In the bottom of the slab the gauges read a reversal in strain direction. By April 2015 both the top and bottom gauges are showing a reduction in positive microstrain and then around September 2015, another reversal in strain direction. Considering the small values of microstrain and the temperature variations, it would appear that the majority of strain is due to the temperature fluctuation and not due to slab sag or clay heave; however, this is not completely clear from Figure 71 and 72.

The expected slab vertical displacement is around 0.1mm at a swell pressure of 65kPa at the centre of the slab, which in bending is around 80 microstrain at the gauge locations from the neutral axis. At the location of the pressure cells and strain gauges between the columns the swell pressure is around 30kPa and so displacement of 0.05mm or 40 microstrain is predicted at S8. Because bending of the slab results in only small values of strain, it is difficult to distinguish genuine bending from temperature effects; but there is a difference of 20 microstrain developed from August 2015 to August 2016 and therefore it is possible that this is this effect of swell pressure.

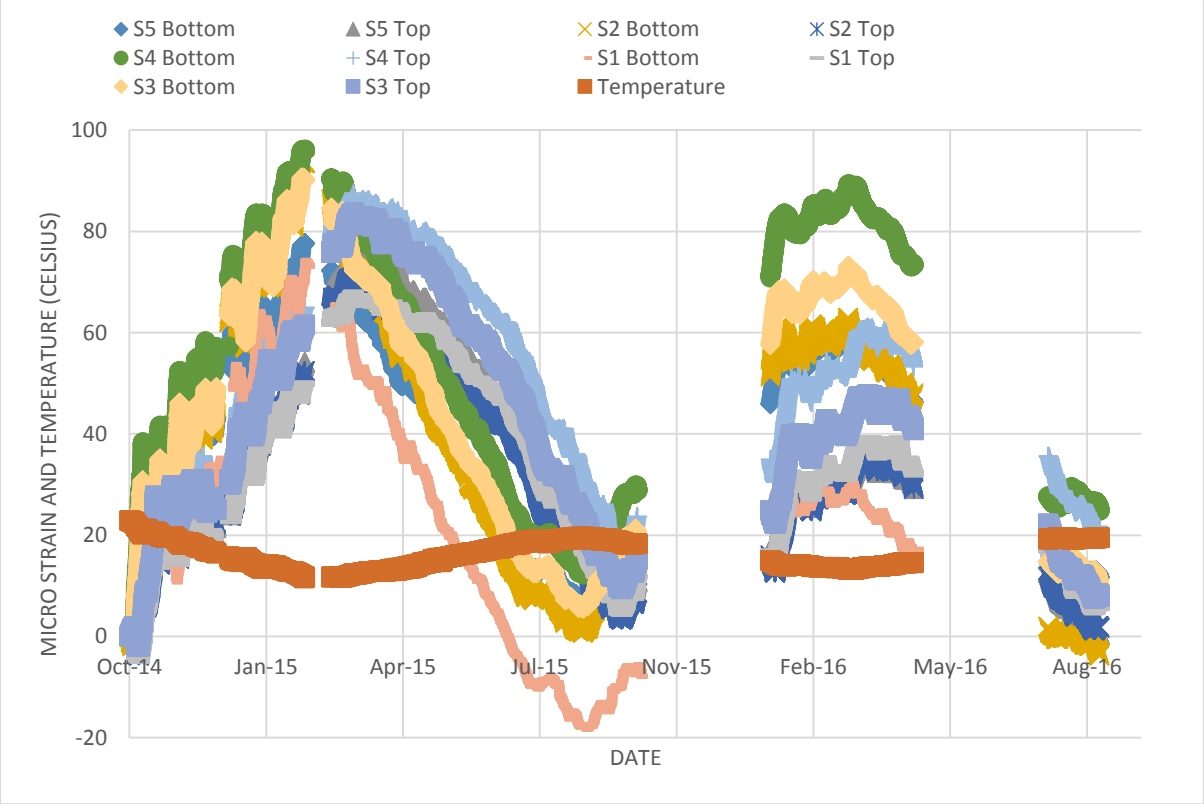

Figure 71: Strain gauges S1, S2, S3, S4 and S5 in the East – West direction in bay 1 shown with temperature (temperature shown as an average from all gauges)

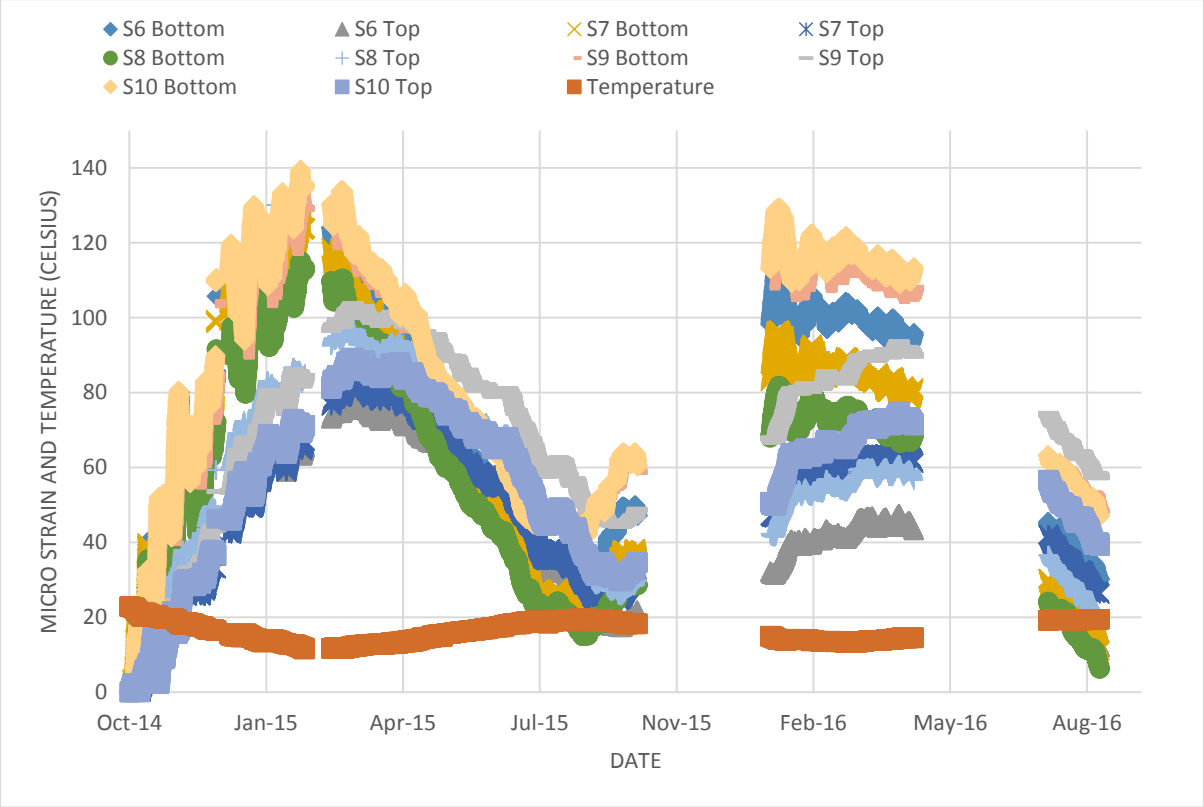

Figure 72: Strain gauges S6, S7, S8, S9 and S10 in the North – South direction in bay 1 shown with temperature (temperature shown as an average from all gauges)

Interestingly, if microstrain is plotted against change in temperature, a clear trend is shown (Figure 73). The trend shows that microstrain is getting smaller with each seasonal temperature cycle, which means that the 20 microstrain that developed over Aug 15-16 shown in Figure 71 and 72 may be a temperature effect that has skewed the data in the positive direction. In other words, starting the data in October may have been too soon. Furthermore, if the point in time where strain was zeroed was taken in Jan 2015, strain would be negatively trending to date and the slab would sagging.

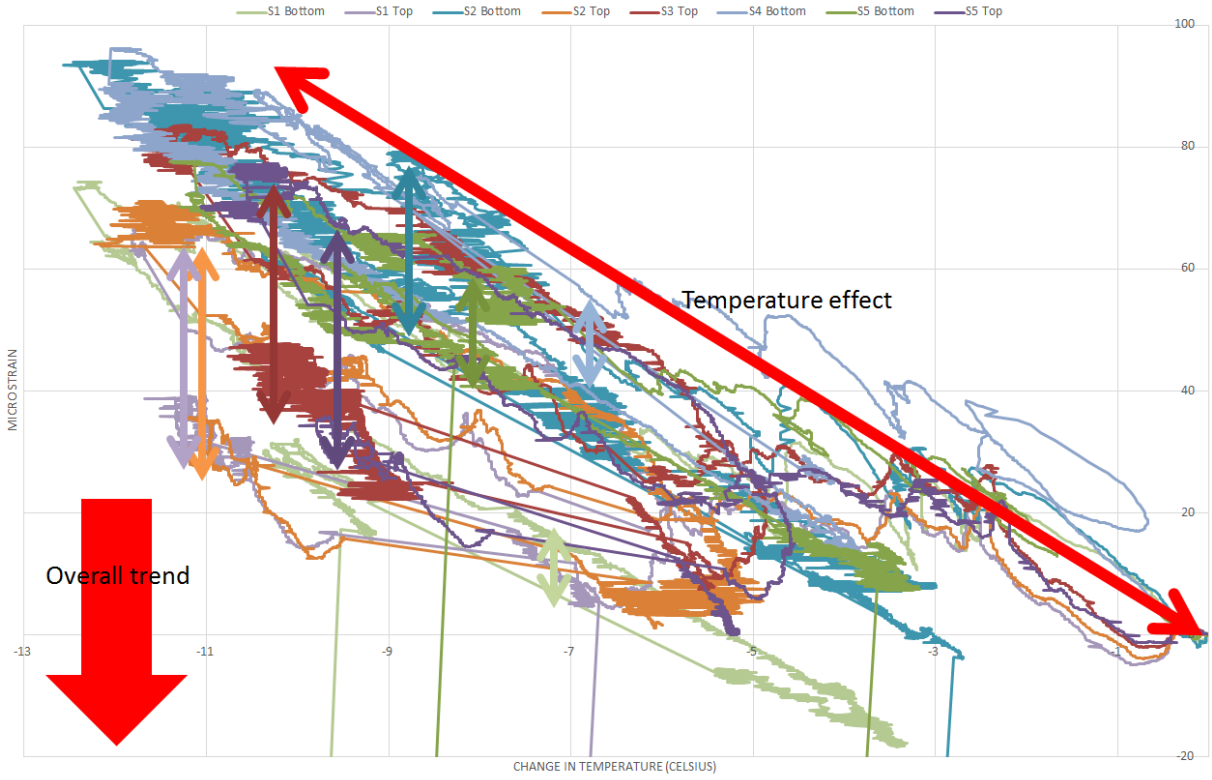

Figure 73: Microstrain vs. change in temperature for strain gauges East-West direction.

If the difference in microstrain at the same temperature but at two time periods is measured, then up to 40 microstrain can be seen in a negative (tension) direction. Therefore, two things can be inferred from Figure 73: firstly, the slab is initially in compression and is likely sagging due to the weight of the wet concrete on the blinding and the soil below. This is backed up by the extensometer data which shows a small settlement after the slab is poured. Secondly, that tension is increasing in the slab. This is likely occurring due to the swell pressure that is building beneath the slab. Additionally, extensometer data shows that the pre-slab pour heave values have been reached in the upper magnet at E1. Note: Using Figure 74, compression and tension can be visualised.

Using Figure 73 and a trial and error method, a correlation between strain and temperature was found. This consisted of the coefficient of thermal expansion (taken as 9 millionths per degree) being multiplied by the change in temperature and then added to microstrain. The results of this are shown in Figure 75 and 76. Note, S3 bottom and S4 top had malfunctions in the temperature readings so no correction could be applied. In general, microstrain fluctuations were reduced when compared to Figures 71 and 72. A general trend towards negative (tension) microstrain was found in the East-West direction. The opposite is true for the North-South direction as positive (compression) microstrain is dominant.

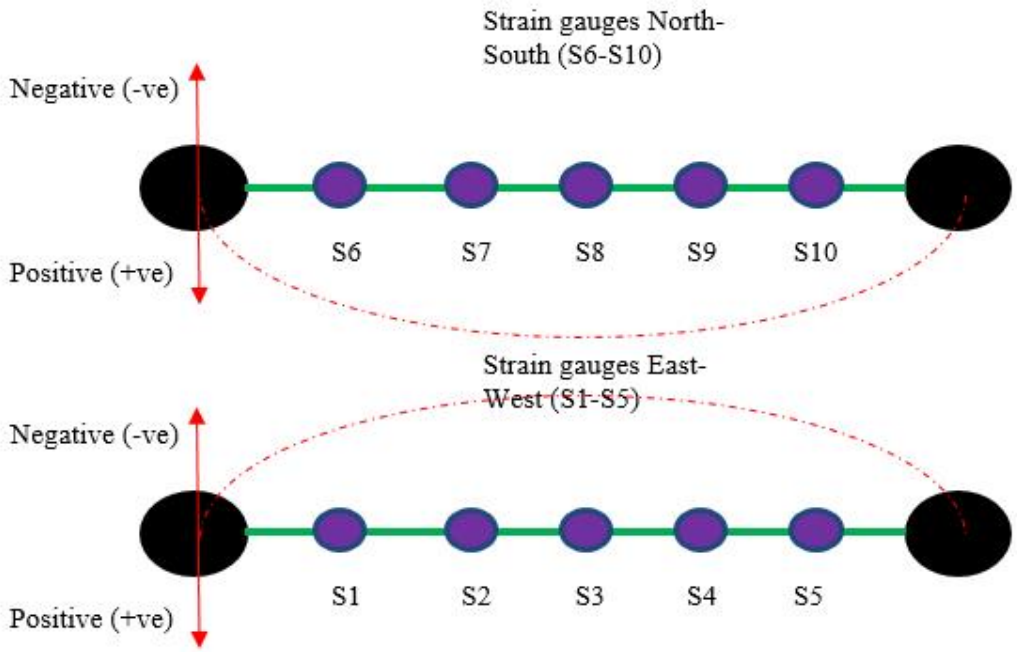

Figure 74: Strain gauge movement visualised

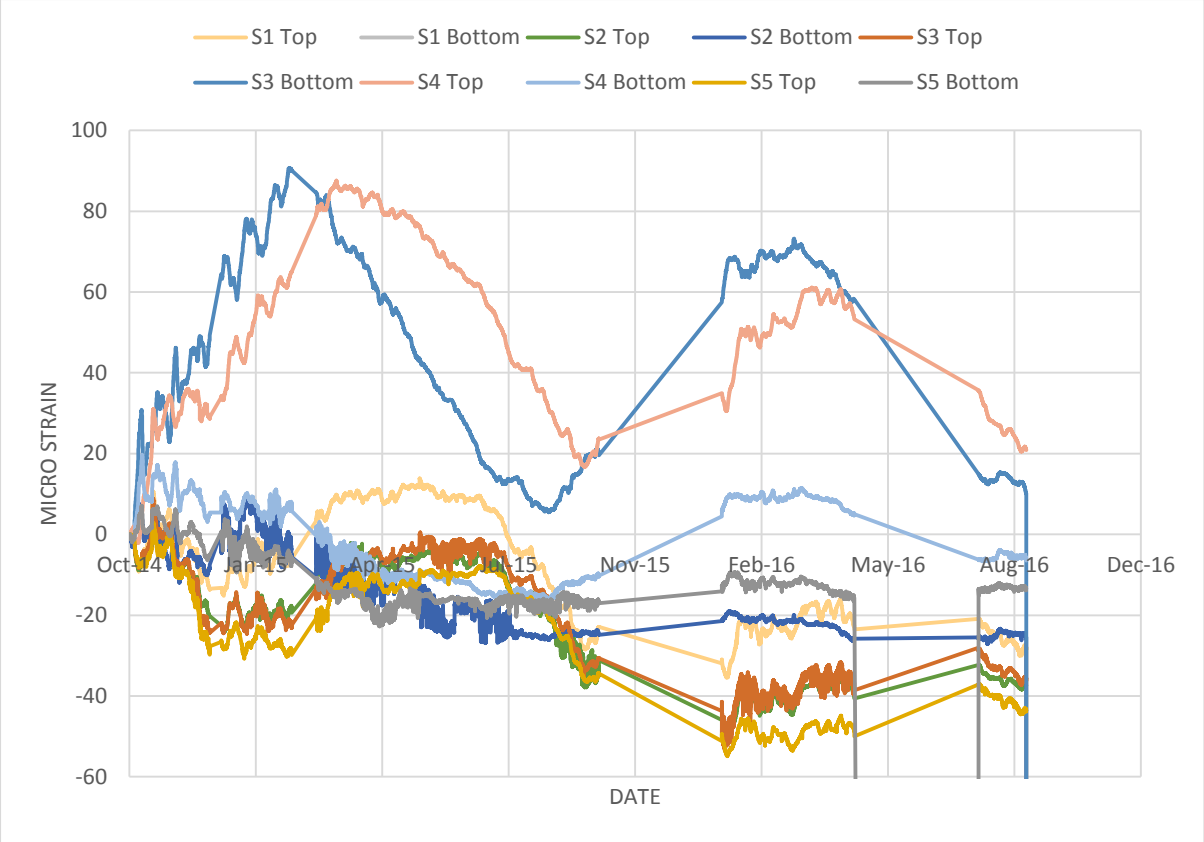

Figure 75: Strains with temperature correction East-West direction

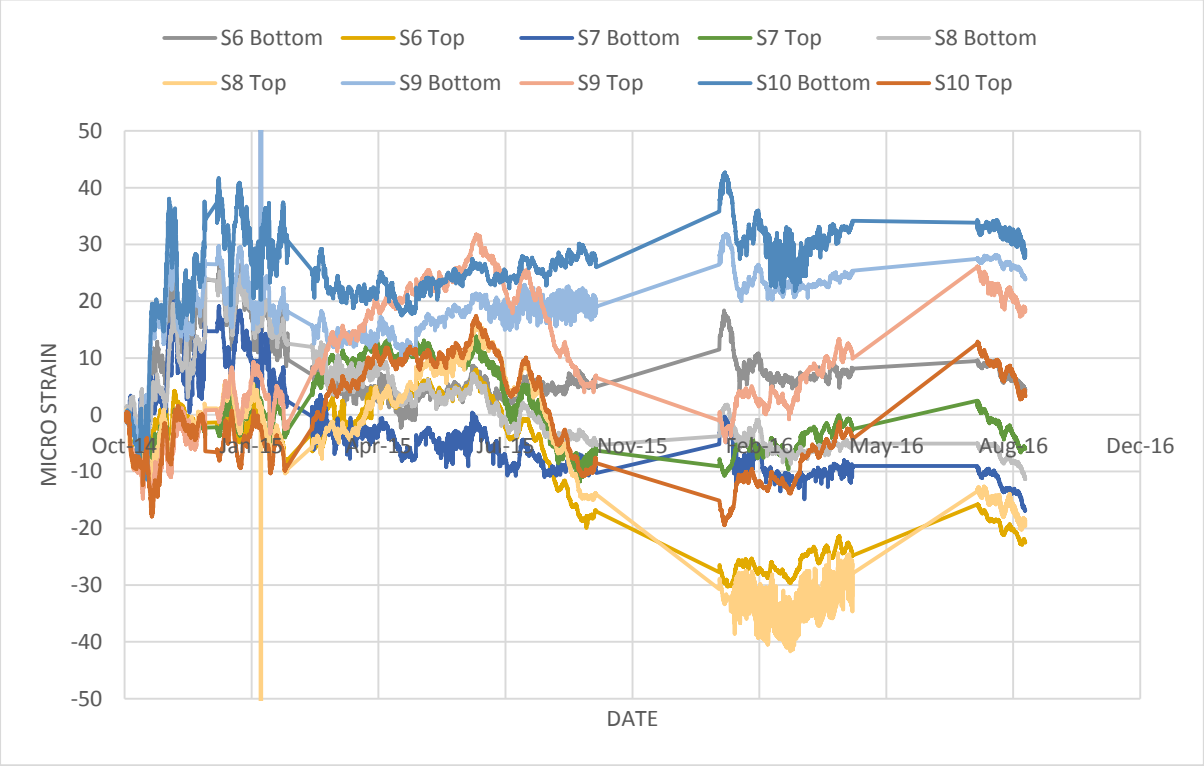

Figure 76: Strains with temperature correction North-South direction

Calculating bending moments

The bending moment (M), is calculated using Equation 4.1 where E is the Young's modulus, I, is the second moment of area and R_c is the radius of curvature.

$$M = EI/R_c \tag{4.1}$$

Using Equation 4.2 and inserting into Equation 4.1 gives Equation 4.3, where y is the distance between the strain gauge and the neutral axis, ε is the strain recorded by the strain gauge which is calculated using the calibration sheets, ε_1 is the strain at the top of the slab and ε_2 is the strain in the bottom of the slab.

$$R_c = y/\varepsilon \tag{4.2}$$

$$M = EI(\varepsilon_1 - \varepsilon_2)/2y \tag{4.3}$$

The value of the Young's modulus was conservatively estimated at 35GPa. The second moment of area is taken per metre for the slab so that $I=1.44x10^{11}mm^4$ and therefore, $EI= 5x10^6kNm^2$. The vertical distance between gauges in each pair (2y) was measured onsite for each set of gauges.

Bending moment results

Bending moment was calculated for each pair of gauges using Equation 4.3. These results are given in Figures 77, 78, 79 and 80. Figures 77 and 78 show bending moments from values uncorrected for temperature and Figures 79 and 80 show bending moments from strain corrected for temperature values.

There is a relatively small variation in bending moment, and it should be noted that site activities have the potential to cause small variations in bending moment due to locally changing loading conditions on the slab. The corrected Figures 78-79 show a small net positive sagging moment but this is generally masked by temperature effects due to the relative exposure of the top gauges to the air and the bottom gauges to the ground. Overall the bending moments fluctuate around zero bending moment, affected more strongly by seasonal temperature variations than ground heave. Note bending moments can be visualised in Figure 81.

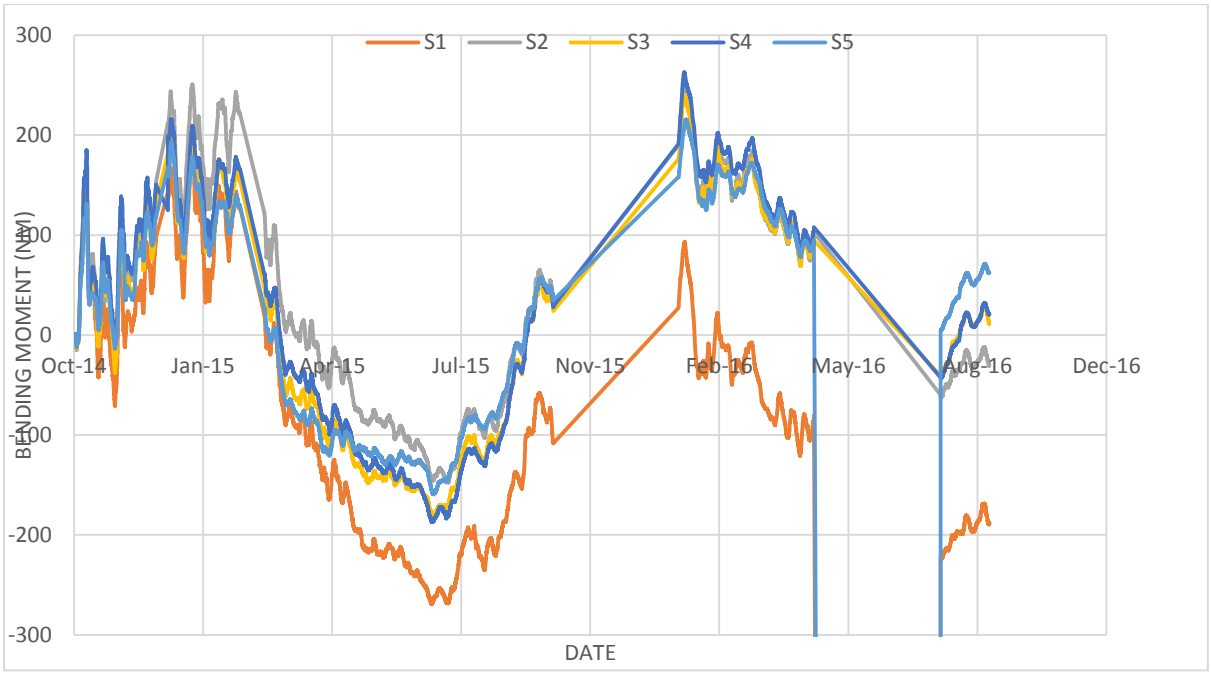

Figure 77: Bending moment: East – West (+/ve shows sag, -/ve shows tension)

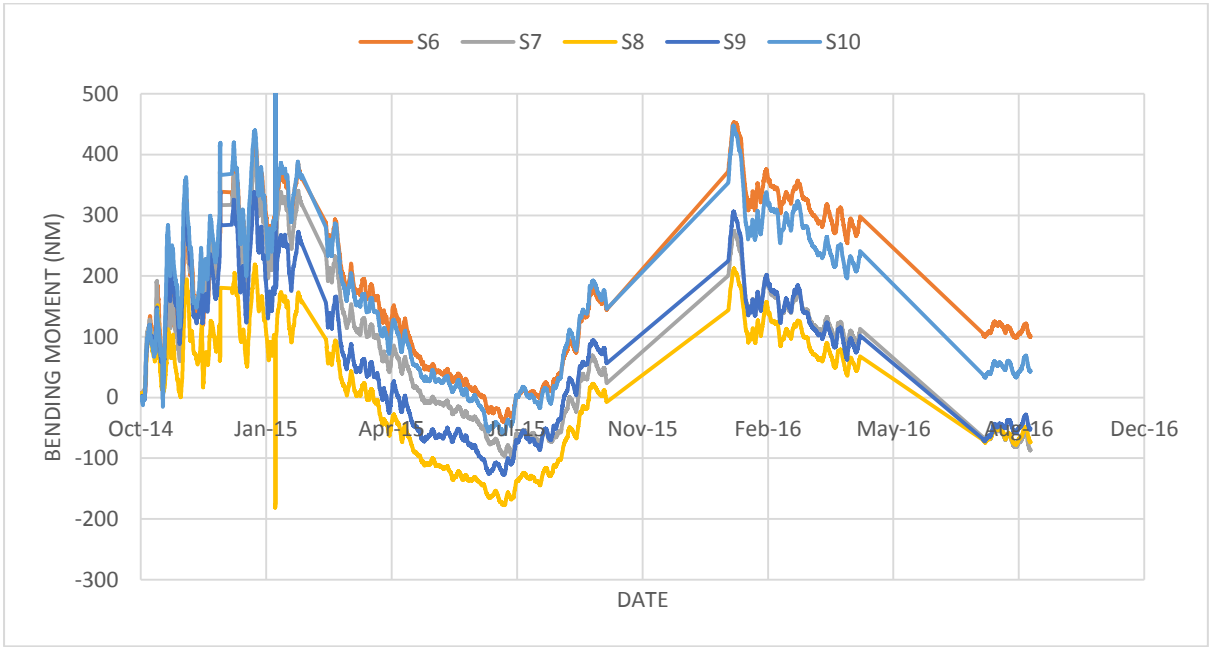

Figure 78: Bending moment: North – South (+/ve shows sag, -/ve shows tension)

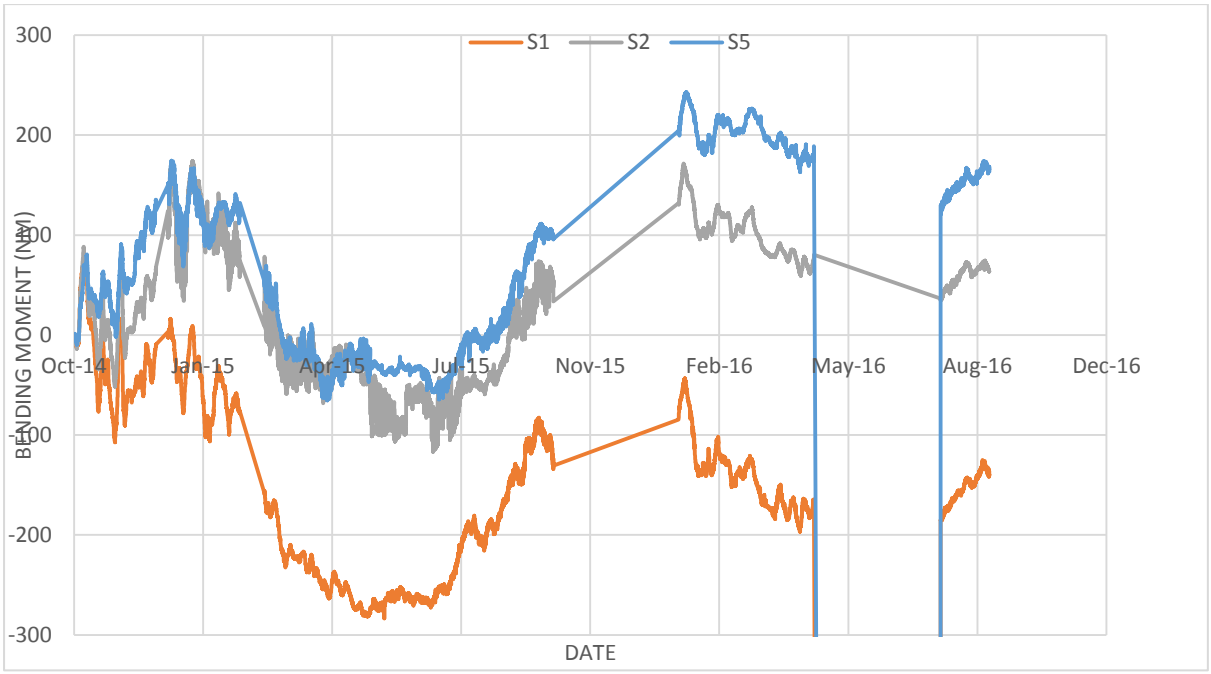

Figure 79: Bending moments corrected for temperature fluctuations East-West (+/ve shows sag, -/ve shows tension)

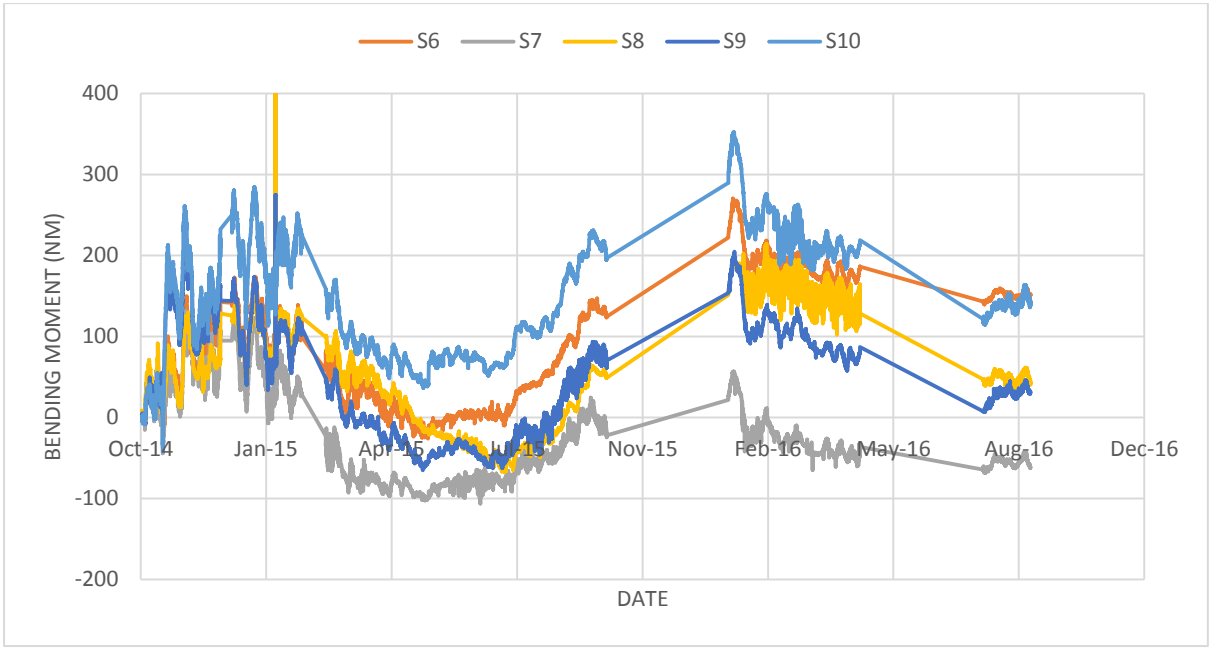

Figure 80: Bending moments corrected for temperature fluctuations North-South (+/ve shows sag, -/ve shows tension)

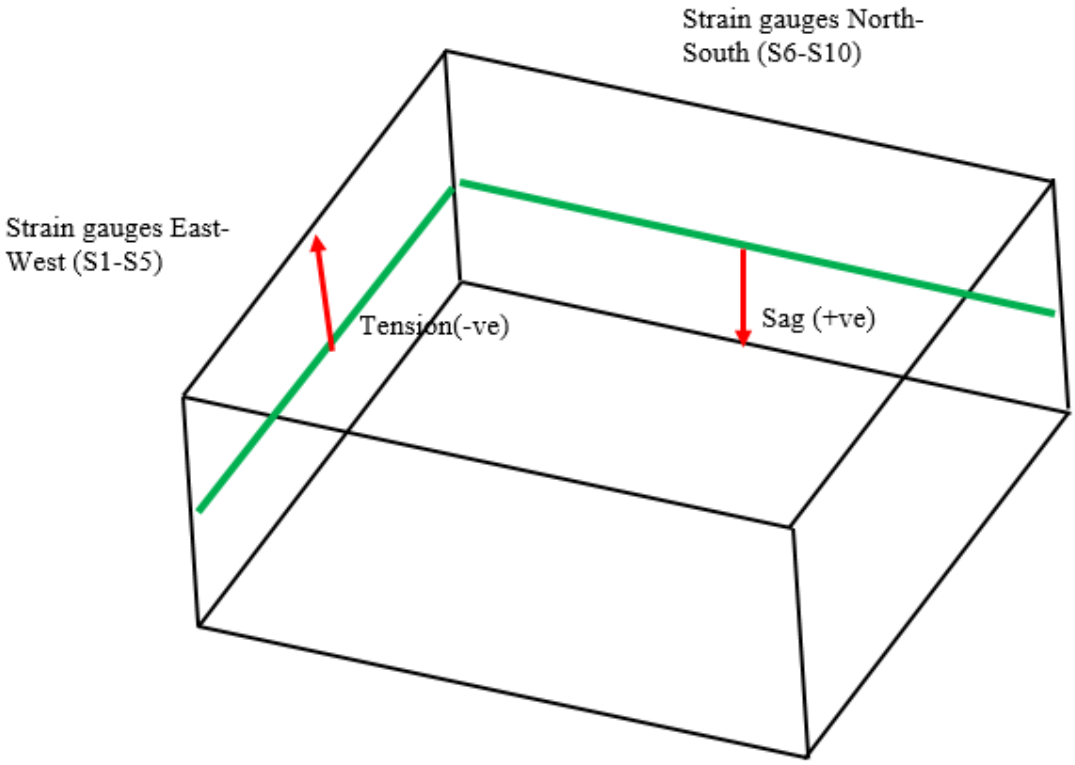

Figure 81: Visualisation of bending moment

In summary, in the East-West direction where pressure cells lay beneath the slab, the pressure recorded beneath the slab agrees with the microstrain predicted. In the North-South direction, no pressure cells lay beneath but it is possible that wall movement towards the excavation is having an effect on the slab. Bending moments are very small and may suggest a small amount of sag in the slab. Overall, slab cooling, seasonal variations and differences in temperature at the top and bottom of the slab, make it difficult to distinguish strains caused by soil movement from temperature.

4.3.5. Further discussion

Pore pressures

Piezometers were installed at VSU to gather data on the behaviour of the ground during the construction of a deep basement; however, the effects of basement excavation are superimposed on an overall trend of pore pressure rise. The expected pore water pressures prior to excavation at P1 are approximately 185-200kPa and at P2 are approximately 165-185kPa based on an earlier site investigation (Mott MacDonald , 2008). However, the values recorded were closer to 50kPa at P1 and 10kPa at P2. This would suggest that a drop in pore pressure must have occurred in the period between site investigation and installation of P1 and P2. The only viable action that can result in a drop-in pore pressures is the unloading of

the ground. This unloading would cause an ‘undrained’ response in the clay soil which results in a drop of pore pressures. The only process pre-installation of the piezometers that involves unloading of the ground is the boring of piles. If the trend at P1 and P2 continued to the point at which the piles were bored, then pore pressures may have been negative.

The first question that needs answering is: has there been a measured drop in pore pressures pre-excavation at any of the case histories in Part 1? The answer: Yes. This behaviour may have occurred at Bell Common during the initial construction of the secant pile wall as a drop in pore pressures are observed 3m and 0.6m behind and in front of the wall, Figure 82 (Tedd, et al., 1984); however, there was some excavation during this stage of construction and without a more detailed construction sequence it is not possible to distinguish the two events. Additionally, at Aldershot Road, pore water pressures were also measured at 1.5m from the West wall (Carder, et al., 1997); construction of which involved excavation for each panel which may have unloaded the ground laterally. This effect can be seen in Figure 83 but the effects of piezometer installation show a steep rise in pore water pressure prior to the drop and no construction data are available during the installation to analyse the construction sequence effects.

A case not discussed earlier is that at Ashford, described by Clark (2006). Clark installed spade cells and piezometers to monitor the wall installation at the Channel Tunnel Rail Link (CTRL) in Ashford, Kent. Pore pressures and lateral stresses were found to drop during excavation of the wall, while after concreting, an excess of pore pressures existed before dissipation to pre-excavation levels.

Finally, for Lions Yard where a more detailed construction sequence and a pore water monitoring scheme that begun before wall and pile installation was present, a drop in pore water pressures are clearly visible before any excavation occurs. This can be seen in Figure 84 where pore pressures drop by around 70kPa at the wall face. Stages 1 and 2 in this sequence are the installation of the wall and piles respectively, while stage 6 is the first major excavation stage. Further analysis by Ng (2004) shows that when monitoring lateral earth pressure before and after wall and pile installation, a “marked” reduction in lateral earth pressure occurred after the installation of the wall. However, a reduction in lateral earth pressures did not occur after pile installation and Ng (2004) says “This was perhaps because the nearest piles were 8m away…”. To add to this statement, the drop in pore pressures from the wall installation may also have been dissipating and this may have obscured a further,

smaller drop from pile installation. Using the argument that wall installation is not 'locally' (to a piezometer close to the boundary) dissimilar to a large diameter pile installation in terms of unloading the ground laterally due to boring or excavating of material, the results at VSU are compared to the data from Lions Yard.

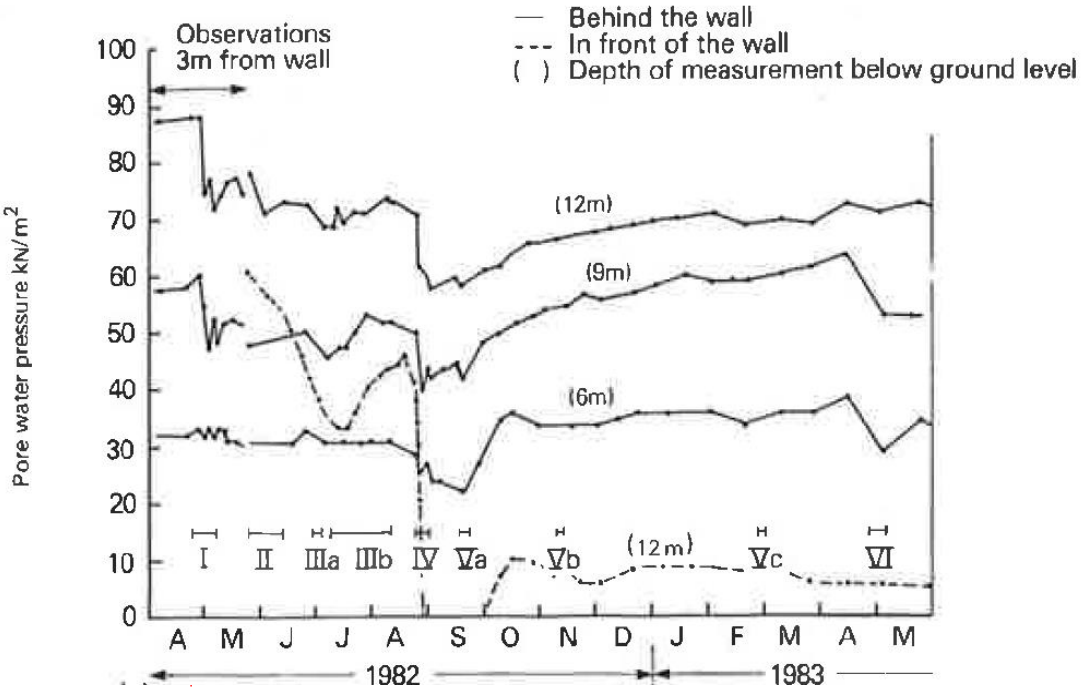

Figure 82: Changes in pore water pressure with time at Bell Common (Tedd, et al., 1984)

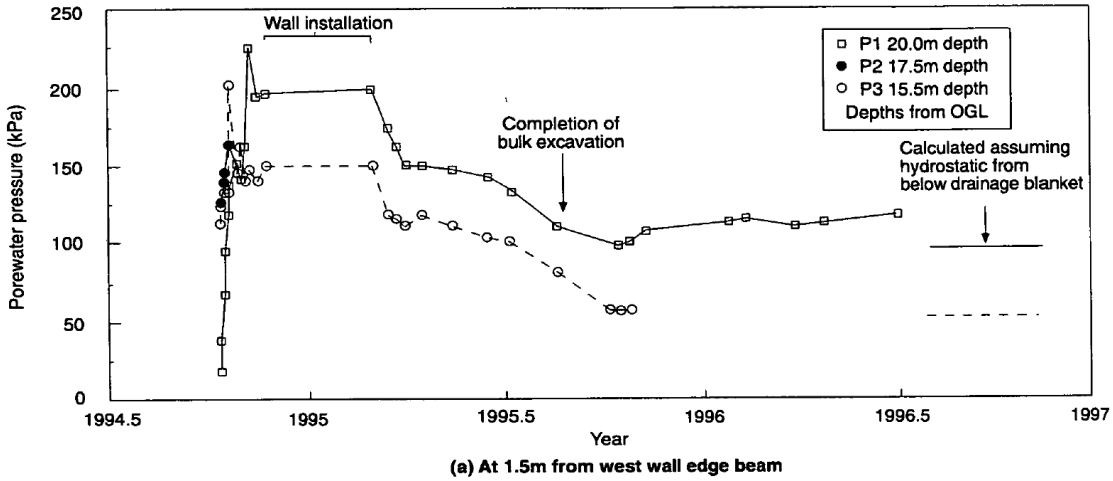

Figure 83: Pore water pressures recorded by pneumatic piezometers at Aldershot Road bypass (Carder, et al., 1997)

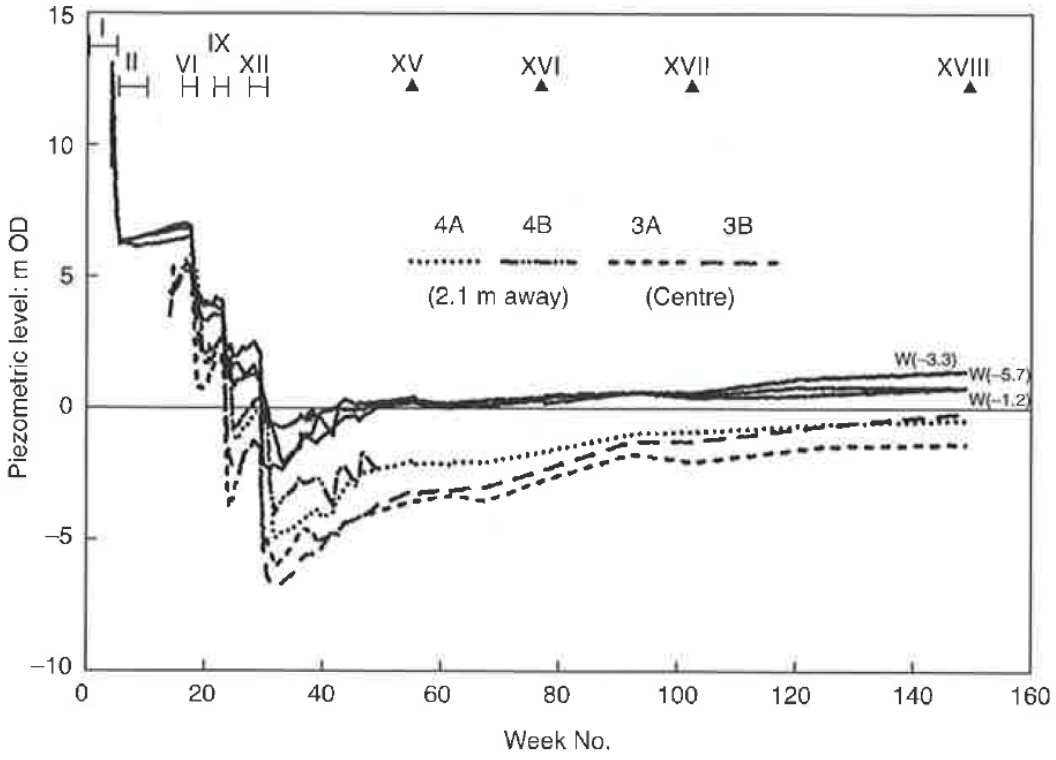

Figure 84: Measured pore water pressures at Lions Yard (Ng, 2004)

An issue faced with the idea that lateral unloading causes a drop in pore pressures is that it has been shown theoretically that for an infinite cylinder in a clay where radial stress changes occur at the boundary of the cylinder, no change in total stress or (in undrained conditions) pore water pressures will occur (Powrie, 2014). However, this theory is based on a series of assumptions. A 'hoop' stress acts in the soil around the circumference of the cylinder and a radial stress propagates from the centre of the cylinder. A key assumption when considering an infinite cylinder is that vertical ground movements are zero and it is this assumption which effectively removes the possibility of effective stress change. Therefore, this existing theory does not help to explain the observed field measurements.

Continuing with the idea that the pore pressures have been altered by pile boring, the following comparisons can be made between Lions Yard and VSU. The location of the piezometers at Lions Yard that measured a 70kPa drop are at the wall face and later on, piezometers were installed 2.1m away from diaphragm wall. While at VSU, P1 and P2 are within 2m of two 1.8m diameter piles and within 3m of two more 1.8m diameter piles; additionally, a secant piled wall is 8m away. To calculate the predicted drop in pore pressures at the piezometers at both Lions Yard and VSU, the process needs to be broken down.

First, to make the analysis for the process of boring or excavating the pile or wall simpler, the assumption that all bores and wall excavations occurred simultaneously is made. Additionally, an Equation is needed to model the predicted change in lateral (radial) stress ($\Delta\sigma_{h\ or\ r}$)which is given as: $\Delta\sigma_{h\ or\ r} = \frac{R^2}{r^2}\Delta\sigma_{PB} \quad for\ r > R$ where R is the radius of the pile, r is the distance from the centre of the pile or wall to the soil element and $\Delta\sigma_{PB}$ is the stress change at the pile bore. This Equation was used by Richards et al. (2006) but was taken from Fjaer et al. (1992).

The calculation has been carried out considering an element of soil in the following cases: close to the bored surface of a single pile at VSU at depth 27mbgl; at the piezometer installed at the wall face at Lions Yard 11mbgl; and at piezometers P1(27mbgl) and P2 (24mbgl), based on four excavated piles. Note: the assumption is that the hoop stress will act in the same way the intermediate stress does during trench excavation. The insitu conditions and conditions immediately after boring and excavations are in Tables 7-8:

Table 7: Insitu conditions pre-construction

Case (Insitu pre-construction)	Total vertical stress (kPa)	Total horizontal or radial stress (kPa)	Total intermediate or hoop stress (kPa)	Pore water pressure (kPa)	Effective vertical stress (kPa)	Effective horizontal or radial stress (kPa)	Effective intermediate or hoop stress (kPa)
Single pile VSU	589	604	604	199	389	409	409
Lions yard wall face	232	445	445	90	142	355	355
P1	589	604	604	199	389	409	409
P2	549	574	574	185	363	389	389

Table 8: After boring of the piles / excavating the wall open and un-cased

Case (After boring)	Total vertical stress (kPa)	Total horizontal or radial stress (kPa)	Total intermediate or hoop stress (kPa)	Pore water pressure (kPa)	Effective vertical stress (kPa)	Effective horizontal or radial stress (kPa)	Effective intermediate or hoop stress (kPa)
Single pile VSU	589	0	604	-2.5	592	2.5	607
Lions yard wall face	232	0	445	-58	290	58	503
P1	589	378	604	123	466	254	481
P2	549	357	574	113	436	245	462

Now concrete is poured into the bores at VSU and into the wall at Lions Yard, the theoretical reload would cause pore pressures to rise to the values given in Table 9:

Table 9: After concreting all piles and walls

Case (After concreting)	Total vertical stress (kPa)	Total horizontal or radial stress (kPa)	Total intermediate or hoop stress (kPa)	Pore water pressure (kPa) (drop from Table 8)	Effective vertical stress (kPa)	Effective horizontal or radial stress (kPa)	Effective intermediate or hoop stress (kPa)
Single pile VSU	589	456	604	149 (50)	439	307	455
Lions yard wall face	232	264	445	30 (60)	202	234	415
P1	589	534	604	175(24)	414	358	429
P2	549	496	574	159 (26)	390	337	415

As can be seen in Table 9 that using this methodology, pore pressure reduction is predicted relatively well at Lions Yard but at VSU the drop in pore pressures is much smaller than measured at the site, and the measured reduction must be caused by a further factor.

One possible suggestion for the disparity between the figures is the borehole which the piezometers sit in themselves. Due to site complications, the borehole was not backfilled sufficiently with grout. By using the same calculation in Tables 8 and 9, it is shown that pore pressures should drop over 150kPa at P1 and P2 by simply under filling the borehole the estimated amount. Combining both figures and ignoring the theoretical cylinder behaviour, the pore pressures reduce by around 170-180kPa at P1 and P2; this is the exact measured fall in pore pressures.

After analysing the case histories, considering Clark's findings and the findings at VSU, it appears the conclusion is that reduction in lateral stresses and pore water pressures are dependent on the relationship between the insitu lateral stresses and the depth to which wet concrete or grout is poured into the excavation. A simple relationship for a soil element on the wall face is proposed in Equations 4.4 and 4.5:

$$\Delta u = \alpha \, {}^{\Delta\sigma_r}/_{3} \tag{4.4}$$

$$\Delta\sigma_r = \gamma D_c - \sigma_{h,0,Dc} \tag{4.5}$$

Where D_c is the depth of concrete poured at the depth of the soil element; γ is the unit weight of wet concrete; α is a dimensionless constant that represents the interaction between wet concrete and clay surface and greater than 1; $\sigma_{h,0,Dc}$ is the preconstruction insitu horizontal total stress at depth D_c.

This relationship can be extended to include behaviour across the site using superposition and the following Equations 4.4 & 4.6-4.7:

$$\Delta\sigma_r = \left[\sum \beta(\gamma D_c - \sigma_{h,0,Dc})\right] \tag{4.6}$$

$$\beta = e^{-\mu r}\frac{R^2}{r^2} \tag{4.7}$$

Where β is a variable based on the distance from each bore. β degrades using the relationship Fjaer et al. (1992) proposed with an added factor to account for greater degradation over distance r; this uses the constant μ where $0 \leq \mu \leq 1$.

Heave values at VSU

Another discussion point is the low measured heave values at VSU described earlier. The main reasons for the low heave could be any of the following:

1. Large piles (1.8-2.1m dia.) at small spacing intervals (~6m) could have caused a significant reduction in heave through friction acting on the soil/structure interface. This can clearly be seen in Figure 69 where the pressure cells closest to the piles show the least pressure rise. Also, removal of nearly 9% of the ground below slab level through boring has reduced the amount of clay free from frictional effects.
2. Small wall movements – wall deflections were mitigated through the installation of a heavily reinforced secant piled wall. Deflections measured by the inclinometers were of the order of a millimetre or two and have rarely reached 5mm across the site. Small deflections would lead to less heave due to volume conservation during the undrained response.

In addition to the primary reasons, there could be the following secondary reasons:

- Suctions in the clay – caused by the lateral unloading of the clay through boring for the wall and piles led to pore water suctions. These suctions restrict heave until they dissipate which would lead to more heave in the future.
- Bottom magnet heave – the bottom magnet at 40m below the base slab (bbs) is used as a reference point but may be subject to heave and due to its proximity to the water table it may be heaving before the magnets above. This might be the case at E2 in Figure 62 between August 2014 and September 2014; there is a notable and consistent (3-4mm) settlement that would not have occurred during the first-floor slab being cast. This may have meant the installations did not correctly capture the full heave.
- Our benchmark for predicted heave ignores the weight of the structure - the 'effective' excavation depth which considers the weight of the roof and first floor slabs being transferred to the soil through the plunge column piles and wall would be greatly reduced in depth. This is because a large force would effectively counteract the unloading through excavation. If the excavation depth were calculated on effective weight removed rather than the predicted heave based on earlier case studies, this

would be closer to 14mm. This may have been possible at the surface of the clay although this was not measured.

Any of the above are plausible and the relatively low magnitude of heave may come from a combination of factors. A counter argument for points 1 and 2 may be Lions Yard which also has piles and a wall which would influence heave. However, at Lions Yard piles are 1-1.4m diameter and are spaced further apart which would significantly reduce their effect.

Future predictions

A final discussion point is to predict future pressure and ground movements. The pressure cells indicate that the piles are restricting heave. Assuming pore pressures at depth continue to reach pre-construction levels, a further 42 (P1 lower predicted values) - 75 (P2 higher predicted values) kPa is predicted as an earth pressure; although this may be a local effect and just coincidence that both the rise in pressures and P1 and P2 are similar to PP1.

Also, it may be assumed that clay which is not as deep as P1 and P2 may not have equalised as far and may contribute further pressure increases. Finally, if water pressures beneath the slab rise to extreme pre-excavation levels (see Figure 68), a further 100kPa would be added to reach a maximum of 175kPa of additional total pressure. As the clay is restricted by the base slab and the slab is barely moving, it would be difficult to see little more than 1-2mm of heave with double the current swell pressure.

4.3.6. Summary

Heave at the base of the VSU excavation and wall movements were small when compared to other case histories. This is due to a combination of factors such as: construction sequence, large plunge columns/piles, small spacing intervals between piles, using a hard-hard secant wall; nevertheless, the measured values show small ground movements can be achieved behind and in front of the wall, contrary to suggestions by Burland Hancock (1977).

Pore pressures gradually rose since the start of monitoring which suggests unloading of the ground prior to excavation taking place. One possible cause is undrained lateral stress relief caused by boring of the piles; however, application of some simple theoretical calculations does not account for the measured pore pressure changes as a result of lateral unloading of the ground. Further investigation is needed into the behaviour of pore pressures when boring into over-consolidated clay. A 3D finite element model would help back-analyse the site, but

the interaction of the pile with the clay during its construction may need to be investigated further.

Pressure cells have recorded some pressure since installation. This pressure is likely to be predominantly earth pressure caused from pore pressure equalisation. The cell measurements suggest that piles not only restrict heave but also the swell pressure on the base of the slab that results from that heave as pressures rose higher at the centre of the slab than closer to the piles.

Strains in the slab show that temperature has a large effect on the results. Before attempting to remove temperature effects, the dominant action on strain was temperature and so strains fluctuated seasonally. Once an attempt was made to remove temperature effects, microstrains in the east-west direction match those predicted using the pressure pads beneath the slab. In the North-South direction, wall inward deflection may be influencing the results.

5. LABORATORY INTRODUCTION, APPARTUS AND METHODOLOGIES

5.1. Introduction

This Chapter focuses on: laboratory literature and apparatus; test procedures and specimen retrieval; and sample descriptions. Firstly, literature specific to the laboratory testing procedures is outlined; giving a brief but useful insight into the sensitivity of small strain testing. Afterwards, apparatus based at The University of Southampton will be introduced. This focuses on equipment used for successful samples but a brief mention is given to apparatus used as part of unsuccessful attempts too. Sample preparation procedures are then described; first, giving site descriptions and outlining block sampling challenges before going into detail about sample trimming to a final specimen size. The samples are described visually with reference to common geological terms.

5.2. Laboratory specific literature

The difference in results between field observations and laboratory experiments is usually subject to interpretation but it has been particularly difficult to use laboratory results to predict heave. Sample disturbance is the main reason for the difference and so considerable care was taken throughout this research to ensure sample quality was maintained.

5.2.1. Stress history & stress paths

Atkinson et al. (1990) defined "recent stress history" as the current load path being undertaken by the soil in relation to the previous stress path and after extensive testing it was shown that the stress path history is significant to how stiff the soil behaves once the stress path is altered. The authors found a rotation of π radians (180^{o}) gave the stiffest response and strain was found to influence how much rotation influenced stiffness, with negligible change in stiffness for any rotation, beyond 0.5% strain.

Gasparre (2005) later confirmed these findings but clarified that the effect of recent stress history on stiffness only occurs when creep is not allowed to occur in the samples before stress paths were changed. This is significant to insitu conditions as changes in stress paths will occur over longer time periods during construction/excavation. If creep does have time to occur, the effect of recent stress history may not be significant to the insitu stiffness. However, the response time may be linked to sample size and recent stress history could have a longer lasting effect insitu.

Stress paths may have a significant influence on the de-structuring of clay, as Takahashi et al. (2005) found that pre-swelling and pre-compression had significant influence on the current recompression/swelling index, with the swelling index in particular increasing more with pre-swelling. These results show swelling destructures the London Clay and demonstrates the sensitivity of the stiffness to soil structure.

Recent stress history is most relevant when consolidating to insitu effective stress state as the focus of the test begins from that stress state. To examine this effect, long and short stress paths were used by Gasparre et al. (2007) on a sample of A3(2) London Clay. They found that there was no significant difference to the results but volumetric strains were minimised on the short stress path.

5.2.2. Strain Rate

The speed at which strain is induced is thought to affect soil behaviour because when unloaded or reloaded rapidly, the soil responds with larger displacements. This is important as the engineering properties of the soil may change; however, Gasparre (2005) found that differing strain rates had only a small effect on London Clay properties. These effects were not larger than 3-4% for an order of magnitude strain rate difference which was concluded to agree with the literature (Tatsouka, et al., 1998).

However, the effect of a quicker strain rate alters the radius of the yield surface Y1, and if reliable capture of small strain stiffness trend is to be captured, a "moderately slow" strain rate of 0.2%/hr on an external displacement transducer is recommended by Gasparre et al. (2014).

5.2.3. Creep

It is recommended by Jardine et al. (1984) that creep rates should be allowed to fall below $1/100^{th}$ of the strain rate prior to testing or further testing; this is particularly relevant before final shearing to failure as can be seen in Figure 85. Here an undrained specimen of London Clay shows overestimation of stiffness when creep in the opposite direction has not be allowed to settle to slower rates. This agrees with the findings of Atkinson et al. (1990) and Gasparre (2005) who found recent stress history to be a factor, particularly when the stress path was at 180 degrees.

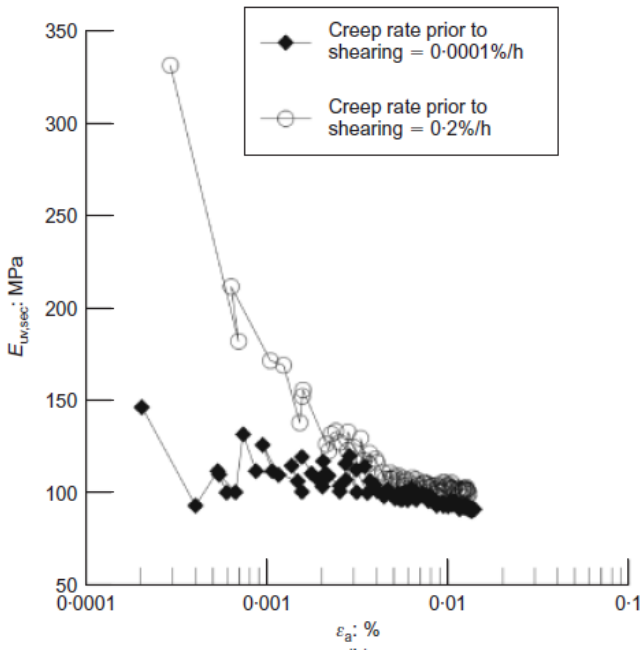

Figure 85: Dependence of undrained secant vertical stiffness on preceding creep strain (Gasparre, et al., 2014)

5.2.4. Fissuring

There are two main influences of natural fissures in clays. The first is strength; Vitone and Cotecchia (2011) studied 'intensely' fissured clays and found that the state boundary surface was not only smaller than for an intact specimen of the same clay but smaller than reconstituted clay, Figure 86. This suggests that the microstructure is significantly affected by fissuring and a weakening of mechanical properties results. In compression, a strengthening of the structure post-yield is shown by a positive hardening contribution (Vitone & Cotecchia, 2011).

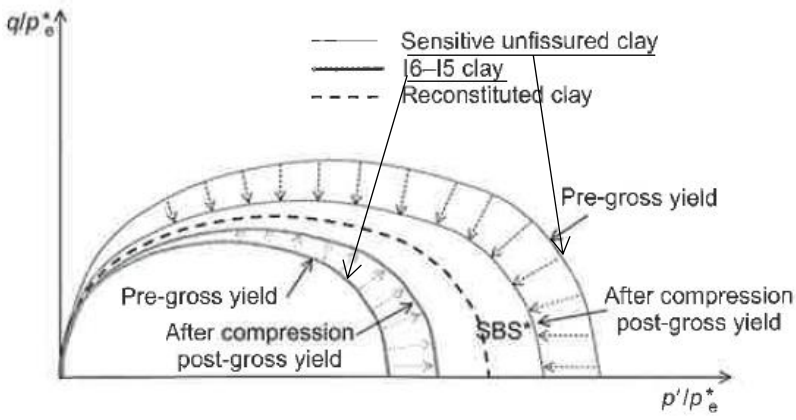

Figure 86: State boundary surfaces of natural and reconstituted clays; I6-I5 clay is fissured (Vitone & Cotecchia, 2011)

The second influence is permeability which significantly increases when a large fracture network exists. Pender et al. (2009) found through CT scanning specimens of Auckland Clay that consolidation pressure contributed significantly to the size of the void structure. This is important because when unloading a soil through excavation, this could open an existing void space and increase bulk permeability.

To model such a scenario, the pore network must be examined. Watabe et al. (2006) have proposed a probabilistic model for saturated glacial tills which is based on the premise that the smallest capillary of several capillaries contacting in a series governs the permeability; this can be visualised in Figure 87.

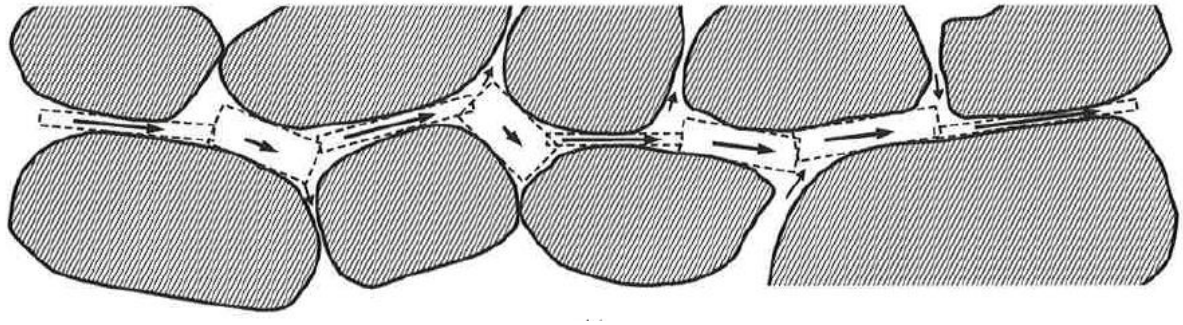

Figure 87: Pore network and water flow path (Watabe, et al., 2006)

5.3. Laboratory Apparatus

5.3.1. Oedometer

The oedometer test reproduces in laboratory conditions one-dimensional compression and swelling through the addition and subtraction of a vertical load to a confined soil sample. The sample is normally held in a water bath and bordered by a porous disc above and below it which creates two-way drainage. In the simplest tests, a series of loads are applied vertically using a loading yoke which results in strains and water flow in one-dimension. To measure the strains a transducer placed on the top platen measures the vertical displacements δ.

The stress and strain conditions are assumed to be axi-symmetric and the friction at the contact between the soil and the ring is assumed to be zero. In this research work 75mm diameter samples were used. The oedometer apparatus is illustrated in Figure 88 and in the laboratory in Figure 89.

The vertical strain ε_a, equals the volumetric strain ε_v, because of the lateral restraint of the sample. The resolution of the vertical displacement transducers was found to be 0.001mm.

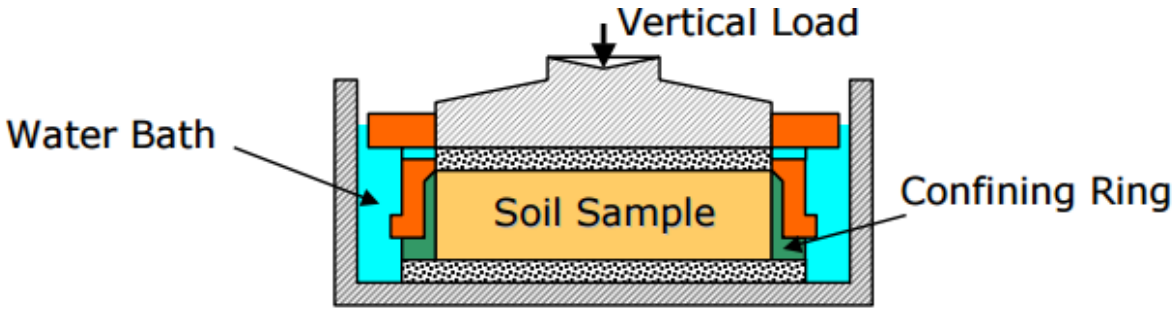

Figure 88: Diagram of Oedometer (Banglasdesh University, 2002)

Figure 89: Oedometers in the lab

Counter-pulley system for low effective stress

In addition to simple oedometer testing, a counter-pulley system was designed to reduce the weight of the top cap. This enables very low effective stresses to be reached and works by placing equal lead weight into each of the four containers which hang off a corresponding pulley; this can be seen in Figure 90. The weight of the top cap and porous disc is normally 625g with the addition of screws making it 850g. The pulley system requires some weight in each container in order for tension to be kept in the cables but theoretically the cap can be lifted so that as little as 10g remains on the sample.

Figure 90: Oedometer with counter-pulley system

5.3.2. Rowe cell

The Rowe cell test in many aspects is similar to the oedometer test as it reproduces one-dimensional compression and swelling in laboratory conditions. The key difference is the ability to control pore water pressures through a pressure volume controller.

75mm Rowe Cell

This apparatus, shown in Figure 91, consists of drainage ports at the top and bottom of the cell. The top drainage port is connected to a drainage tube in the loading ram which moves as the sample settles/heaves. The bottom drainage port is a single hole at the centre of the sample in the cell base which then outputs from the apparatus to one side of the cell base. The two drainage ports allow pore pressure to be controlled from either or both ports.

Between the drainage holes, porous discs are placed and then filter papers are placed between the discs and the sample. This ensures maximum vertical flow and minimises saturation and consolidation times. Pressure is applied to the sample through a hydraulic ram which consists of a cylindrical metallic face with an O-ring lying behind it to stop leakage between the

sample and the upper chamber where the ram pressure is held. The upper chamber and drainage ports are connected to pressure volume controllers through nylon tubing.

Pressures are measured using pore pressure transducers on entry to the upper chamber to measure the total stress being applied to the sample and at the base of the cell measuring pore pressures in the base of the sample, while pore pressures are controlled through the top drainage port. The cell dissembles into top, base and sidewall sections and O-rings also seal the top and bottom of the cell with the sides of the cell. As the stem is a moving part through the upper chamber, silicon grease needed to be applied to minimise friction and to reduce leakages.

Due to problems getting this apparatus to work effectively, results from this apparatus are not presented.

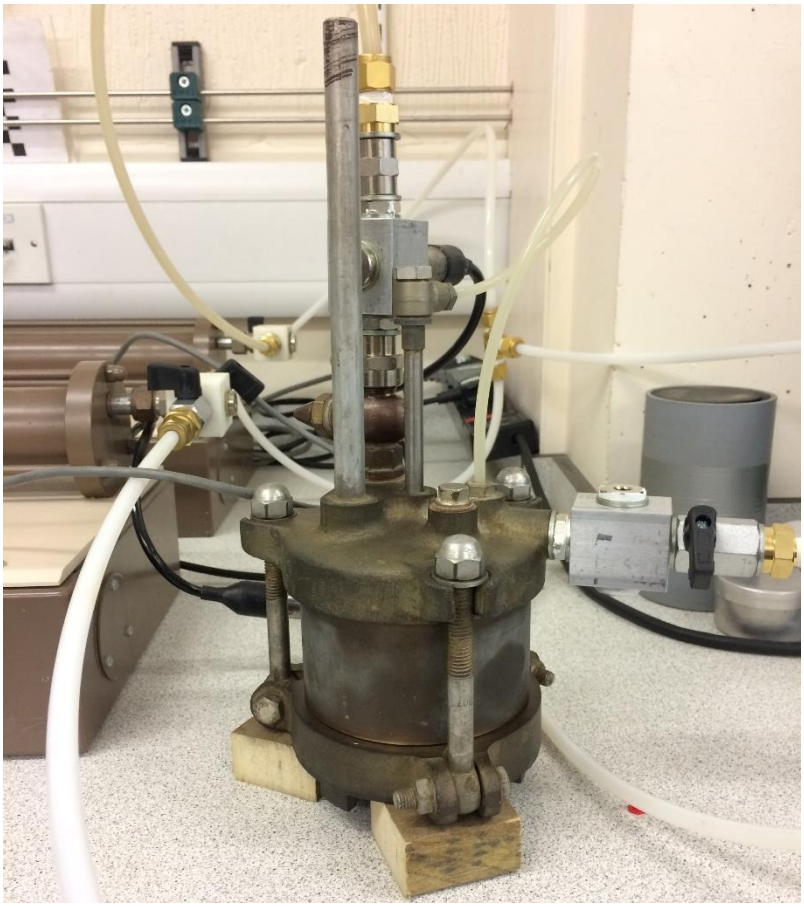

Figure 91: 75mm Rowe Cell

100mm Rowe Cell

The 100mm diameter Rowe Cell or hydrocon hydraulic oedometer as its named by the manufacturer Wykeham Farrance can be seen in Figures 92-94 and consists of a similar

arrangement to the 75mm Rowe Cell. Axial pressure can be applied by filling the upper chamber with deaired water and connecting a pressure/volume controller to the connecting tap. A chamber pressure valve mounted on top of the apparatus is used to make sure no air remains in the chamber.

A flexible diaphragm separates the chamber with the specimen and a stem which is used for measuring vertical displacements and for providing back/pore pressures passes through the chamber and the flexible diaphragm. The loading ram then connects to a tap which can then be connected to a pressure/volume controller. Porous discs are placed both sides of the specimen to ensure even saturation. At the base there is another entry point that connects to a further tap which can be connected to a pressure/ volume controller.

As a connection at the top and bottom exists for control of back/pore pressures, the option to saturate and control the pressures through a single controller or through two separate controllers is an option. In this case, a single pressure/ volume controller is used to apply a single back/pore pressure to the top and bottom of the specimen.

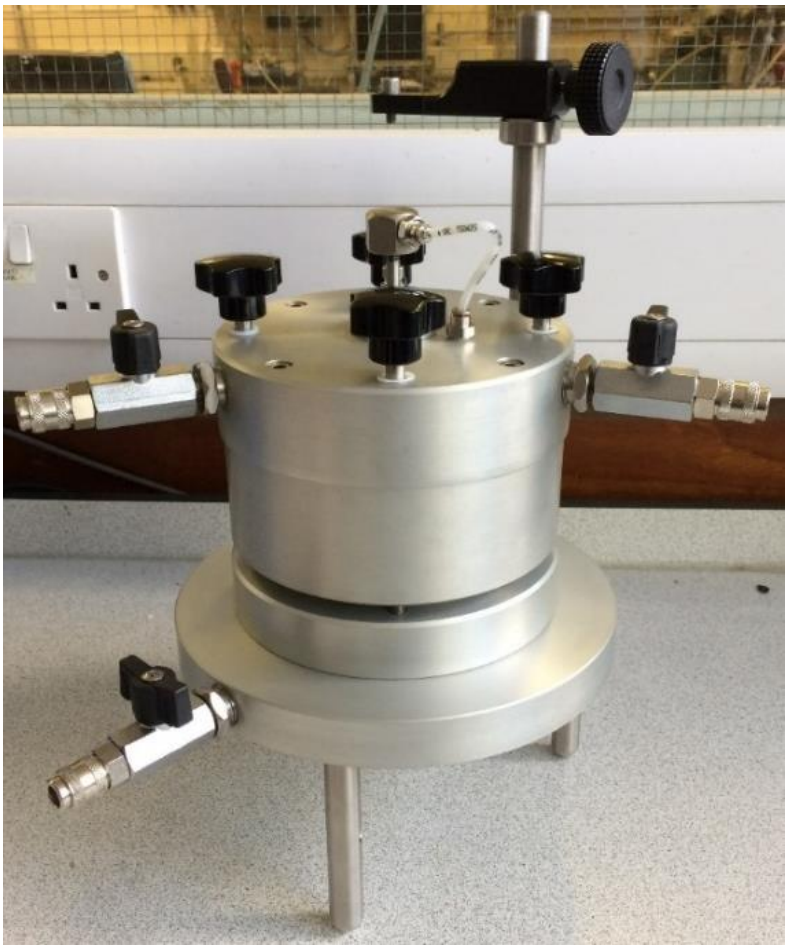

Figure 92: 100mm Rowe Cell

A feature of this particular model is that pressures of up to 3500kPa can be applied without dead weight; however, this pressure is limited by the pressure/volume controllers provided by GDS which provided a maximum of 2050kPa of pressure.

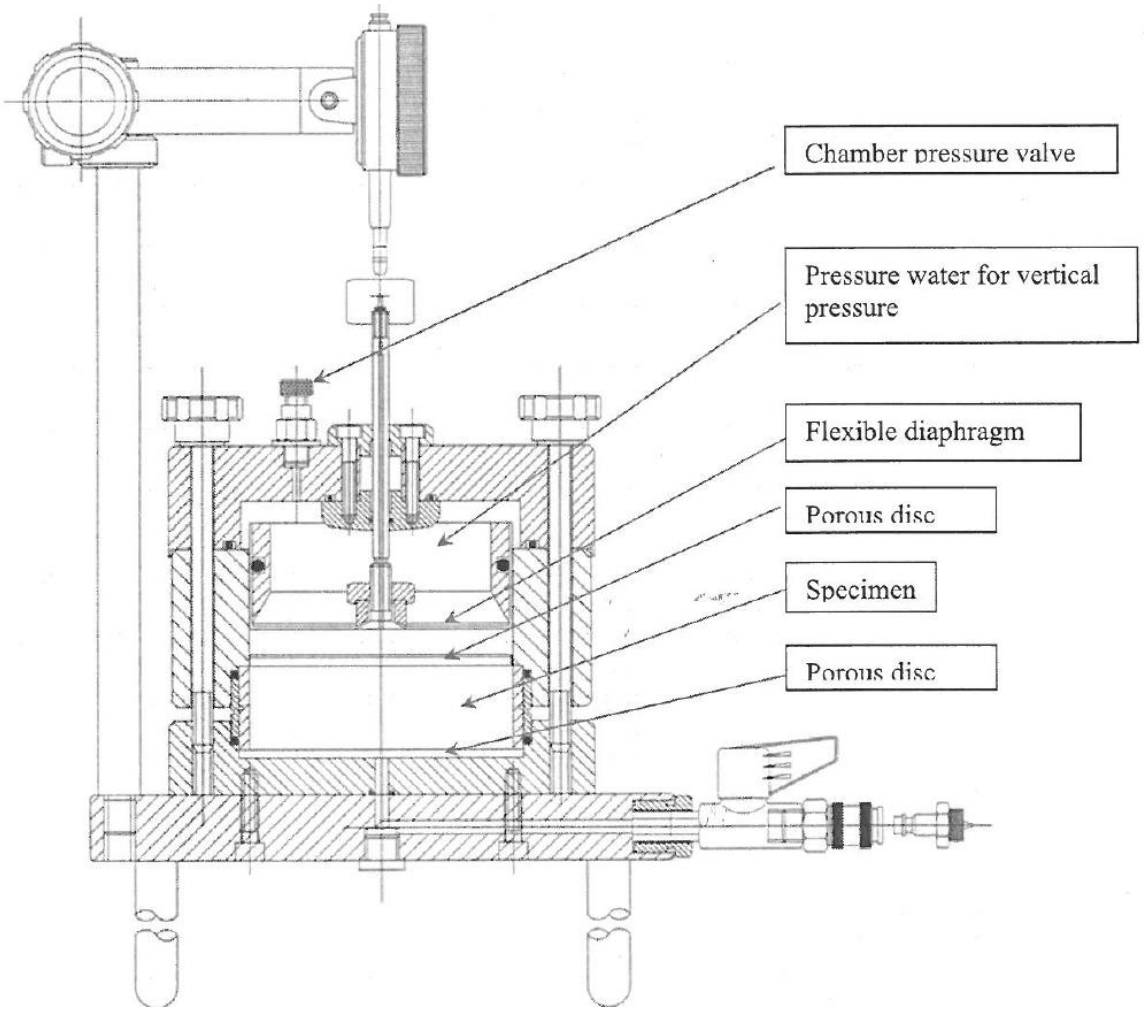

Figure 93: Illustration of Rowe Cell internal (Wykeham Farrance, 2015)

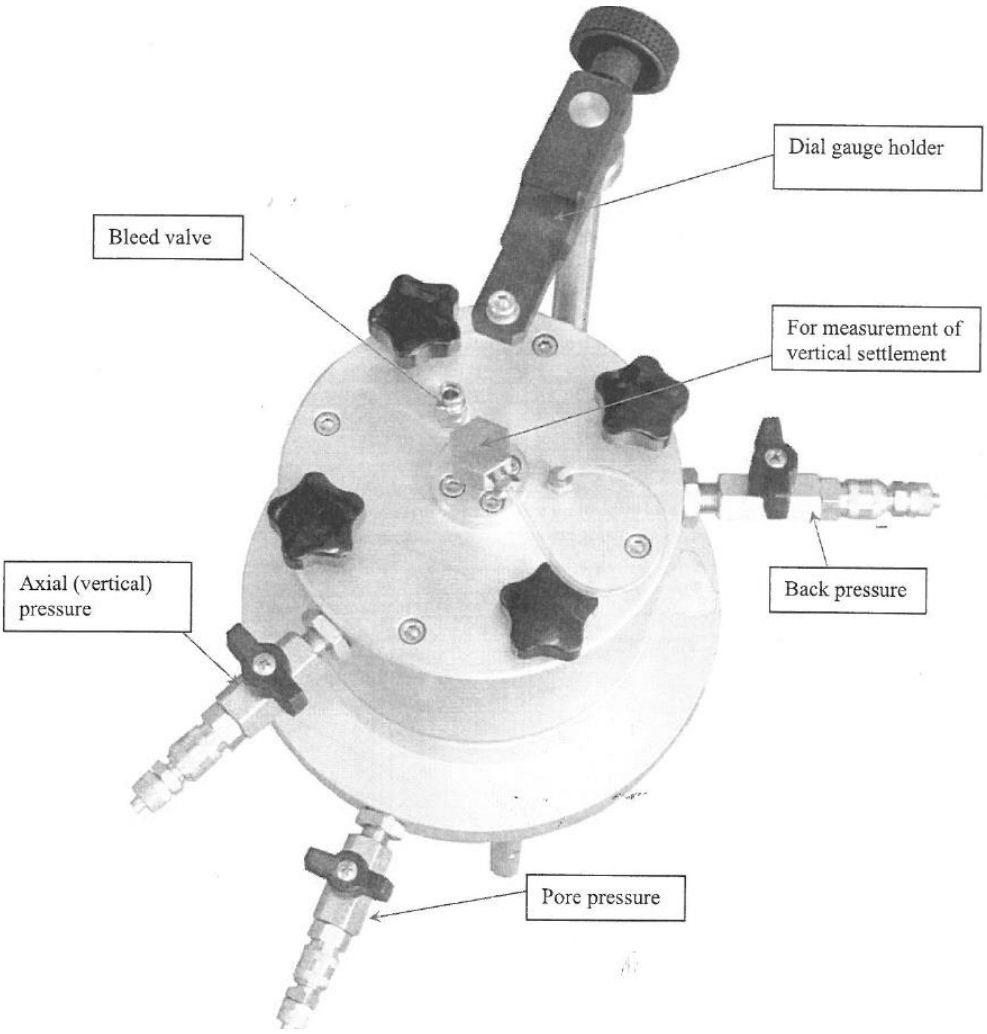

Figure 94: Illustration of Rowe Cell external (Wykeham Farrance, 2015).

5.3.3. Triaxial apparatus

There have been three triaxial apparatus used in this research. Modifications have been made to accommodate the addition of bender elements into the 38mm and 100mm diameter triaxial samples. An illustration of a typical triaxial apparatus arrangement is given in Figure 95.

Out of the three triaxial apparatus, only one arrangement proved effective at fulfilling the quality of data sought. Nevertheless, all three apparatus are described below.

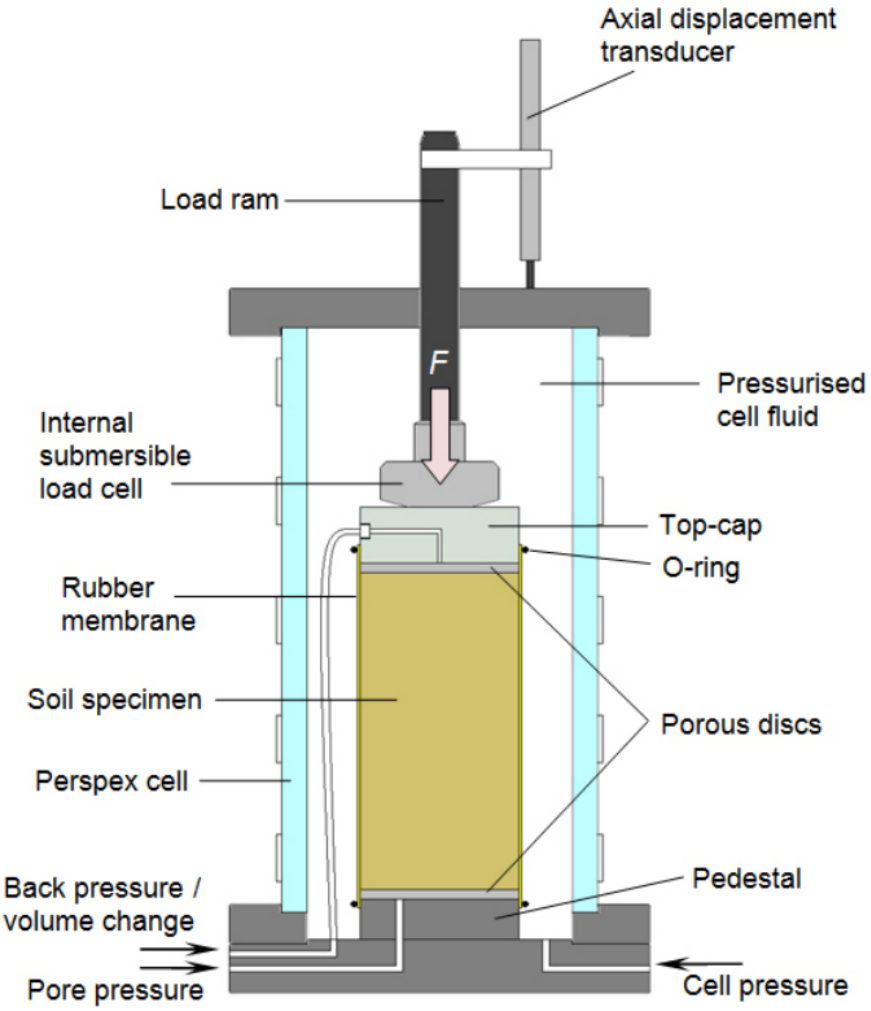

Figure 95: Illustration of standard triaxial cell set up (Rees, 2013)

Bender element system

The bender element system is provided by VJTech and consists of: a bender scope seen in Figure 96; Clisp studio which runs as a data collection and analysis software; bender elements, which are described later for each apparatus; and cabling to connect the system. The software runs on a custom-built desktop which runs on a separate unit to the GDS software to avoid conflict. Both the 38mm and 100mm systems run through the single bender

element system but only a single set of recordings can be recorded at once so the cabling must be plugged/unplugged accordingly.

Figure 96: Bender scope VJTech VJT1020

38mm Triaxial apparatus

The triaxial cell can be pressurised up to 1700kPa and is provided by VJTech. There are four inserts at the base of the cell which provide cabling for the bender elements and for a single LVDT. This can be seen in Figure 97.

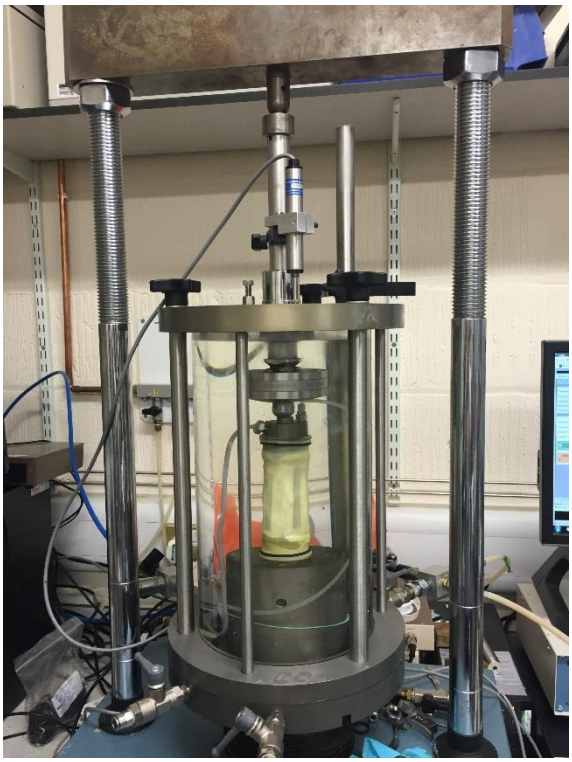

Figure 97: Cell for 38mm diameter testing (100mm diameter capacity) with first successful sample inserted

Bender Elements

The bender elements for the 38mm dia. triaxial apparatus are made by VJTech and can be seen in Figure 98. These bender elements fit into the top and bottom caps so specially designed porous discs are hollowed out so they sit around the bender element in the centre of each cap.

Figure 98: 38mm bender element acting as a top cap

Load Cell

The internal submersible load cell is provided by GDS and has a range from 0-4kN. The connection between the load cell and the top cap is achieved using a half ball seated in a conical shaped notch.

100mm Triaxial apparatus

The 100mm diameter triaxial apparatus is shown in Figure 99 with a sample set up and does not differ fundamentally from the illustration in Figure 95. The key difference is the access ring which allows local instrumentation to be brought into the pressurised cell.

Figure 99: First sample with membrane attached

Bender elements

The bender elements that fit into the triaxial apparatus for the 100mm dia. setup consist of a pair which fit into the top and bottom caps, Figure 100. These come with porous discs that have pre-existing spaces in the centre for the bender elements. Additionally, a lateral set of bender elements are mounted onto the specimen itself. The system uses the same bender scope and software as the 38mm setup.

Figure 100: 100mm dia. bender elements in top and bottom caps (VJtech, 2015)

Axial and radial LVDT's

The LVDT's measure local displacements by using two parts, a main body and an armature which penetrates this body. The depth of penetration alters the voltage outputted by the device. The output signal can then be sent to an amplifier before being read by the datalogger. The LVDT's are connected onto the sample using plastic mounts superglued to the sample membrane, the mounts must be the correct distance apart and must be aligned perfectly for accurate measurement. This is achieved using a spirit level, ruler, and permanent markers. One mount is used to hold the body of the LVDT and the other provides a platform for the armature to push against. For the radial LVDT, a ring which surrounds the sample is glued to the centre of the sample ensuring the mounts are level. Care to allow room for the bender elements, mid-height pore pressure transducer and axial LVDT's is needed.

Mid –height pore pressure transducer

The mid-height pore pressure probe has a porous shell and can be pushed into most triaxial samples. This is not the case here as samples were generally very stiff and so preparation of the sample was needed in advance. Firstly, a hole was drilled at the mid-height. Then, once the membrane was attached, a hole was created by piercing the membrane over the drilled hole carefully and stretching it. Once stretched the probe could be pushed through the membrane and into the drilled hole. A small amount of remoulded material was applied to the

end of the probe to ensure good connection and minimise the effect of suctions in the sample. Additionally, O-rings were placed around the probe-membrane connection and then L-sx (Hydraulic sealant) was used to cover any potential gaps that were missed.

Load Cell

The internal submersible load cell is provided by GDS and has a range from 0-5kN. The connection between the load cell and the top cap is achieved using a half ball seated in a conical shaped notch. The load cell was similar to the 38mm set-up.

Stress Path Triaxial Cell

The replacement for the 100mm diameter triaxial apparatus was a Bishop and Wesley apparatus. This unit was in a poor state when it was proposed for research on this project. Several modifications were made to accommodate bender-aided small strain testing. This involved drilling into the sides to create additional access ports.

Over two years, every part of the apparatus was taken apart and reassembled and/or replaced. Eventually a sample could be installed into the apparatus and this is shown in Figure 101. Detail is not provided of this apparatus because due to laboratory complications, no useable results were obtained after over two years of testing.

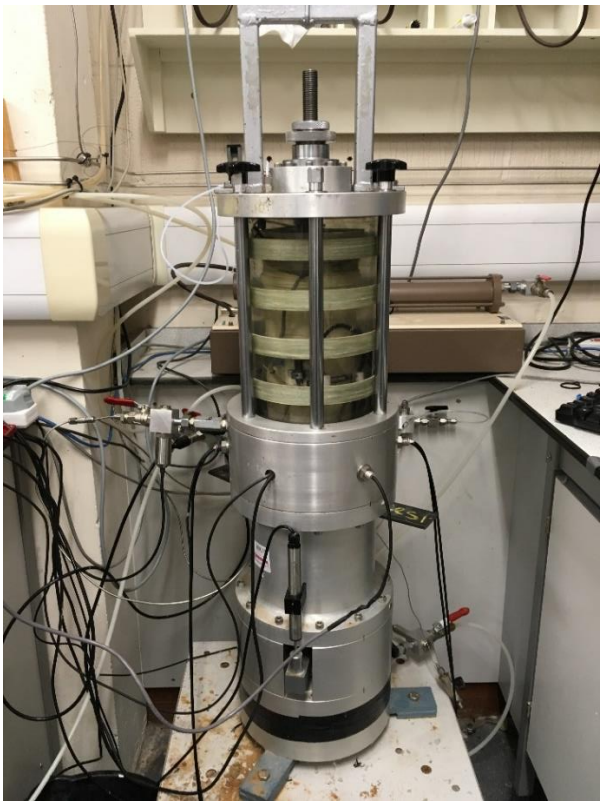

Figure 101: Stress path Triaxial apparatus

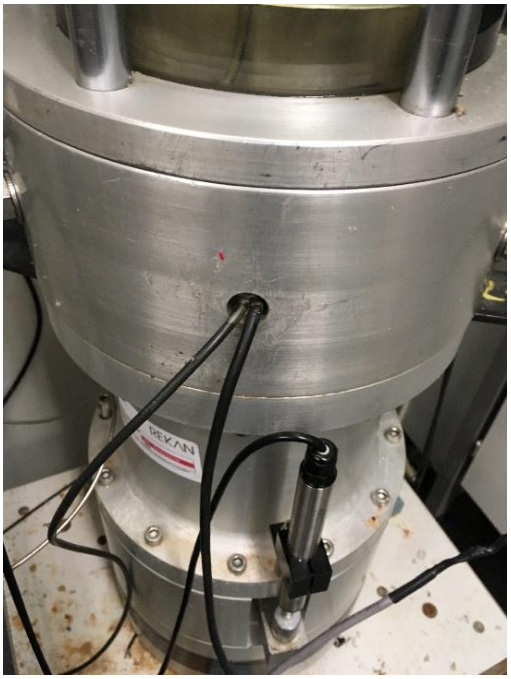

Figure 102: Drilled holes for access

5.3.4. Calibrations and resolutions

All of the transducers and load cells were calibrated against a Budenberg dead-weight tester. Linear calibration was assumed in all cases so to minimise errors associated with this, when calibrating an instrument, particular attention was given to the range expected in the upcoming experiment. The transducers have an accuracy of no worse than +/-0.1kPa while the load cell +/- 0.001kN. The GDS pressure/volume (P/V) controllers appear to have the worst resolution as they typically read +/-0.5kPa of the required pressure. When everything was calibrated, the two P/V controllers were not correctly zeroed and so they read a 16kPa difference when measuring the same pressure. Using the other calibrated pressure transducers to confirm the true pressures, adjustments were made to the zero offset.

All the LVDT's were calibrated against a micrometer which has a resolution of +/-0.01mm. The LVDT's themselves would have a resolution which translates to +/- 0.001%.

5.4. Block Sampling

The opportunity to block sample was made available by Mott Macdonald and enabled by the cooperation of numerous contractors on each of the sampled sites. This is an extremely rare opportunity as very few block sampling opportunities exist and none (to the author's knowledge) have been conducted at such great depths. Block sampling itself is desired due to the potential reduction in sample disturbance when compared to other sampling methods.

Four block sampling days over three sites using a combination of staff and students resulted in: four blocks of London Clay Unit B taken from Victoria Station Upgrade (VSU); three blocks of London Clay Unit A2(upper); four blocks of London Clay Unit A2(lower) both taken from Blomfield Box; and two blocks of UMB taken from Moorgate Shaft. The depths the blocks were excavated for each sampling visit were: 12m; 32m; 37m and 40m below the ground surface, respectively.

5.4.1. Moorgate Shaft and Sampling

Samples were excavated from the base of the Moorgate shaft, the location of which is shown in Figure 103. Moorgate Shaft was constructed as part of Crossrail; a new transport link for London. The shaft itself accommodates a western ticket hall which is an expansion of Moorgate's current London Underground Ticket Hall.

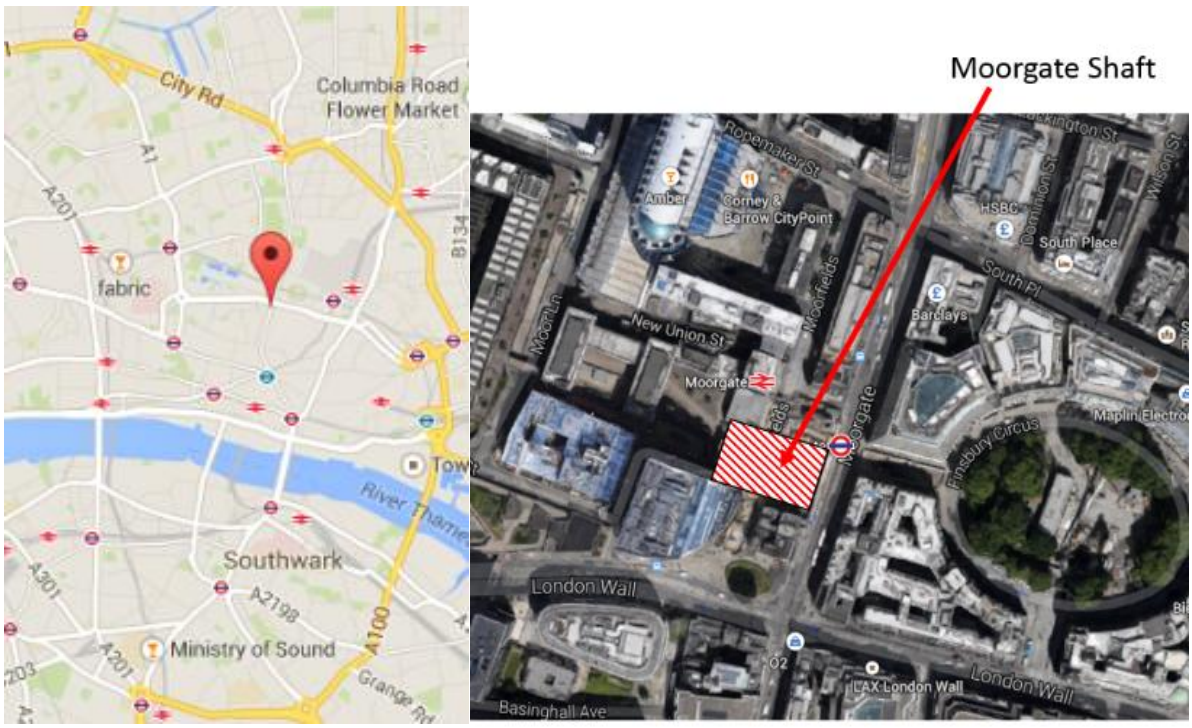

Figure 103: Location of Moorgate Shaft – Central London using Google Maps (Google, 2015)

At Moorgate, the excavation sequence was carried out in a series of stages and begun towards the end of 2013 with 4m of excavation through made ground. A further 6m was excavated into the New Year where some alluvium was removed. In spring 2014, 6m more excavation of the river terrace deposits and some London Clay ensued, then a month later a further 7m of excavated London Clay was removed. A further 4.5m of London Clay was removed in mid-summer 2014 two excavation periods in late summer removed 4m and 8m respectively; at this point any Harwich Beds and the top of the Lambeth group had been removed. The depths

of overlying strata are given in Figure 104 and the depth of sampling is 40m below ground level. These depths show differences caused by lateral variation across the site.

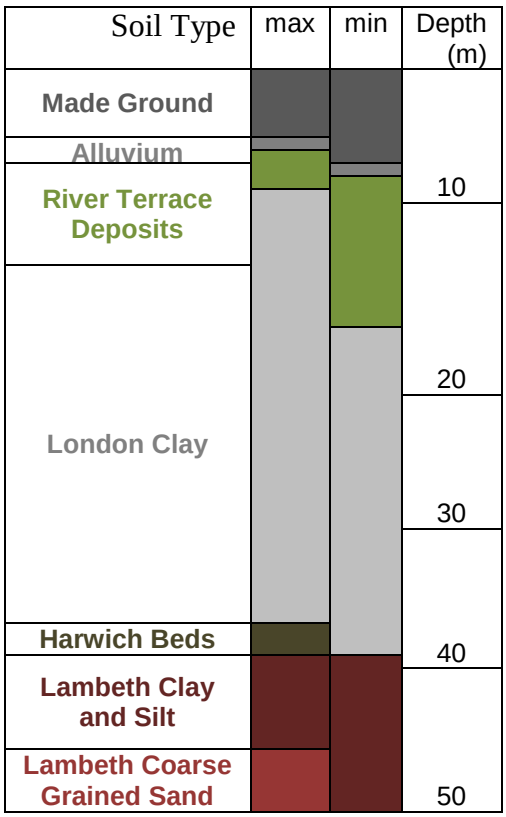

Figure 104: Maximum and minimum depths of overlying strata at Moorgate Shaft, taken from borehole data.

At Moorgate, limited safe working space meant that a large excavator excavated a large lump of soil by first creating a bench and then dislodging a large section of soil from the bench by forcing the bucket into the side with the intention to cause failure in the horizontal plane; Figure 105. Once lifted from the ground, some trimming was conducted in order for the lump to be suitable to be lifted to the surface which was achieved using a crane, Figure 106.

At the surface, trimming was initially done with a jack hammer as the clay was very stiff to hard and the intention was to take two samples from the very centre of the block, Figure 107. Once close enough, garden tools such as spades, edging blades, wood chisels and forks were used to create a block sample. Increased care was given the closer the sample came to its final dimensions. The biggest issue was not causing failure but simply trimming as the clay was difficult to penetrate.

Figure 105a): Bench created by excavator at Moorgate in UMB, 40m depth b) Excavator lifts a large 'lump' from the ground by forcing forks into the sides at the base of the lump.

Figure 106a): Excavator trims 'lump' using fork end to the bucket b) Excavtor placed 'lump' into a cage where it is craned to the surface.

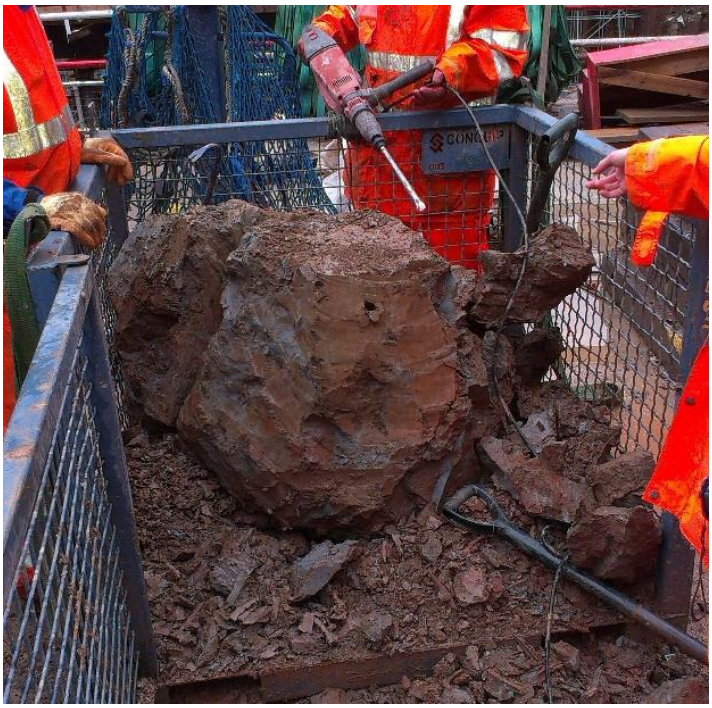

Figure 107: The UMB 'lump' is further trimmed initally by pnumatic drill.

Once an approximately 300x300x300mm block was created, layers of cling film and aluminium foil were wrapped alternatively over the block before placing a wooden box round the sample. To remove the block sample from the remaining larger soil lump, excavation was needed underneath the sample too which was ultimately carried out using the jack hammer. Finally, a layer of cling film and foil were further wrapped over the bare surface then around the wooden protective box.

After transport back to The University of Southampton, further wrapping commenced with cling film, foil and refuse bags. The blocks were then stored in a temperature-controlled laboratory.

During the Moorgate block sampling six U100 tubes were pushed into the UMB material to obtain specimens for oedometer testing. Each of these tubes had a sharp cutting blade on one end and were pushed into the ground using a large excavator. However, the 22T excavator struggled to push the tubes into the stiff clay and two tubes buckled under the pressure. Out of the six tubes, two had useable samples; the preparation of which are discussed in 5.5.

The two block samples taken from this site on 28th August 2014 are light brown with red mottling, and patches of grey blue clay exist where larger fissures propagate. Based on a brief inspection, clay was the dominant particle size. The clay could not be dented by a fingernail onsite meaning it is ‘hard’, despite heavy rain during excavation dampening the samples.

After further analysis at the University of Southampton the orientation of the block samples when compared to the grey blue clay banding/fissuring suggested that perfect vertical alignment of the blocks was not achieved, see Figure 108. The orientation was tracked using photographs and the base of the excavated block lay not along the bottom of cage but rather across one corner. This orientation was confirmed through further examination of the excavated block samples prior to laboratory testing suggesting that this misalignment may be between 95-115 degrees, as shown in Figure 108. Perfect orientation exists when the orientation of a block sample mirrors that insitu so that the block has vertical and horizontal faces, as vertical parameters differ to horizontal parameters.

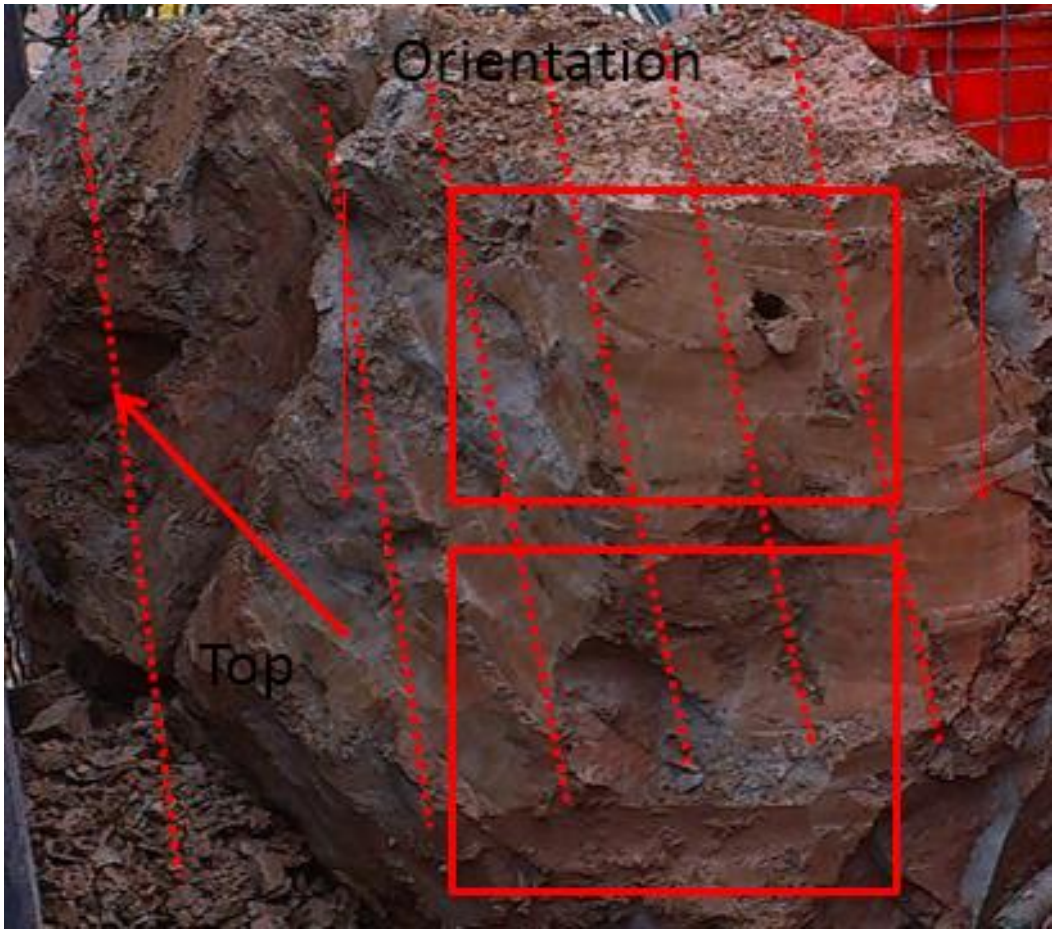

Figure 108: Block sample orientation – Rectangles show where the blocks were taken and the dashed lines show the orientation of the block

5.4.2. Blomfield Box and Sampling

At Blomfield box, (see Figure 109 for location) the construction sequence through the soil profile in Figure 110, was complex and involved multiple small excavations followed by casting of blinding and then floor slabs. This was due to the close proximity of neighbouring buildings. Additionally, the site was constantly dewatered which increased the suctions in the soil.

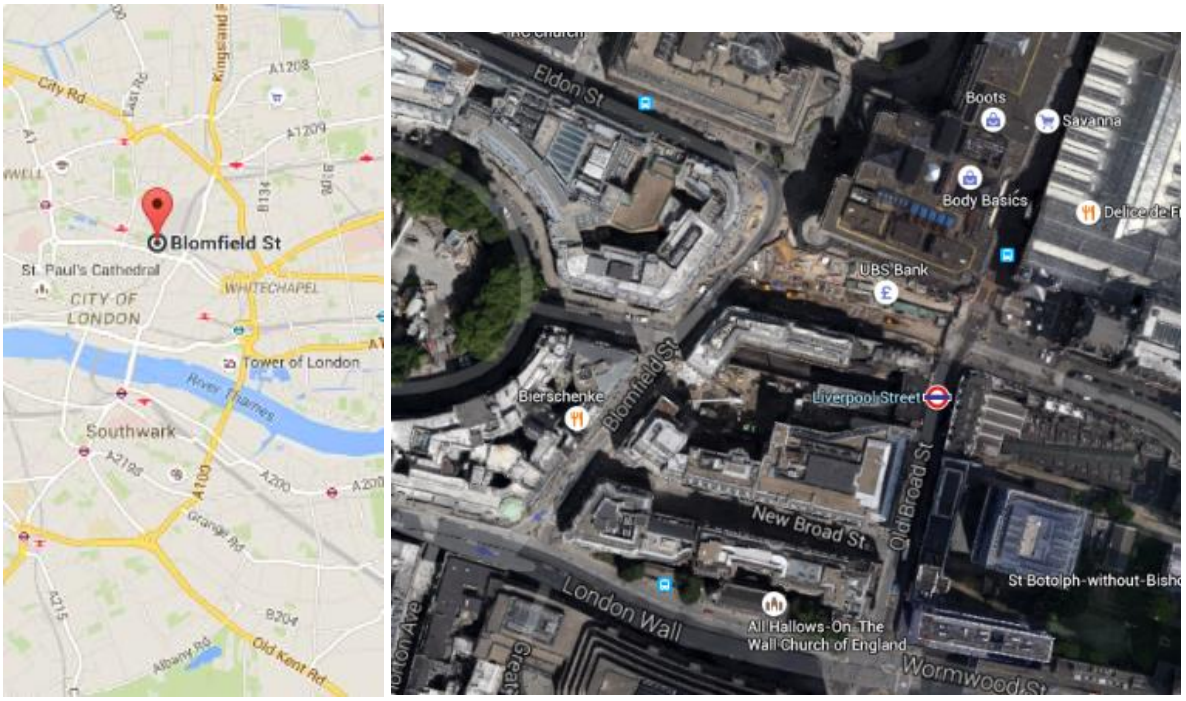

Figure 109: Location of Blomfield Box – Central London using Google Maps (Google, 2015)

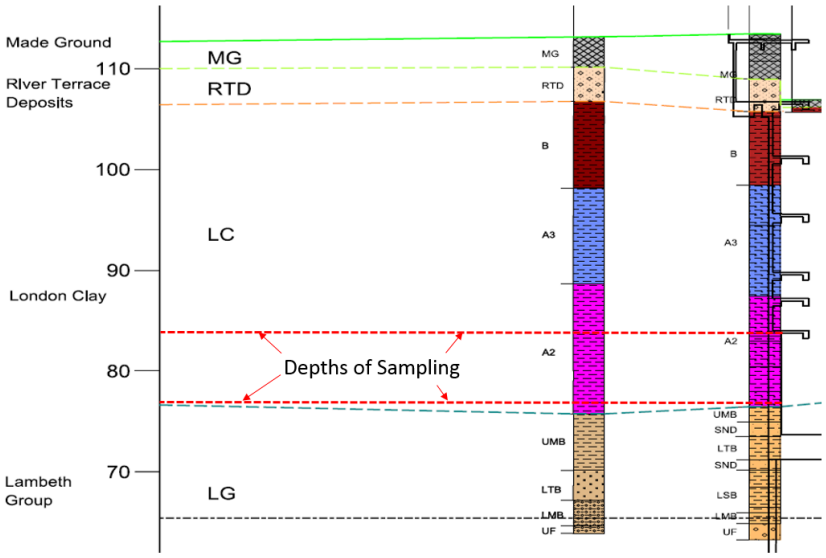

Figure 110: Depth of sampling on soil profile log at Blomfield Box (Cruttenden, 2014)

At the upper level at which London Clay Unit A2 was sampled, the clay was visibly cracking and had laminations; cracking could have resulted from changes in the stress state (loading and unloading) during excavation of the Box, or from pre-existing fractures. Also, it contained fossilised wood fragments. The lower sampling level within LC Unit A2 was quite different to the clay found above. Cracking was not an issue but silt and sand partings were found infrequently. Wood fragments were not found but pyrite was found frequently. On review both the upper and lower London Clay Unit A2 samples fit the description of unit

A2(2) upper and A2(1) lower. This is expected as the lower sampling level is close to the base of London Clay at Blomfield and Hight et al. (2007) found on samples from Heathrow a clear difference at the bottom of A2 where the clay becomes sandy glauconitic (Harwich Formation).

There were two sampling days at Blomfield Box, both took a very similar approach. Firstly, a bench was created using an excavator, this looked as it does in Figures 111a and 111b. Once a suitable bench was created, the sampling team could excavate a trench to start forming a perimeter around a block, which could then be further trimmed into a block sample. The trench was excavated around a corner in the bench Figure 111a to form a block of plan dimensions 1m x 1m. This was initially achieved with the aid of a pneumatic drill due to the stiffness of the clay. Once a perimeter was created, hand tools were used to 'chip' away at the edges of the 1m x 1m block until a block of around 35cm x 35cm was created with depth of around 40cm. At this point, more careful trimming using wood chisels to 'carve' the sides of the clay in a single motion from the top of the block to the base; this ensured a flat, smooth finish. Once the block fitted within the wooden sample box, cling film and foil was wrapped around the block (Figure 113a) and then the box was replaced over the now 300 x 300 x 300mm block. To remove the block from the ground, a lateral force was applied to the block which caused a failure 2-5cm below the base of the box. At this point the block could be rotated 180 degrees and wrapped again in cling film and foil. Orientation was logged and then finally, once all the blocks were retrieved from the ground, a skip was used to haul the blocks out of the excavation (Figure 113b) and then the blocks were immediately transported to the temperature-controlled laboratory at The University of Southampton to be rewrapped.

There was very little difference in the sampling procedure used either time at Blomfield; however, the experience was quite different. On the first sampling day at 32m depth, the clay appeared to be 'dry' as fractures in multiple directions were encountered with spacing 5-20cm; these fractures were not deep. Other fracturing was also found to occur laterally. This fracturing appeared to be pre-existing to around 30cm below the excavation depth on the day. Horizontal laminations every 5-10cm made it impossible to obtain a block from this depth; therefore, a deep bench was created. Also, fossilised wood fragments were frequently encountered with pyrite nodules visible throughout.

On the second sampling day, a sandy bed was apparent at 15cm below the top of the bench and below this the clay was sandy and glauconitic. All the blocks were taken from this

section below the sandy bed. A pre-existing failure plane was used as the base of the first blocks and a shorter block which slid off along this plane (Figure 112) was wrapped to be used as a block for horizontally cut samples.

Figure 111a): Bench created by excavator at Blomfield Box in London Clay Unit A2(1) b) Shows depth of the bench

Figure 112: Failure along an existing fracture

Figure 113a): Block sample is wrapped in cling film and foil b) Crane brings all block samples to the surface in a skip.

5.4.3. Victoria Station Sampling

At VSU Northern ticket hall, see Figure 45 in section 4.2 for location, the construction sequence (Figure 47) begun with unload through the removal of Bressenden Place Road and replacing it with a roof slab. The next stage involved a 5m unload and then reload through casting of the 1st floor slab. Next the excavation was taken to 9m below ground level and then reloaded again with the upper basement slab. Finally, further excavation down to 12m below ground ensued where the block sampling occurred. See section 4.2.3 for geotechnical interpretation.

At VSU, sampling was conducted at the depth of the lower base slab, 12mbgl. At the time of sampling, the excavation had not reached this depth and so some excavation to the required sampling depth was needed. As to not disrupt site activities too much, an area approximately 4x4m was chosen at the centre of the site and an excavator removed approximately 1m depth of soil. At this point, a 1m deep bench was created at the four edges of the 4x4m excavated area, though excavation to 2m depth relative to the original floor level in the centre of the 4x4m sampling area. Some additional safety measures were made to ensure safe working within the benched excavation, these included the addition of steps, scaffolding and a secondary bench to half the depth of the main bench.

Working in the bench and trimming the excavated sampling area from the corners, the sampling process was identical at this point to the other sampling days. Although this Unit of London Clay was much less stiff and so no pneumatic drill was used. In fact, the lower stiffness meant that the wood chisels were too aggressive to trim the block at close quarters. There were several problems encountered with sampling at this site around the fragile nature of the blocks which appeared to fracture in every direction without any great force applied to them. Several blocks were lost before successful blocks were obtained. The clay appeared homogeneous but a 5-10cm fracture network that dramatically increased with drying was apparent throughout.

5.5. Oedometer methods

5.5.1. Intact specimens

Trimming

These specimens were taken from a variety of sources such as block samples, U100 tubes and bagged offcuts taken during block sampling. The samples taken from block samples were

trimmed using a similar methodology for oedometer, Rowe cell and triaxial specimens. This consisted of using hand tools such as wood chisels, saws and knives while keeping the remaining block wrapped with film and foil.

Offcuts were used for practice specimens, but care had to be taken when handling these offcuts as some moisture loss had occurred to a varying degree, and trimming using hand tools varied in difficulty. Some material was very easily carved to the final specimen size using a wood chisel while some of the first UMB offcuts needed several hours to take off a few millimetres. If possible, the geometry of the offcut was noted and the remaining material was rewrapped.

For U100 tube specimens, a section to work with was cut with a hack saw from the U100 sample and then placed on a device which pushes the material through a U100 tube. The U100 tube was then rewrapped to ensure minimal moisture loss. The section was then trimmed to the specimen size, ensuring the specimen was taken from the centre of the cylindrical block of soil.

The final dimensions of the oedometer specimens were approximately 75mm in diameter and between 14.5-20mm in height.

Test procedure

The intention of the testing procedure was to minimise disturbance and destructuring of the specimen before it was swelled from insitu effective stress. This was achieved by placing the specimen in a containment ring which had silicon grease around the rim to minimise friction. The specimen in the ring was then placed in the oedometer apparatus with filter papers either side. The porous discs which bounded the specimen were dried in the oven for 24 hours prior to the start of the experiment.

The nominal weight of the oedometer cap and arm was then placed on the specimen. For the initial tests, a period to check nothing moved was not carried out but for later testing a creep stage of up to 24 hours was allowed and then the displacements were re-zeroed. Consolidation then ensued on a varying stress path which started and finished at different points depending on the test. The intention was to apply incremental loads at no more than twice the previous load on the hanger until 3 times the estimated insitu effective stress was applied to the sample. At this point the specimen was flooded with deaired water. If any swelling occurred, further load was applied to limit swelling strain. 24-72 hours passed before the specimen was unloaded to 95% of insitu effective stress in stress decrements and

then the specimen was reloaded to insitu effective stress. A creep stage of 48 hours was allowed before unloading to 10% insitu effective stress in 6-10 stress decrements. All stress changes were applied after 24 hours as the practice specimens indicated that this was sufficient to ensure near-complete consolidation/swelling. Once reaching 10% insitu effective stress, the stress paths changed according to the test; for some tests the specimens were reconsolidated, for other tests the specimens were unloaded further. This methodology was proposed to the author by Tony O'Brien (2013) as a way to minimise unwanted swell prior to reaching the desired stress range.

The time interval between stress increments was explored in several initial exploratory tests. In an ideal setting, pore pressures could be measured in the sample and a computer would log data so that when approaching the end of primary swelling intervention could occur. Unfortunately, it was not possible to have this kind of set up in the laboratory. Before any tests begun, a consolidation test was conducted on each material and found that 95% consolidation was reached for all but one test within 24 hours for a range of specimen heights and stresses. The only test that did not fall within this range was a stress of 3MPa that was applied to a 19mm high specimen of UMB. As 3MPa was only ever applied as a swell reduction technique, this was considered irrelevant to the testing procedure and a 24-hour time interval was chosen.

5.5.2. Reconstituted specimens

The reconstituted material prepared to BS 1377-2: 1990 at The University of Southampton was kept in plastic containers at a moisture content in excess of the liquid limit. To achieve this deaired water was added periodically to the container.

To prepare a specimen a glass board was used with two metal spatulas to further mix in additional de-aired water to increase the moisture content to around 125% of the liquid limit. The material was mixed and left repeatedly to ensure no 'lumps' are left. When the material was ready, the metal spatula was used to fill a containment ring with the material. The rings are the same as the ones used for an intact specimen and are 75mm diameter and vary between 14.5-20mm height. Some reconstituted test samples were prepared by Fugro who followed a similar approach to forming the samples.

Once the specimen was prepared it was placed in the oedometer apparatus and deaired water used to fill the chamber. The oedometer cap was placed on the sample and then a 24-hour creep stage was applied with the displacement measured. After the creep stage, small

incremental loads were applied starting at just 0.5kPa at first to ensure uniform settlement. After 10kPa was applied, the load increments follow a similar structure to intact specimens. In most cases, the maximum pressure of 3MPa was applied before unloading in decrements. After reaching 100kPa, the specimens followed different stress paths depending on test.

5.6. Rowe Cell

The preparation of Rowe cell specimens was similar to that of the oedometer and triaxial specimens. The key difference is the final specimen size which was 75mm diameter for the first Rowe cell and 100mm diameter for the second. The height of the specimens varied but was between 25-30mm for the 100mm Rowe cell.

The first tests on both Rowe cells were conducted to mimic the stress path consolidation of the oedometer specimens; this was to provide a comparison. The specimens were consolidated through an increase in ram pressure until the applied vertical stress was 1.5MPa. The specimens were then flooded and keeping the difference between the ram pressure and back pressure the same, the ram pressure was increased to the maximum able by the pressure volume controllers, 2MPa. The samples were flooded from top and bottom to minimise saturation time. A back pressure of 500kPa ensured the air dissolves into the deaired water.

Saturation was confirmed by a B-value test. This was conducted by shutting the back-pressure valves but leaving the pore pressure transducer valve open to the specimen. The change in pore pressure should reach 95% of the changes in total stress applied by the ram to the sample. As the deeper material is considered very stiff or even ‘hard’, 90% is a more realistic target (Das, 2008).

Once saturated, an unload to 95% insitu effective stress, reload to insitu effective stress and then creep stage of 48 hours follows like the oedometer testing. Initially, the load in/decrements are discrete and 24 hours was used between load steps.

It came apparent early on that saturation using the method described would not be achieved quickly and so all tests after this were saturated using the following method. First, insitu effective stress was applied to the sample using the ram pressure. Saturation then begun by increasing ram pressure at 50kPa intervals every 24 hours until 2MPa of ram pressure was reached. At this point, the back pressure was increased at 50 kPa intervals every 72 hours. B value tests were conducted before every increase in back pressure. The back pressure was

increased until a credible B-value was reached. In some cases, this was when the back pressure almost matched the ram pressure.

Once saturated, the effective stress was increased by decreasing the back pressure and ram pressure at different rates. The back pressure was reduced at 50 kPa every 24 hours and the ram pressure was reduced 25kPa every 24 hours. This was continued until the estimated insitu effective stress of the sample was reached again. At this point, the ram and back pressure were decreased/increased at 25 kPa intervals every 24 hours until the back pressure equalled 600kPa and the ram pressure created the same effective stress in the specimen.

At this point, a creep measurement was taken by leaving the sample for 72 hours at these pressures. In all cases, swelling occurred at this pressure so the ram pressure was increased to double the effective stress. Pressure was held here between 72 hours and 1 week. The ram pressure was then lowered to 95% effective stress conditions and held for 72 hours. Finally, insitu effective stress was again applied and held there for between 1 and 2 weeks. At this point creep was assessed and if creep strain was too large then another cycle of loading was applied at a higher stress. It is noteworthy that the methodology is similar to the oedometer test procedure but includes extended time steps to account for greater sample size.

5.7. Triaxial testing

5.7.1. Trimming block sample

For the initial trimming a variety of techniques were required. The more brittle samples were hand trimmed from the block using saws, sharp knives and wood chisels. Care was taken to keep the rest of the block sample covered with cling film and foil to minimise moisture loss.

For some samples, a prism of size slightly larger than the final intended sample dimensions was cut from the main block and then mounted separately on a soil lathe where it was more carefully trimmed. This process was completed with the help of others to minimise drying as it caused fracturing, particularly with the London Clay Unit B2.

Several blocks of London Clay Unit B2 were particularly difficult to trim. Fractures would form when the block dried and after taking moisture content tests to confirm what moisture loss was required to achieve this it was found to be less than 0.5%. This suggests that the fractures are pre-existing, something that was also an issue on site when creating the blocks themselves. As fractures were forming in all directions initial trimming was more luck than

judgement and very few samples were successfully formed and only one was successfully tested.

London Clay Unit A2 was the opposite of this. Samples were easily trimmed as seen in Figure 114; other samples shown in Figure 115. Precise trimming was easily achieved with a Stanley knife which was found to be the best tool to carve an accurate 38mm diameter sample. The increase in larger particle content was noticeable on trimming. Sand content was much higher with sandy bands encountered. The sandy bands are not reflected in the particle size distributions discussed in Chapter 6.

Figure 114: Initial trimming of a sample from block

UMB can be described as a difficult material to accurately trim. The material is ‘hard’ and sharp tools struggle to carve the surface. The apparent structure gave no indication to when a fracture will occur. Even careful trimming was found to lead to a failure due to, for example, a small pocket of loose material being at the centre of the specimen. The best tool for trimming this material was a new Stanley knife blade but even with this tool the success rate of getting a sample ready to be placed in the apparatus was around 10%. One added complication when trimming was allowing for bender elements. These required slots to be made. For UMB this proved unsuccessful without unwanted chips being formed on the surface. This was believed to be the cause of a longer bedding period when a shearing load

was applied to the sample. This occurred as particles likely rearranged and localised failures occurred around the bender element slot.

Figure 115(a-d): During trimming of samples, near completion. a) London Clay Unit B2 100mm dia. b) Lambeth Group UMB 38mm dia. c) London Clay Unit A2 100mm dia. d) UMB 38mm dia.

5.7.2. Preparation of the triaxial apparatus

To ensure perfect saturation and dissolution of air bubbles trapped in the drainage lines, the cell pressure was kept at 800kPa for at least 48 hours before use and between experiments. The pressure was kept higher than necessary as a final leak test. Leaks were commonly found, particularly in early testing. Leaks were dealt with according to the severity. If a leak was minor and did not affect the test results significantly then it was managed by refilling the pressure/volume controllers when needed.

Leak testing became the most important aspect of preparation. The author cannot stress enough how important it is to test all the apparatus at max pressures for extended periods. Sealants were frequently needed. Particularly on brand new equipment delivered from VJ Tech which could not maintain a pressure higher than 200kPa without leaking.

Porous discs that sat between the caps and the specimens were placed in a vacuum chamber with de-aired water to ensure no air remained in the system.

5.7.3. Preparation of the samples

Once the correct shape of the sample had been accomplished through trimming, it was weighed and the dimensions were carefully measured using callipers. The porous discs that form part of the top and bottom caps were first oven baked to ensure no water remained in the discs before being deaired by saturating in deaired water in a vacuum for 24 hours.

Filter papers were placed around the specimen's circumference and tops to facilitate drainage and help with initial saturation. Strips of filter paper running the length of the sample were kept distant from where the mid-pore pressure transducer would be placed. These were dampened before placing and once placed were immediately sealed in by closing the membrane and platens. A small amount of swelling was expected but a dry filter paper would have the reverse effect and maintaining position of the paper on the sample would have been difficult. The LVDT's were then mounted to the membrane using glue and accuracy of placement guaranteed using a permanent marker. This is seen for the stress path cell in Figure 116.

The mounting of the bender elements and mid height pore pressure probe was achieved using the following methodology. First a small hole was created in the membrane using a sharp tip, then this hole was stretched carefully open using two small palette knives. A slot in the specimen was then created using a screwdriver. The mid-height pore pressure transducer could be pushed into this hole with some remoulded material on the tip. Some O-rings were

pre-placed on the transducer so that when the membrane was carefully stretched over the transducer the O-rings would seal the membrane around the transducer. Lsx hydraulic sealant was then placed over the O-rings and transducer to ensure any small leaks are sealed. The bender elements were similarly installed, except much greater care was needed to not rip the membrane or disturb the specimen. The sample could now have a cell pressure higher than the expected effective pressure applied following Gasparre (2005).

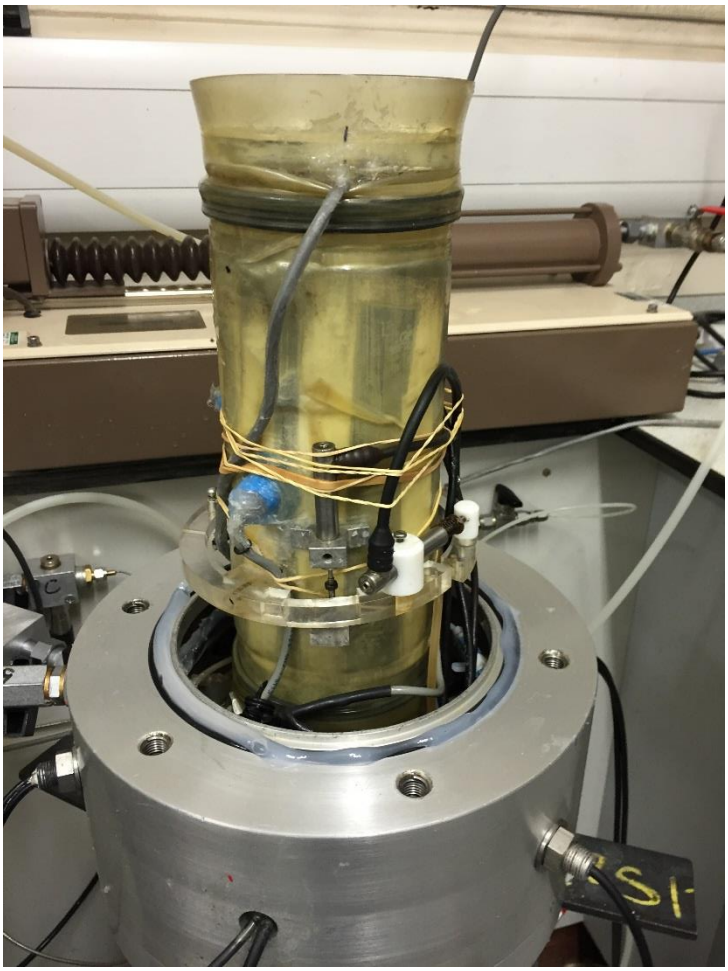

Figure 116: Mounted local instrumentation in the stress path cell

Pore pressures were now allowed to stabilise for 24 hours and then checked by applying a small additional cell pressure. This was achieved by measuring the change of pore pressure divided by the change of radial stress which should show values close to 1 and show convergence of the mid and base pore pressure transducers (GDS, 2013). For the 38mm diameter samples, an external pressure transducer was used. This transducer was calibrated to be most accurate in the expected back pressure range.

Unfortunately, as with the Rowe cell, saturation for some samples was difficult and, in these cases, the same procedure was followed as described in 5.6.

Figure 117: Sample pressurised in the 38mm diameter triaxial cell and ready for testing

5.7.4. Test procedures

Three materials were tested in the triaxial or stress path apparatus. Tests which start from insitu stress to investigate elastic parameters, yielding stresses and small strain behaviour on 100mm and 38mm dia. samples were intended to be sheared in both drained and undrained cases; however, due to complications, this was not possible. Overall, drained compression from insitu stress was the only successful test and the procedure is given below.

Samples from four principal depths were saturated following the same procedure as for the Rowe Cell in 5.6 except the sample was not loaded beyond insitu effective stress, see Figure 118 for the applied stress path. Once at their relative in-situ stresses, given in Table 10, shearing the samples to failure commenced; drained at a shear speed controlled using the load frame of between 0.00001-0.00004mm/min; however, due to time restrictions the specimens were not sheared drained to failure and once the critical small strain data was obtained, specimens were then sheared undrained to failure. The data for the specimens shearing undrained to failure are not presented in this thesis.

The creep rate was monitored using the LVDT and had to fall below 0.000025mm/min before testing begun. Note: This rate falls below the resolution of the LVDT and so the creep rate needed to fall below 0.036mm over 24 hours and once reached the specimen was further held

for another 24 hours. The elastic parameters of the soil and the limits of the elastic kinematic surfaces were measured in each test where possible from in situ stress. The voltages of the internal transducers were re-zeroed before starting each stress path, in order to have the maximum accuracy of readings. The shearing was controlled by the constant strain rate pump.

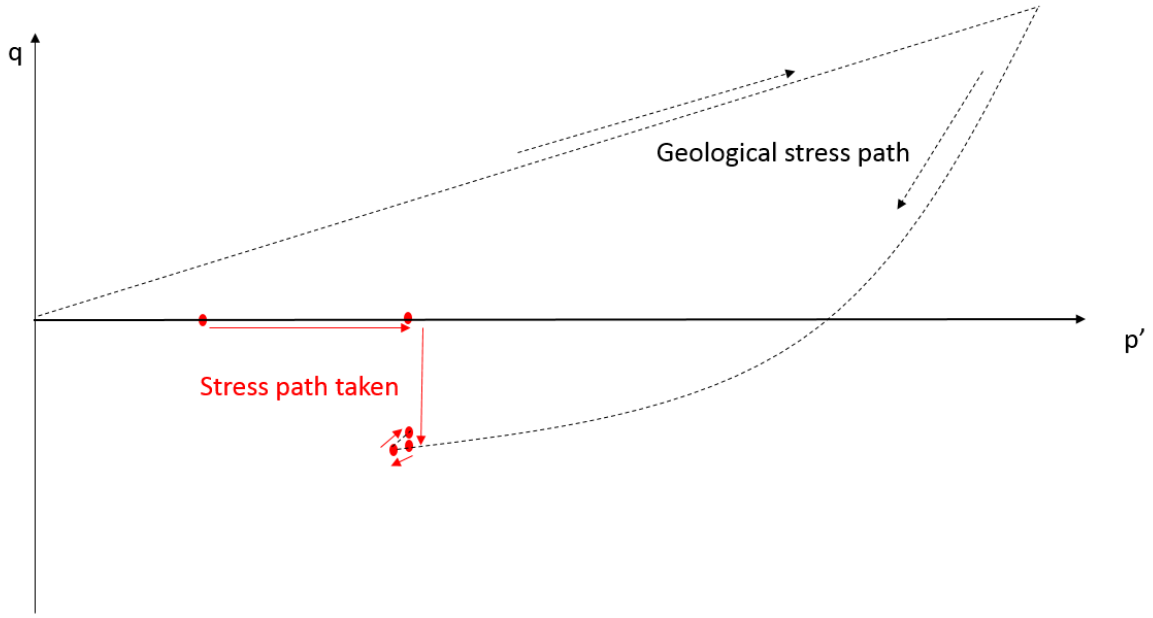

Figure 118: Stress path applied to triaxial specimens to obtain insitu conditions

Material	K0 estimation based on site data	K0 Used	Total stress reduction (kPa)	Measured pore pressure pre-excavation (kPa)	p' (based on K0 estimate) (kPa)	p' used (kPa)	q estimated (kPa)	q used (kPa)	Estimated pre-consolidation pressure (kPa)
UMB	1.05	1.1	723	153	594	600	-36	-60	4000
A2(2)	1.025	1.1	530	132	407	430	-13	-40	3300
A2(1)	0.975	1.1	670	125	534	580	17	-55	3300
B (2)	1.25	1.2	280	70	257	240	-56	-40	1500

Table 10: Estimates of insitu soil stresses prior to excavation and stresses applied to triaxial samples of requiste materials to represent the insitu stress

Stress probes *were to be* performed on samples, which were equipped with local axial and radial LVDTs and bender elements. Due to laboratory complications this did not happen.

5.7.5. Temperature effects

Temperature fluctuations heavily influence the results when looking at very small strains. To counteract this, the laboratory is temperature controlled within 1 degree Celsius and the apparatus is wrapped in an aluminium foil blanket to minimise temperature variations experienced. The temperature variation was monitored using thermometers and up to 0.1 degrees Celsius variation was considered successful. However, a long list of complications occurred which resulted in variations in temperature of +/- 5 degrees for one test.

The first measure of temperature control is the environment the tests took place. The 'temperature-controlled room' was controlled using air conditioning. No windows exist in this room and ventilation is controlled. Unfortunately, this system broke during testing and it took over 6 months to replace. During this time small strain testing was abandoned. This time coincided with summer which caused large temperature variations.

The second measure was a blanket wrapped around the cell, Figure 119. The effect of the blanket was not known as due to laboratory compilations internal thermometers were not installed into any of the apparatus described. However, thermometers were placed next to the apparatus underneath the thermal blanket. Unfortunately, temperature corrections could not accurately be achieved because of the lag in heat exchange between the air and the water in the apparatus. Therefore, the temperature results are averaged for every 60 seconds to remove small fluctuations which skew the results at very small strains.

Figure 119: Wrapping around the cell to regulate temperatures

6. SOIL DESCRIPTIONS & ONE-DIMENSIONAL TESTING

6.1. Introduction

In this chapter, results from soil characterisation tests are presented and then compared to results from literature specific to the formation each sample was taken from; this gives context to the block samples collected across London. Following on from soil characterisation, the structure is examined at a microscopic scale using a scanning electron microscope. The images created enable the author to correlate the characteristics of the soil to its microstructure. Next, one-dimensional tests on intact and reconstituted samples in oedometer and Rowe cell apparatus are presented and discussed with the intrinsic and intact characteristics examined. This behaviour is then given engineering relevance through comparisons with literature.

6.2. Atterberg Limits

Atterberg limits were conducted in compliance with BS1377-2: 1990 and are shown in Table 11. The data collected extensively by Mott Macdonald Ltd, Crossrail and many sub-contractors at the sites where the samples were collected are compared to measured data on the block samples obtained by The University of Southampton. It should be noted that only a small amount of material obtained from block samples was tested at The University of Southampton and the greater range of values obtained from large numbers of borehole samples is to be expected. Data taken from Crossrail (Black, 2009) is not exclusively taken from each test site and large bodies of data are grouped together. In the case of the Atterberg limits stated in Table 11, data are taken from Royal Oak Portal to Liverpool Street Station where Liverpool Street Station is within one mile of both Moorgate and Blomfield box. For Figures 120 to 126, data shown is for all Crossrail sites across London and so a wide range of values are expected.

Results from testing materials taken from block samples at The University of Southampton are shown as red dots on each Figure. When compared to data from Crossrail the results from The University of Southampton fall within the ranges found by Black (2009). Furthermore, each of the London Clay units retrieved from the sites as blocks are similar in their plasticity, which is high. The sampled UMB when compared to Crossrail data are clayey and consequently has higher plasticity than much of the strata as described in older text (Ellison, et al., 2004). The liquid limit found for UMB in the laboratory was variable but averaged at

the higher end of data presented by Black (2009). Bulk densities sit on the higher end of the suggested values for London Clay but are around the median for all materials.

Overall, London Clay varies much less than UMB, even over its differing lithological units; this is likely to be due to the greater uniformity of the clay resulting from a marine depositional environment.

Table 11: Atterberg limits

Limit	LC Unit B2 at VSU	LC Unit A2(low)	LC Unit A2(upp)	UMB
Plastic Limit	22-32% (Mott MacDonald Limited, 2008)	18-28% (Black, 2009)	21-32% (Black, 2009)	15-35% (Black, 2009)
	28-29% (measured)	25% (measured)	27-28% (measured)	26-27% (measured)
Liquid Limit	70-80% (Mott MacDonald Limited, 2008)	50-70% (Black, 2009)	60-87% (Black, 2009)	26-80% (Black, 2009)
	70-75% (measured)	66-70% (measured)	70-71% (measured)	55-68% (measured)
Plasticity Index	40-55% (Mott MacDonald Limited, 2008) – decreasing with depth	22-58% (Black, 2009)	23-57% (Black, 2009)	25-50% (Black, 2009)
	Measured average: 44%	Measured average: 43%	Measured average: 43%	Measured average: 39%

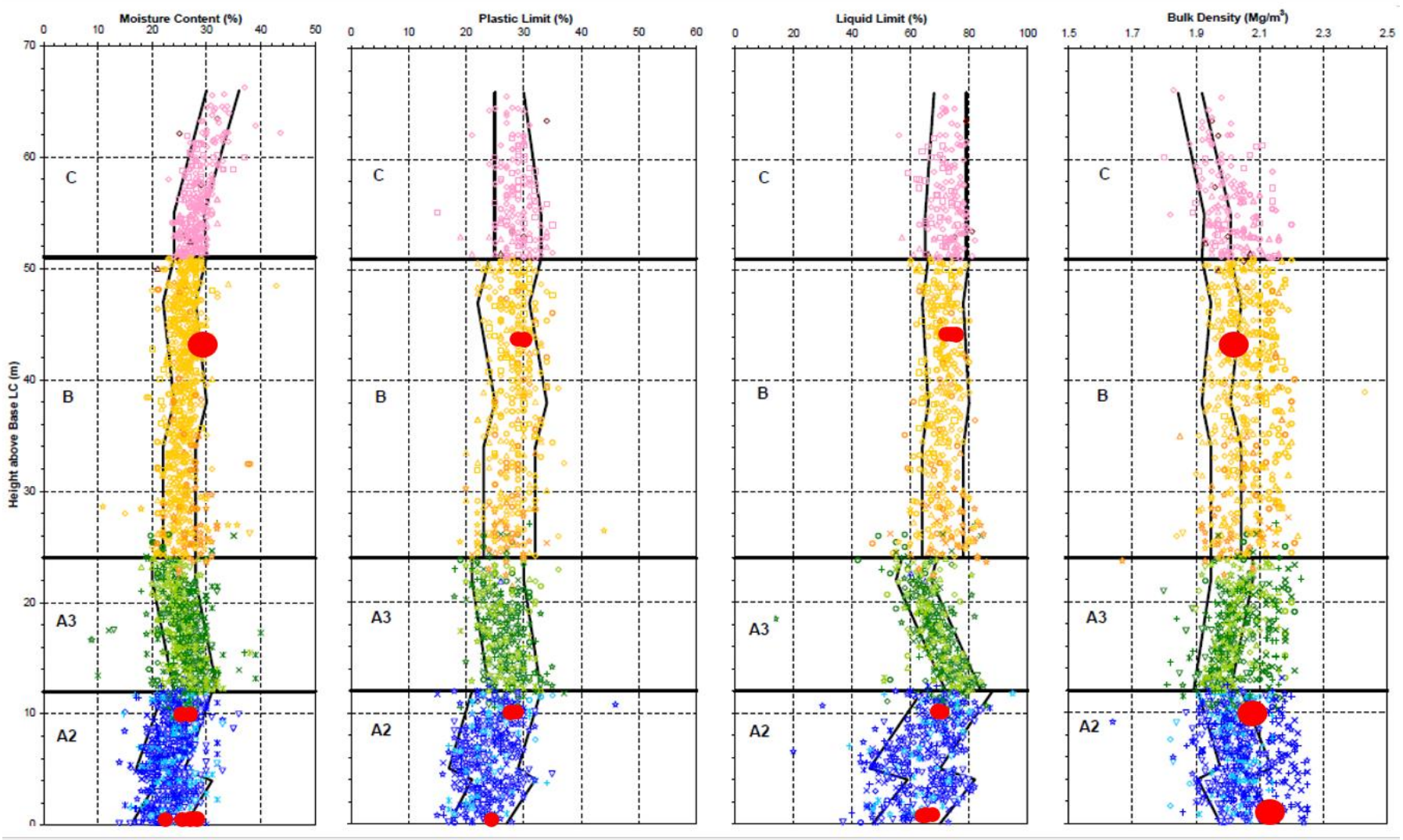

Figure 120: Moisture content, plastic limit, liquid limit and bulk density results from block samples in the laboratory, superimposed using red dots onto Crossrail data (Black, 2009) –London Clay

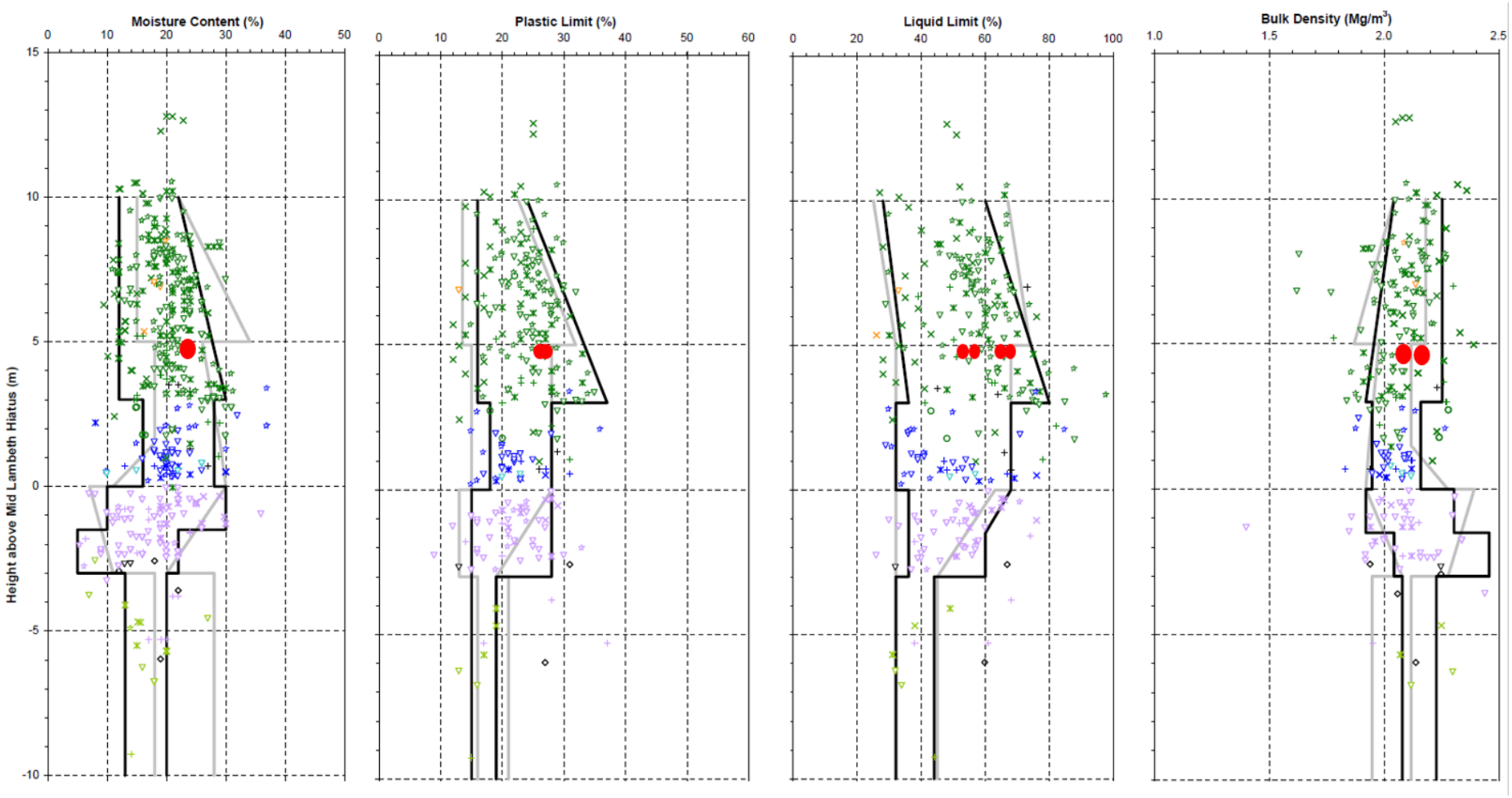

Figure 121: Moisture content, plastic limit, liquid limit and bulk density results from block samples in the laboratory, superimposed using red dots onto Crossrail data (Black, 2009) - UMB

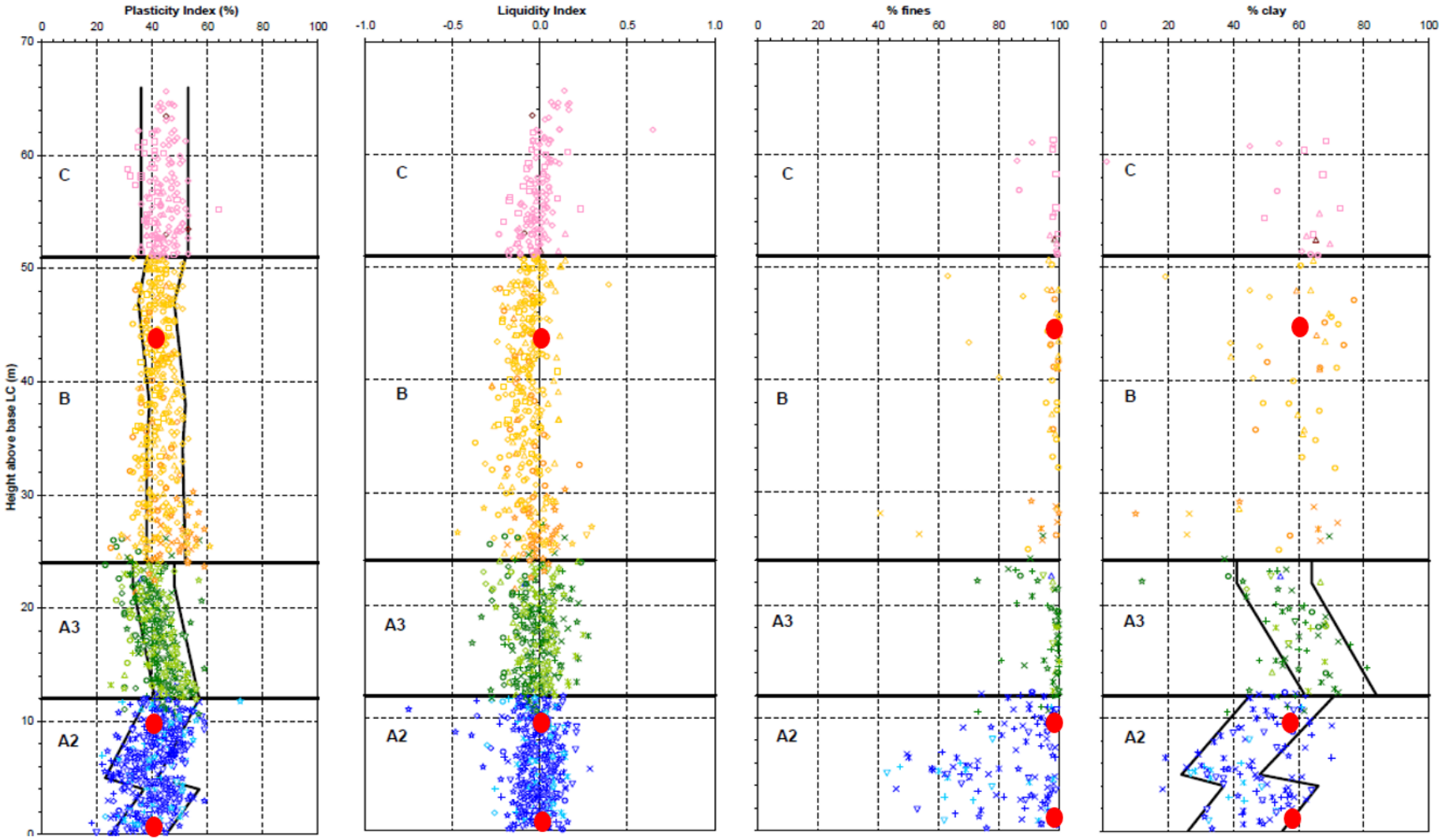

Figure 122: Plasticity Index, liquidity index, % fines and % clay ($_{hydrometer}$) from block samples in the laboratory, superimposed with red dots onto Crossrail data (Black, 2009) – London Clay

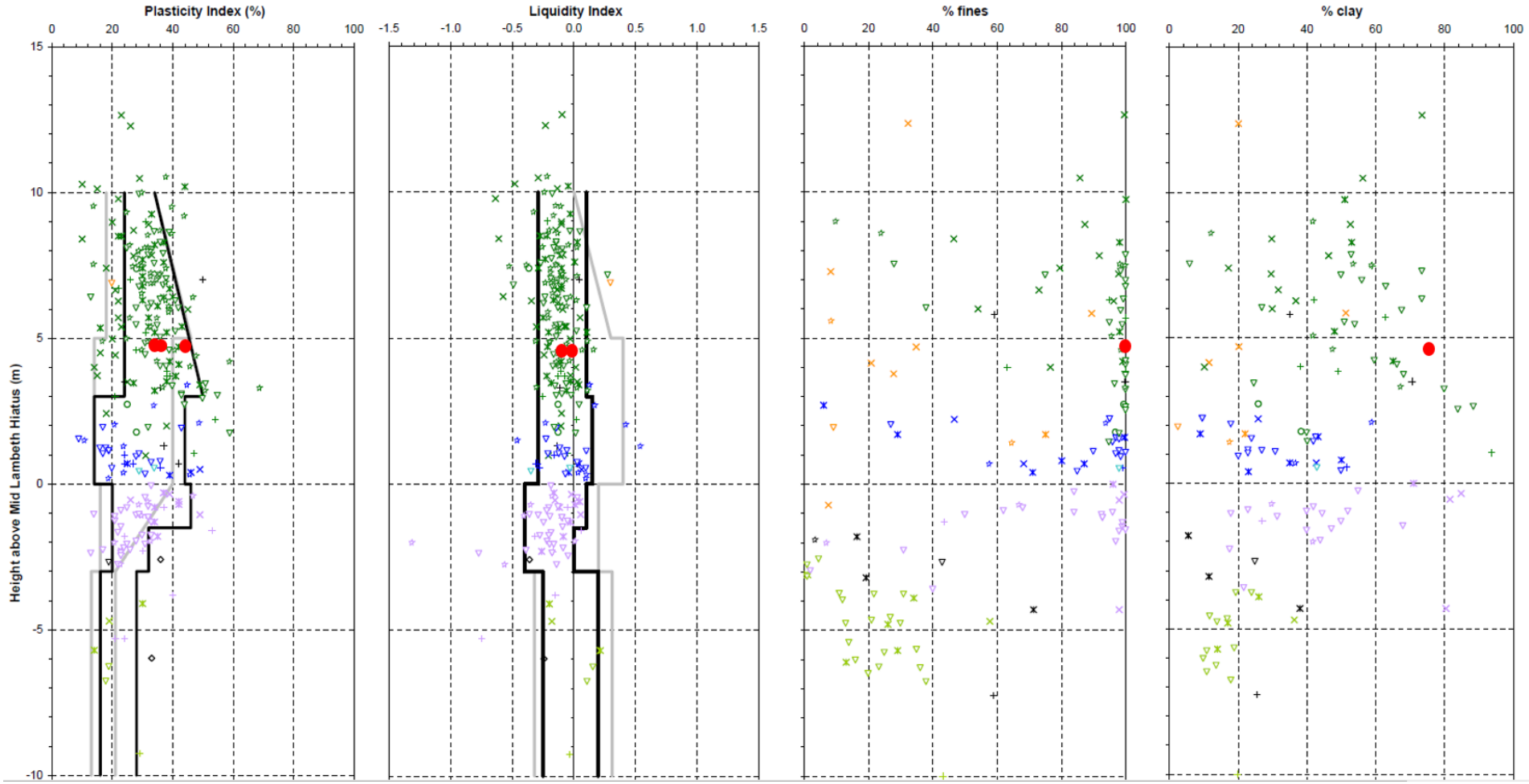

Figure 123: Plasticity Index, liquidity index, % fines and % clay (hydrometer) from block samples in the laboratory superimposed with red dots onto Crossrail data (Black, 2009) - UMB

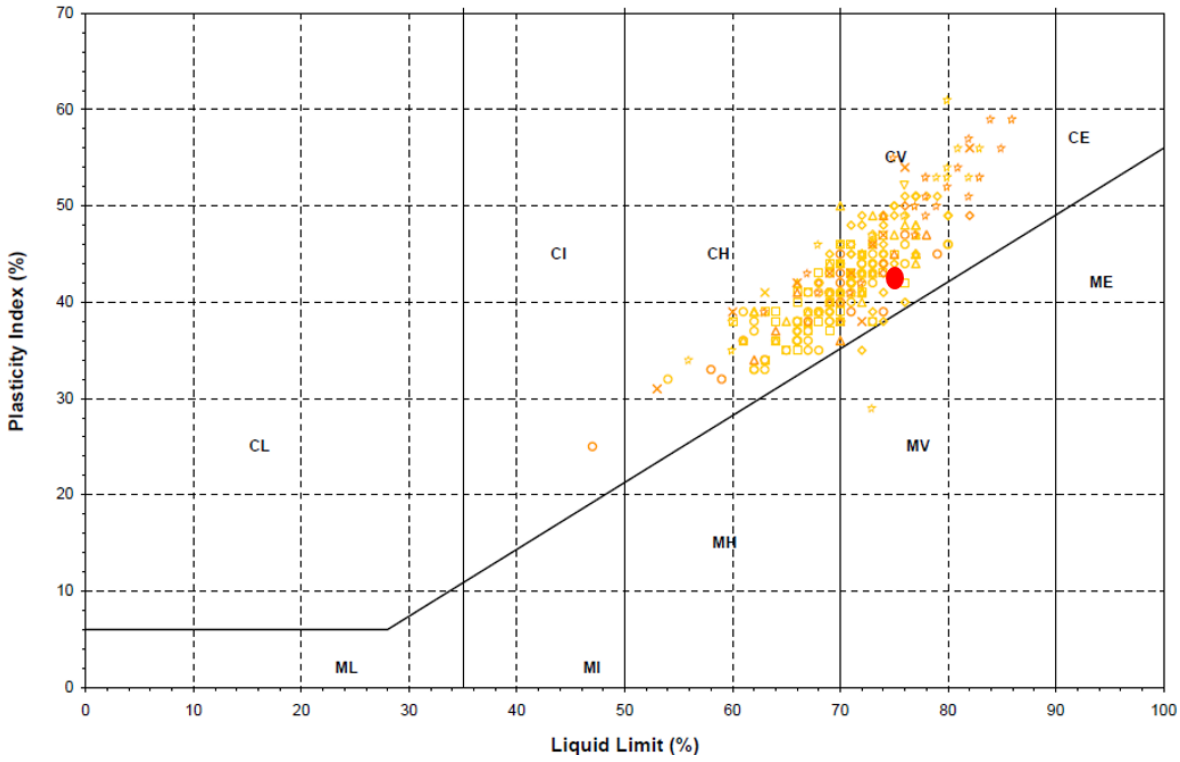

Figure 124: PI vs LL Unit B from block samples in the laboratory - Red dot is superimposed onto Crossrail data (Black, 2009)

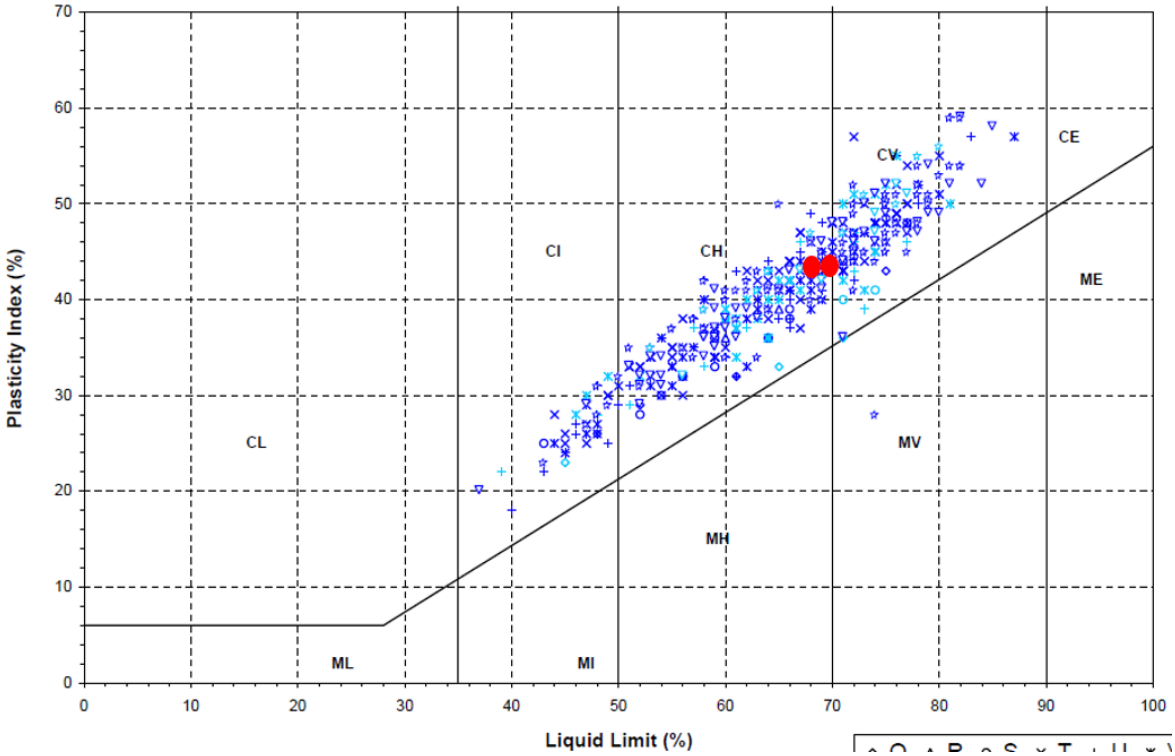

Figure 125: PI vs LL Unit A2 from block samples in the laboratory - Red dots are superimposed onto Crossrail data (Black, 2009)

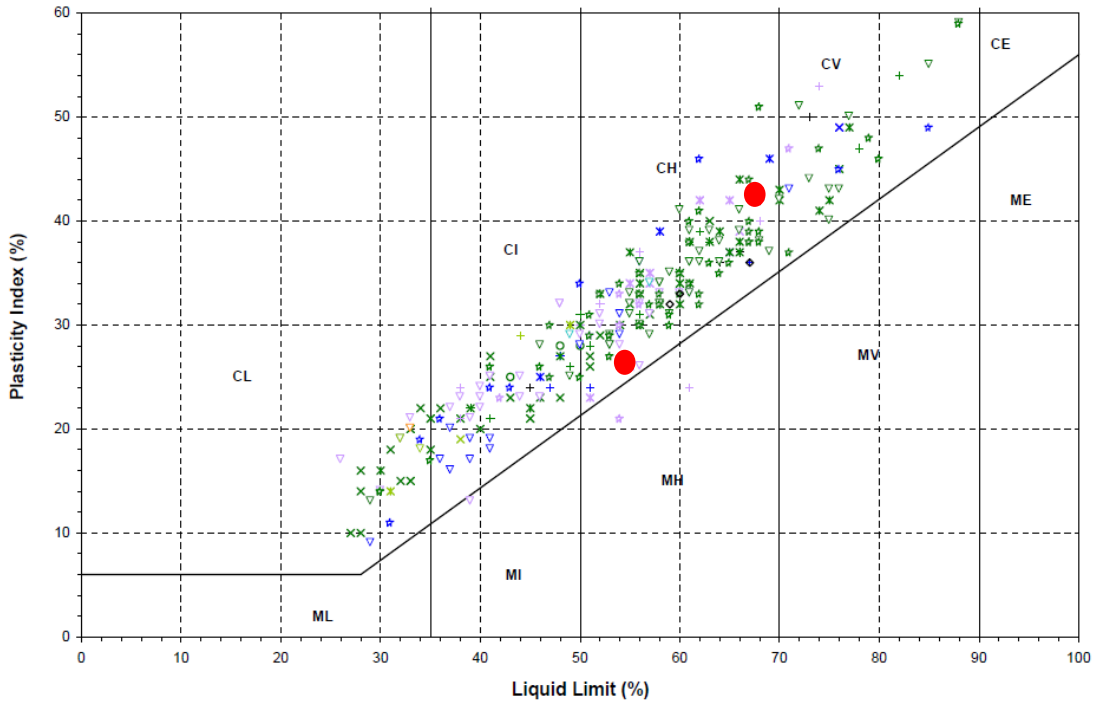

Figure 126: PI vs LL UMB from block samples in the laboratory - Red dots are superimposed onto Crossrail data (Black, 2009)

6.3. Scanning Electron Microscope (SEM)

SEM was conducted at National Oceanography Centre Southampton (NOCS) under the guidance of Dr Richard Pearce.

6.3.1. London Clay Unit A2

In Figures 127 (a) – (f) images from small samples obtained from the excavated blocks at both depths with different magnification 200-2000x are shown. At low magnification the particles appear to be well packed with consistent orientation for each sample. As magnification increases, strands of what appears to be bacteria become apparent on the upper sampling block. The bacteria would likely have been transferred to the sample by a member of the block sampling team sent to site.

Both samples have silt particles and minerals such as feldspar visible. Each sample has a disturbed fabric; more so with the sample from the lower part of A2 which may be an effect of preparation. Unfortunately, orientation between samples was not consistent due to a misunderstanding at preparation stage but this has given an opportunity to compare different orientations in a very similar material. What was clear regardless of orientation, was that clay platelets are aligned as would be expected from being heavily over-consolidated.

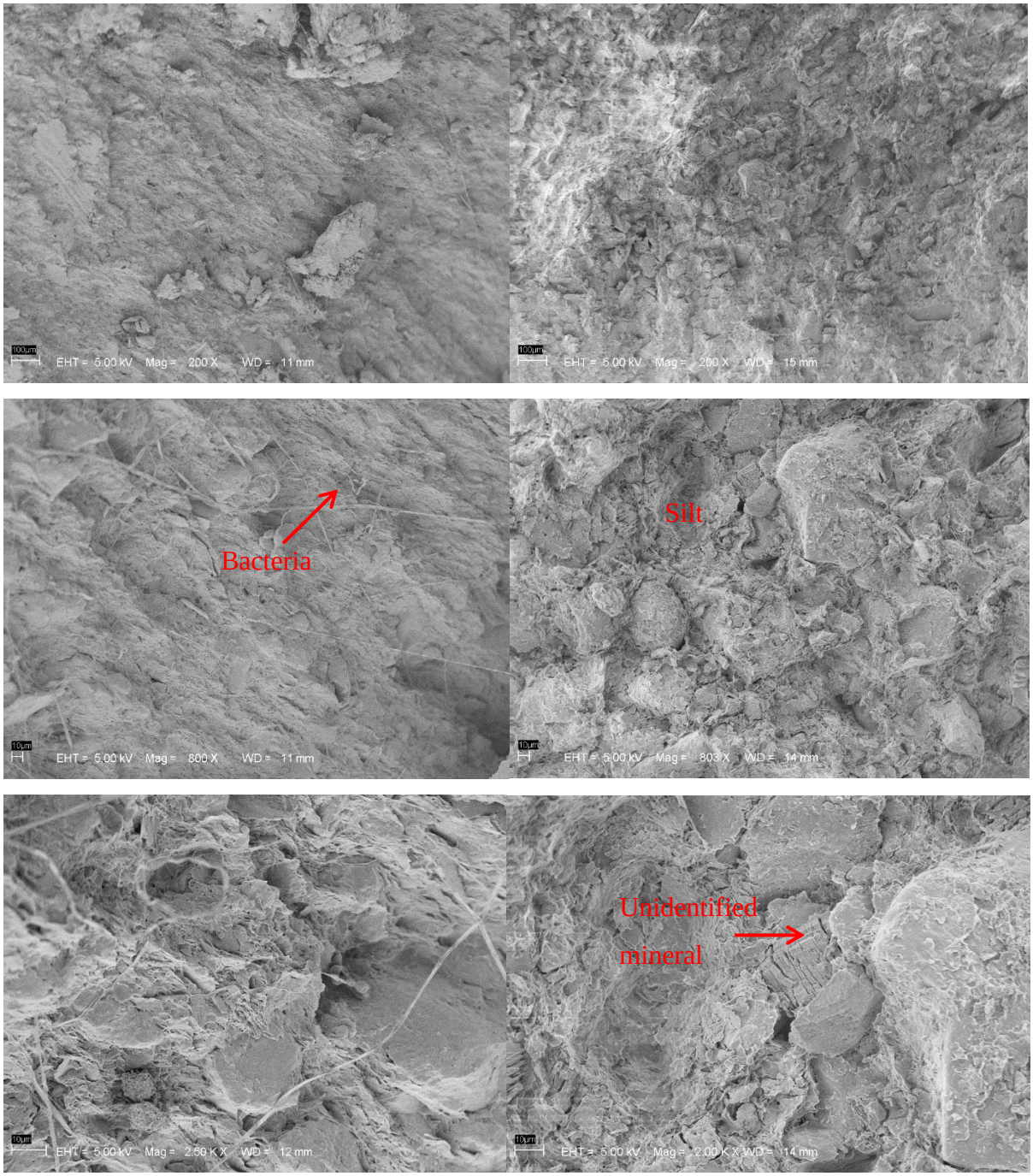

Figure 127(a,b,c,d,e,f)): London Clay Unit A2: taken from the upper sampling level on the left and the lower sampling level on the right - magnification 200-2k

In Figures 127 (e)-(f), at 2.5K magnification, the fabric has inconsistencies with metal cations, bacteria, and feldspar visible at varying orientation. In Figures 128 (a)-(f), higher magnification confirms the presence of pyrite and bacteria. While 15k magnification shows orientated particles, which have edge-face contacts and the majority are rough. There is also distortion to the layering and an open clay structure. This may be explained by unloading and shear movements in the soil caused by excavation; or most likely by sample preparation.

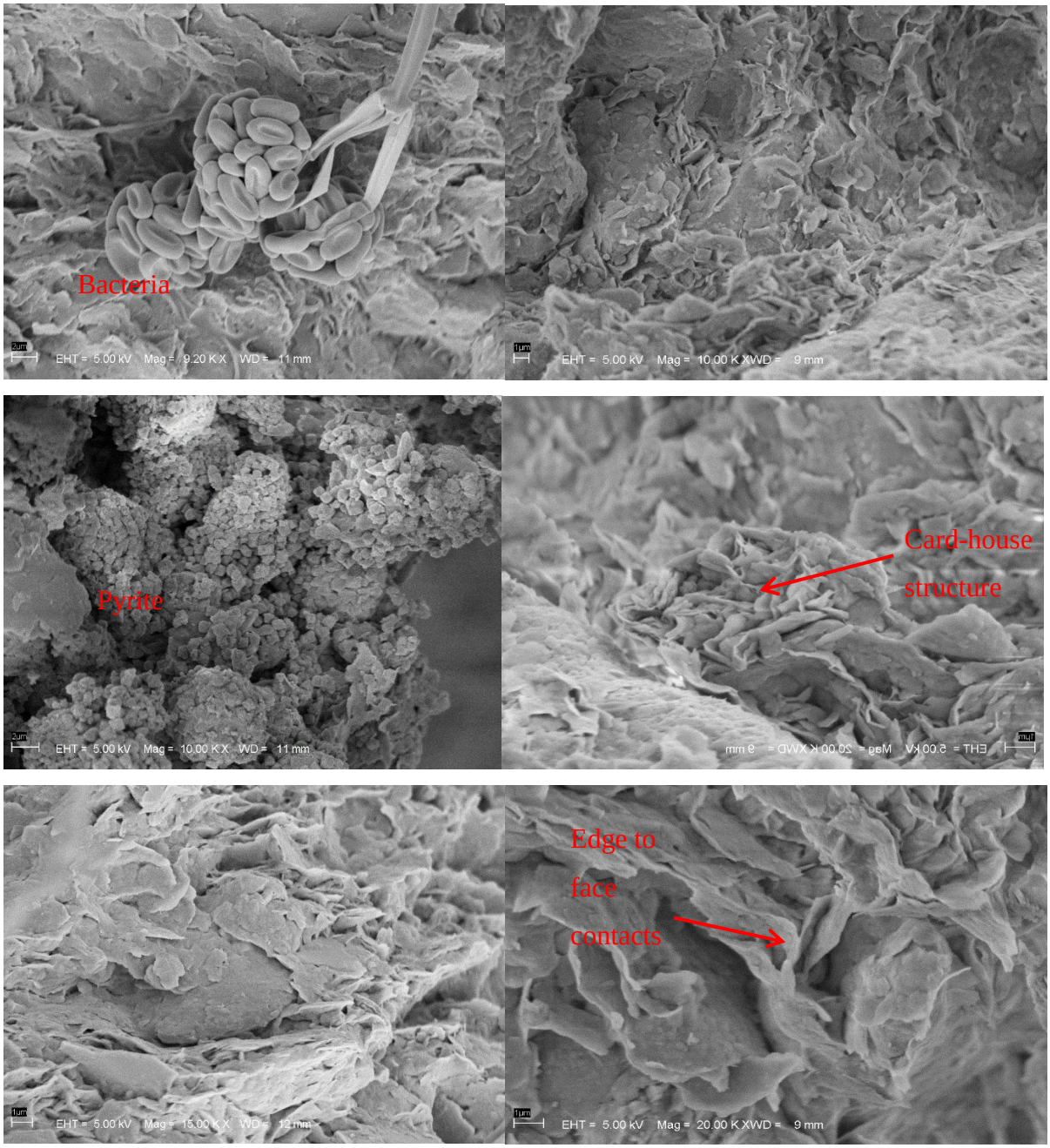

Figure 128 (a,b,c,d,e,f): London Clay Unit A2: taken from the upper sampling level on the left and the lower sampling level on the right - magnification 10k-20k

6.3.2. London Clay Unit B2

In Figures 129 (a) – (f), at lower magnifications there is a clayey appearance with some silt. The material is much less packed than unit A2 as a structure and orientation is visible at much lower magnification. At 2.5k and 10k magnification the orientation can be seen to be orientating around minerals and has a more consistent ‘card-house’ structure which appears to suggest a shear force; this could be the higher K0 value or could be explained through the ‘undrained’ movement resulting from excavation. Furthermore, as the walls of the excavation compress the ground laterally, it is possible the clay plates could be forced over each other to

form this structure while causing ‘undrained’ heave. On the other hand, this could be the natural deposition of the material. In addition, this lithological unit is thought to have a smaller preconsolidation pressure.

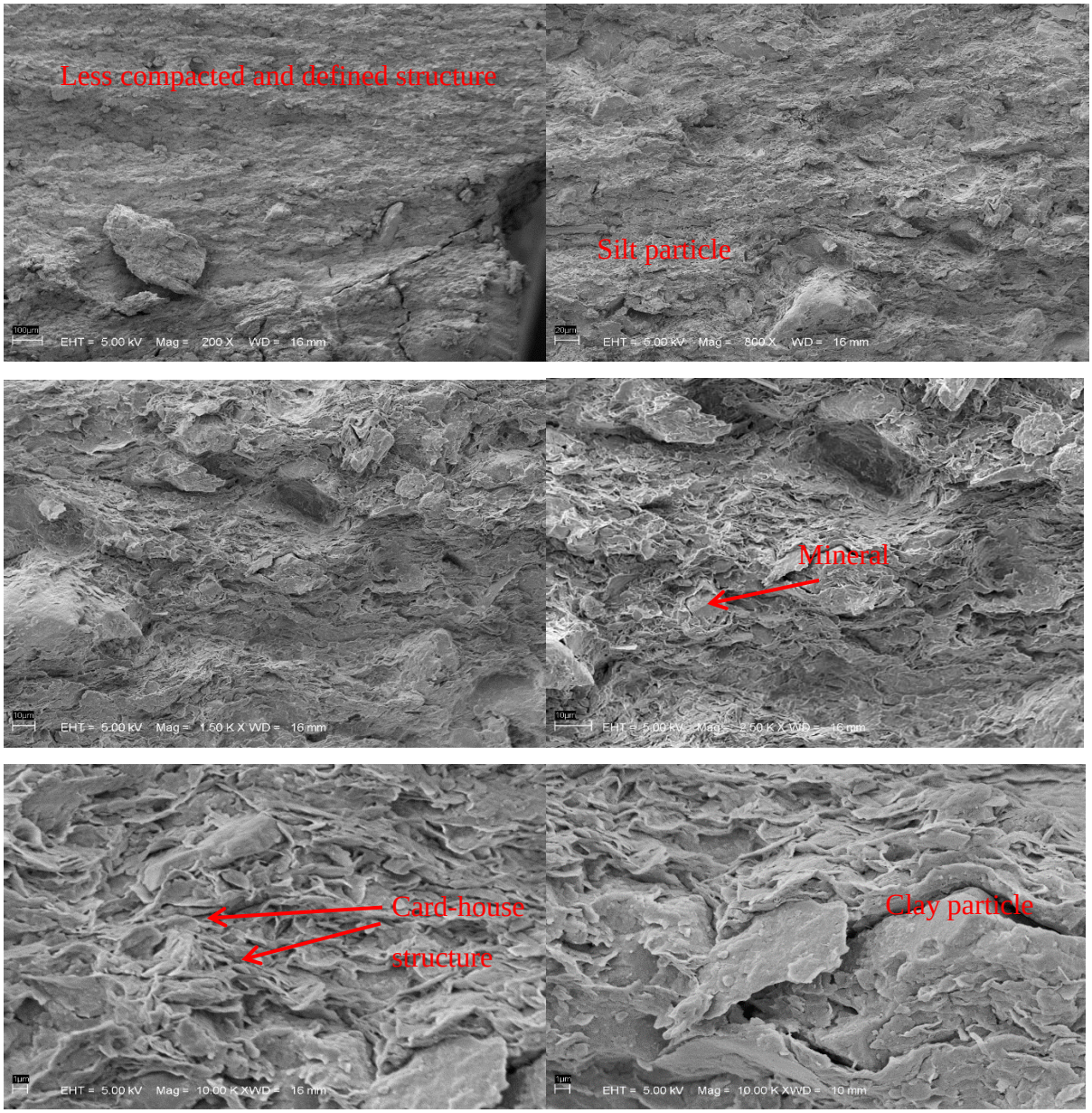

Figure 129 (a,b,c,d,e,f): London Clay Unit B2 magnification 200-20k

6.3.3. Lambeth group (UMB)

In Figures 130 (a) – (f), a very clayey structure is visible at all magnifications with a very dense pack of clay particles. Additionally, there is a strong layering with little lateral distortion when compared to a lot of the London Clay. This may be due to the reduced K_0 value or the higher maximum preconsolidation pressure. Where lateral distortion occurs, particles sit edge to edge which may suggest different rates of same directional displacement;

possibly due to heave. Minerals were not visible in this sample but some feldspar was. The orientation of the sample was not ideal for viewing the structure of the fabric and the imaged 'clayey patches', shown as a large flat surface, were most likely created in sample preparation.

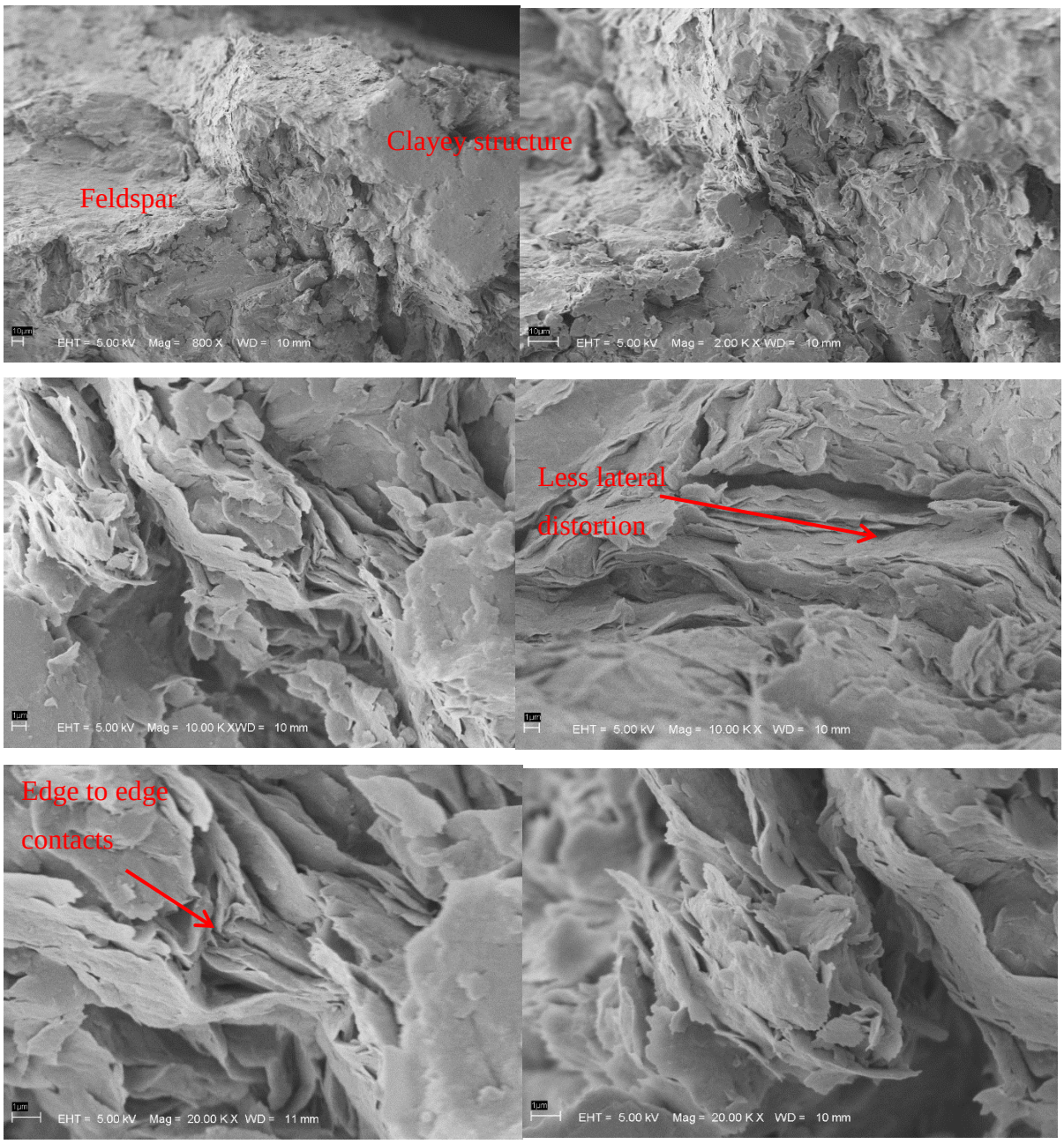

Figure 130 (a,b,c,d,e,f): Lambeth group UMB magnification 800-20k

Overall, SEM work identified some hints that depth effects the clay structure due to stress history and/or shear effects through excavation. The deeper clays were much denser and the London Clay has a greater variation in composition. Unfortunately, due to limitations of time

and experimental procedure, a follow up study taking great care to examine a horizontal orientation vs a vertical orientation has not been possible.

6.4. Clay Mineralogy

6.4.1. X-Ray Diffraction (XRD)

Bulk samples

The preparation process was conducted by Dr Richard Pearce at National Oceanography Centre (NOC) University of Southampton. The samples were initially ground in a tungsten carbide tema mill for approximately 1 minute. Thereafter the powder samples had an internal standard of 25% by weight of corundum added, followed by grinding under isopropanol in a McCrone mill for 8 minutes using corundum beads. Samples were side-loaded, to avoid preferred orientation, and run on a PANalytical X'Pert pro diffractometer machine fitted with a Cu X-ray tube. The machine operating conditions were set at 35kV, 40mA utilising automatic slits and a step size of 0.02º 2θ at 1 second/ step.

Semi-quantitative analysis of the sample was undertaken using a least squares method similar to that used in the Microsoft Excel-based programs RockJock (Eberl, 2003), and FULLPAT (Chipera & Bish, 2002).

Precision values and detection limits for bulk mineral analysis of crystalline materials are generally of the order of ±0.5-2% and for total clay, precision values of ±10-20% (of the amount present) are likely. Minerals quoted as present, but which are close to the detection limit should not be relied upon as an accurate record. Additionally, if standards do not closely match actual minerals there can be a mismatch resulting in errors in quantification. It is likely that the clay standards fall into this category.

In Table 12 the results of the bulk analysis show that UMB has a large proportion of clay with small component minerals such as Feldspar and Quartz. While the units of London Clay have similar constituents in slightly different proportions; this could be due to the similar marine depositional environment.

Table 12: XRD bulk analysis of samples. All values shown in %

Sample (all taken from block samples)	Mineral								
	Calcite (CaCO3)	Dolomite	Goethite	K-Feldspar	Plagioclase Feldspar	Pyrite (FeS2)	Quartz (SiO2)	Total Clay	Total Sum
Lambeth group UMB	0.2	0.8	3.5	0.1	2.3	0.2	10.0	83.0	100.0
London Clay Unit A2 (upper sampling)	0.0	0.8	0.0	2.5	4.2	0.8	20.9	70.8	100.0
London Clay Unit A2 (lower sampling)	0.0	1.5	0.0	2.5	3.6	0.8	26.4	65.2	100.0
London Clay Unit B2	0.0	1.6	0.0	3.0	4.1	0.8	23.6	66.9	100.0

Clay samples

The <2μm clay mineral fraction was separated according to Stokes' Law, and the samples analysed using standard clay techniques after saturation with Mg^{2+} ions. Samples were run as air-dried, ethylene glycolated, and with heated preparations to 375ºC and 550ºC. Saturation with ethylene glycol confirms the presence/ absence of expandable clay phases (e.g. smectite, vermiculite, mixed layer illite/smectites), and heating to 550ºC assists with identification of chlorite and/ or kaolinite. The semi-quantitative analysis method for the clays was based on that detailed by Biscaye (1965), results are presented as closed sum calculations. The machine operating conditions are the same as for the bulk samples.

Smectite peaks at 5 and 6 degrees for ethylene glycolated and air-dried respectively. Illite peaks between 8 and 9 degrees. Kaolinite + Chlorite peak around 12 degrees. Kaolinite peaks around 24.5 degrees and Chlorite peaks around 25.5 degrees.

The results of the XRD clay fraction are given in Table 13, see Appendix for graphs. The tables show similarity between London Clay A2 from the upper and lower sampling. This would be expected from soil from the same unit. Also, UMB has the lowest percentage of smectites (the mineral with highest swell potential) relative to the clay mass but has the highest clay proportion. Some fluvial sediments can undergo diagenesis and 'illite-isation'; this might explain the lower smectite content of the UMB (Pearce, 2014).

Table 13: Clay mineralogy results from XRD testing at NOCS

Sample Name	Clay Mineral				
	Chlorite	Kaolinite	Illite	Smectite	Total Clay
Lambeth group UMB	6.3	16.5	33.8	43.4	100
London Clay Unit A2 (first sampling)	3.5	7.9	26	62.6	100
London Clay Unit A2 (second sampling)	4	8.6	26.8	60.6	100
London Clay Unit B2	5.2	13.3	31.8	49.7	100

6.4.2. Clay Fraction

Tests of clay fraction, were conducted by K4 Soils Laboratories (Watford, UK) using the sedimentation by pipette method (BSI, 1990, Part 2, Section 9.4) and the hydrometer method (BSI, 1990, Part 2, Section 9.5) on samples prepared in accordance with BSI (1990, Part 1, Section 7.3 and 7.4.5). The results are given in Table 14 and the graphs are in Appendix. The results show that the pipette method shows the lowest clay fraction while the XRD gives the highest clay fraction; this was also found by Redshaw (2015). UMB consistently has the highest clay fraction which is unexpected when compared to the data found by Ellison et al. (2004) who found clay fraction to be between 2-50% for UMB. Also, there is little difference between any of the London Clay units.

The data here sit within the bounds of the data provided by Crossrail. For UMB, Crossrail samples were between 15 and 70% clay fraction but the method for determining the clay fraction was mixed and it may be higher had samples consistently been analysed with XRD.

In Figures 131-133, data from K4 soils are superimposed onto Crossrail samples. What is found is that UMB sampled in blocks from Moorgate is very clayey and sits high on the particle size plots. In fact, it sits beyond the envelopes derived from results over Crossrail route sections A to H. As for London Clay, the data sit around the average for particle size and distribution of particle size.

Table 14: A comparison of clay fraction results

Method	Material (Clay fraction/Clay mineral fraction %)			
	LC Unit B	LC Unit A2(1)	LC Unit A2(2)	UMB
Hydrometer	61	59	57	74
Pipette	52	46	47	75
XRD	66.9	65.2	70.8	83.0

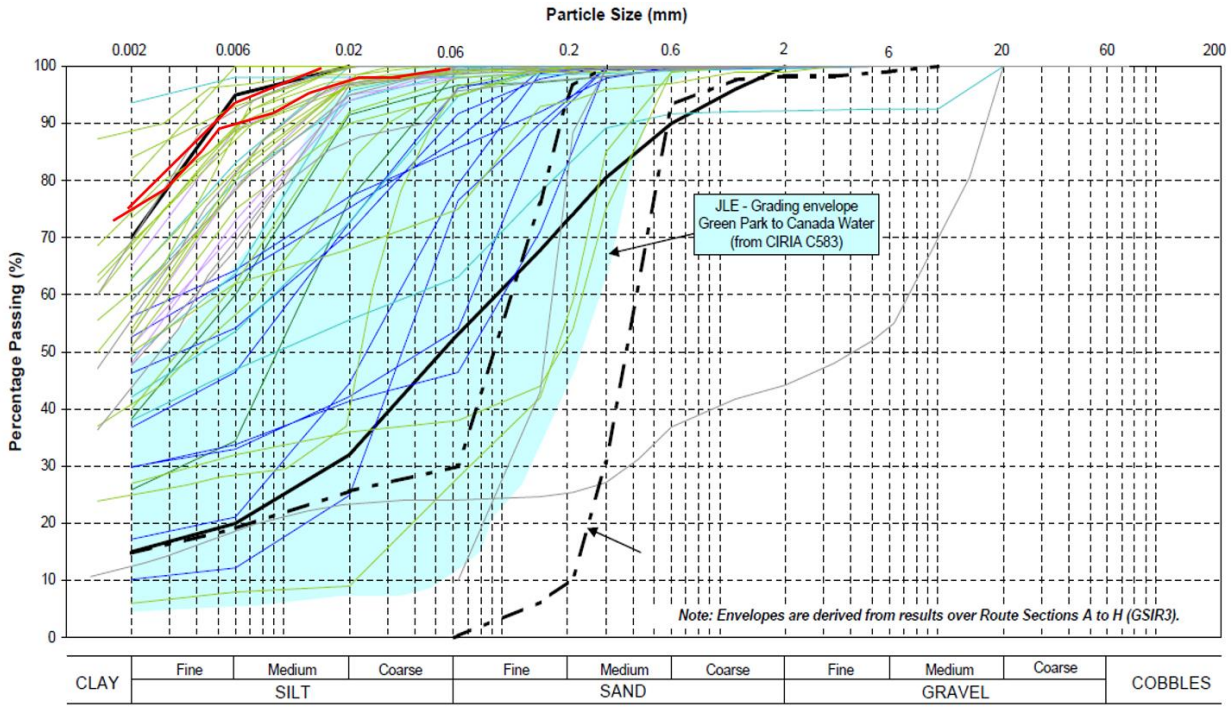

Figure 131: Clay fraction for UMB conducted by K4 soils superimposed onto Crossrail data

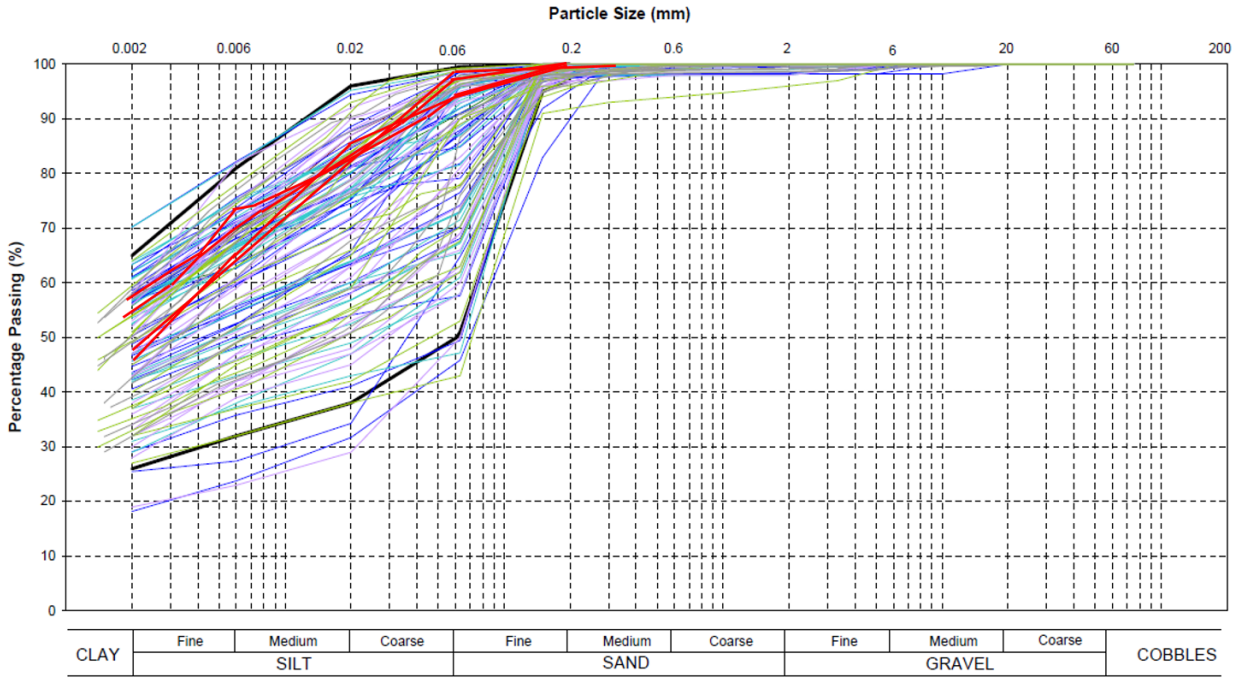

Figure 132: Clay fraction for A2 conducted by K4 soils superimposed onto Crossrail data

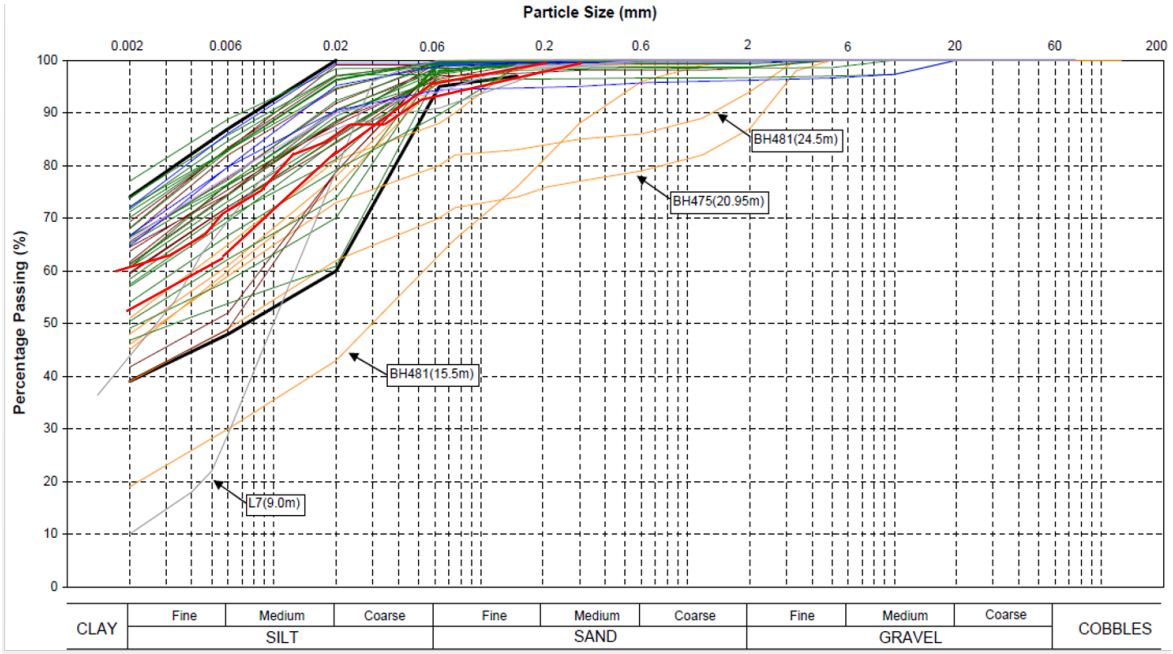

Figure 133: Clay fraction for B2 conducted by K4 soils superimposed onto Crossrail data

6.5. Oedometer testing - Intrinsic behaviour

One dimensional consolidation (oedometer) tests on reconstituted material have been conducted at the University of Southampton and by Fugro in accordance with BS1377: Part 5: 1990. Each test investigated the behaviour in a destructured state due to the nature of creating a reconstituted material. The testing procedures were described in 5.5.2 but were primarily designed to obtain the key parameters: intrinsic compression index c_c^*; intrinsic swelling index c_s^*; and void ratio at 100kPa e_{100}^* , given in Equations 6.1-6.3, which can then be used in conjunction with intact specimen data to analyse the materials using the stress sensitivity framework.

$$c_c^* = e_{100}^* - e_{1000}^* \tag{6.1}$$

$$c_s^* \; or \; c_r^* = e_{100}^{**} - e_{1000}^* \tag{6.2}$$

Where, $e_{1000}^*$is the void ratio at 1000kPa and $e_{100}^{**}$is e_{100}^* on an unload-reload line in void ratio – stress space. The void index, Equation 6.3, can be used to compare material behaviour against the intrinsic and sedimentary compression lines.

$$I_v = e - e_{100}^*/c_c^* \tag{6.3}$$

Most of the tests conducted on reconstituted samples were conducted by Fugro due to limitations on apparatus availability. The initial moisture content of each test used the liquid

limit given in section 5.3 Table 11 as a reference point. All the tests on reconstituted material are shown in Table 15 with void ratio and moisture content shown at the start of the test.

The reconstituted samples OR1-OR8 are broadly similar in their compressive and swelling behaviour, Figures 134 and 135. This would be expected between the units of London Clay as there is similarity in depositional environment and mineralogy. However, UMB was deposited in a terrestrial environment and therefore, is naturally variable and has a different mineral composition; the most striking of which is varying oxidation of the iron causing mottling of UMB. The similarities between UMB and London Clay are: approximately proportional compositions of clay, silt and sand; both are heavily overconsolidated; both have been under very high compressive pressures before erosion, >5MPa (Entwisle, et al., 2013); and both have experienced pedogenic processes. These similarities may be more important in engineering terms than the differences, as the result when destructured is similar compressive and swelling behaviour.

Taking a closer look at the values in Table 15, there is a larger variation between intrinsic parameters for UMB samples OR1, OR2 and OR3 than other materials. This may be because OR1 and OR2 were tests by the author on 75mm diameter samples and OR3-OR8 are conducted by Fugro on 50mm diameter samples. Another explanation may be the different initial moisture content in the specimen, as taken from the trimmings. The effect of testing at a different moisture content would alter the intrinsic properties as found by Burland (1990).

The following equations were used to attain dry density, initial void ratio and specific gravity:

$$\rho_{dry} = 100 * \rho_{Start}/(w_{Trim} + 100) \tag{6.4}$$

$$e_{0,recon} = G_s/\rho_{dry} - 1 \tag{6.5}$$

$$G_s = M_{dry}/V_s \tag{6.6}$$

$$V_s = V_T - V_V \tag{6.7}$$

$$V_V = m_w/\rho_w \tag{6.8}$$

$$V_T = \pi r^2/h_{sample} \tag{6.9}$$

In Figure 136, all materials compress approximately along Burland's intrinsic compression line in void index vs effective stress space which is expected (Burland, 1990) but during the

swell phase on Figure 137, the values of swell are less than that previously measured for London Clay (Gasparre, 2005). Gasparre (2005) found the intrinsic swelling index to be 0.15 for all tested units of London Clay. In void index – effective stress space the tests OR3-OR7 all have a very similar swelling index and plot with the same gradient (Figure 137).

Table 15: Reconstituted samples

Specimen	Material	Initial void ratio e0	Moisture content from initial trimmings	Dry density (Mg/m^3)	G_s	c_c^*	c_s^*	e_{100}
OR1	UMB	2.165	1.04*LL	0.92	2.91	0.53	0.20	1.42
OR2	UMB	2.345	1.27*LL	0.84	2.81	0.5	0.18	1.27
OR3	UMB	2.308	1.20*LL	0.86	2.85	0.42	0.10	1.14
OR4	LC B2	2.711	1.21*LL	0.77	2.87	0.48	0.12	1.31
OR5	LC B2	2.600	1.22*LL	0.77	2.77	0.42		1.22
OR6	LC A2 (UPP)	2.453	1.22*LL	0.80	2.75	0.44	0.09	1.22
OR7	LC A2 (LOW)	2.368	1.24*LL	0.81	2.72	0.44	0.10	1.19
OR8	LC A2 (LOW)	2.373	1.21*LL	0.82	2.75	0.46		1.18

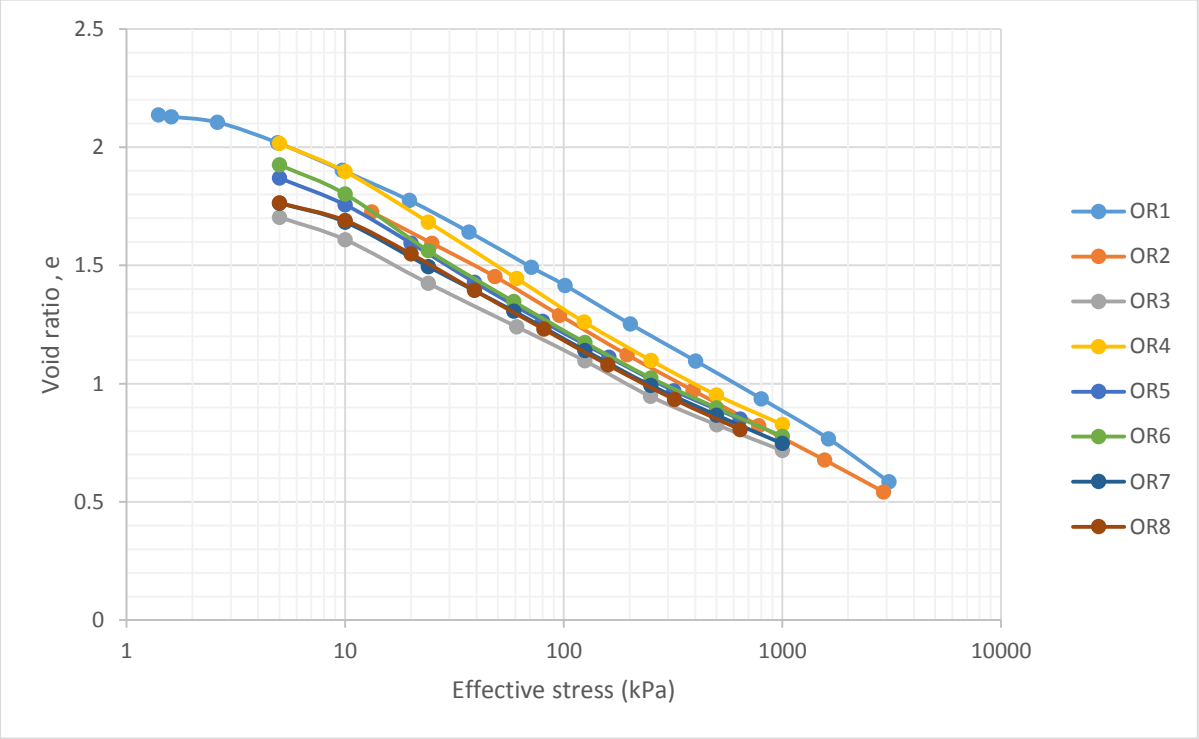

Figure 134: Behavour of reconstituted samples in virgin compression in void ratio effective stress space.

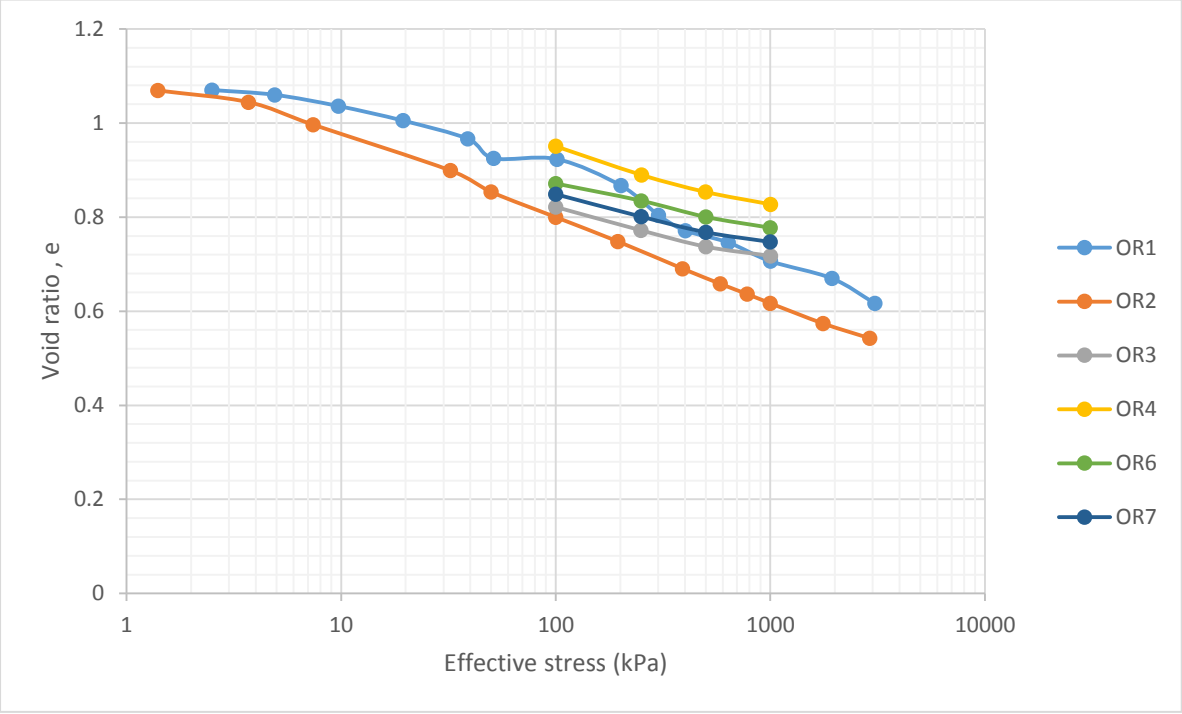

Figure 135: Behaviour in swell of reconstituted samples in void ratio effective stress space.

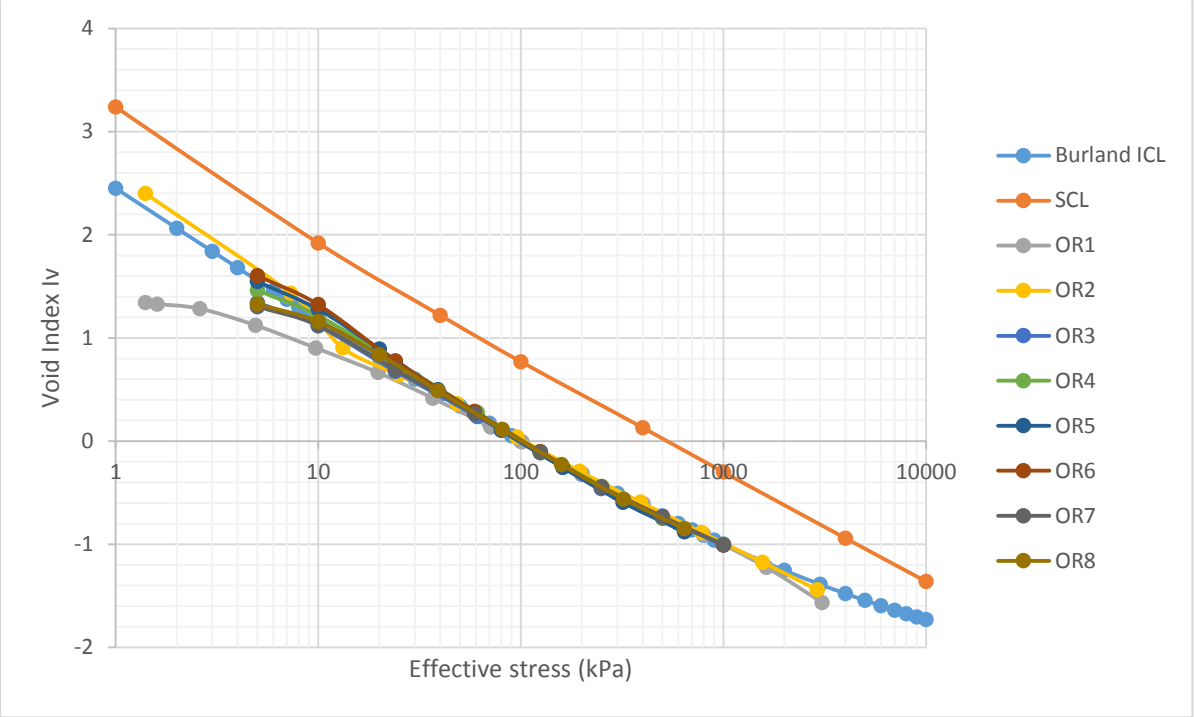

Figure 136: Behavour in compression of reconstituted samples in void index effetive stress space, shown against Burland's ICL (1990)

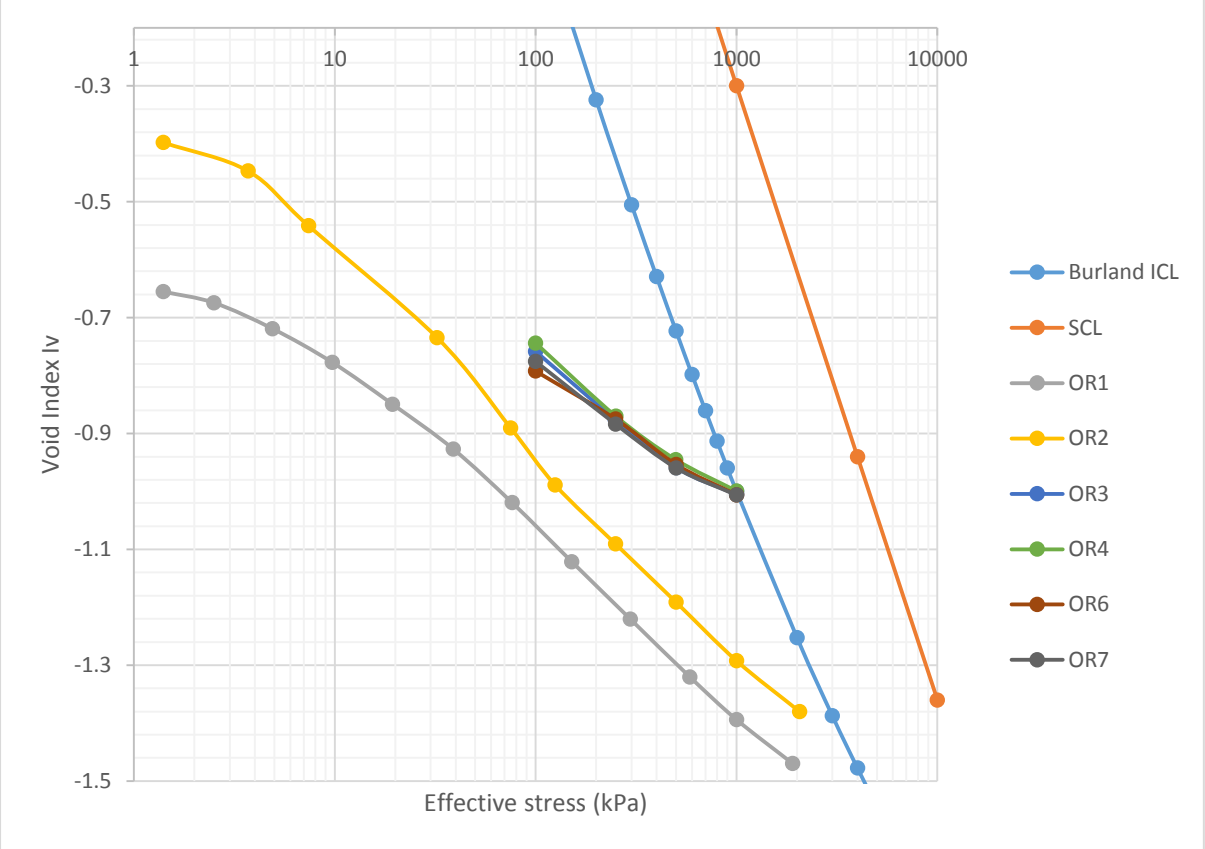

Figure 137: Behavour in swell of reconstituted samples in void index effetive stress space, shown against Burland's ICL (1990)

6.6. Oedometer testing - Intact behaviour

In the Tables and Figures below, the behaviour of intact specimens is shown. A range of sample qualities were tested due to the progressive nature of learning the art of sample preparation in materials that are very difficult to trim. A holistic view is best when judging the quality of each sample and a brief mention to the causes of disturbance to each sample are summarised in Table 16.

The reasons for the difficulty trimming the samples was mainly due to the materials behaving in a brittle manner; particularly if they start to dry a little through exposure and it becomes difficult to trim perfect samples. There was a particular difficulty found with the stiffer materials from greater depth; but, contrary to the experience discussed in Section 5.7.1 one block of Unit B2 London Clay in particular was much more easily trimmed into precise samples. This block didn't crack like the others and firm pressure could be applied to obtain samples.

On the whole, sample quality improved as the author became more experienced at trimming them. The accuracy of void ratio, densities and specific gravity (if using Equation 6.6 where $V_s = V_{sol}$ from Equation 6.13) can all be affected by a slight inaccuracy when weighing each sample at each stage. For example, it is the belief of the author that the moisture content of samples O17, O18 and O19 at the end of the test is incorrect, possibly due to some wet filter paper being included in the weight.

Another inaccuracy in sample volume, caused by chipping, could account for the high variability of specific gravity shown in Table 16. Reconstituted material was not used to fill gaps or chips in samples as tests looked at swell behaviour and destructuring of the samples through wetting pre-test is undesirable. Overall, inaccuracies can be potentially spotted through repeatability of tests. Results are not given to a greater accuracy than three significant figures due to potential accumulation of minor sources of error.

The following Equations were used to calculate bulk density and initial void ratio for intact samples:

$$\rho_{Bulk} = M_{start}/V_{Start} \tag{6.10}$$

$$e_{0,intact} = w_{Start}G_s \tag{6.11}$$

Where, M_{start} is the mass of the sample at the start of the test, $V_{Start}$is the volume of the sample at the start of the test – estimated using the diameter of the ring and three height

measures of the sample, and w_{Start} is the moisture content of the sample – taken from trimmings. It should be noted that the moisture content was later confirmed by drying the specimen after the test and back calculating using volumes. The issue with Equation 6.8 is that initial moisture content from trimmings would range based on numerous factors such as block sample/specimen exposure leading to a wide range initial void ratios; therefore, Equation 6.12 was used to calculate the void ratio at the start of the test.

$$e_{0,intact} = V_{V,start}/V_{Sol} \tag{6.12}$$

$$V_{Sol} = V_{T,Finish} - V_{V,finish} \tag{6.13}$$

$$V_{V,finish} = m_w/\rho_w \tag{6.14}$$

$$V_{V,start} = V_{T,Start} - V_{Sol} \tag{6.15}$$

In Figure 138 it can be seen that a wide range of void ratios are exhibited during testing but the gradients of each line remains similar. The average initial void ratio, calculated using Equation 6.9, for each material are: 0.73, 0.76 and 0.81 for UMB, A2 and B2 respectively. This is expected as UMB is a deeper material and is thought to have experienced higher pressures. However, the difference in void ratios may be higher as chipping in the sample edges creates voids. This will create an artificially high void ratio. As discussed in section 5.5.1 the difficulty in preparing the material is due to its brittle behaviour. This could be due to 'pockets' of weaker material that are the result of a fluvial deposition or low moisture content of the specimen.

The average bulk densities using Equation 6.7 are 2.04, 1.99 and 1.96 Mg/m^3 (3.s.f) for UMB, A2 and B2 respectively. This is to be expected and agrees with the literature; but if reconstituted material had been used to fill in chips then the bulk densities of UMB and A2 would be higher. Finally, the average particle densities, calculated using Equation 6.6, are 2.88, 2.77 and 2.76 for UMB, A2 and B2 respectively. Again, it is the author's belief that these values are slightly altered by sample quality but, the trend agrees with the literature.

The specific gravities of London Clay are plotted against results from Crossrail sites in Figure 139. The results consistently sit above the data and design line from Crossrail (Black, 2009); however, Gasparre, 2005 found specific gravities commonly between 2.75-2.77.

Table 16: Summary table of intact specimen tests

Specimen	Material	Orientation	Sample quality	Initial water content %	'Wetting' pressure (x insitu effective stress kPa)	Initial Bulk Density (Mg/m^3)	Initial void ratio, e0	Specific gravity, Gs	Specific gravity from literature, Gs(ass)
O1	A2 (LOW)	Not known	From offcut; some edge chipping	21	2.6	2.0	0.69	2.70	2.75
O2	A2 (LOW)	Not known	From offcut; some edge chipping	24	3.3	2.0	0.66	2.74	2.75
O3	UMB	Not known	From offcut; some edge chipping	19	4	2.1	0.69	2.90	2.85
O4	UMB	Vertical	U100 tube; a lot of edge chipping	23	5	2.0	0.79	2.86	2.85
O5	UMB	Vertical	U100 tube; a lot of edge chipping	23	5	2.0	0.76	2.88	2.85
O6	UMB	Vertical	U100 tube; some edge chipping	21	5	2.1	0.71	2.93	2.85
O9	B2	Vertical	Block sample; minimal chipping	29	1	2.0	0.76	2.77	2.75
O10	B2	Vertical	Block sample; minimal chipping	29	2.5	1.9	0.80	2.72	2.75
O11	A2 (UPP)	Vertical	Block sample; minimal chipping	27	1.9	2.0	0.78	2.71	2.75
O12	A2 (UPP)	Vertical	Block sample; minimal chipping	27	1.8	2.0	0.78	2.71	2.75
O13	B2	Vertical	Block sample; minimal chipping	29	2.4	1.9	0.76	2.77	2.75
O14	A2 (LOW)	Vertical	Block sample; minimal chipping	27	2.1	2.0	0.77	2.77	2.75
O15	A2 (LOW)	Vertical	Block sample; minimal chipping	30	2.5	1.9	0.84	2.75	2.75
O16	A2 (LOW)	Vertical	Block sample; a lot of chipping	21	3.4	1.9	0.77	2.71	2.75
O17	UMB	Vertical	Block sample; minimal chipping	24	0.1	2.0	0.74	2.93	2.85
O18	UMB	Vertical	Block sample; minimal chipping	24	1	2.0	0.77	2.91	2.85
O19	UMB	Vertical	Block sample; minimal chipping	24	3.1	2.0	0.73	2.78	2.85
O20	B2	Horizontal	Block sample; minimal chipping	29	0	1.9	0.84	2.71	2.75
O21	A2 (LOW)	Vertical	Block sample; minimal chipping	21	1	2.1	0.79	3.03	2.75
O22	A2 (LOW)	Vertical	Block sample; minimal chipping	21	1.1	1.9	0.75	2.79	2.75
O23	B2	Vertical	Block sample; minimal chipping	29	1.8	2.0	0.87	2.83	2.75
O24	A2(LOW)	Vertical	Block sample; Fugro prepared	22	0	2.0	0.73	2.80	2.75
O25	UMB	Vertical	Block sample; Fugro prepared	21	0	2.1	0.67	2.84	2.85

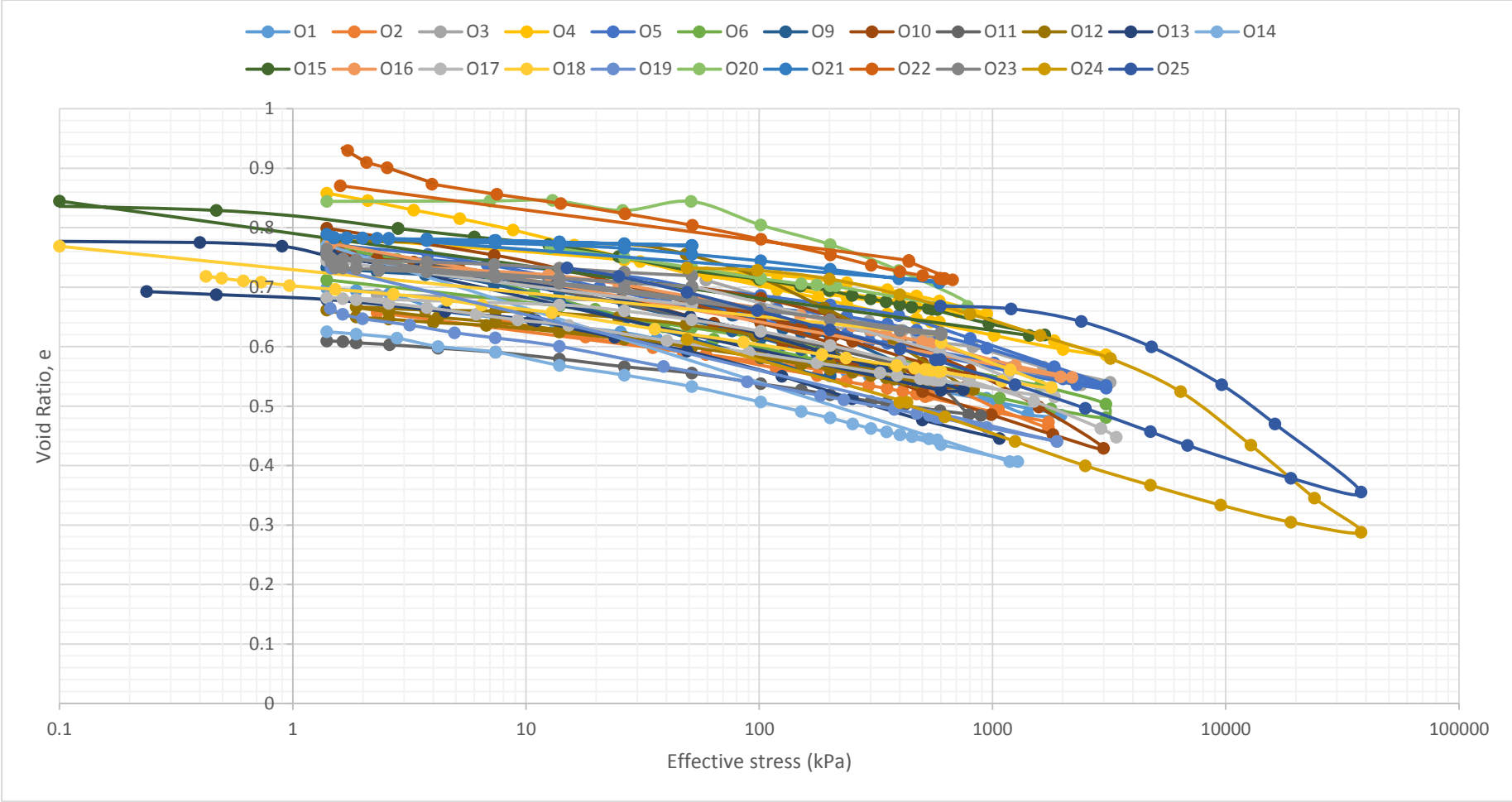

Figure 138: All intact specimens plotted in void ratio vs effective stress space

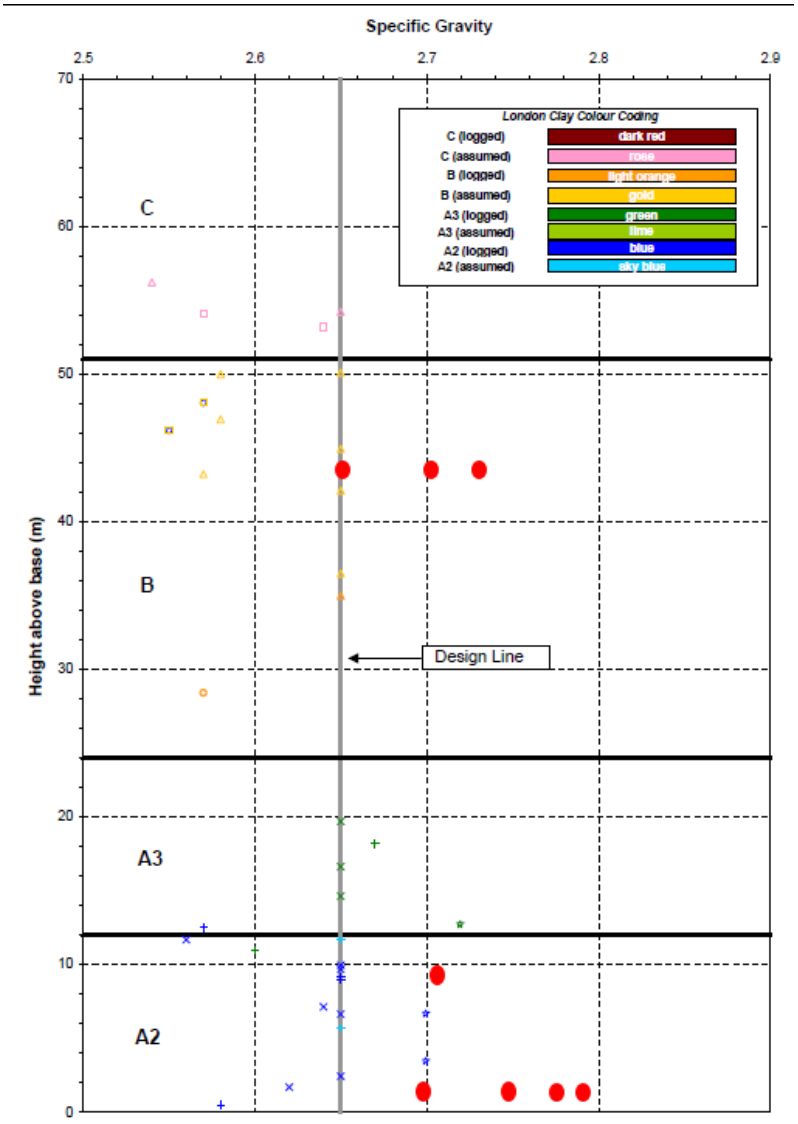

Figure 139: Measured specific gravities using Equation 6.6 of intact specimens superimposed onto Crossrail data

There were initially 25 intact specimens but only 23 have been presented in Figure 140-143 due to laboratory complications. The first tests O1 and O2 were practice samples taken from offcuts on site. The samples are likely to be more disturbed and are of unknown orientation, and this is clearly visible in Figure 141 when both O1 and O2 are less stiff than the other samples (which are all but one vertically orientated). The behaviour of the samples taken from U100 tubes when compared to block sample are also less stiff. In fact, it is surprising a greater disparity does not exist between these stiffnesses considering the process of obtaining a U100 sample, where shear effects from the tube wall can cause sample disturbance. This may indicate a resilience of the material to local effects when compared to clays from shallower depths.

Examining the UMB results on Figure 140, void ratios are consistent and all tests appear to act along the unload-reload line. This suggests testing was conducted below pre-consolidation pressure. On test O25 where the effective stress was taken to 30MPa, behaviour is consistent in consolidation until around 1MPa where a significant increase in consolidation occurs.

Results for LC A2 on Figure 141-142 are less consistent at first glance than UMB but, O21 and O22 which sit at higher void ratios than the other results were saturated at a lower effective stress. It is possible destructuring has taken place causing a greater void space. Otherwise, the results mirror the behaviour of UMB at pressures that could be experienced in the ground. Another notable result is O15 which was unloaded to low effective stress before being reloaded. As lower effective stresses are reached, swelling of the sample likely causes it to de-structure and on reconsolidation the void ratio sits higher than during unload. Comparing LC A2 lower and upper on Figure 141 and 142, behaviour is similar with no notable differences.

LC B2 behaviour on Figure 143 is inconsistent and this is a surprise as the preparation of oedometer samples was trouble free and chipping was largely avoided. Tests O23 and O20 both have higher void ratios but were taken from different block samples, while the other test specimens were taken from another block sample again. The difference could simply be explained by inconsistencies in the material between block samples. On visual inspection there was more sand in the block which produced O23 but the clay content appeared similar giving a material in both cases that was firm-stiff. Unlike the other materials tested, the gradient of the stress-void ratio path increases quickly around 200-600kPa on Figure 143. This is likely due to the lower stresses experienced insitu.

Table 17: Insitu effective stresses

Material	Total vertical stress reduction (kPa)	Measured pore pressure pre-excavation (kPa)	p_0' used (kPa)	Pre-consolidation pressure (kPa) (Black, 2009)
UMB	723	153	600	4000
A2(Upper)	530	132	430	3300
A2(Lower)	670	125	580	3300
B (2)	280	70	240	1500

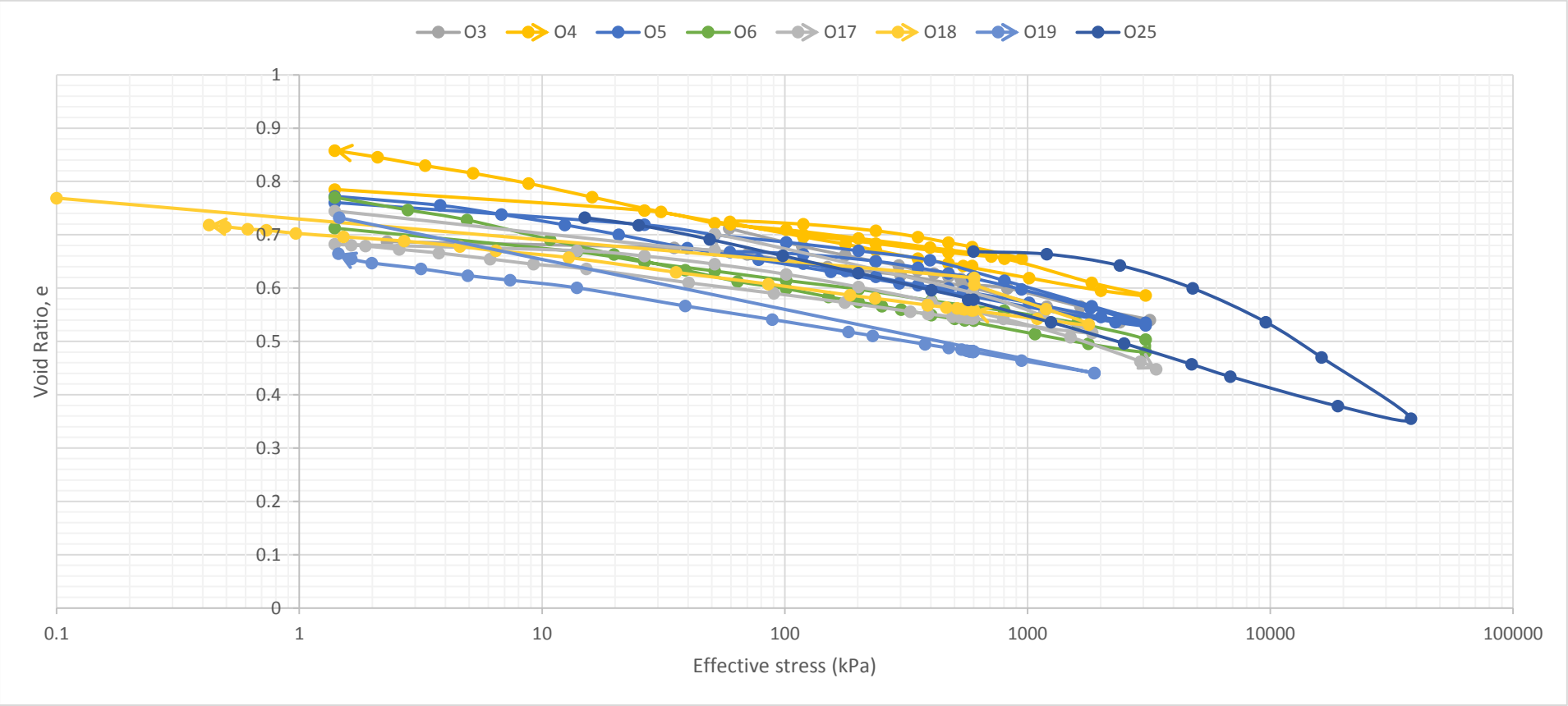

Figure 140: UMB specimens plotted in void ratio vs effective stress space

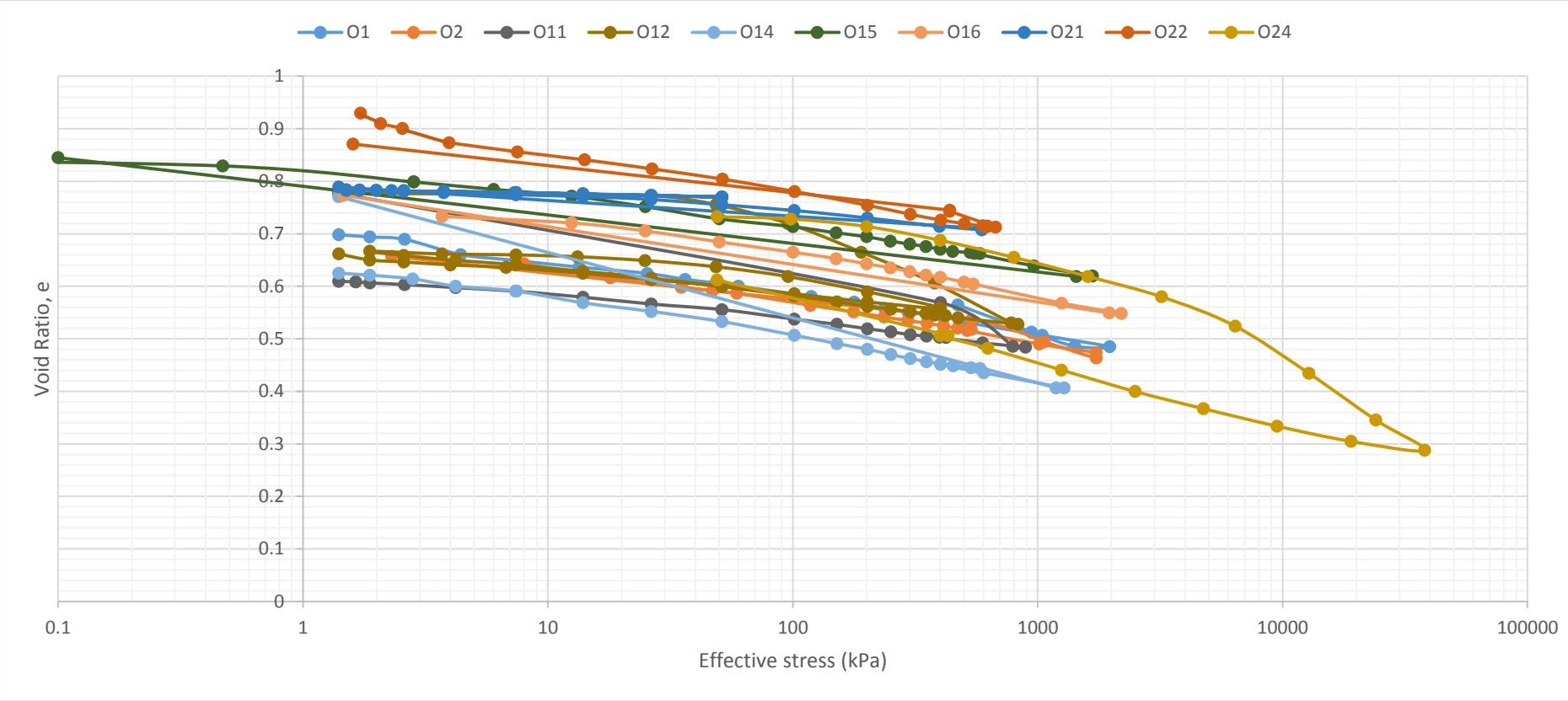

Figure 141: London clay Unit A2 (lower) plotted in void ratio vs effective stress space

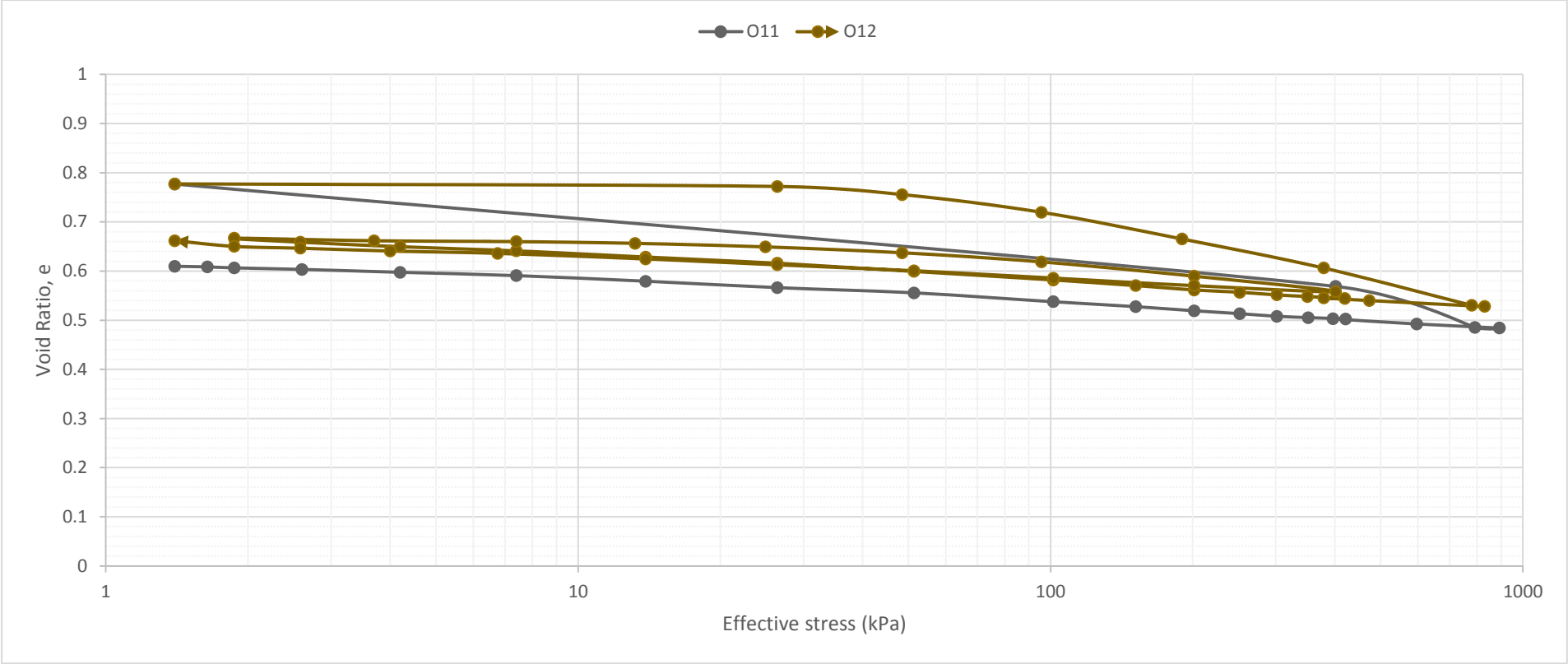

Figure 142: London clay Unit A2 (upper) plotted in void ratio vs effective stress space

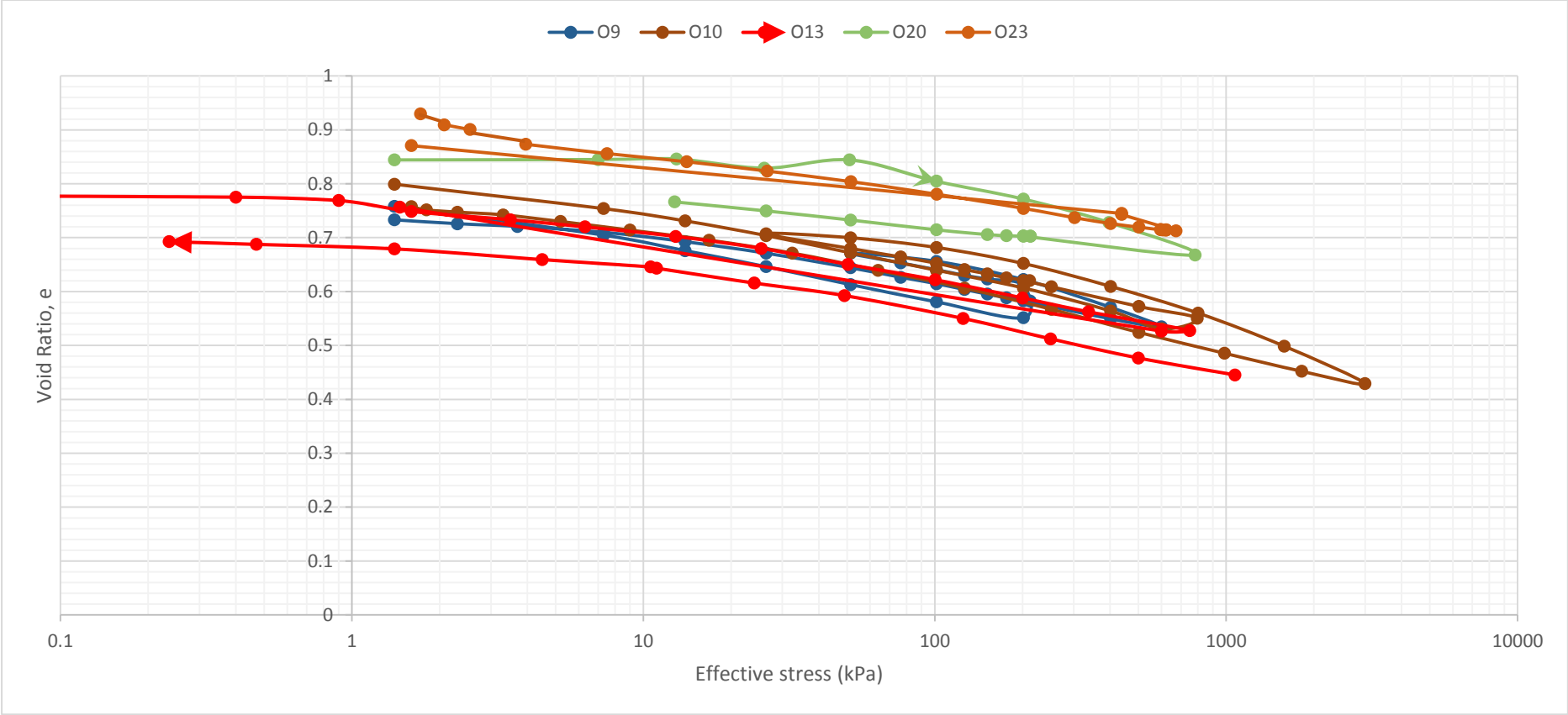

Figure 143: London clay Unit B2 plotted in void ratio vs effective stress space

6.6.1. Clay behaviour on wetting

The behaviour of clays when in contact with changing insitu water pressure is important for deep basement design as swelling or swelling pressure due to changes in effective stress can occur when water pressures are changed by environmental influences. In the case of deep basements in London, a rise in water table due to the reduction in water extraction is being monitored (Environment Agency, 2018) and is predicted to reduce effective stresses across London. In this case, the results of swelling pressure are important to predict long term ground movements.

When wetting a specimen of overconsolidated clay, it will attempt to swell if the stress applied to the specimen is lower than swelling pressure 'locked' into the matrix of the clay by suctions. Therefore, it is good practice to wet a specimen at the predicted swelling pressure. A column in Table 16 shows the 'wetting' pressure (point at which the specimen came into contact with de-aired water via flooding the apparatus) of each sample. Initially, a conservative approach of the methodology proposed by Tony O'Brien (2013) (Section 5.5.1) was undertaken. At first, tests O1-O6 were consolidated without wetting at 24-hour time intervals to both examine the consolidation curve while losing moisture and to minimise disturbance to the sample; however, when each sample came into contact with de-aired water, they either swelled or 'collapsed' under wetting. Samples should have been losing moisture as they were consolidated and therefore the reaction would be to swell on wetting with a higher swell pressure or collapse due to the loss of stiffness resulting from unsaturation and significant pore water tensions.

After test O6 the time spent consolidating before wetting was re-evaluated and brought down by reducing the time intervals between load steps. This was considered by the author most effective at 8-hours with the initial load on the sample increased to 25% insitu effective stress. This meant that within 24 hours the specimen experienced insitu effective stress and it can be inferred that moisture loss would be reduced. In addition to the methodology being altered to suit the specimen behaviour, the wetting pressure was re-evaluated too. Initially a value around 2-3x insitu effective stress was sought but from test O11 onwards a stress between 1-1.5x insitu effective stress was used to wet some samples and if swell occurred weight was added until no swell occurred (as before).

Two exceptions to this methodology are tests O20 and O17. O17 was intentionally wetted at 10% insitu effective stress to evaluate stiffness loss after destructuring (results discussed

6.6.4), while O20 was taken from a block sample with particularly sandy clay and it was the author's suspicion that a low stress wetting would disturb the specimen less than high stress wetting.

Overall, most samples started to swell when wetted and weight was added to mitigate regardless of the saturation pressure. On average, the additional weight on the hanger required to stop swell on wetting ranged between 0-250kpa. Exceptions are O6 and O18 which collapsed on wetting which can be seen in Figure 144 as both consolidate without the addition of load when saturation begins.

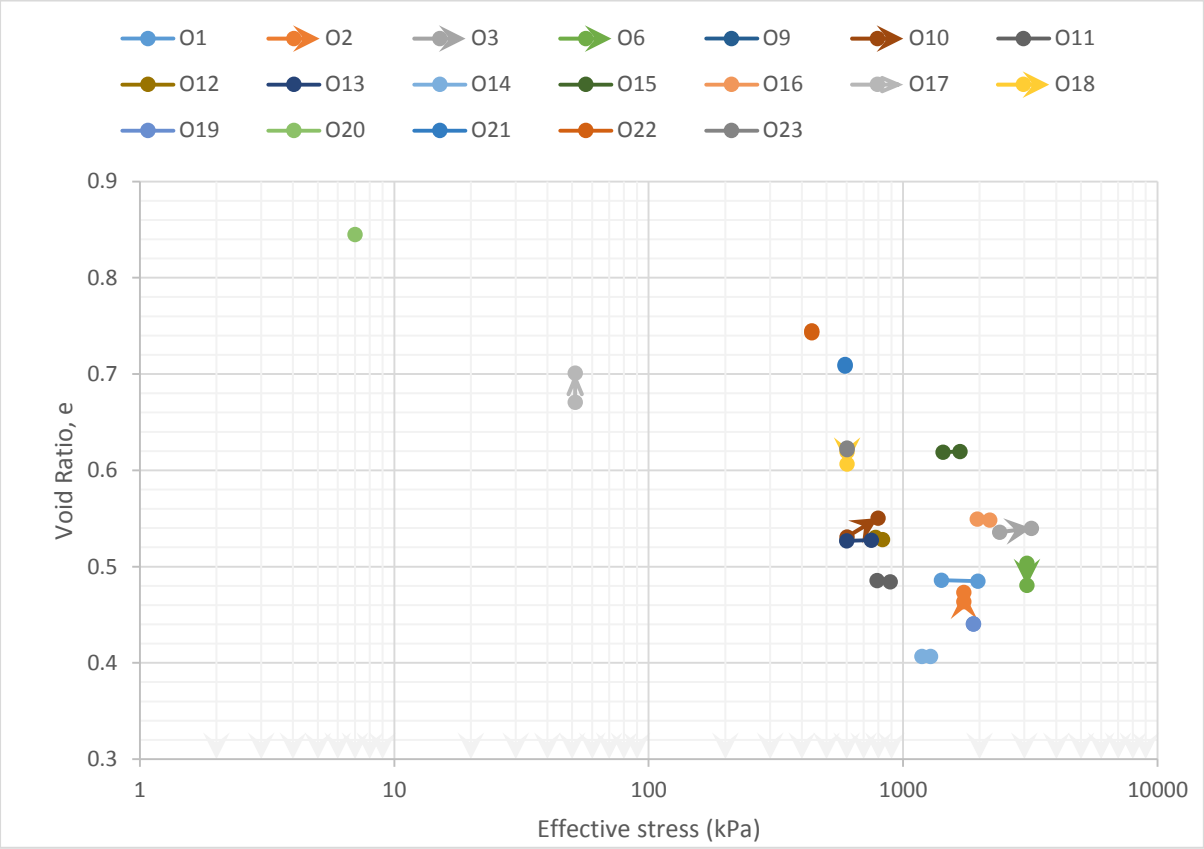

Figure 144: Saturation behaviour of intact specimens

One clear conclusion from wetting at different pressures and consolidating at different speeds is that longer time spent consolidating before wetting leads to larger values of swell. This is likely due to the samples being less stiff from destructuring more on contact with de-aired water and agrees with the argument earlier that they will have dried out more and this leads to greater suctions. Additionally, it is difficult to predict the swelling pressure of specimens and a wide variety of behaviour presented for similar materials

Of all the materials, London Clay A2 swelled the least on saturation which was not expected due to the higher smectite content of the material. Consolidating quickly dry and then saturating at a stress around 1x insitu effective stress prevented swell. As for London Clay B2, early testing showed stresses of 3x insitu effective stress were needed to prevent swell on saturation but later tests from a different block sample (the sandy sample mentioned earlier) show that stresses as little as 25% of insitu effective stress prevented the same swelling. This demonstrates the challenges of defining characteristics of materials considered relatively homogenous.

6.6.2. Stress sensitivity

An important testing process is to examine the sensitivity framework proposed by Burland (1990). Using the techniques discussed by Chandler (2000) and visualised on Figures 145 and 146, the stress sensitivity and yield stress ratio (YSR) was found using Figure 147. The stress paths shown on Figure 145, O24 and O25, were saturated at the start of the test and were conducted by Fugro as the pressures needed were not possible at The University of Southampton. Stress sensitivity is shown in Equation 6.13 and YSR is the ratio between yield stress and insitu effective stress.

$$S_t = \sigma_{vy}/\sigma_\theta^* \tag{6.16}$$

Where S_t =Stress sensitivity ratio, σ_{vy}= total vertical stress at yield, σ_θ^*= stress which the consolidation curve crosses Burland's Intrinsic Compression Line (ICL).

The results in Figure 147 are obtained by evaluating where a significant change in gradient of the void index when plotted in void index- effective stress space takes place. For post-sedimented, overconsolidated clays this occurs beyond Burland's Intrinsic Compression Line (ICL) and is subject to a degree of interpretation. Ideally, repeat tests are used but in this case, it was not possible so a range of suggested values for the yield stress are proposed and shown with dashed lines on Figure 147 to show the process behind the values. The interpreted results are obtained using Cotecchia and Chandler (2000) and are shown in Table 18 and compared with results obtained by Gasparre (2005). From these tests, it was shown that UMB and A2 has a post-sedimentation structure. Also, the strength and stress sensitivities which are approximately the same for post-sedimentary structures are of low sensitivity which is not surprising considering the high stresses involved. Finally, the yield stress ratio is similar to the Overconsolidation ratio (OCR) which is to be expected.

Table 18: Stress sensitivity framework

Specimen	Material	YSR (interpreted)	Stress sensitivity ratio	Yield stress (MPa)	OCR
Gasparre, (2005)	B2	3.3-24	1.2-2.9	0.8-7	6-12
O24	A2 (low)	10.5	1.9	6	5-6
O25	UMB	5.3-15.8	2.1-3.3	3.2-9.5	6-7

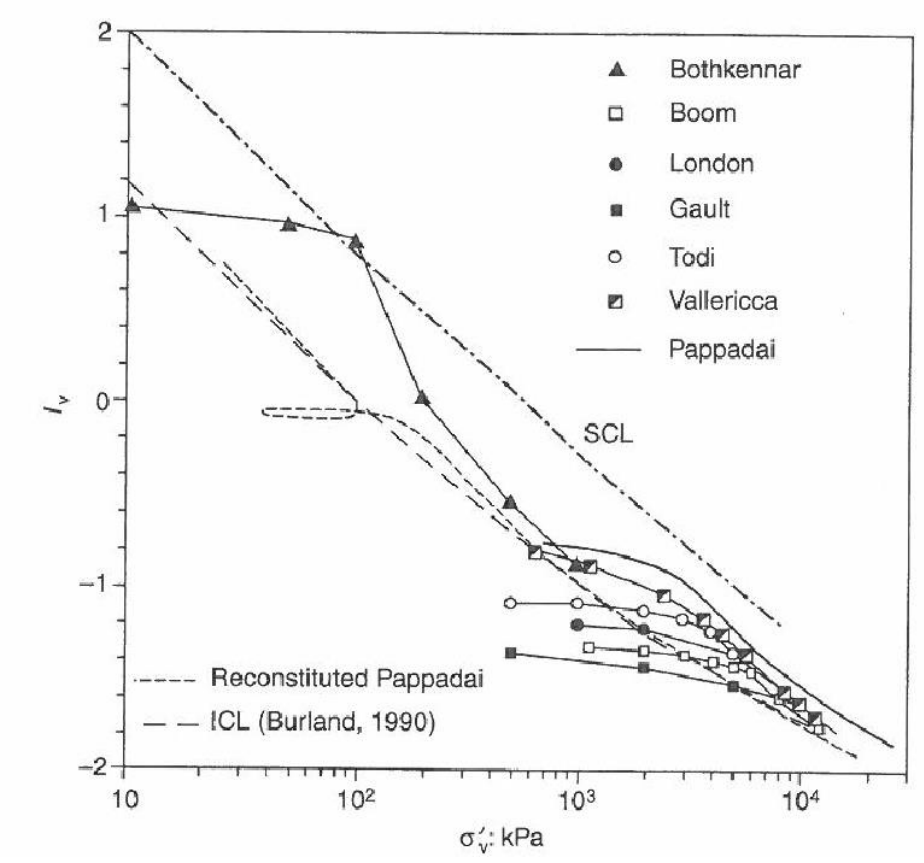

Figure 145: One dimensional compression of natural and reconstituted clays plotted against the void index (data from Samuels, 1975; Bishop et al., 1965; Burland, 1990; Smith, 1992; Coop et al., 1995; Burland et al., 1996; Cotecchia, 1996) taken from Cotecchia and Chandler (2000).

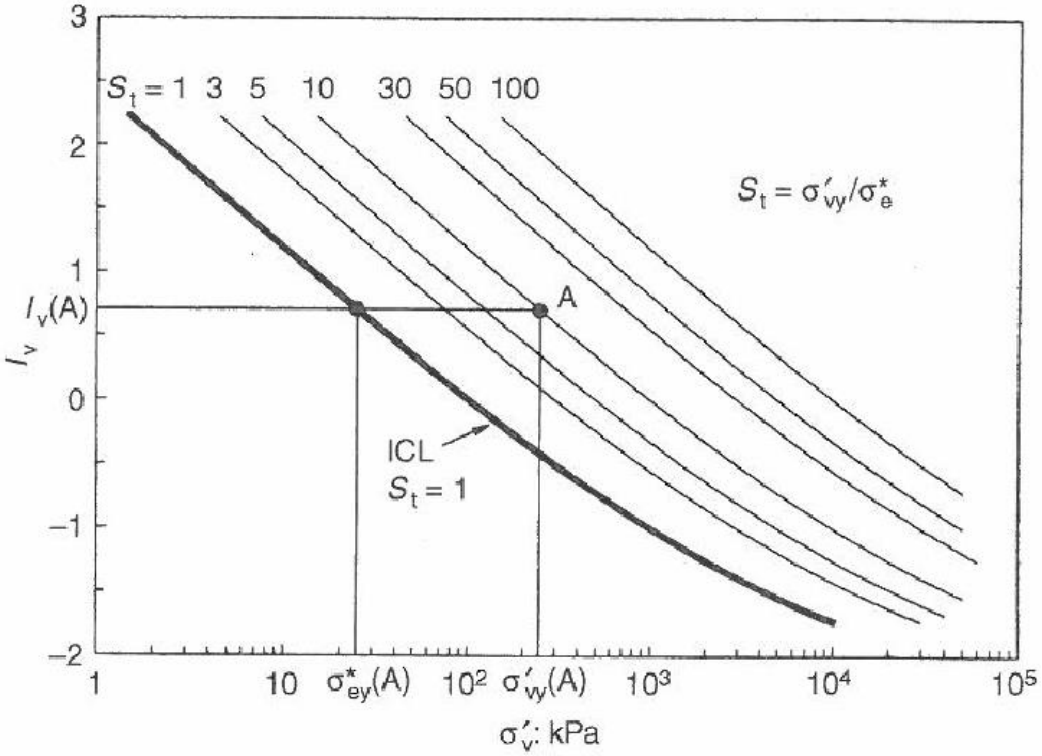

Figure 146: Sedimentation compression curves in idealised sensitivity framework. The ICL is taken from Burland 1990 and this image is taken from Cotecchia and Chandler (2000).

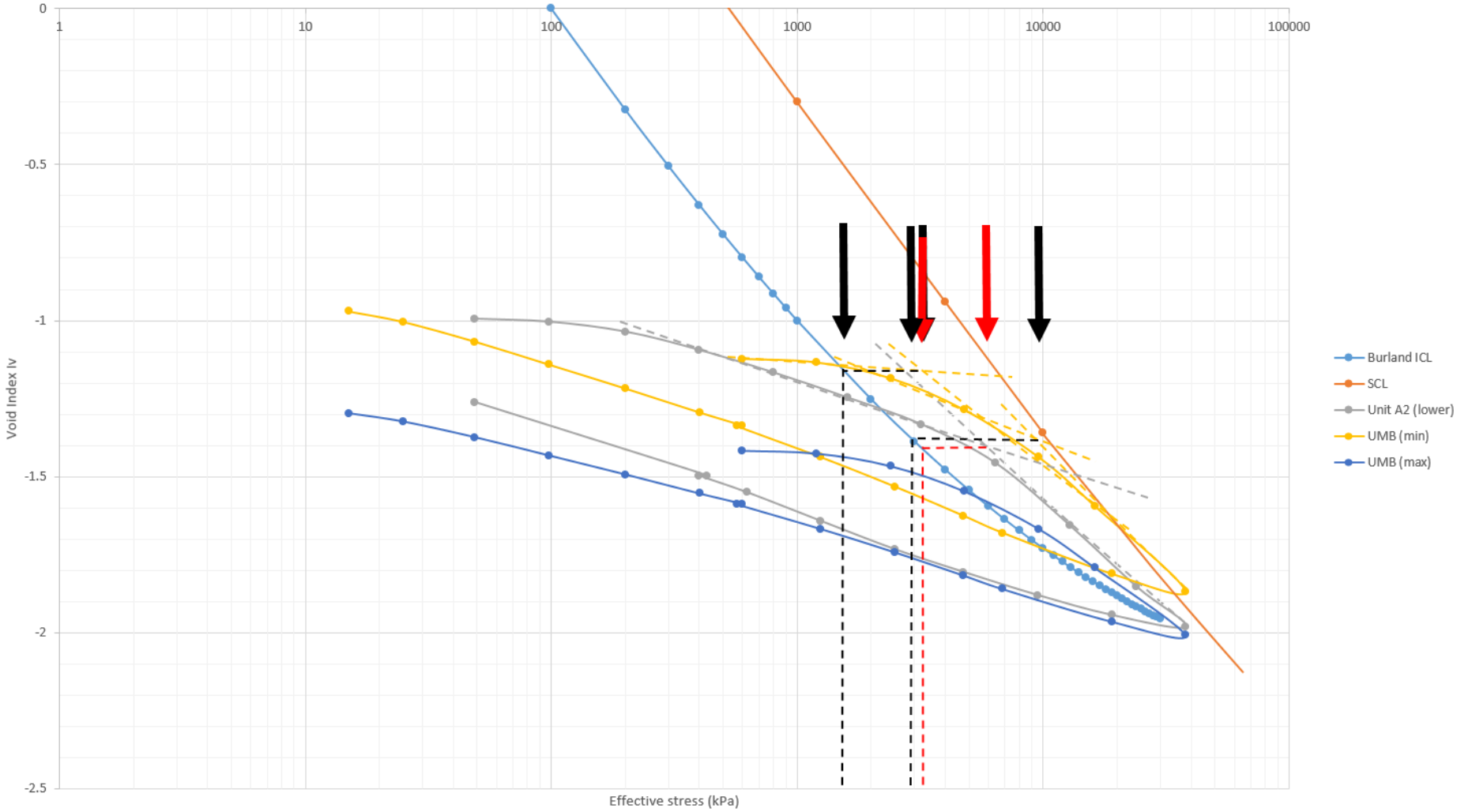

Figure 147: Sensitivity framework in void index vs effective stress space. The points highlighted are the yield stresses and corresponding stress at the ICL for the same void index. From these the stress sensitivity and yield stress ratio are obtained.

6.6.3. Stiffness degradation at large strain

Examining the one dimensional Young's modulus stiffness behaviour of intact specimens when unloaded from an initial vertical effective stress equal to insitu mean effective stress, $p'_0 = \sigma'_{v,p'_0}$, (Note:, $\sigma'_v \neq p'$ in an oedometer as K0 is not equal to 1) is best done material by material before comparing between them.

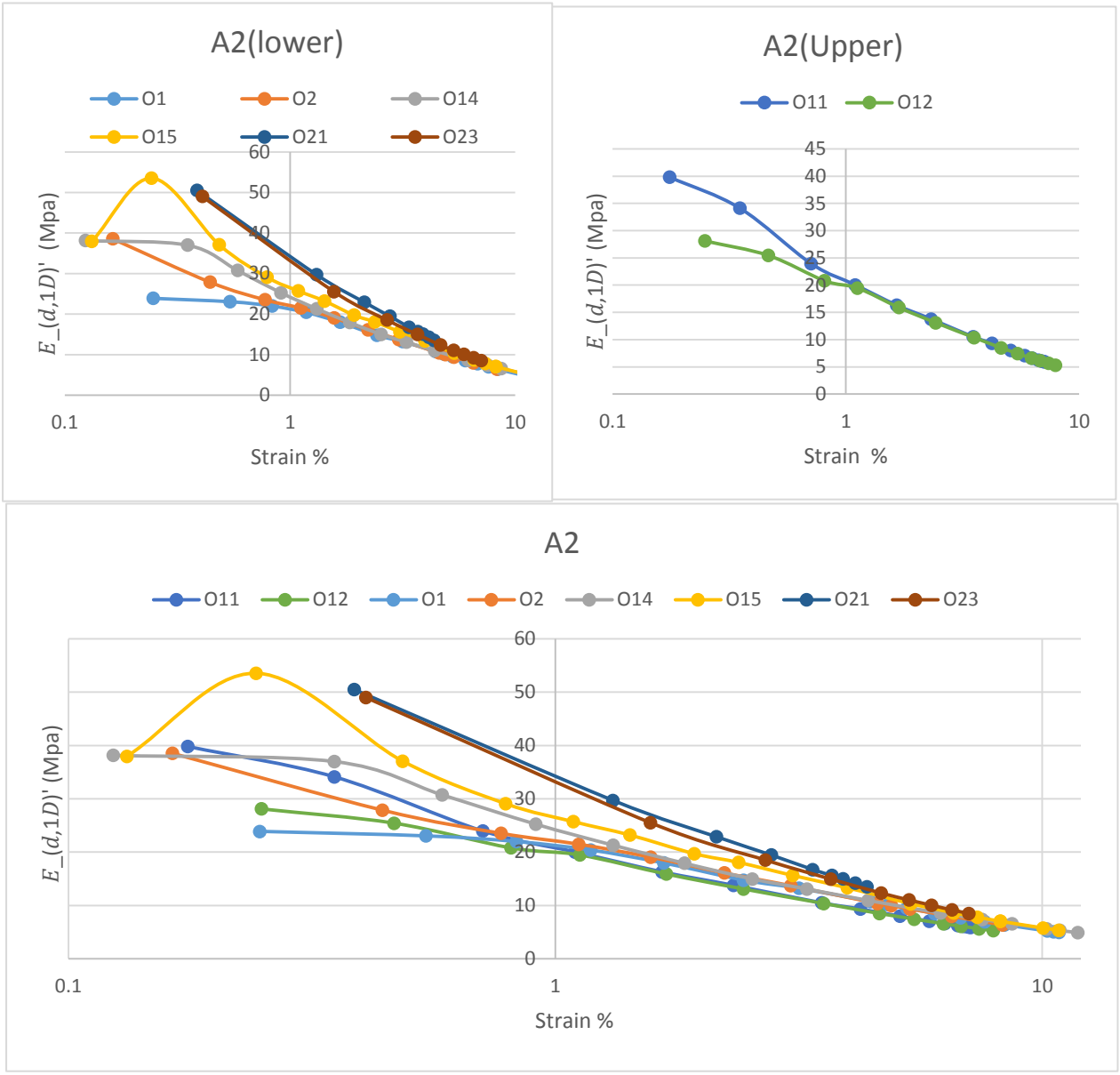

Figure 148: Large strain stiffness degradation of London Clay Unit A2 (upper and lower) on unloading from σ'_{v,p'_0}

Firstly, London Clay unit A2, the general trend is an approximately linear reduction in the one- dimensional stiffness, $E'_{d,1D}$ vs % strain in semi-log space. This is the expected behaviour for OC clays at large strain (Figure 148). The values of $E'_{d,1D}$ are 20-35Mpa at 1% and 10-20MPa at 3% with the degradation converging and reaching a minimum value of the order of

3-4MPa. Interestingly, left at very low stresses, the strain from insitu effective stress did not exceed 12% (Figure 148).

The results for UMB may be examined where smaller load steps were used at stresses close to insitu effective stress (there are some values of stiffness collected at strains smaller than 0.1%). Temperature effects are likely to be responsible for the variation below 0.1% as the oedometers sit in a North-East facing laboratory with windows in which the sun can cause changes in room temperature (the digital dial gauges have an accuracy of +/-0.005 to +/-0.01% depending on specimen size). However, it is clear below 0.1% strain that the behaviour acts differently and this will be explored further in Chapter 7. As for strains above 0.1%, $E'_{d,1D}$ is between 30-75MPa at 0.1%; 20-30MPa at 1%; 15-20MPa at 3% and a minimum value around 5MPa (Figure 149). Strains of up to 15% were measured.

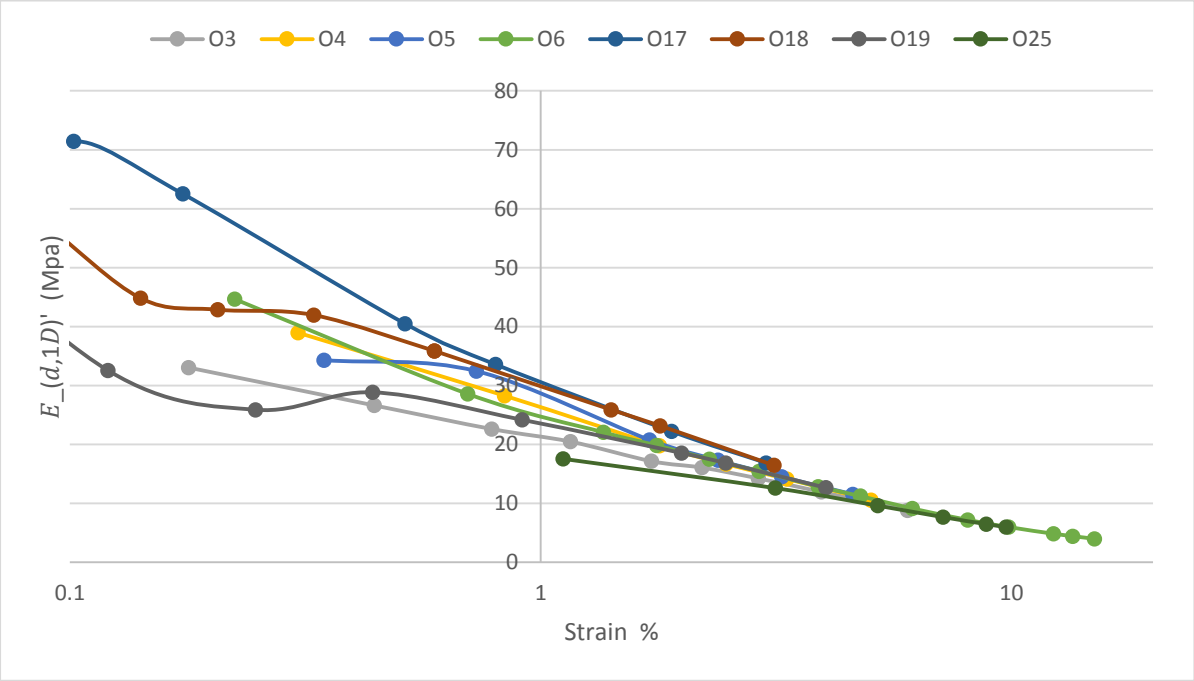

Figure 149: Large strain stiffness degradation of UMB on unloading from $\sigma'_{v,p_0'}$

For London Clay unit B2, two tests were conducted from insitu stress. Both these tests show a much less stiff material than the others tested and have a one-dimensional drained Young's modulus $E'_{d,1D}$ around 7-7.5MPa at 1% strain from insitu (Figure 150).

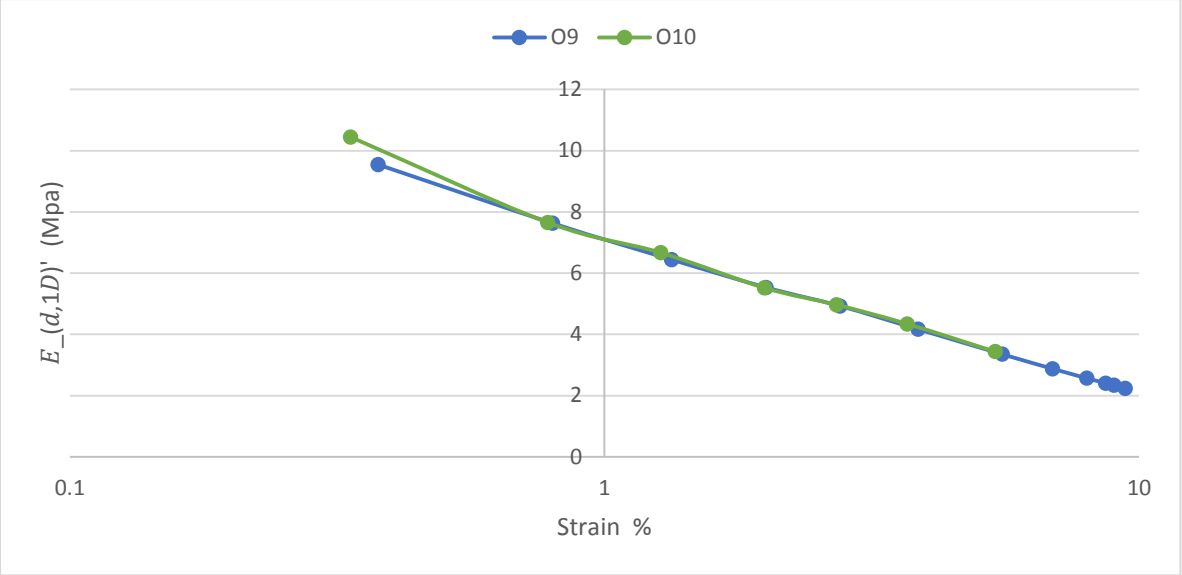

Figure 150: Large strain stiffness degradation of London Clay unit B2 on unloading from σ'_{v,p'_0}

Plotted together in Figure 151, the results show that the insitu depth of the material influences stiffness greatly when unloaded from insitu effective stress, with the deepest material the stiffest at all strains unloaded from insitu.

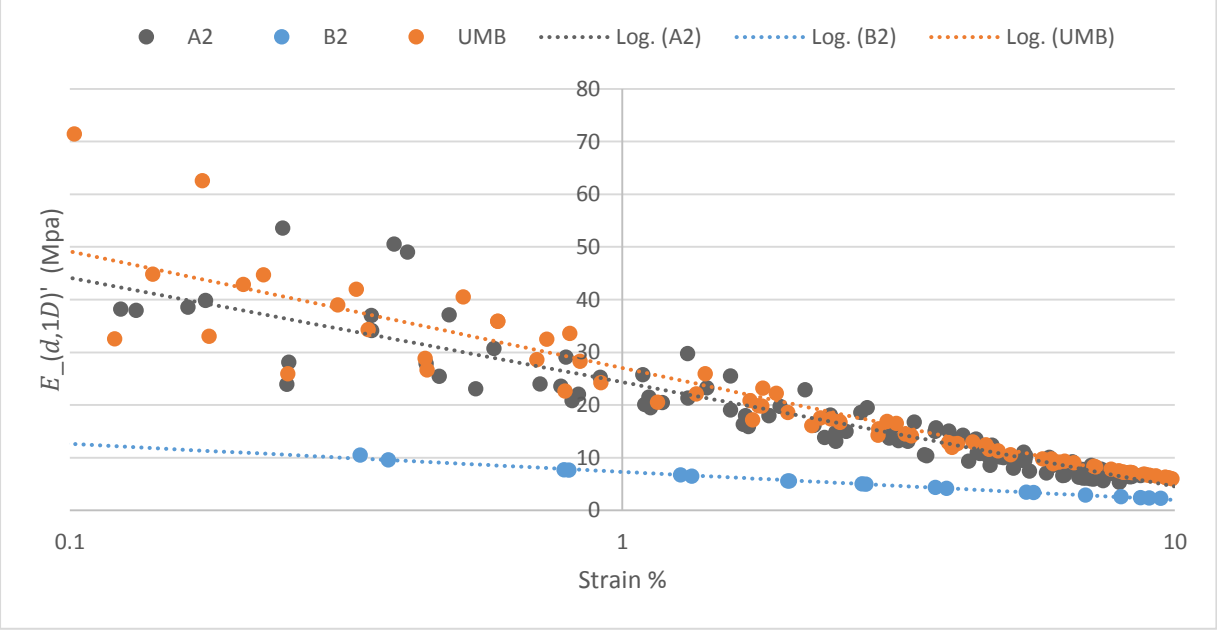

Figure 151: Comparing large strain stiffness degradation on unloading from σ'_{v,p'_0}

However, when compared normalised by a vertical effective stress,σ'_{v,p'_0}, equal to the average insitu effective stress, p'_0 (Table 16 for values)., the behaviour of each material is very similar. London Clay A2 upper and lower in Figure 152 are within 5 (MPa/MPa) at 1% strain and in Figure 153 it could be argued that London Clay A2 behaves the stiffest at strains 0.1-

1% while Unit B2 is the least stiff. However, UMB and Unit A2 have nearly identical average normalised stiffness between 0.1-10%.

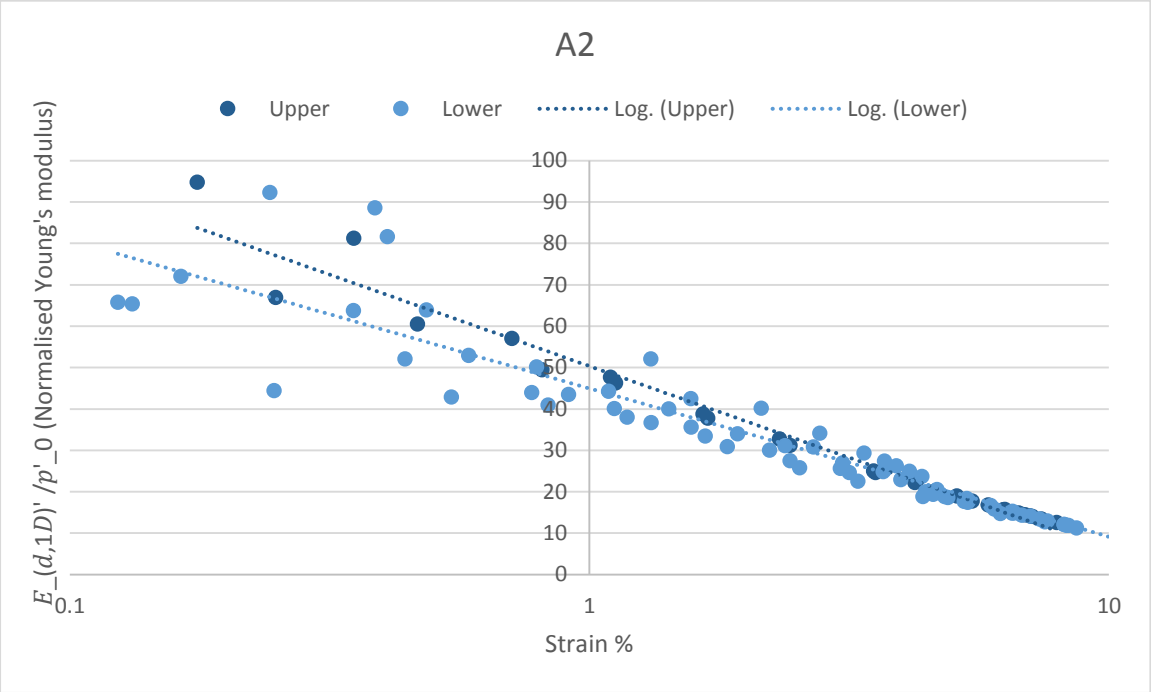

Figure 152: Normalised stiffness of London Clay Unit A2 using insitu effective stress. Comparing the upper and lower sampling material.

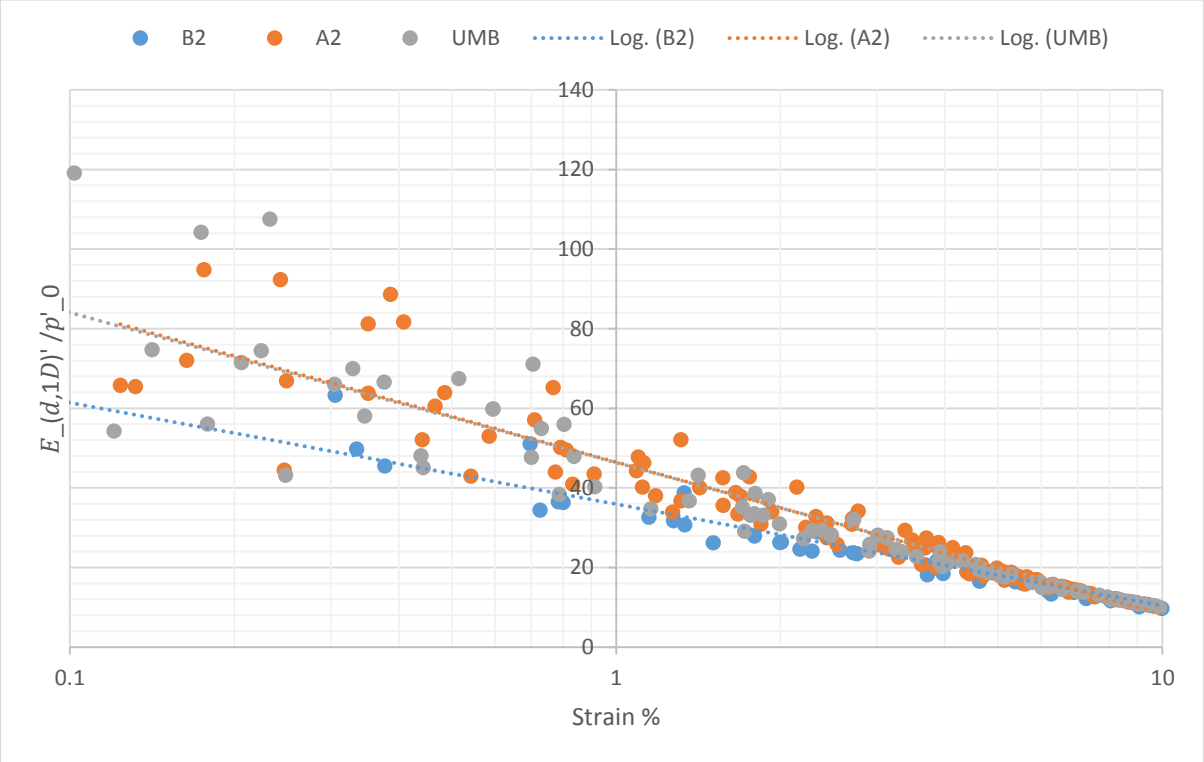

Figure 153: Strain from insitu effective stress when normalised using insitu effective stress

To examine the relationship between normalised effective stress and unloading from vertical effective stress equal to insitu mean effective stress in more detail, two further tests were conducted where the objective was to start to unload A2 and B2 London Clay specimens from the mean effective stress experienced by UMB insitu (Figure 154) which was 600kPa. The results show that similar to the normalised plot, A2 is stiffest while in this case B2 and UMB act similarly but at larger strains they are all pretty close. The conclusion of this study could be that p' may be an effective normalising value and further evidence of this may be Figure 155 which has all unloading lines plotted against strain and then normalised by the average effective stress the unload begun from. This Figure shows a large scatter of results but it is important to note that some unload lines occurred after potentially destructive swelling on initial saturation, and some are a second or third unload-reload cycle that could have experienced creep during the test.

In the case of samples taken from Moorgate, Blomfield box and VSU the information is there to back -analyse soil parameters. Results in 5.6.4 show consistently: 0.5% strain $E'_{d,1D}/p'_0$=58, at 1% strain $E'_{d,1D}/p'_0$=45, at 3% strain $E'_{d,1D}/p'_0$= 25, at 10% strain $E'_{d,1D}/p'_0$= 10. The results have low deviation. It is therefore advised where ground movements are important to the design of a deep basement that p'_0 is accurately assessed pre-excavation.

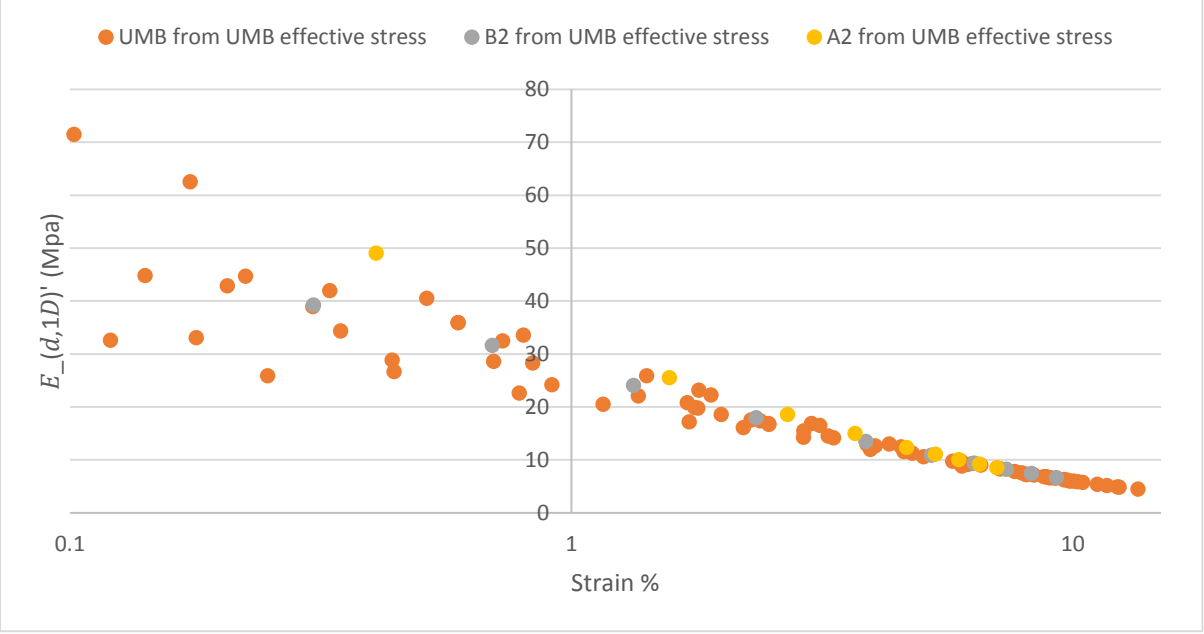

Figure 154: Strain from UMB insitu effective stress % (using tests O20 and O21)

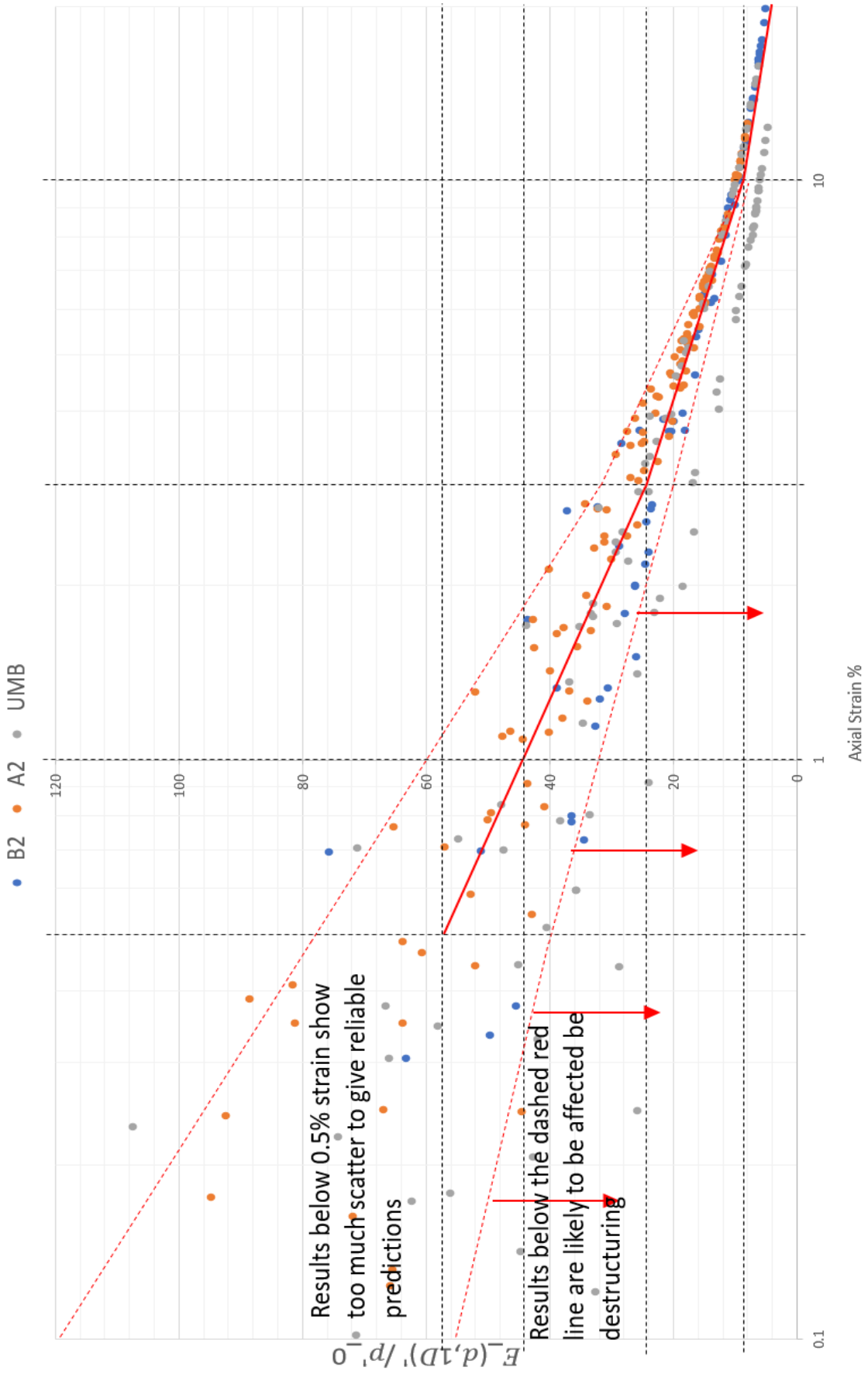

Figure 155: Normalised unloading of all intact samples and all unload-reload cycles

6.6.4. Swelling parameters

It is not uncommon to see plots of strain against effective stress or alternatively void ratio vs effective stress. Strain index is used by some authors to measure swell sensitivity while swelling index is more commonly used for crude onsite swell predictions.

What is usually demonstrated is that between 10-90% insitu effective stress, the gradient of the line in strain (or void ratio) vs log effective stress is uniform and a constant called the strain index, c_{ss} (Equation 6.15) (or swelling index, c_s, for void ratio plots – Equation 6.14), is used to represent this gradient. This behaviour can be clearly seen in Figure 156 for Unit A2 where all tests appear to have an approximately linear relationship. However, behaviour either side of 10-90% effective stress may not act in the same way (i.e. may not follow a linear relationship) and this can be seen in Figure 157. Here, as lower effective stresses are reached the strain differences are large. This is partly due to differences in the initial starting stresses but may also be due to differences in the clay contents in each sample. The greatest variation in behaviour exists for UMB which has the most varied composition due depositional environment. Due to the sensitivity of starting stresses and the large range of strains at low effective stresses, the data may be more usefully plotted as the strain index against normalised effective stress.

$$c_s = \Delta e / \Delta log \sigma'_v \tag{6.17}$$

$$c_{ss} = \Delta \varepsilon_v / \Delta log \sigma'_v \tag{6.18}$$

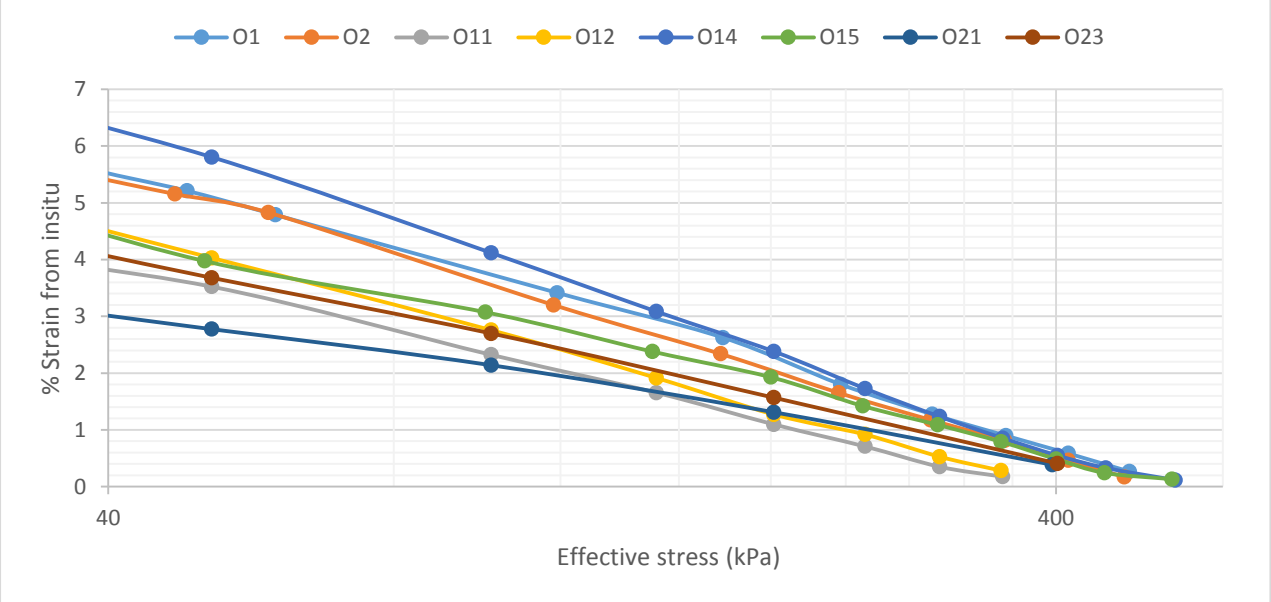

Figure 156: Demonstration that the gradients of the lines are approximately linear in strain vs log effective stress space.

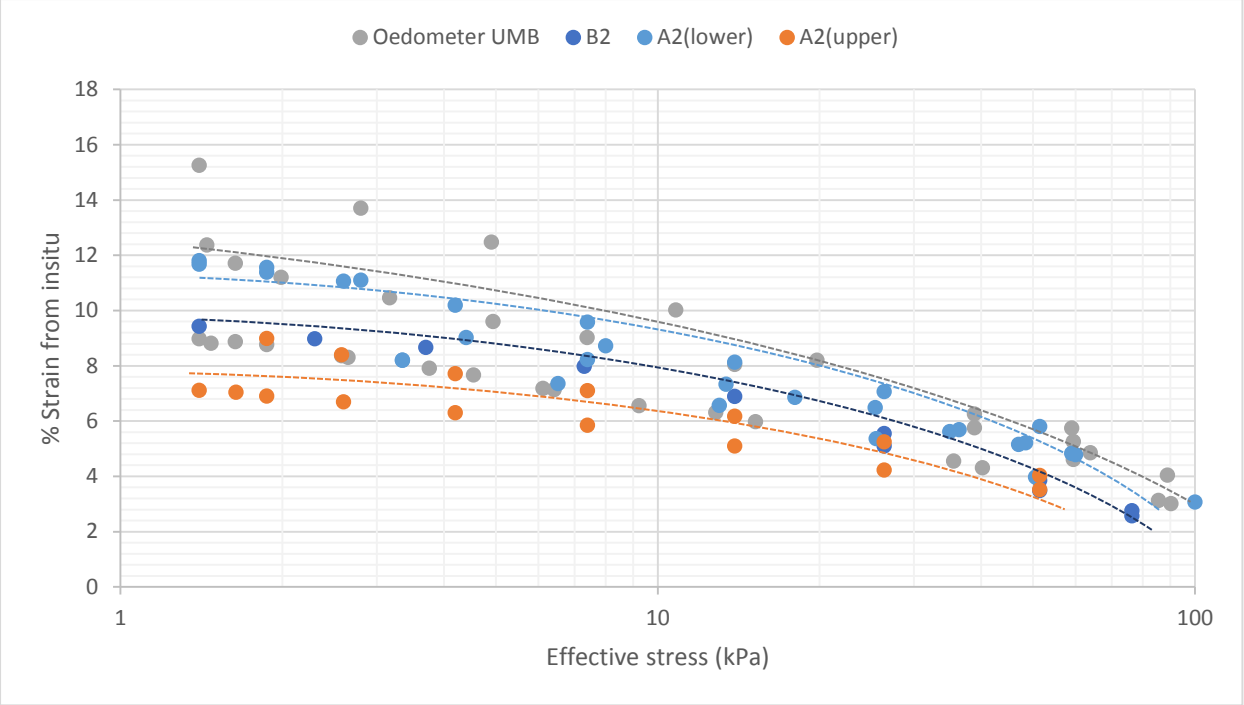

Figure 157: Intact specimens in strain vs log effective stress pace at low effective stresses.

When examining strain index vs effective stress normalised using $\sigma'_{v,0}$ then shown as a % of insitu effective stress, it is clear that between 10-90% that behaviour is not entirely linear. In fact, strain index for Unit A2, Figure 158, peaks between 60-70% unload from insitu effective stress. Therefore, it would be better to model the strain index as a curve.

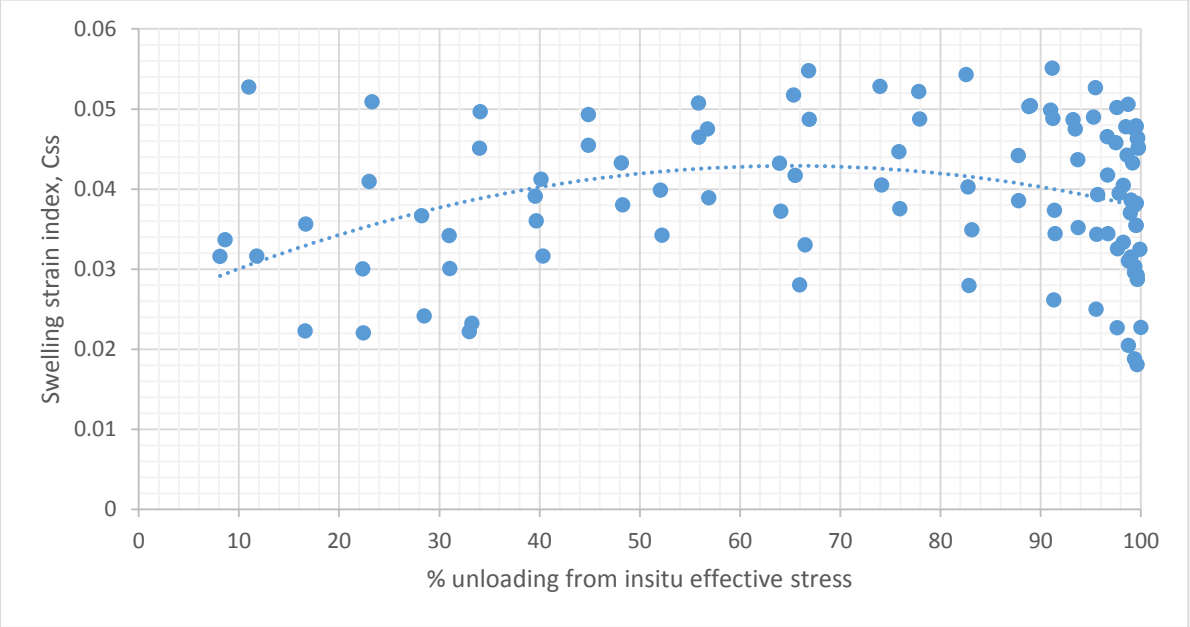

Figure 158: Strain index vs. % unload for Unit A2. Curve fit using poly. Function

Plotting all intact specimen unloaded from their insitu effective stress a clear pattern emerges (Figure 159). Swelling strain index starts small and then reaches a peak value between 50-90% unload before beginning to decline again as nearly all load is removed from specimens.

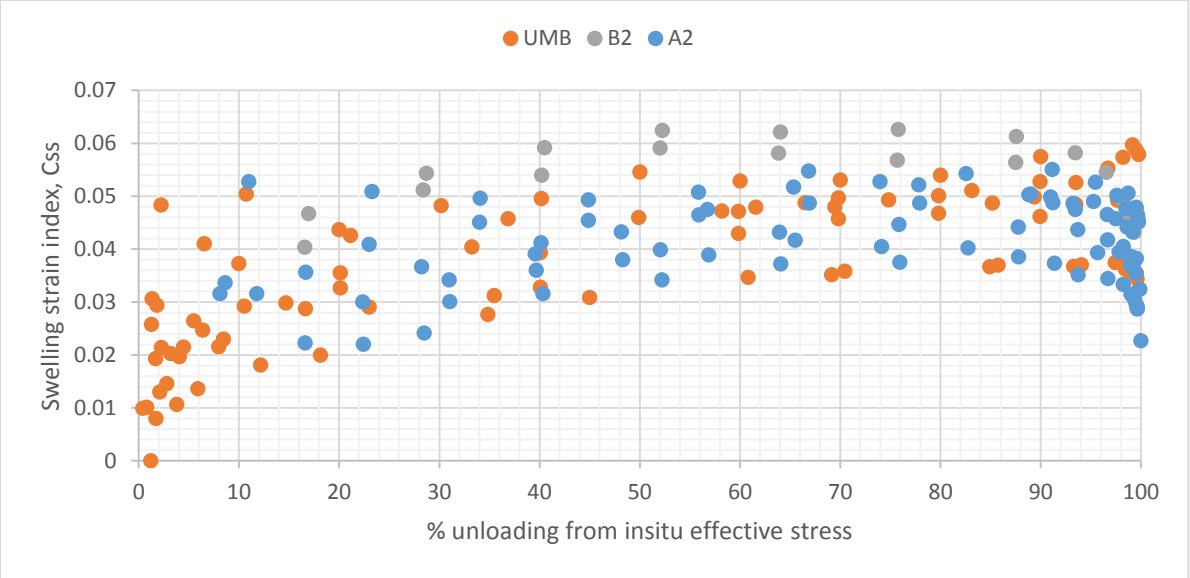

Figure 159: Swelling strain index vs. % unload for intact oedometer specimens - all materials

It is also common to plot void ratio vs log effective stress. Like strain vs log effective stress, the gradient of the line can be represented using a value called the swelling index, c_s (Equation 6.14). This can be plotted in a similar way to strain index and is shown in Figure 160. This Figure shows that swelling index follows a similar pattern to strain index and a designer may then use the tables of % unload (Table 19) to find a value c_s for % unload an element of soil experiences. This would assume that unload was gradual or was controlled through unload steps, an example being basement excavation. Furthermore, because the oedometer testing unloads incrementally, much like top-down construction of a deep basement, these tests results are comparable to insitu conditions.

To further examine the trend of the swelling index data, additional data from unload cycles not starting at insitu stress is combined with the data in Figure 160 and plotted in Figure 161. Then data were filtered using a function in excel to order the x-axis values from 0-100% and a moving average found by taking the average of every 15 data points. This shows that the least square fit in Figure 160 is an oversimplification of the data and misses subtle differences between each material. Firstly, the London Clay Unit A2 and UMB material both act similarly until around 90%. At this point Unit A2's swelling index begins to fall proportionally quickly while UMB's swelling index continues at an approximately constant

value until much later. Unit B2 also behaves as UMB at lower effective stresses and continues to swell at a higher rate than Unit A2 until a much lower effective stress. These key differences at lower effective stress are examined further in 6.6.5.

To look at the rate of change of the swelling index further the change of swelling index between two unload steps is taken for all unload steps and then divided by the change in effective stress and multiplied by the effective stress at the start of each unload step. This is shown in Equation 6.16. The value of effective stress acts as a normalising value and gives more significance to changes at lower effective stresses.

$$(c_{s,1} - c_{s,2}) / \left(\frac{\sigma'_1 - \sigma'_{,2}}{\sigma'_1}\right) = \sigma' \left(\frac{\partial c_{s,1}}{\partial \sigma'}\right) \qquad (6.19)$$

The value given by Equation 6.16 is then presented in Figure 162 against % unload. Interestingly, the data show that there is a significant difference in behaviour along the unload % axis. The rate of change of the swelling index is greatest initially and quickly declines as expected. The plot has a comparability with stiffness degradation vs. strain. One clear conclusion from this would be that small unloads below 10% of insitu stress cannot be modelled effectively by a swelling index constant and a non-linear stiffness degradation analysis would be more appropriate. It should be mentioned that at 0-10% unload, a high amount of error exists due to poor resolution of the oedometer apparatus +/-0.05% strain.

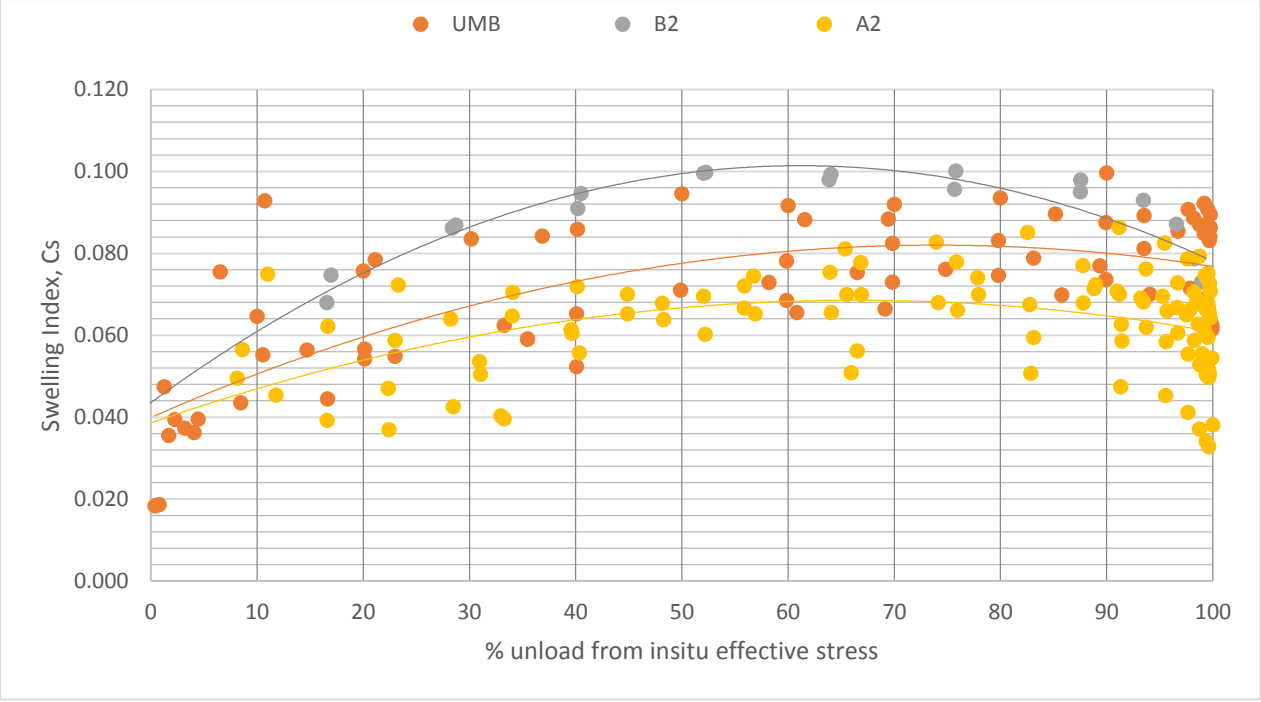

Figure 160: Swelling index vs. % unload for intact oedometer samples unloaded from insitu effective stress with least squares fit to data

The swelling index can be predicted using the following table:

Table 19: % unload vs average swelling index per material

% unload	UMB (c_s)	A2 (c_s)	B2 (c_s)
10	0.050	0.047	0.062
20	0.060	0.054	0.074
30	0.066	0.060	0.086
40	0.073	0.064	0.094
50	0.078	0.067	0.099
60	0.08	0.068	0.102
70	0.082	0.068	0.100
80	0.082	0.067	0.094
90	0.08	0.065	0.088
100	0.077	0.062	0.078
(Black, 2009) 0.1-100%	0.054	0.048-0.081	0.037-0.1

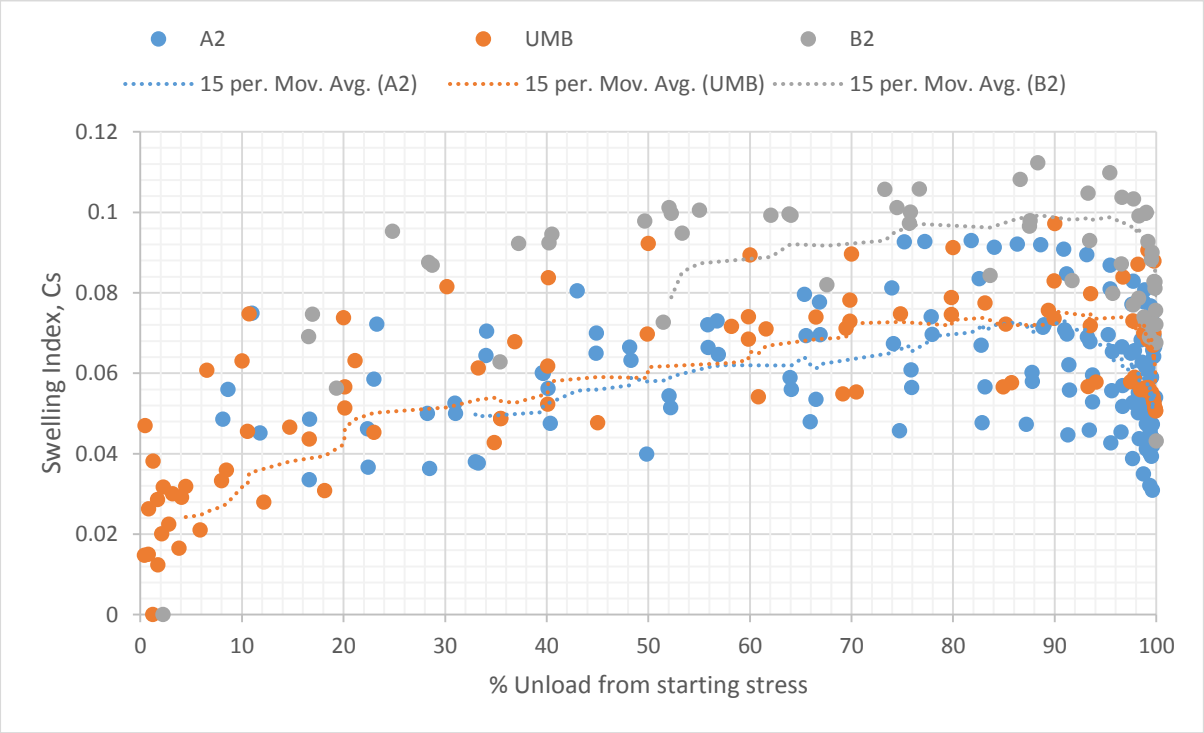

Figure 161: Swelling index vs. % unload from all tests. The data are filtered and reordered so a moving average can be applied

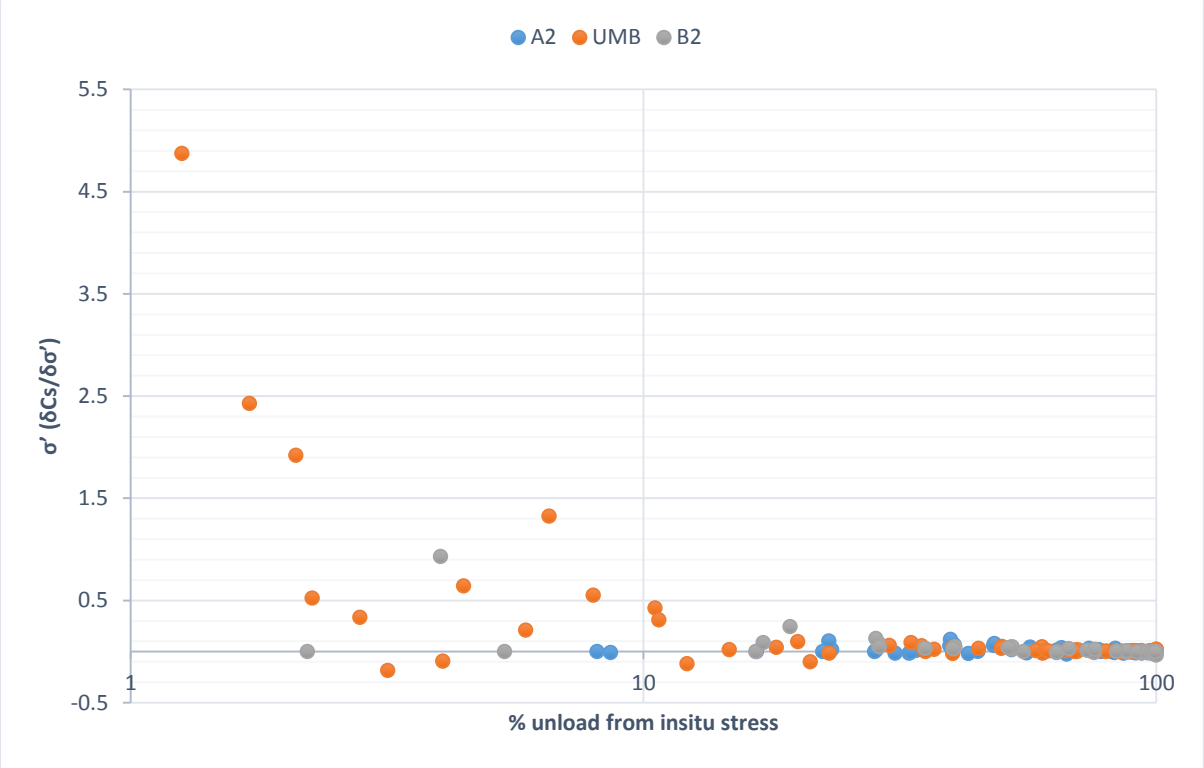

Figure 162: Effective stress, σ' multiplied by the change of swelling index (δc_s) divided by the change of effective stress (δσ') vs. % unload for intact oedometer samples with both least squared and a linear fit to data

Swelling indices are useful for most cases calculating heave resulting from excavating deep basements as they are simple but disturbance of the soil (caused by sampling and construction activities) leads to potential over-prediction of swell. To overcome this issue, the swelling index data can be plotted against LL*clay fraction % to give an indication of the sensitivity of the clay to disturbance.

In Figure 163, a redrawn version of the plot produced by Mesri et al. (1978) can be seen. Mesri et al. (1978) applied unload and then reload (termed cycles) to clays to examine the behaviour. They found that the greater number of cycles reduced the stiffness of the clay and therefore the swelling strain index increased for each cycle. It is proposed that the clay's structure becomes more and more disturbed for each cycle and that high sensitivity clays become disturbed more easily. It would be expected that structured or aggregated soils sit close to the undisturbed line. The intact oedometer data sits around the 1st cycle line which is what one would expect as basement excavation followed by a single oedometer reload and then unload to insitu effective stress is the 2nd cycle. On the other hand, the remoulded specimens do not sit as high up on this Figure as Mesri et al (1978) found on their sample

clays. This suggests low swell sensitivity of the clay which means the structure is less sensitive to being altered.

Note: If swell sensitivity is measured fairly well using the Equation: remoulded swelling strain index /undisturbed swelling strain index, taken from Schmertmann (1969), the values are: 1.56, 1.57 and 1.61 for B2, A2 and UMB, respectively. This means they all have low sensitivity with UMB having the greatest sensitivity. Values of 1-2 are low, 2-3 medium, 3-4 high, and 4+ very high.

Also, on Figure 163, the arrows represent the range of clay fraction and liquid limit values found for each material with data plotted around the average. This demonstrates the variability of the materials and the difficulties putting the data on the plot. UMB particularly had varied clay fraction and liquid limits but behaved similarly for the tested intact oedometer specimens.

With the specimens having low sensitivity one might expect the swelling indices to be applicable to insitu calculations but as Ng, (2004) found at Lions yard, laboratory measured values of the swelling index are typically 2-3 times higher than site measured values. In Figure 163, taking the average value of clay fraction x liquid limit % and the undisturbed line, the swelling strain index is predicted to be 0.017, 0.018 and 0.02 for London clay unit A2, Unit B2 and UMB, respectively. The laboratory measured values are 2-3 times larger than these.

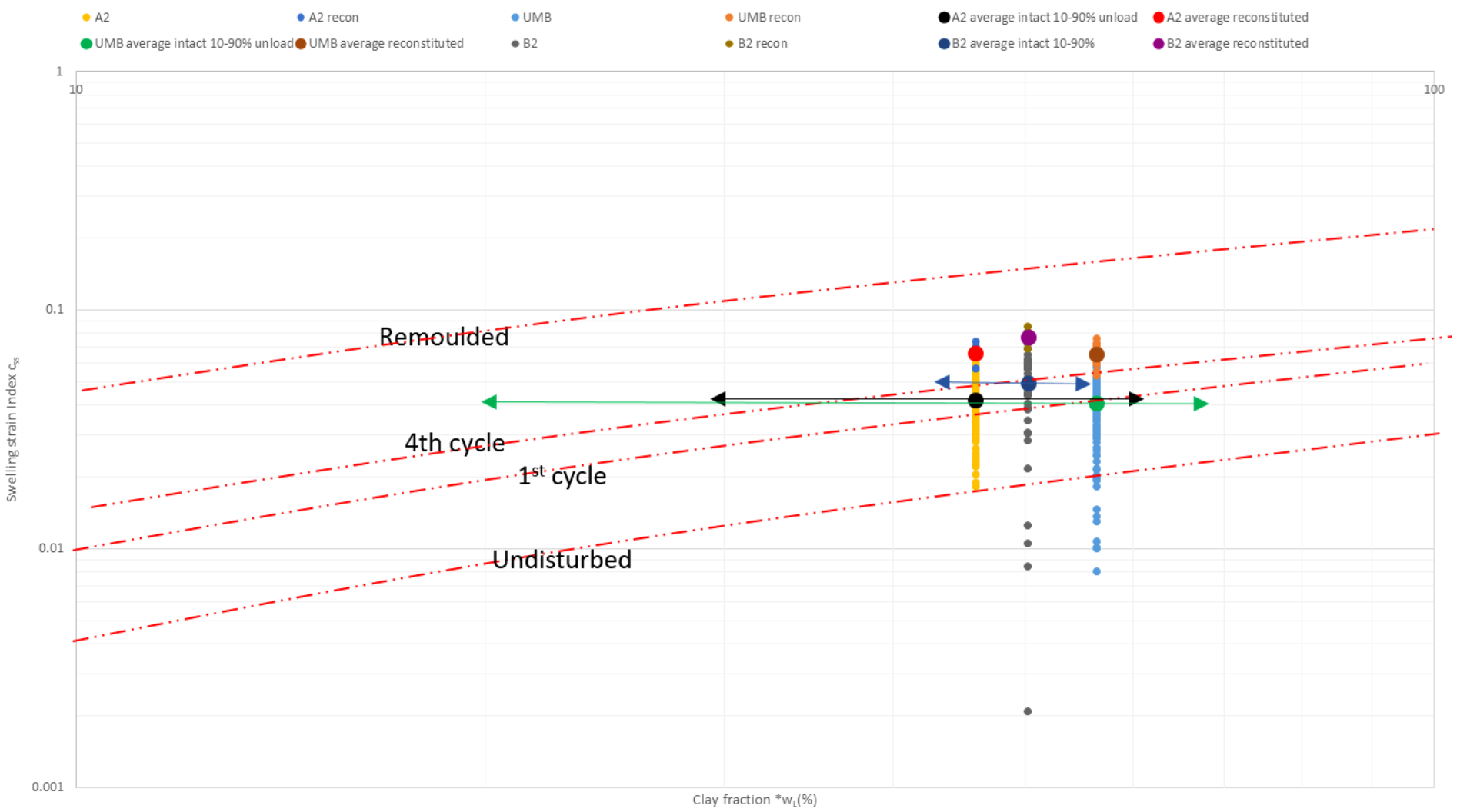

Figure 163: Swell sensitivity showing swelling index c(s) vs. Clay faction * liquid limit (%). Redrawn from Mesri et al. (1978). Red dashed lines represent unload/reload cycles. The 1st cycle would be unloading due to excavation, reloading to insitu effective stress then unloading for testing.

6.6.5. Low effective stresses

From Section 6.6.4 showing swelling and swelling strain indices vs effectives stress, the region between 0-5% unload shows a significant increase in indices values which corresponds to stiffness degradation. In general, strains below 0.1% exist in this region and this is discussed in Chapter 6. The other region where indices reduce is in between 90-99% unload. In this case, low effective stresses are examined. This region is complex due to issues with creep and sensitivity to changes in laboratory temperature. Looking at swelling behaviour at 95-99% unload on Figure 164, the swelling index only tails off slightly in most cases. However, each test behaves differently at low effective stresses and some UMB tests on Figure 164 have swelling index value that are rising until 99% unload. Furthermore, using Figure 165, it is clear that each material behaves differently at low effective stress. The rate of change of swelling index remains largely positive for UMB, while for the other materials there is a clear 'tail' off towards negative rate of change of swelling index.

This becomes more visible on Figures 166 and 167. Here as each test swells at lower effective stresses a difference in behaviour is noted. For the majority of London Clay tests the gradient becomes flatter and for UMB the gradient remains steeper for longer. This effect can be seen in Figure 164 where each test in yellow (LC unit A2) has a swelling index that begins to fall around 95% until 99% where it drops off significantly. As for tests in red (UMB) where the swelling index continues to rise from 95-99% before tailing off. The difference in this behaviour could be due be several factors; first, the clay content of the samples as UMB has generally the highest clay fraction. Second, it could be the effects of creep, because all tests shown here have time intervals that could induce creep.

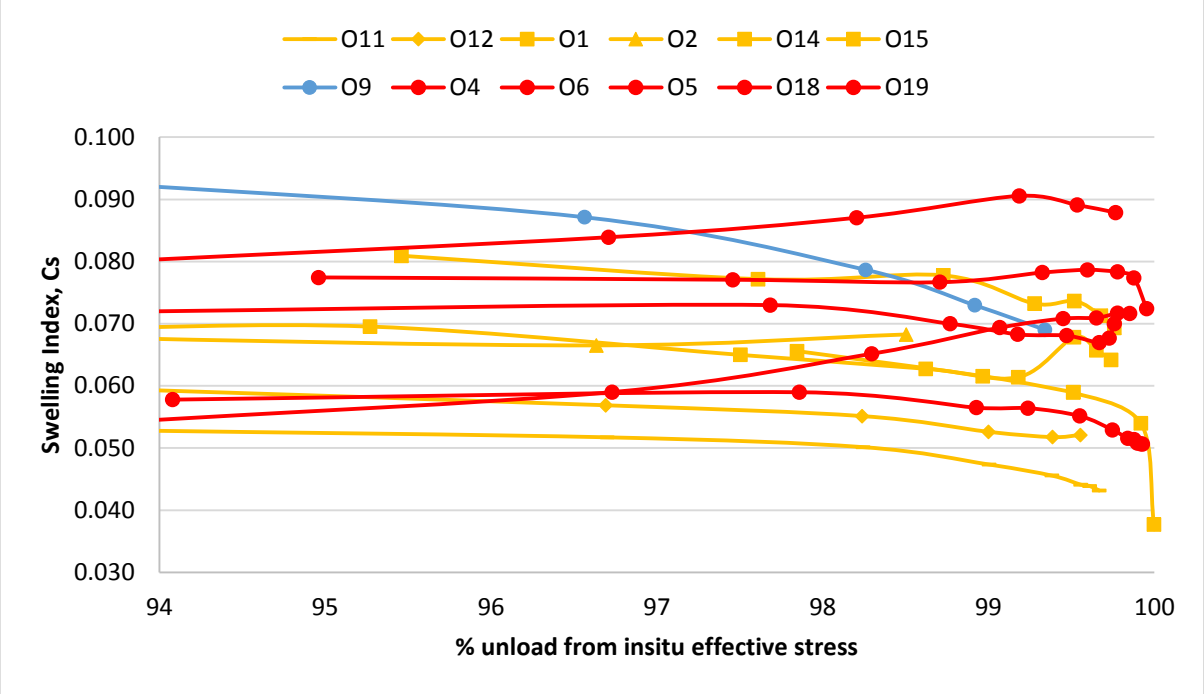

Figure 164: Swelling index vs. % unload - very low effective stresses. UMB (red), A2 (yellow), B2 (blue).

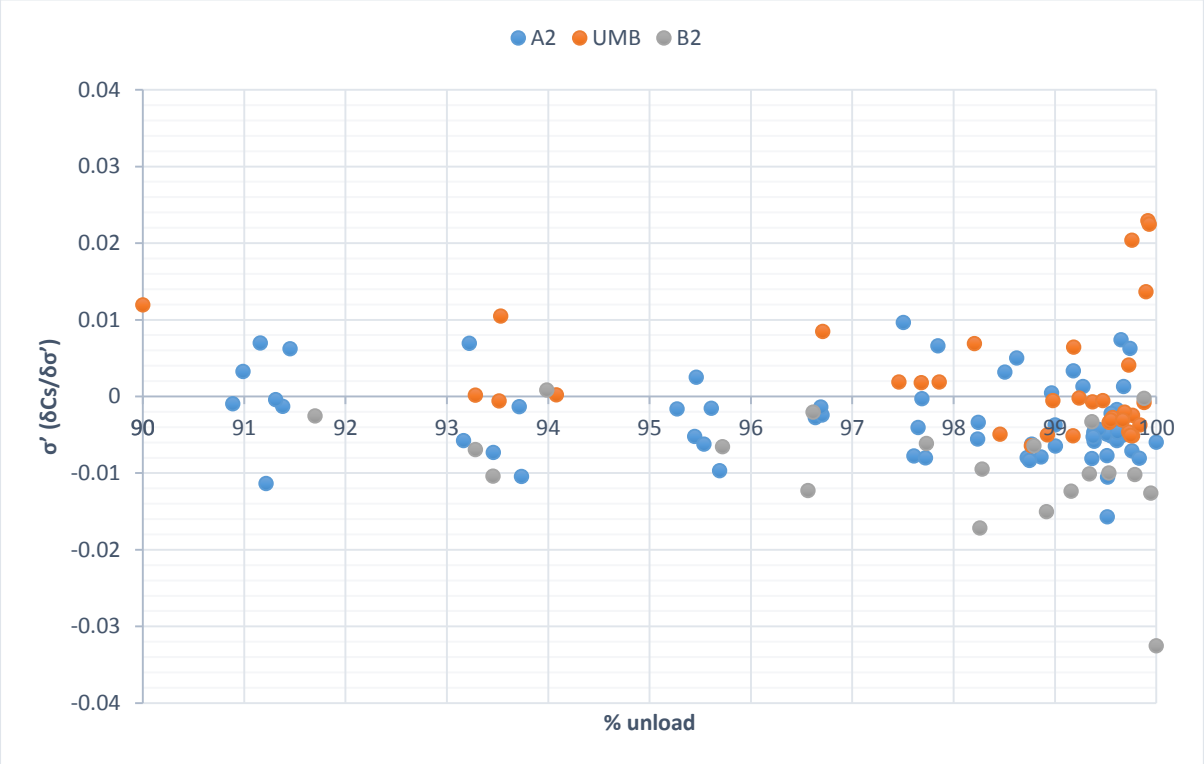

Figure 165: Rate of change of swelling index

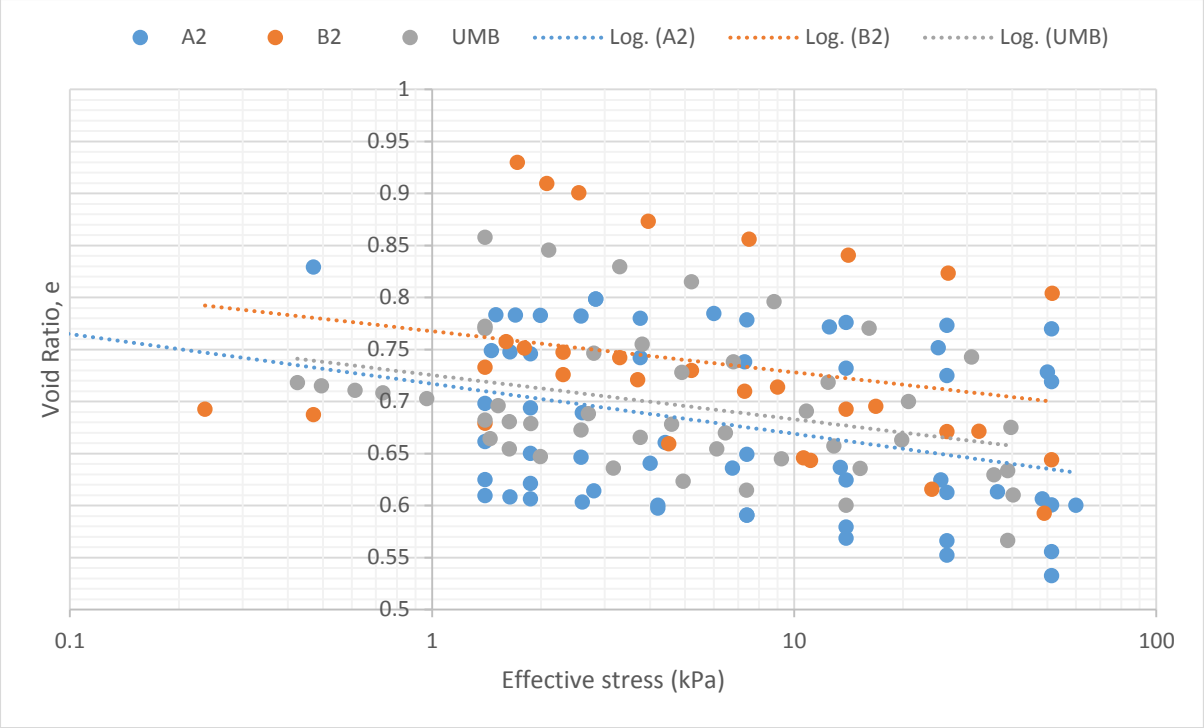

Figure 166: Void ratio effective stress space for low effective stresses

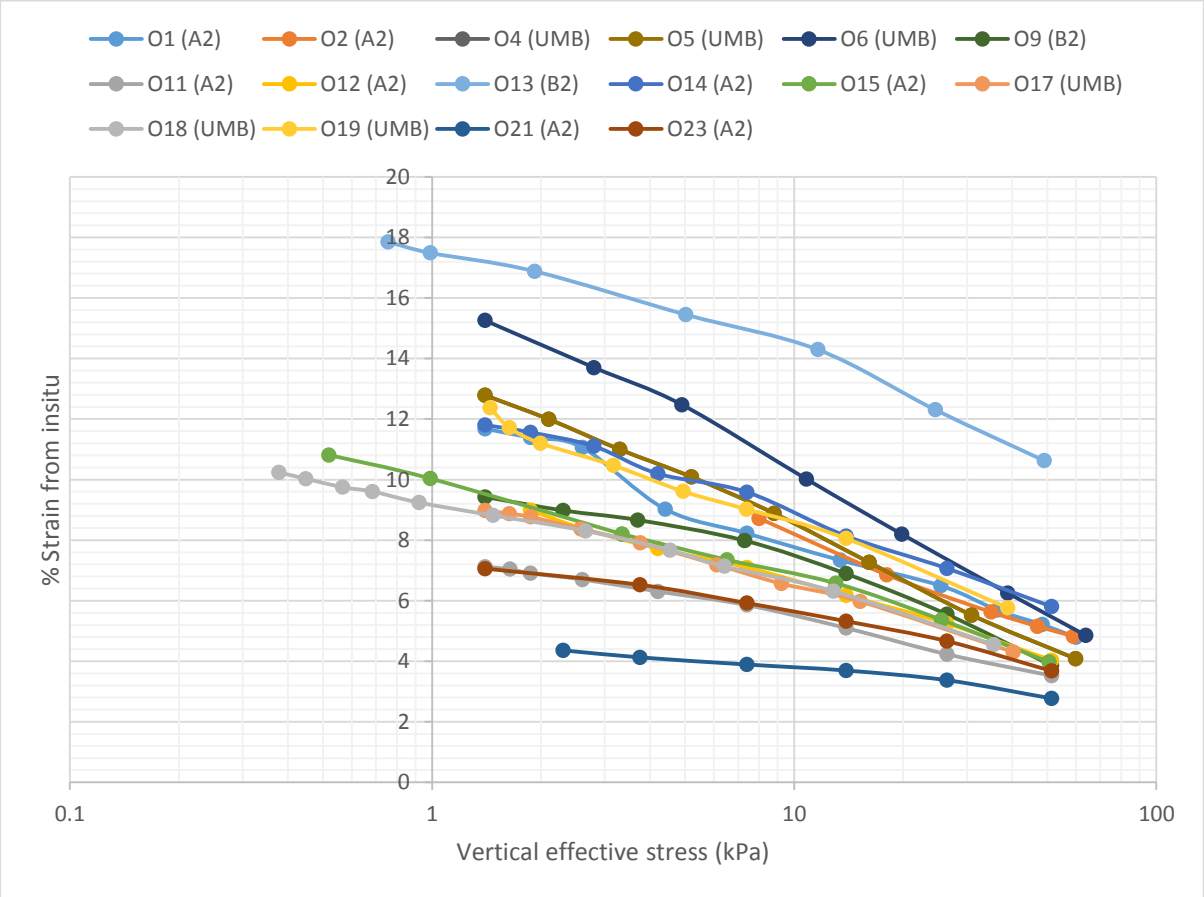

Figure 167: Unloading of samples at low effective stresses

6.6.6. Length of time interval between stress increments

Tests O11 and O12 (London Clay Unit A2) were used to compare swell behaviour (Figure 168). These tests were carried out to address concerns about occurrence of creep at low effective stresses. O11 and O12 underwent a swell at 24 hour intervals then O12 was reloaded to 400kPa and then unloaded at 48-hour intervals. What was expected was an increase in the gradient of the unload-reload line but instead the gradient was shallower with an exception to the final datum point which saw a sharp rise in swell. The reload-unload cycle may have had more of an influence on the second unload cycle than the 48-hour intervals. This suggested that the gradient of the unload line should be similar whether a 48 hour or 24-hour time step is used, but it was not conclusive. Therefore, two further tests were conducted with reload-unload cycles that run in parallel.

The tests first followed the same stress path. Both were saturated at insitu effective stress, then were unloaded to a nominal weight (1.5kPa) in 8 decrements. Finally, each specimen was reloaded to 50kPa and was left to consolidate for 48 hours. At this point specimen O21 was unloaded by 50% every 24 hours while O23 was unloaded by 50% every 72 hours. Once at nominal weight the specimens were reloaded to 50kPa, allowed to sit for 48 hours and the process was repeated with O21 unloaded every 72 hours and O23 unloaded every 24 hours. The results are in Figure 169 and show differences between tests.

Both tests behave similarly on first unload and both show the reconsolidation does not follow the same path. However, after this point O21 reloads and unloads along the sample stress-strain path showing the second unload did not further contribute to disturbing the specimen. As for O23, the second unload conducted at 72-hour time intervals effected the second reconsolidation as the same strain was not reached. This suggests that longer time intervals do induce some creep. In the case of O23, around 1% strain can be considered creep on the second reload-unload cycle. In other words, a 24 hour time interval is correct as the primary component of swell is measured; however, any longer may induce creep that will effect reconsolidation if further testing on the sample were desired. It should be noted that pore water pressures would have been beneficial but were not monitored.

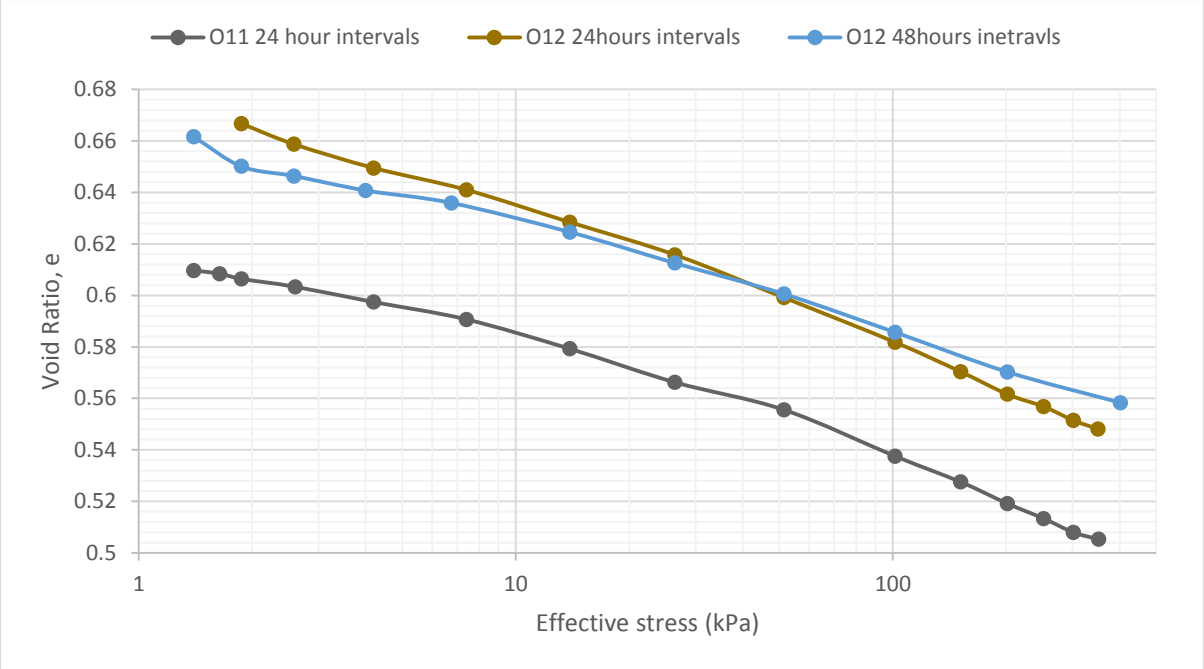

Figure 168: Difference between 24 hour and 48-hour time intervals on London Clay A2

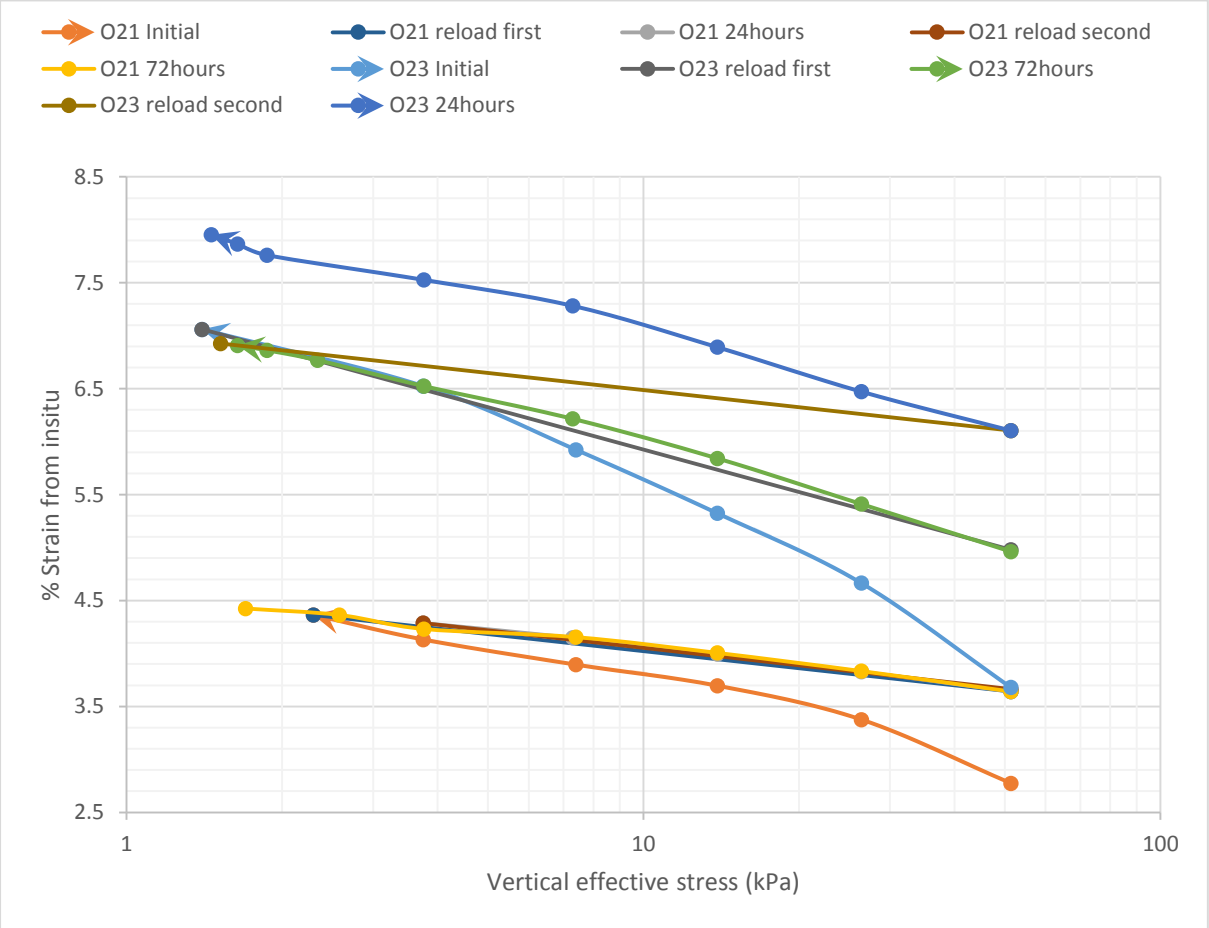

Figure 169: Unload-reload cycles for tests O21 and O23 – London Clay A2

6.6.8. Comparing sample orientation

It is believed that OC clays are highly anisotropic and although the focus of this research is on behaviour of clays on unload, test O20 on London Clay Unit B2 was conducted with a horizontal orientation in order to examine the difference in behaviour in unload.

The O20 sample showed greater stiffness than the other tests conducted for vertically orientated samples. Unloading by 5kPa intervals gave small strain responses. When compared to O22 (Unit B2 with vertical orientation) which begun unload at around 2.5 times the vertical effective stress O20 begun at, the behaviour is initially similar, while at larger strains the stiffness of O20 degraded faster (Figure 170)

Overall, O20 in the horizontal orientation was more than twice as stiff. This is expected for London Clay (Nishimura, 2005).

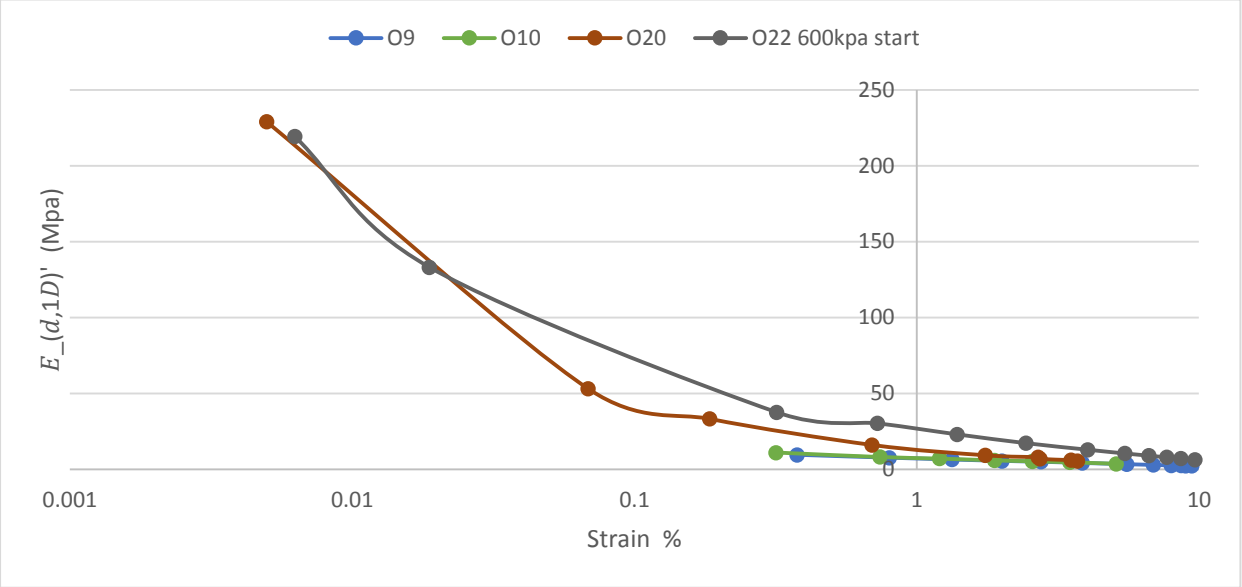

Figure 170: Comparing horizontally cut sample O20 with vertically cut samples are with test O22 which was unloaded from a greater effective stress

6.7. Rowe Cell Testing

6.7.1. Intact behaviour

In addition to oedometer tests, Rowe cell testing was conducted to compare with the results obtained. The Rowe cell apparatus benefits by being a larger specimen which should lead to less disturbance during preparation of specimens. All specimens are taken from block sample and were trimmed in accordance to section 5.6.

The stress paths taken differed based on limitations of the apparatus. The intention was to flood each sample at insitu effective stress, consolidate to mitigate any effects of destructuring, unload to 95% insitu effective stress and then bring back to insitu effective stress. Once at insitu effective stress the specimen could be left for up to two weeks before unloading. In reality, the specimens would not always be fully wetted at insitu effective stress, requiring a larger back pressure on the sample and thus a reduction in effective stress. In the case of R4, nearly all effective stress was removed so that back pressure nearly equalled the cell/ram pressure.

Struggling to obtain a wetted sample was the main issue with the apparatus but this issue was compounded by the limit of 2MPa of the pressure volume controllers. If the controllers had a limit of 3MPa to match the cell then wetting at insitu effective stress may have been possible because higher back pressures would have aided the wetting process. Additionally, a mid-height pore pressure transducer would have made the process of working out whether the sample was fully wetted much easier. It took several months and a large number of B-Value tests to establish the samples were not wetting at insitu effective stress. Note: The desired B-Value was 95%.

Another issue faced was a lag in stress change, this became apparent when following a stress path to get to insitu effective stress before unloading. At times, unloading would cause consolidation or loading caused swelling. This behaviour indicated that the time interval between stress change needed to be increased and it was found that 72 hours was effective. However, the load step prior to 95% insitu effective stress and to insitu effective stress were lengthened to 1 week each to ensure equilibrium of the sample at these stresses.

In Table 20, a summary of the key measured variables is shown. Comparing with Table 15 shows that the samples had similar initial properties with an exception being R1 where the

sample experienced some drying out prior to the test begun. Saturation pressures were lower than for the oedometer due to the issues discussed.

Table 20: Summary table of intact specimens for Rowe cell tests

Specimen	Material	Orientation	Initial water content %	Effective stress at saturation (x insitu effective stress kPa)	Bulk Density (Mg/m^3)	Initial void ratio, e0	Specific gravity Gs
R1	B2	Vertical	23	7.1 (1st saturation method used)	2.0	0.78	2.83
R2	UMB	Vertical	22	0.08	2.1	0.87	2.81
R3	UMB	Vertical	21	0.16	2.2	0.80	2.73
R4	A2 (lower)	Vertical	27	0.01	2.1	0.83	2.80
R5	A2 (upper)	Vertical	21	1	1.9	0.69	2.74

In Figure 171, R1 is shown in consolidation and for a swell cycle. The first data point looks out of place on the Figure and is possibly caused by the lag in the system as a result of shear effects between the ram and the walls of the Rowe cell. This is a common problem with the Rowe cell apparatus – silicone grease was applied to the walls of the cell for future tests to prevent this.

The specimen was consolidated to 2MPa where it was left for a week. Then it was unloaded to 95% insitu effective stress and reloaded to insitu effective stress (240kPa). The sample was then left for a week. A series of load decrements are then applied showing a clear trend.

A comparison between Rowe cell and oedometer tests for Unit B2 taken from the same block sample are shown in Figure 172. At 1% strain the R1 is 1.87 times the one-dimensional stiffness of O9 and O10. The difference between specimen volumes (V) are R1 is 2.76 and

3.45 times larger than O9 and O10, respectively. Considering sample surface area (SA), R1 has 1.88 and 2.02 times more surface area than O9 and O10, respectively.

$$V = h_{sample}\pi {r_{sample}}^2 \tag{6.20}$$

$$SA = (h_{sample}\pi d) + 2\pi {r_{sample}}^2 \tag{6.21}$$

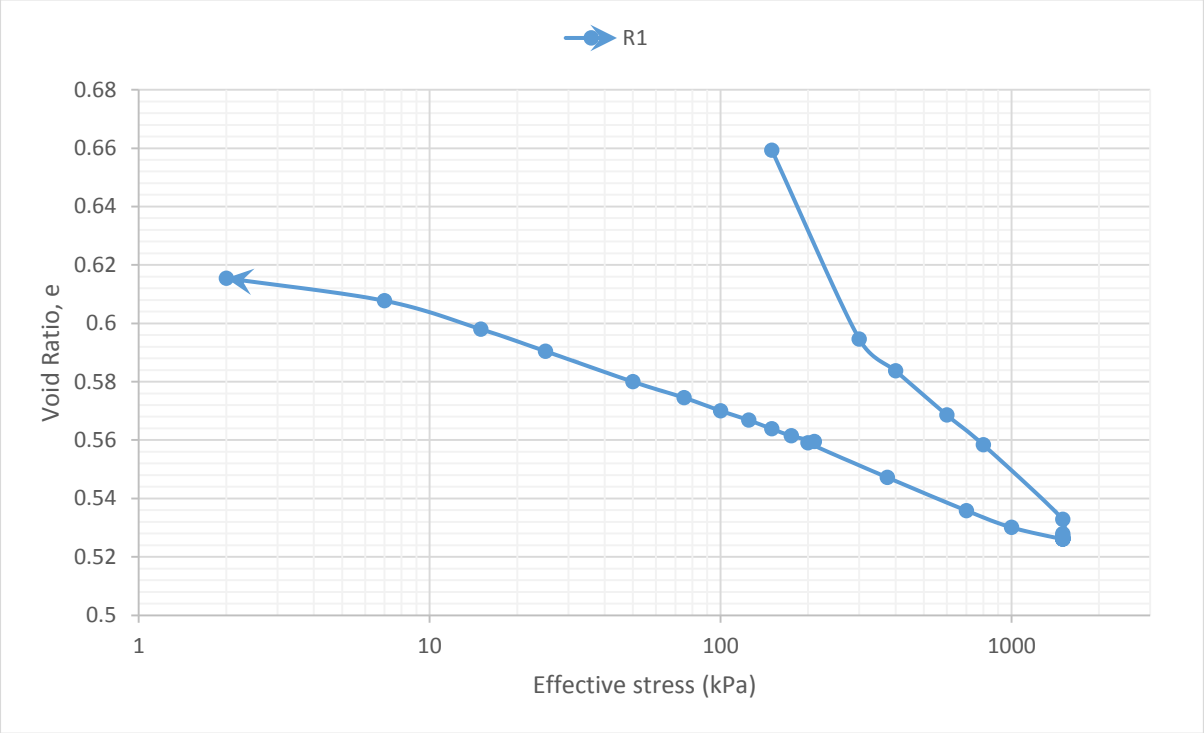

Figure 171: Unit B2 Rowe cell specimens plotted in void ratio vs effective stress space

In Figure 173 two swell cycles are shown for R2 and R3; both specimens are UMB. R2 is taken to 2MPa before being unloaded to 50kPa. The specimen is then reconsolidated to 2MPa and unloaded again to 80kPa. Examining R2 closer, on the first consolidation and unload cycle, as R2 reaches 2MPa and is unloaded the response of the sample is to consolidate. This is likely to be lag in the system caused by full consolidation not being reached before being unloaded. This is further confirmed when the specimen is reconsolidated as the specimen reaches a lower void ratio at 2MPa. Both gradients of the swell lines for R2 are similar.

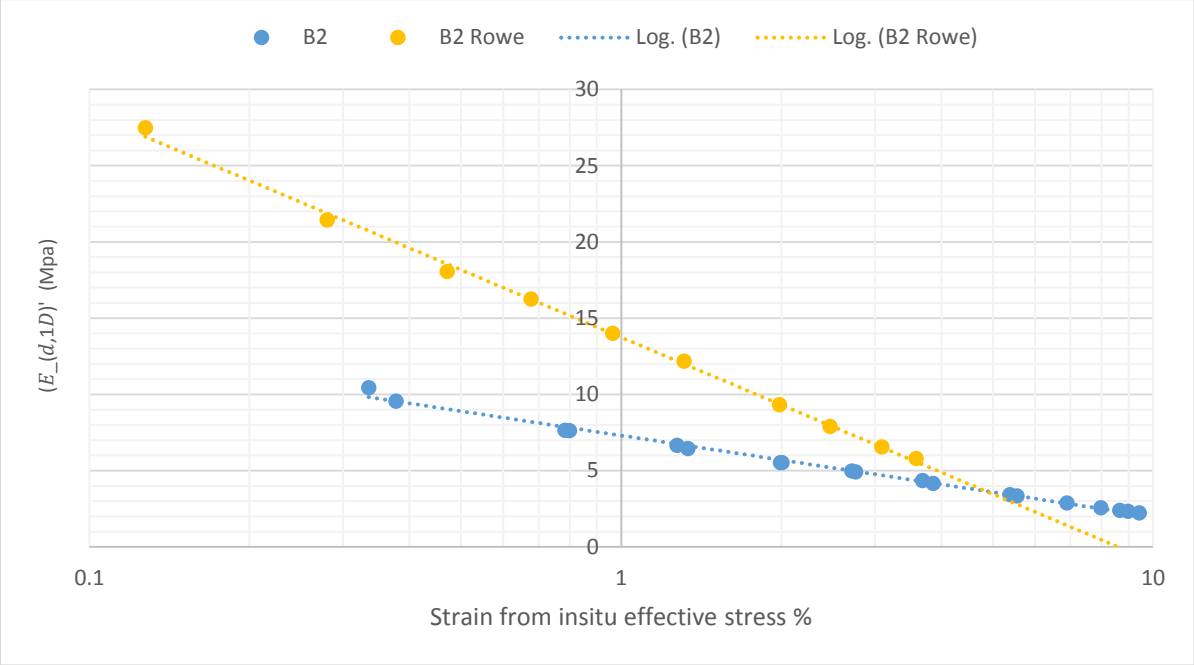

Figure 172: Comparing large strain stiffness degradation of London Clay Unit B2 on unloading from insitu effective stress in Rowe cell and oedometer

R3 is first shown from insitu effective stress and is then unloaded to 100kPa before being reloaded to 1MPa. Finally, the specimen is unloaded in small decrements every 72 hours. Both gradients of the swell lines for R3 are similar. The second swell for R3 shows in detail the gradient of the swell line. Each decrement shows a consistent response in the system with there being the occasional data point showing very little swell followed by a data point which shows greater swell; this further demonstrates friction on the Rowe cell walls.

It is worth noting that more than one swell cycle was examined for tests R2 onwards. This was because each test took such a long time to prepare it was preferred that the effect of repeatability was examined over attempting more samples.

A comparison between Rowe cell and oedometer tests for UMB are shown in Figure 174. At 1% strain the R1 is 1.48 times the average one-dimensional stiffness for O3, O4, O5, O6, O17, O18 and O19. The average difference between sample volumes is 2.79 times larger for Rowe cell samples and average surface area differences are 1.89 times larger for Rowe Cell samples.

Examining the effect of sample size further, Figure 175 shows a comparison between Rowe cell and oedometer samples that have a ratio between specimen specific area (surface area / specimen volume) less than 0.16 and oedometer samples that have a specific area greater than

0.16. Rowe cell specific area ~0.11. The Figure clearly shows the greater the specific area the smaller the stiffness of each specimen.

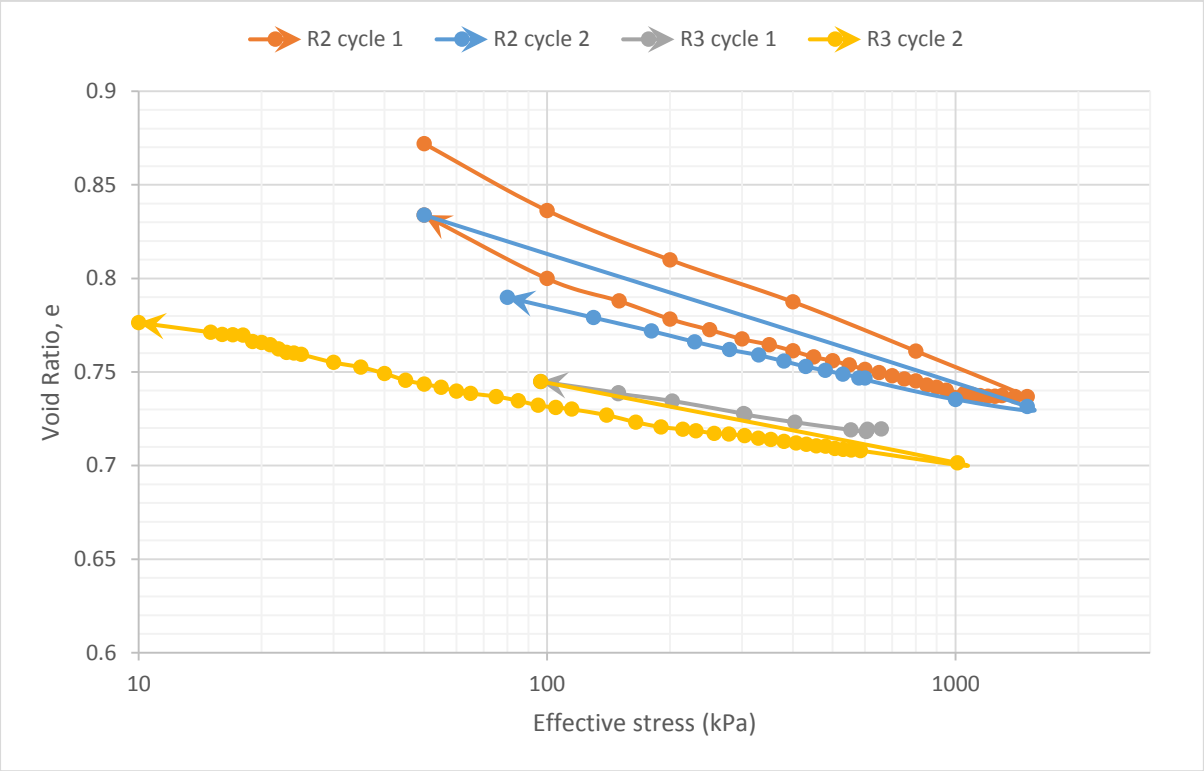

Figure 173: UMB Rowe cell specimens plotted in void ratio vs effective stress space

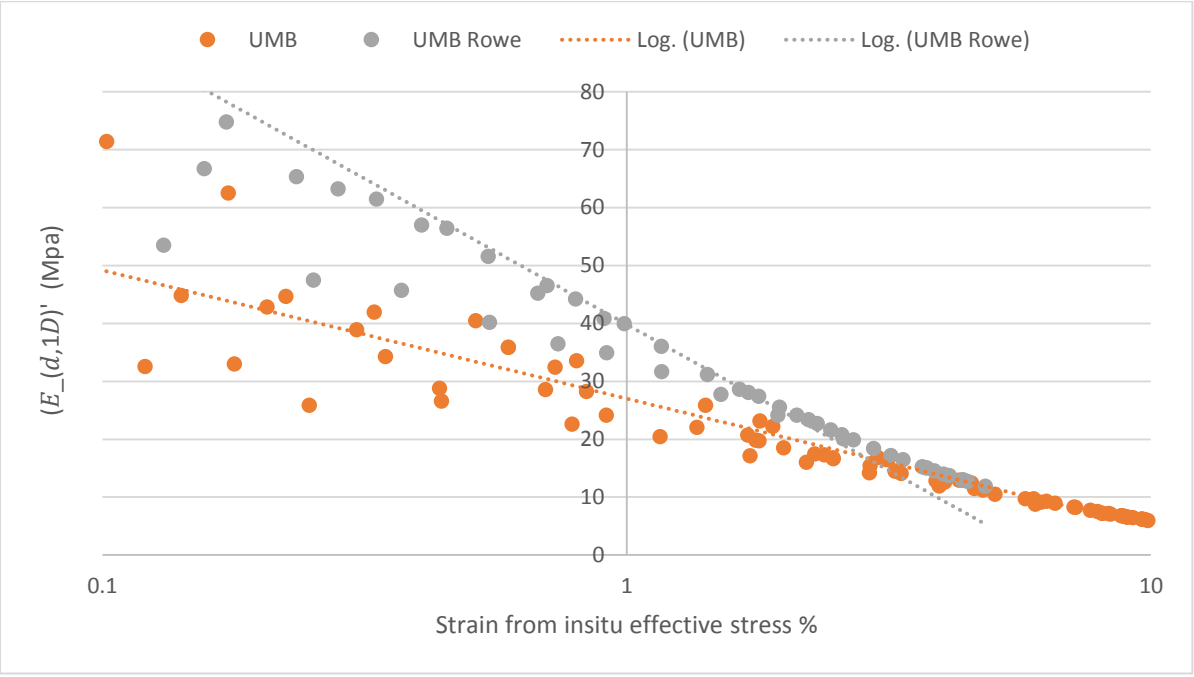

Figure 174: Comparing large strain stiffness degradation of UMB on unloading from insitu effective stress in Rowe cell and oedometer

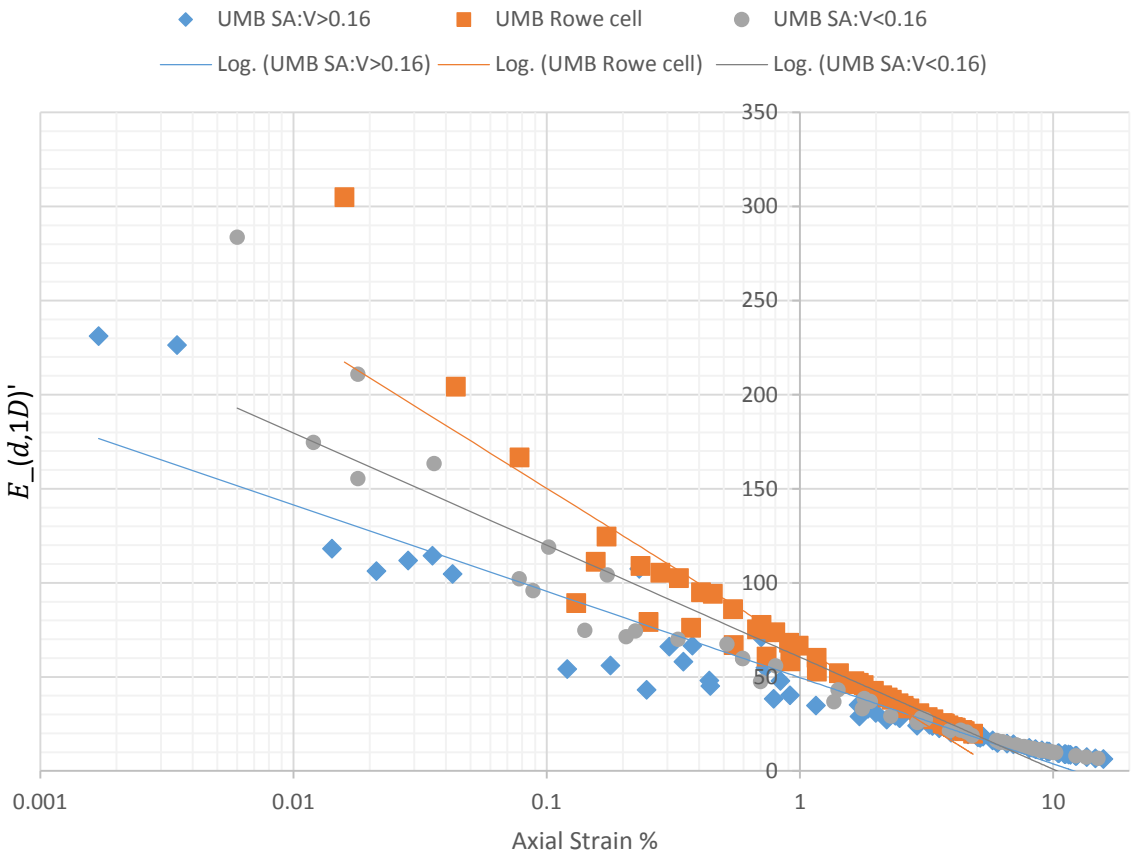

Figure 175: Comparing normalised stiffness degradation of UMB on unloading from insitu effective stress for different specific areas (termed SA:V)

In Figures 176 and 177 the behaviour of R4 can be seen. The specimen follows the stress path described earlier but a week-long rest at insitu effective stress (600kPa) was an insufficient amount of time to allow the sample to consolidate fully. After a further 15 days (5 unload steps at 72 hours between each step) the sample is reconsolidated and shows further consolidation from cycle 1 to cycle 2. This demonstrates the complexity of testing accurately for smaller strains using apparatus best suited for large strain analysis. Nevertheless, both cycles show similar small strain behaviour with cycle 2 concluding at 8% of insitu effective stress.

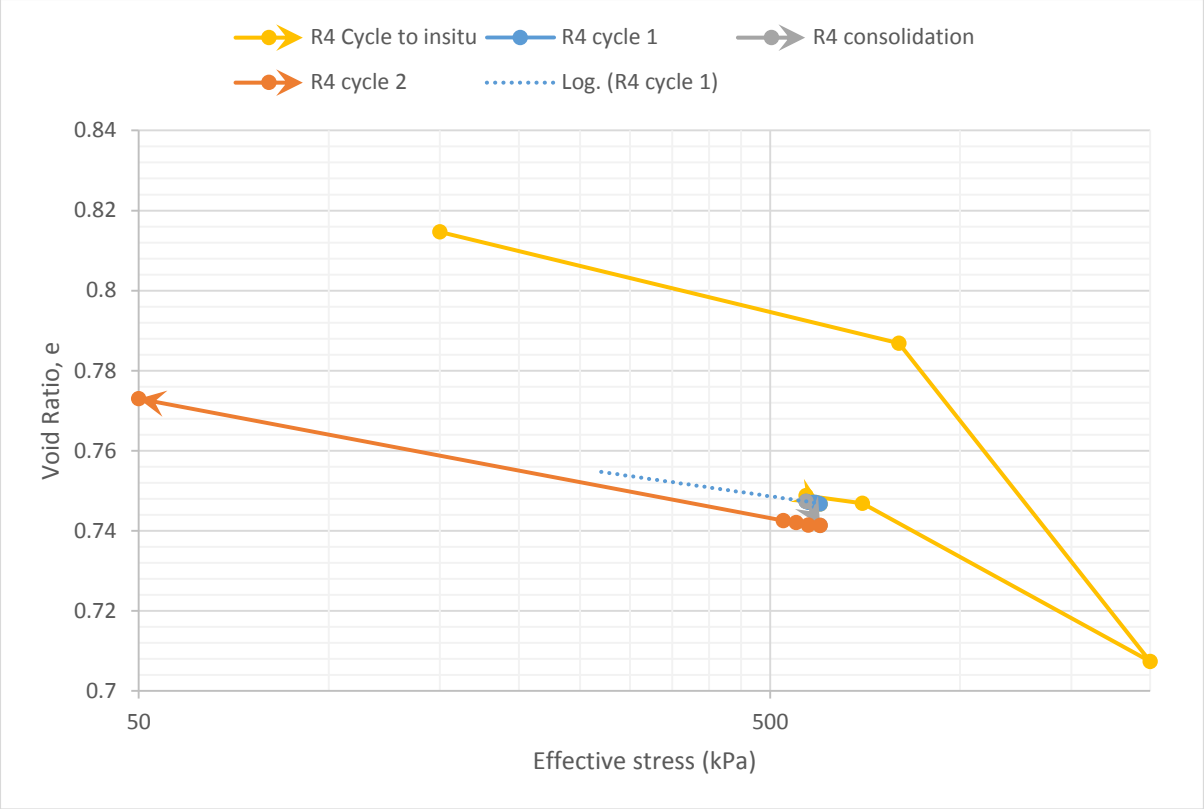

Figure 176: Unit A2 lower Rowe cell specimen plotted in void ratio vs effective stress space

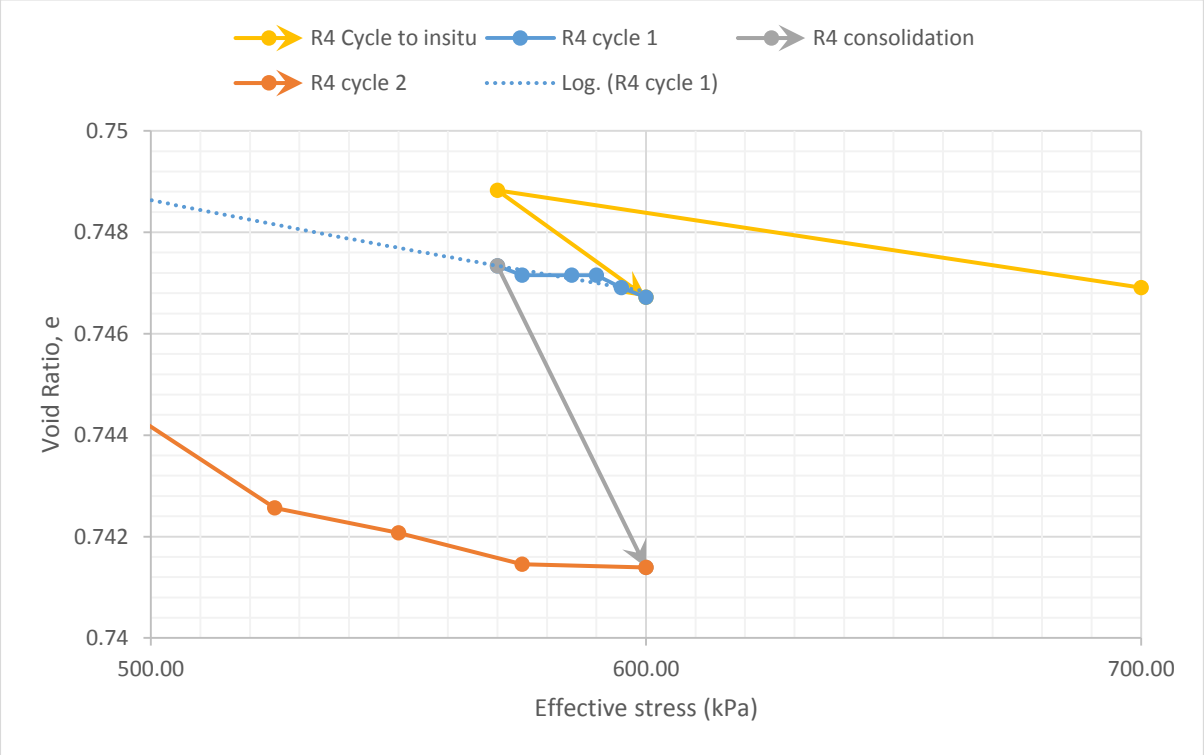

Figure 177: Behaviour around insitu effective stress - Unit A2 lower Rowe cell specimens plotted in void ratio vs effective stress space

In Figures 178 and 179 the swell cycles of specimen R5 are shown. Cycle 1 and cycle 2 both show lag when the first load decrement is applied. This may be a fundamental issue with the Rowe cell apparatus as the specimen was left for several weeks to stabilise at insitu effective stress before each of the unload cycles. Examining cycle 2 in more detail, it is clear that the gradient of the swell line in semi-logarithmic space is non-linear. However, there may be an effect from hysteresis that cannot be ignored. Throughout Rowe cell testing, the specimens have been slow to respond to changes in stress and the stress path used in oedometer testing, which is party designed to remove the effects of hysteresis, was not used due to the limitations of the apparatus. Overall the hysteretic effects may only influence the first few unload steps from insitu effective stress but this may lead to over-prediction of the stiffness.

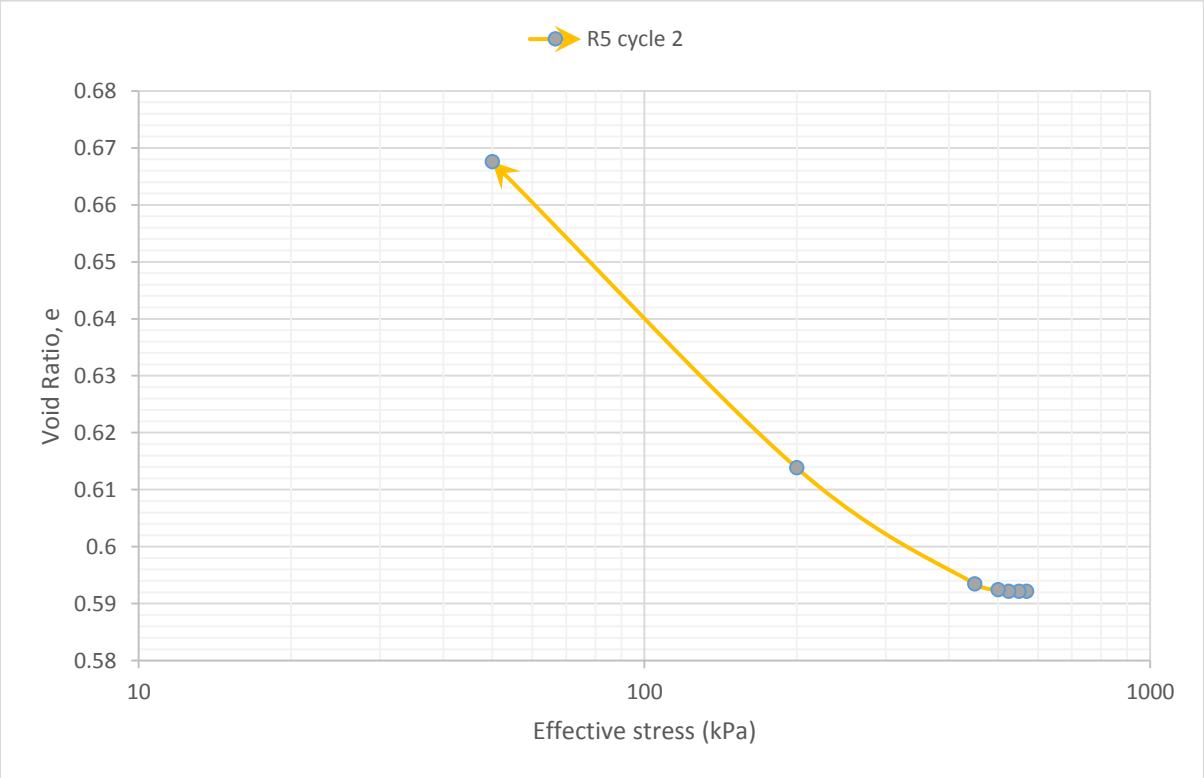

Figure 178: Unit A2 upper Rowe cell specimens plotted in void ratio vs effective stress space

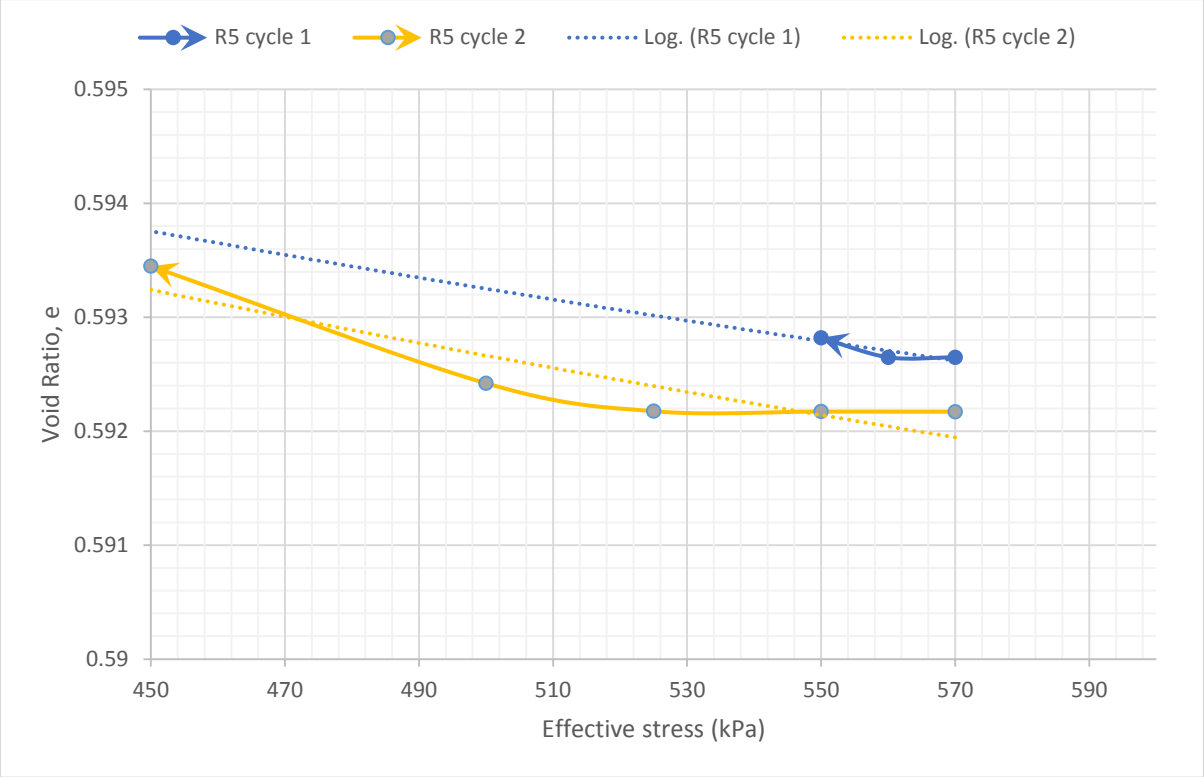

Figure 179: Behaviour around insitu effective stress - Unit A2 upper Rowe cell specimens plotted in void ratio vs effective stress space

When plotted together in Figure 180, there are wide ranges of results with a general trend towards greater stiffness with sample size and sample depth insitu.

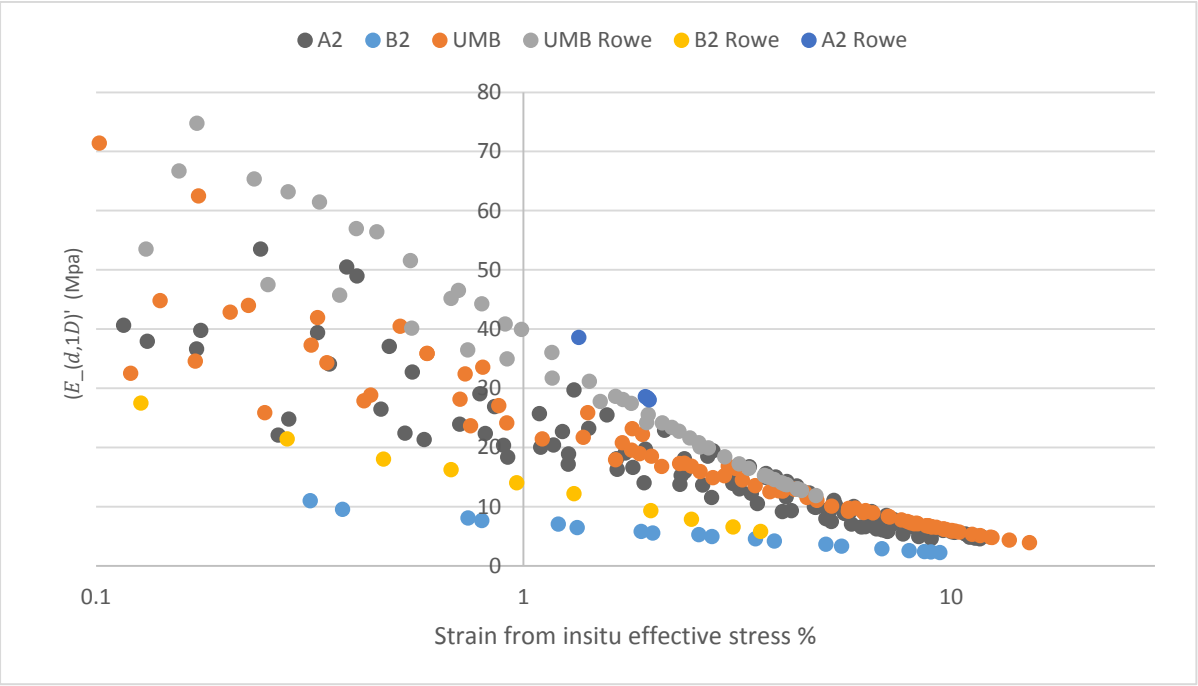

Figure 180: Comparing Rowe cell data with oedometer for large strain behaviour in Young's modulus vs effective stress space

6.7.2. Small(er) strains

When considering smaller strains from tests R1-R5 and then comparing with oedometer data in Figures 181 and 182, it is clear that sample size influences stiffness at smaller strains. Oedometer sample stiffnesses at strains below 0.1% are comparable with the relationship with effective stress with strains after 0.1% as the gradient of stiffness degradation continues at a similar rate. However, at smaller strains Rowe cell samples have stiffnesses much greater than the stiffnesses after 0.1%. This demonstrates that sample size has a large effect on the behaviour of OC clay at smaller strains. This small strain data will be used again in Chapter 7 to compare with triaxial data.

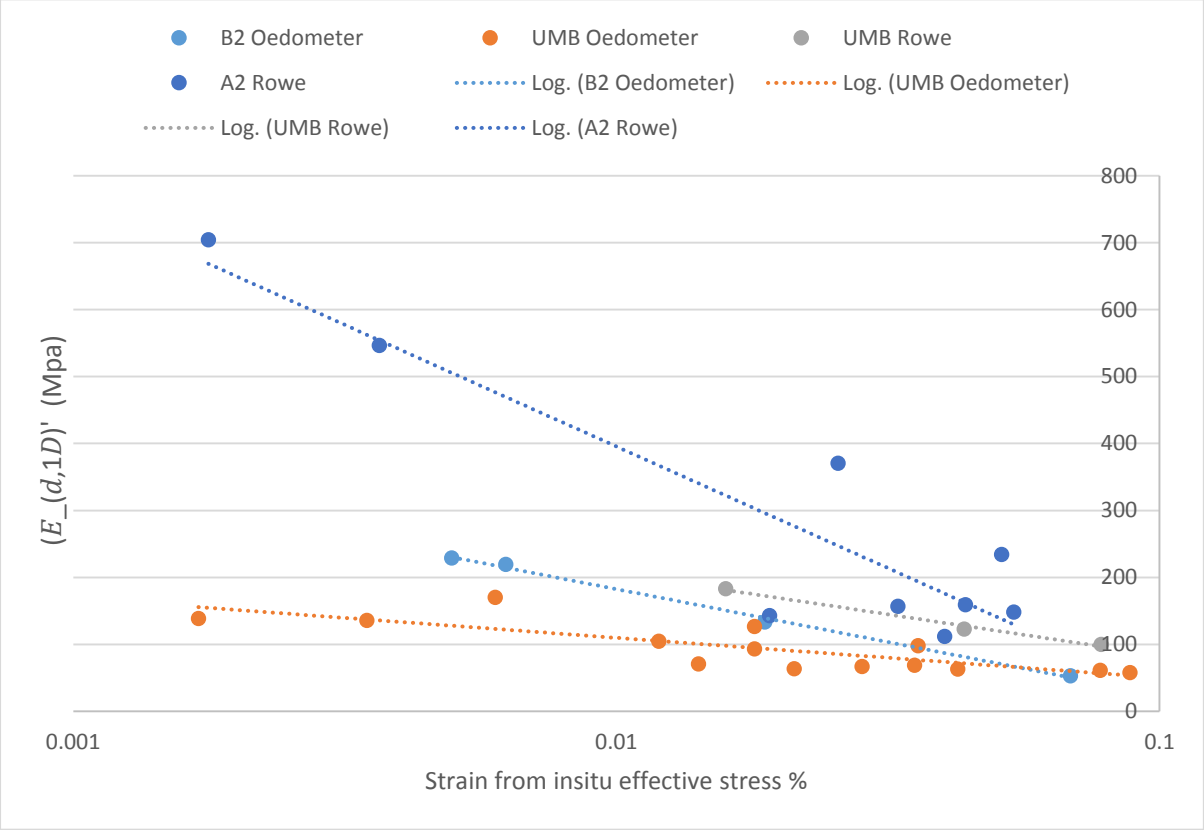

Figure 181: Comparing Rowe cell data with oedometer for small strain behaviour in Young's modulus vs effective stress space

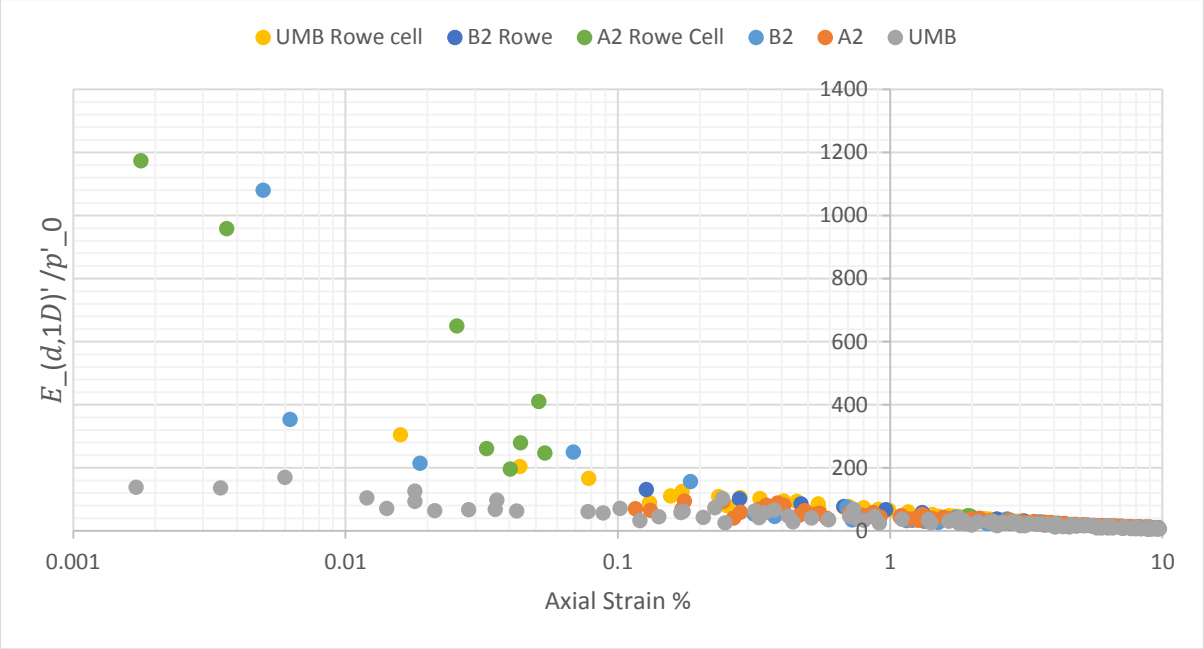

Figure 182: Comparing Rowe cell data with oedometer when normalised by insitu effective stress

6.7.3. Swelling parameters

As well as increased stiffness at small strains, Rowe cell specimens continued to act stiffer throughout each test. When converted into swelling index all Rowe cell data sits below oedometer data in Figure 183. Additionally, when plotted on Mesri et al's Figure 184, data for the Rowe cell sit close to the undisturbed line while oedometer data sits between the 1st and 4th cycle line.

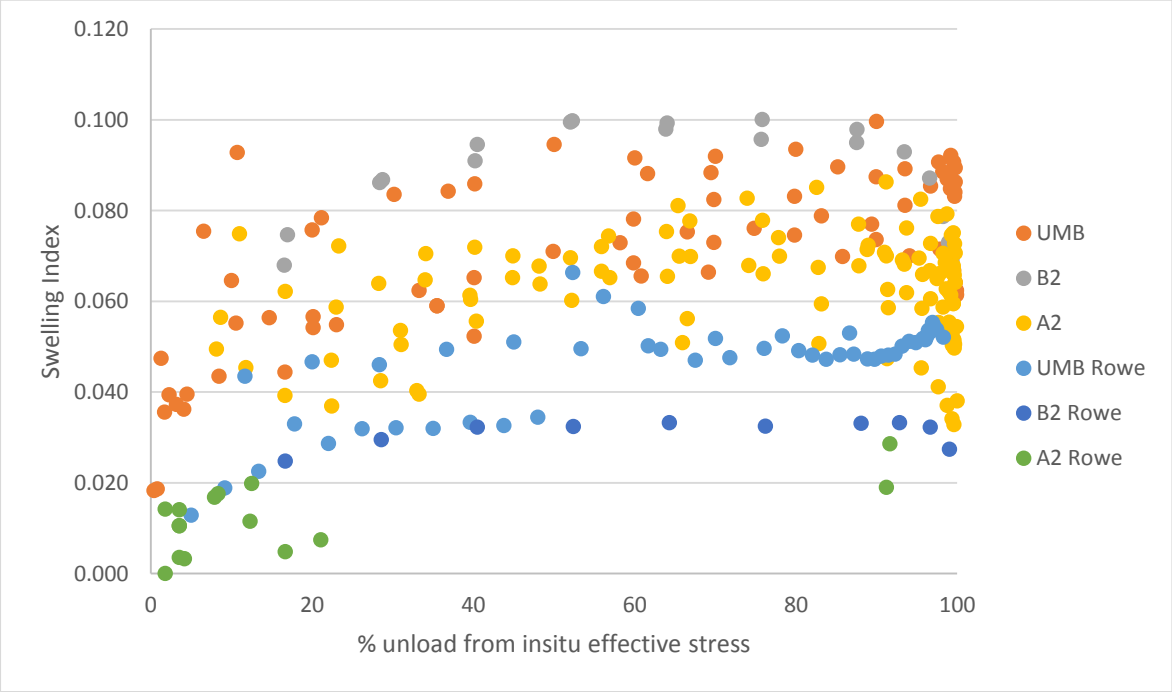

Figure 183: Comparing Rowe cell data with oedometer for swelling index

If swell sensitivity is measured using the Equation: remoulded swelling strain index /undisturbed Rowe cell swelling strain index, taken from Schmertmann (1969), the values are: 3.82, 3.00 and 3.15 for B2, A2 and UMB, respectively. This means they all have medium sensitivity with B2 having the greatest sensitivity.

In general, heavily overconsolidated clays have lower sensitivity due to lower moisture contents and for oedometer data this theory holds as B2 has the highest overconsolidation ratio but Rowe cell data does not follow this trend. UMB is more sensitive to disturbance than A2.

When comparing with Crossrail data the influence of disturbance becomes even clearer. Crossrail samples were collected using high quality rotary cores and compared with samples taken from block samples in this thesis. The data are in Figure 185 and it is clear that using the ranges of LL and clay fraction in the report, all Crossrail data sits higher on the Figure than the data in this thesis. If swell sensitivity is calculated from the Crossrail undisturbed data and the remoulded data in this thesis, the values are: 1.12, 1.02 and 1.20 for B2, A2 and UMB, respectively.

Overall, the data from the Rowe cell shows the apparatus has huge potential for examining overconsolidated clays. The additional volume leads to a less disturbed sample and with careful preparation methods the data can better represent insitu one dimensional problems such as basement excavations. However, there are difficulties with the apparatus as it is currently best suited to large strain testing. The apparatus could be improved with some modifications such as: a mid-height pore pressure transducer; a frictionless ram; and high-pressure pressure/volume controllers (3 MPa).

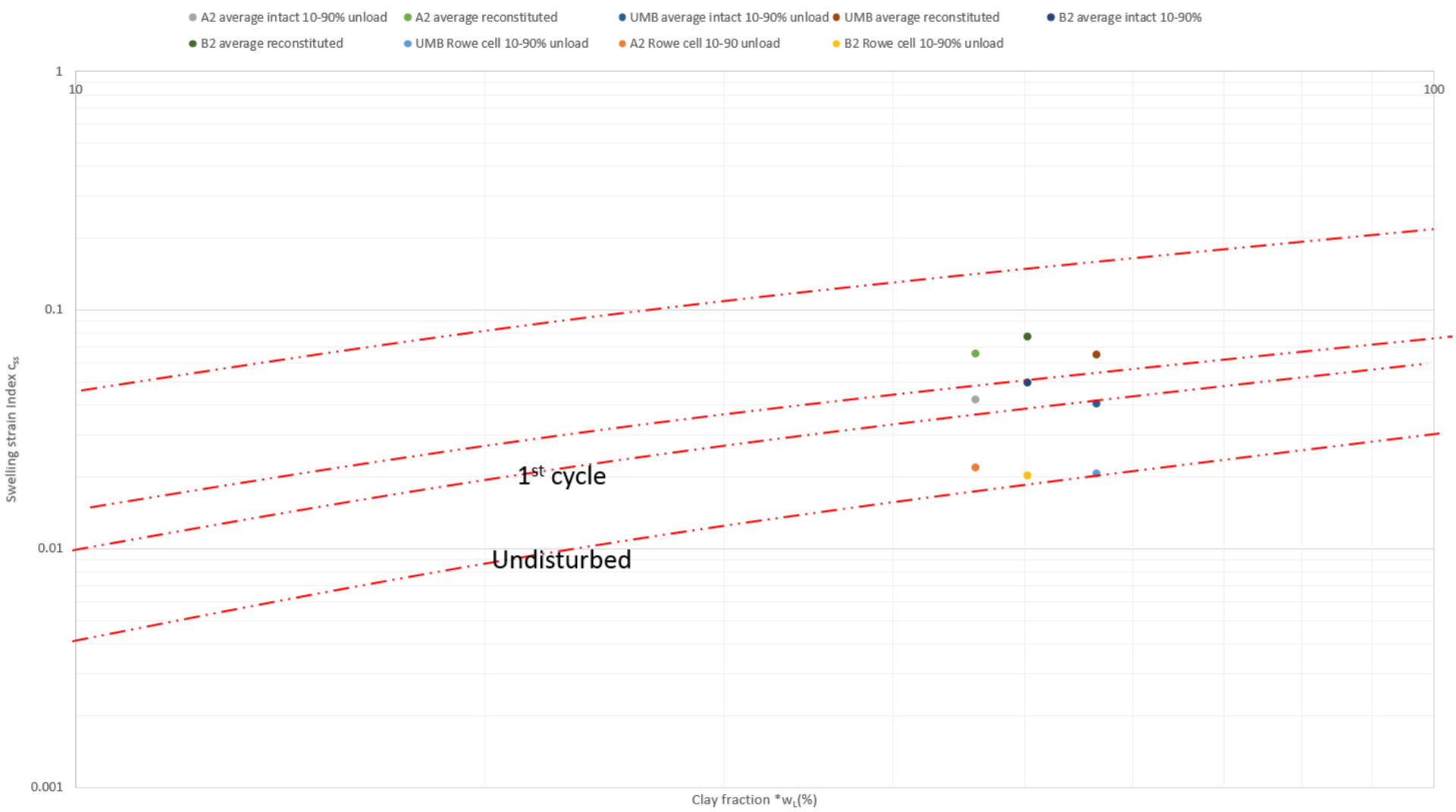

Figure 184: Redrawn diagram from Mesri et al. (1978). This plot shows reconstituted oedometer samples, intact oedometer samples and Rowe cell specimens.

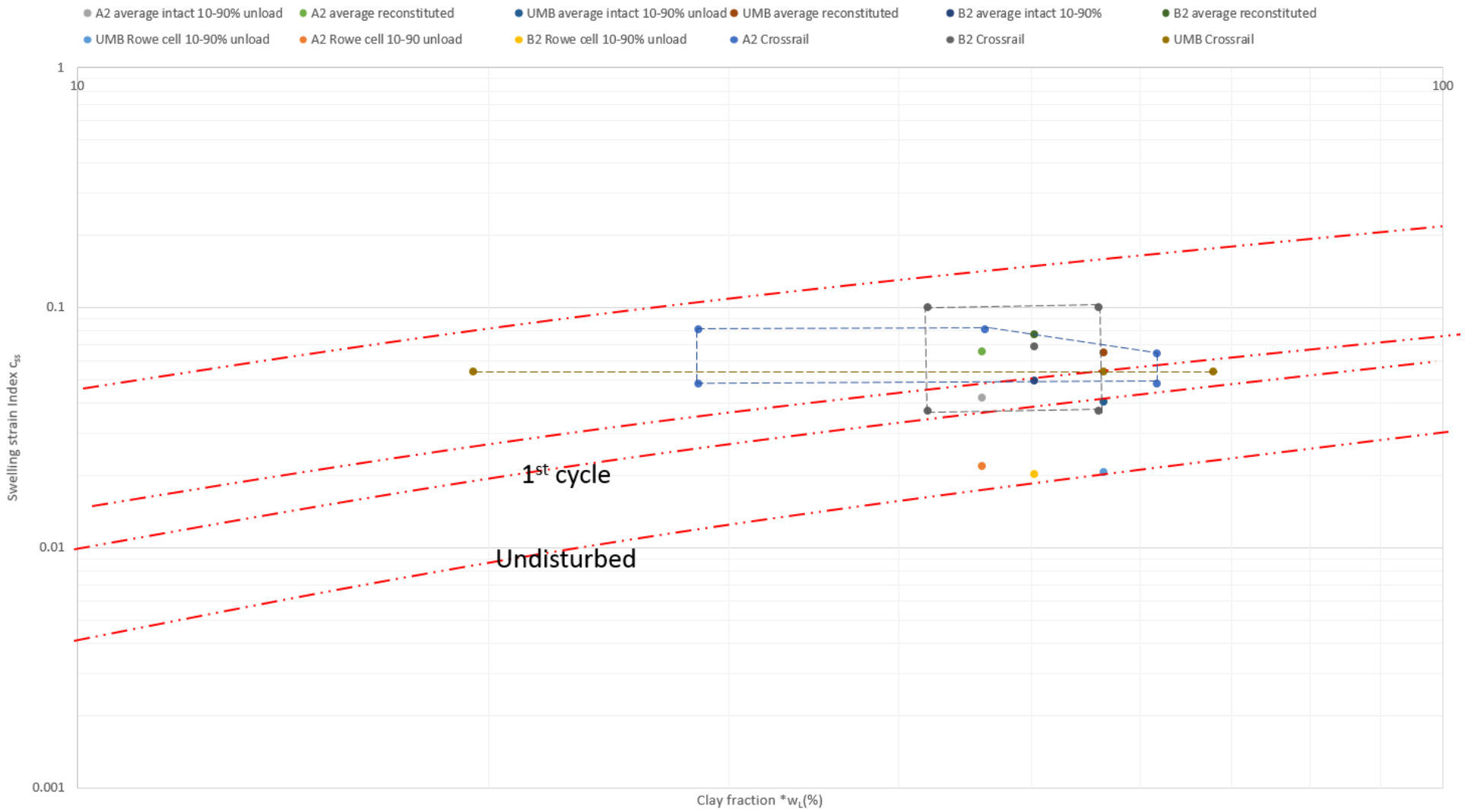

Figure 185: Swell sensitivity using Crossrail data which is shown within the boxed regions against the data in Figure 185

6.8. Summary

Oedometer and Rowe cell testing was conducted to better understand the unloading behaviour of overconsolidated clays from their insitu effective stress states. Unloading was found to *generally* be slightly non-linear in semi-logarithmic space (e -log σ' or v – log σ'). What has been observed is that behaviour can be clearly divided into categories as follows:

- Strains below 0.1% - Stiffness decreases dramatically up to this strain and appears non-linear in degradation; swelling/strain indices are highly non-linear. % unload below 6%
- Strains 0.1-0.5% - Stiffness degradation begins to change from non-linear to linear - % unload 6-35%
- Strains 0.5-1% - Stiffness degradation appears linear (approximately consistent values of swelling/strain indices are reached) - % unload 20-45%
- Strains 1-3% - Stiffness degradation appears linear but at a decreased rate - % unload 35-90%
- Strains 3-6% - specimens trend towards a non-linear degradation of stiffness - % unload 65-100%
- Strains greater than 6% - Stiffness degradation is minimal but all specimens appear to degrade non-linearly towards a critical stiffness - % unload 85-100%

Stiffness in large strain is broadly similar when normalising using insitu effective stress. This is useful for designers of deep basements as ever deeper basements are constructed into these materials. Stiffness degrades *approximately* linearly between 0.5%-3% strain (20-60% unload) on a semi-logarithmic graph meaning constants could be used to predict the variation of one-dimensional modulus with strain.

Sample disturbance plays an important role in laboratory testing. It was found that using larger specimen sizes decreased the amount of sample disturbance the specimens experienced; therefore, an increase in stiffness was observed. Due to the larger specimens, small strain testing is possible using a Rowe cell but there are numerous issues with saturation and consolidation times for heavily over-consolidated clays. This method needs further investigation and may prove an alternative to complex triaxial testing, for obtaining stiffness values at larger strains.

Although mineralogy differed between materials, the dominant influence on behaviour was stress path taken. Care is needed when considering swell, moisture content, apparatus influence, sample size, temperature effects and sample preparation. The stress path suggested by T. O'Brien (2009) proved to be effective at reducing hysteresis effects and appeared to minimise sample destructuring on saturation.

From testing on time intervals between unload steps and specific creep testing, it was found that creep becomes an issue when testing at low effective stresses. Care is needed when designing oedometer tests that specifically examine data at low effective stresses. As a minimum requirement data should be plotted in real-time so that the end of primary swelling behaviour can be observed before unloading further. The author suspects that stiffness degrades slower than the observed as the results start to incorporate creep above 90% unload. Further work is needed to examine this effect.

Specimens act much stiffer in the horizontal plane. Although this effect was not examined in great detail, anisotropic models will better represent insitu behaviour.

7. TRIAXIAL TESTING

7.1. Introduction

A comprehensive and detailed plan was proposed which aimed to examine small strain behaviour of the materials collected from sites across London. The investigation was to consider elastic properties and combine with bender element data in order to characterise the soil at small strain. This data would be combined with oedometer and Rowe cell data to give a holistic view of soil behaviour. Unfortunately, due to difficulties with testing equipment, which extended over a two-year period, only a fraction of the planned testing procedure reached fruition. Outlined in this Chapter are bender-aided triaxial compression tests on London Clay unit A2 and UMB for 38mm diameter samples. Some additional bender element data exists for unsuccessful attempts of triaxial compression.

7.2. 38mm diameter triaxial specimens

The opportunity to use relatively undisturbed block samples for triaxial testing is an extremely rare opportunity as very few block sampling opportunities exist and none have been conducted at such great depths. All the tests presented are drained axial compression carried out very slowly to record small strain stiffness of samples from insitu effective stress. Drained tests take months to complete due to shearing speeds (0.00001mm/min) and are rarely conducted despite being essential for modelling OC clays long-term.

The stress path taken for all samples is given in section 5.7.4, and this follows a similar process to that applied to oedometer samples. The limitation was the pressures that could be achieved and this did change the procedure for each sample. There were several tests which did not reach the shearing stage and only the tests that did are presented here. There are 3 keys tests: T1, T2 and T3 where T1 and T3 were UMB and T2 was Unit A2. The tests were designed to better understand the relationship between stiffness and small strain. This data could then be compared to data from Crossrail to evaluate the benefit of using block samples over rotary core.

7.2.1. Stiffness degradation results and discussion

The analysis procedure for these tests was complex and after each test the process improved. This can be seen in Figures 186-194 as the accuracy at small strains improves. For T1 raw data are shown normalised using p’ in Figure 186. There are numerous data points at discrete strains because the local strain gauge mounted on the specimen was not accurately calibrated

at the starting strain (local strain gauges often become less accurate if calibration voltages are not taken close to the starting strain). What this Figure does not show is the numerous values that equated to ‘negative strains’ and ‘negative Young’s moduli’; these were recorded due to temperature effects which influenced the results. Note: temperature effects occurred in T1 as the room temperature control in the laboratory malfunctioned, causing the temperature to slowly increase.

To obtain a clearer pattern in the data there are two methods to smooth out the data applied to this data. The first, averages the data at a space in time; this equates to taking an average strain and stress for every 1 minute and then plot the results for each average 1-minute block of data. This includes negative strains and negative stresses which are not seen on the logarithmic plot in Figure 186. As values are recorded every second, any data spikes are averaged over 59 other data point reducing the graph distortion. This can be seen in Figure 188 where the discrete data points are replaced. In this Figure, strain above 0.05% show a clear trend but below this there is too much distortion to see a clear pattern except around 0.02% where it appears the peak of the data exists. Although this method has helped smooth the data, the limitations of the data in range and resolution are distorting the view of the usable data.

The alternative method is to take all the data, remove fluctuations that are greater than 1000% of the average and plot it in descending order of values so that the largest Young’s modulus is plotted first and then the second largest Young’s modulus plotted second and so on. This can be done using excel so that all the associated data rearrange with the Young’s modulus data. A time average of this data can then be taken. Therefore, you are attempting to remove the temperature fluctuations for T1, Figure 188. Note: a large amount of negative strains occurred as the temperature was slowly increasing. Therefore, when averaging all the data using the first method, a large negative strain would bring the average of 60 data points down significantly to values that can be seen on Figure 187. An attempt was made to correct the data for temperature but this was not possible due to the location of the thermometer in relation to the specimen.

To summarise, T1’s raw data are scattered considerably below 0.01% strain (Figure 186). When the data are averaged with time it shows an increase in stiffness from 0-450MPa (E’ not E’/p’) over 0.001%-0.02% (Figure 187). This effect cannot be explained; however, it is clear the calibration for the local strain measurement was insufficiently accurate at small

strains and considerable room temperature variation occurred during the period of measurement. When averaged with just positive values the drained Young's modulus peaks around 540MPa at 0.007% strain for p'=600kPa (Figure 188).

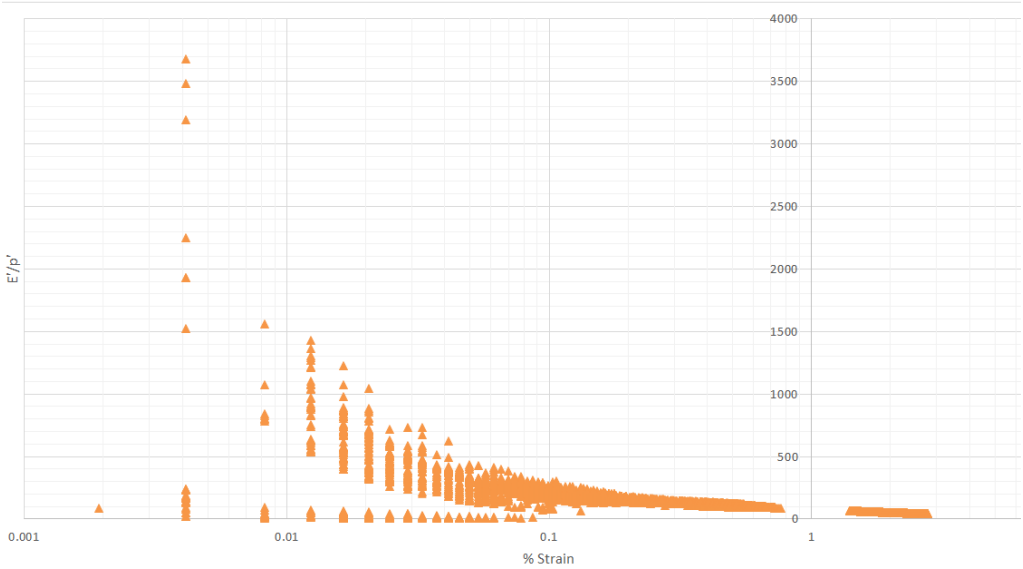

Figure 186: Positive raw data for T1 in compression from insitu effective stress, shown against local strain (gap around 1% strain is data loss)

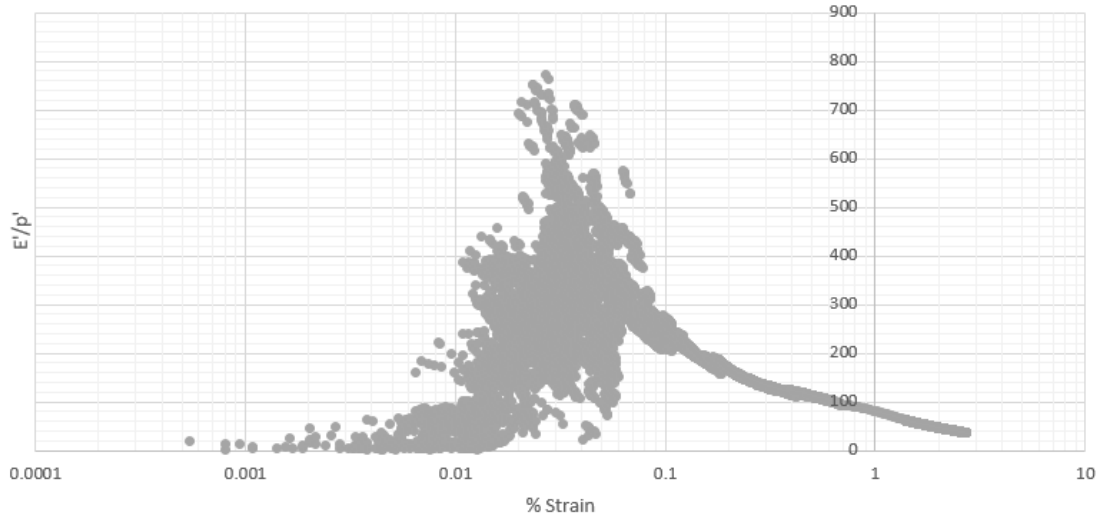

Figure 187: T1 data averaged with time – large scatter due to temperature fluctuations, shown against local strain

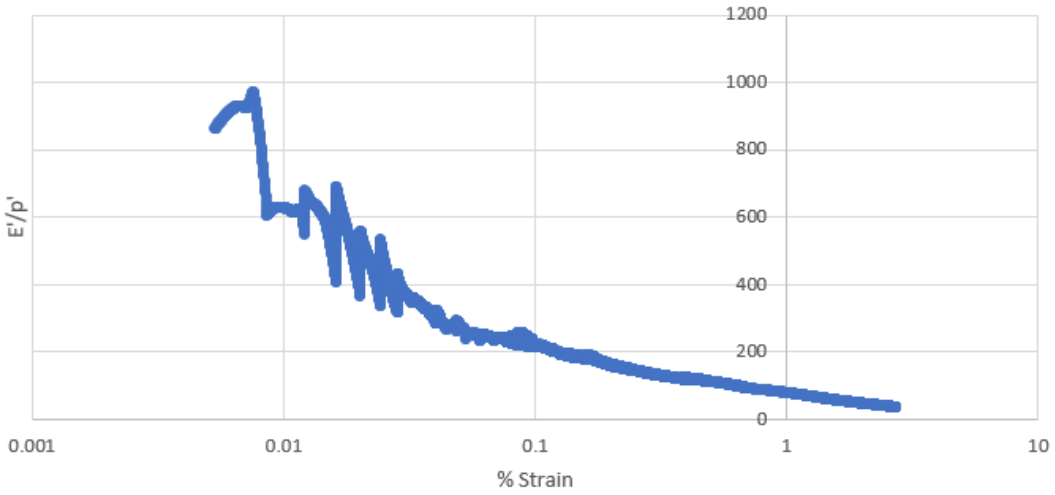

Figure 188: T1 averaged without time, shown against local strain

For T2 raw data are less scattered at small strains as temperature was better controlled (Figure 189). When averaged with time, an increase in stiffness occurs from 0-1150MPa over 0.0001%-0.002% (Figure 190). This could be an issue with the specimen or the apparatus. If it is the specimen, it could be sand particles in a sandy band that are rearranging under load. While if it is the apparatus it could be the alignment of the load cell in the top cap cup. If this is not perfectly centred the load cell would register an increase in stress while gradually sliding into correct alignment; this would suggest flexure exists in the specimen. When averaged without time, Figure 191, a similar pattern emerges.

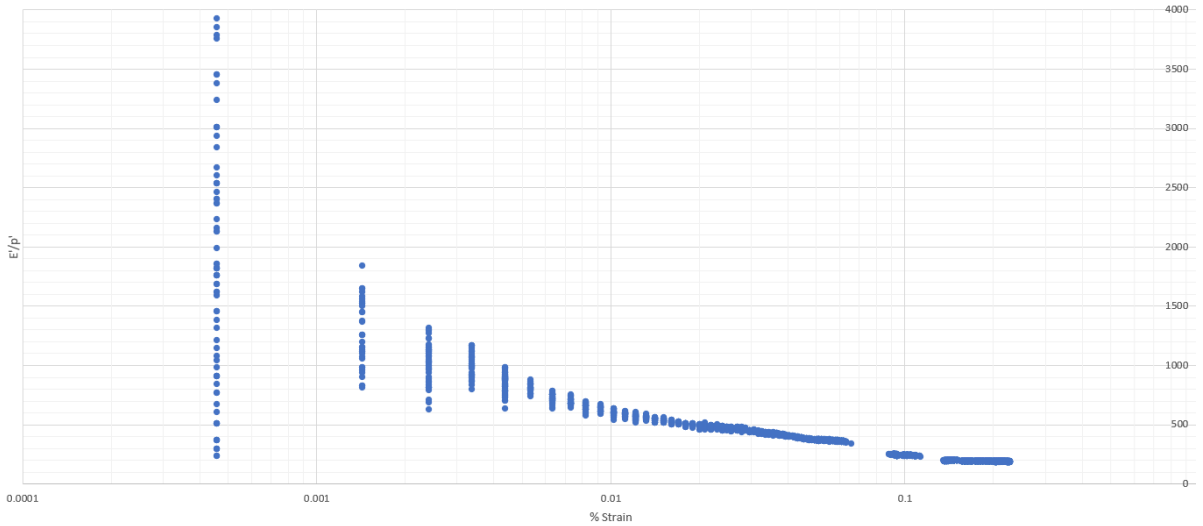

Figure 189: T2 raw data, shown against local strain

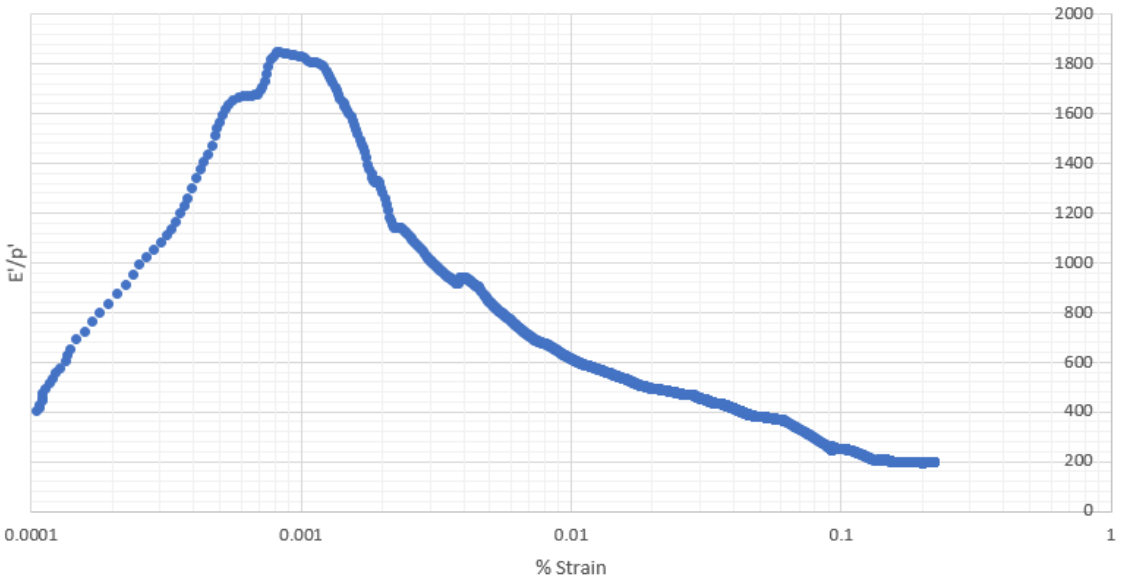

Figure 190: T2 averaged with time, shown against local strain

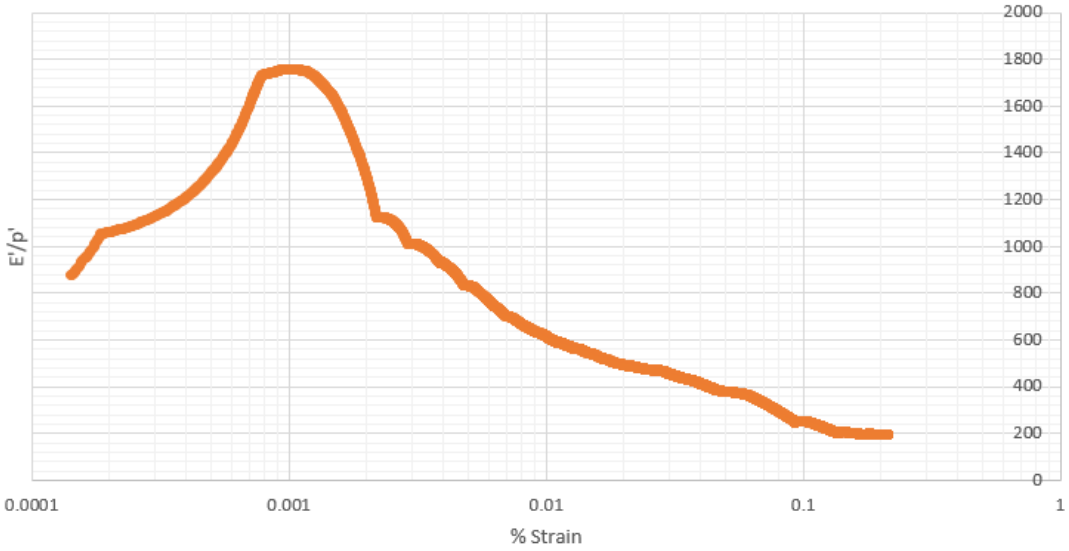

Figure 191: T2 averaged without time, shown against local strain

Specimen T3, shown in Figures 192-194, had a much-improved methodology for triaxial preparation and a high level of accuracy is achieved at very small strains (accuracy is discussed in 5.3.4). Averaged with time (Figure 193), at very small strains (<0.001%) the vertical drained Young's modulus is approximately constant which is to be expected for very stiff OC clay. The value of the initial vertical drained Young's modulus equates to approximately 1800MPa. On both Figures 193 and 194 there is a disturbance around 0.0008% strain, shown in Figure 193 as a spike and on Figure 194 as a drop followed by a spike; these correlate well with the expected Y1 yield surface found by Gasparre, 2005.

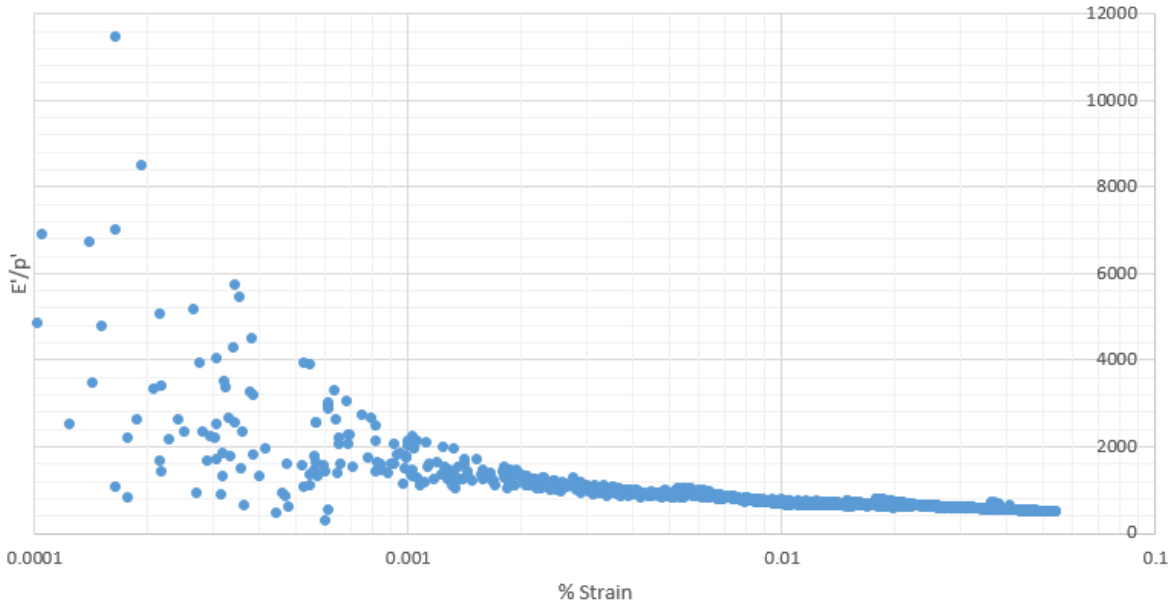

Figure 192: T3 raw data

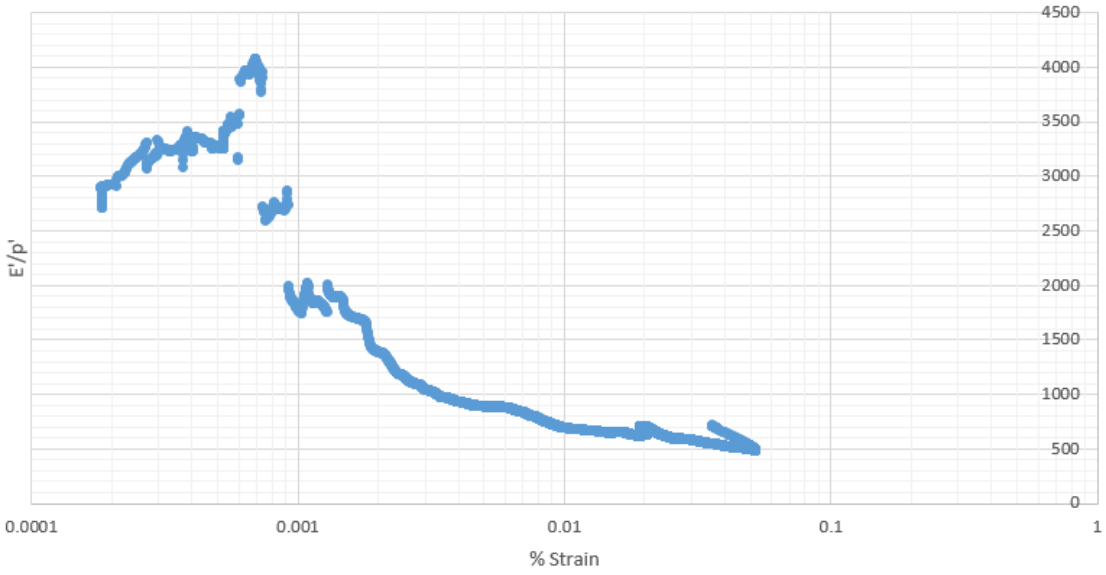

Figure 193: T3 averaged with time

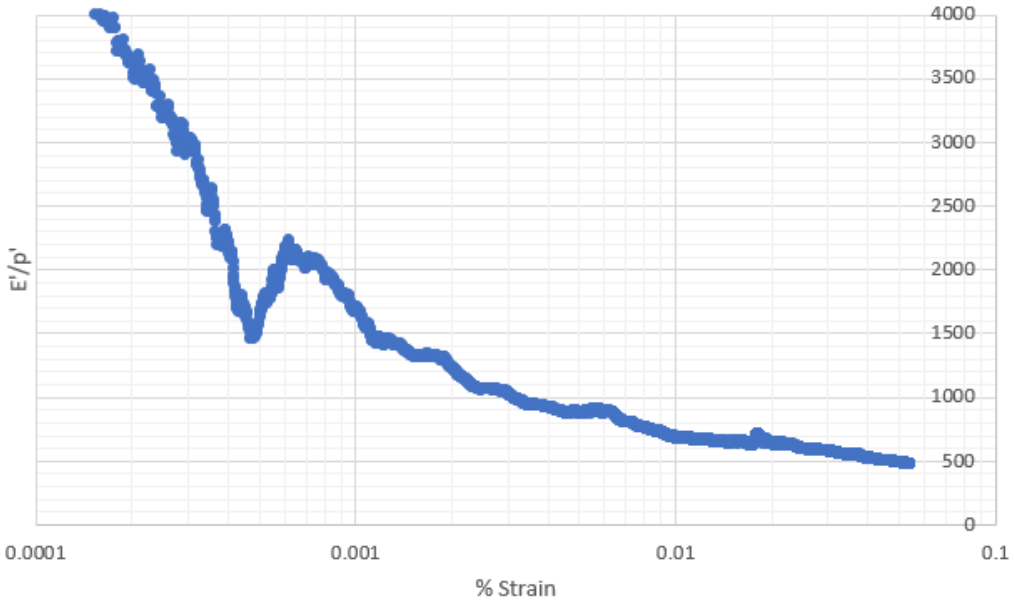

Figure 194: T3 averaged without time

When comparing UMB data from tests T1 and T3 (Figure 195), it is clear that at strain 0.01-0.1% the data align which suggests that the effects of temperature are primarily confined to small strains in test T1.

Additionally, the values for E' are approximately 2GPa for strains <0.001% for T3, are 500MPa at 0.003%, 400MPa at 0.01% strain for T3, 350MPa at 0.03% for T1 and T3, then 150MPa for T1 at 0.1% strain.

In Figure 196, London clay unit A2 from test T2 can be seen unnormalised. E' is approximately 1GPa at strain 0.001%, 450MPa at 0.005%, 360MPa at 0.01%, 200MPa at 0.08% and 150MPa at 0.1%. This shows that UMB and London Clay A2 have similar values of E'.

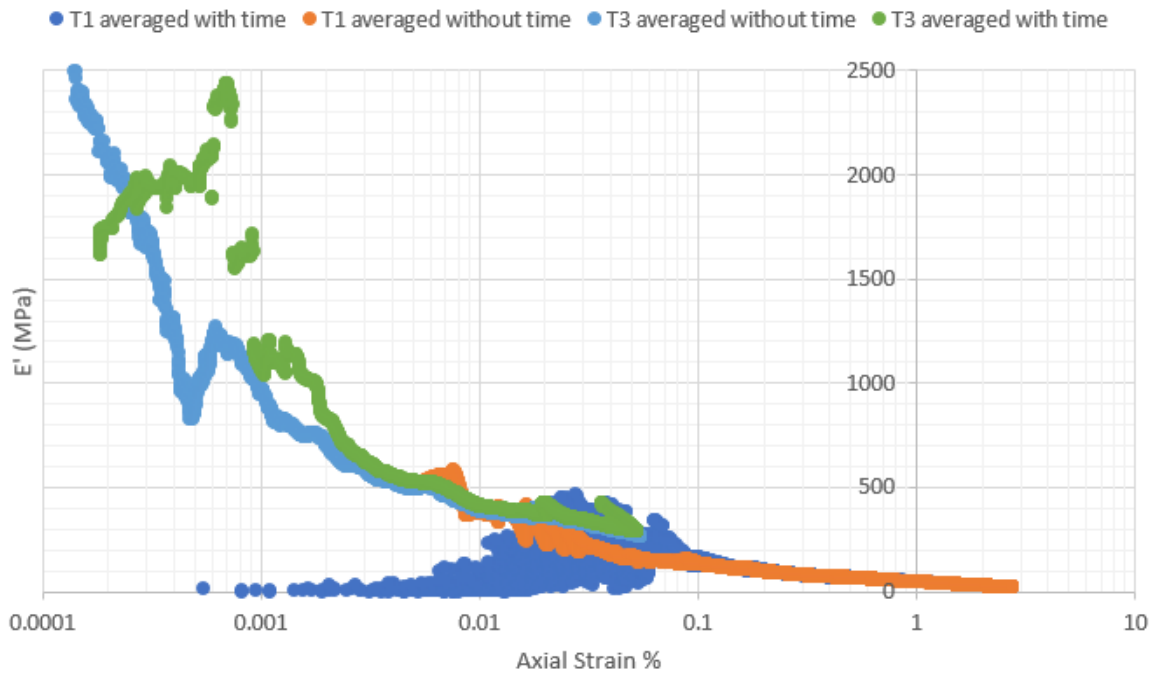

Figure 195: UMB data shown unnormalised

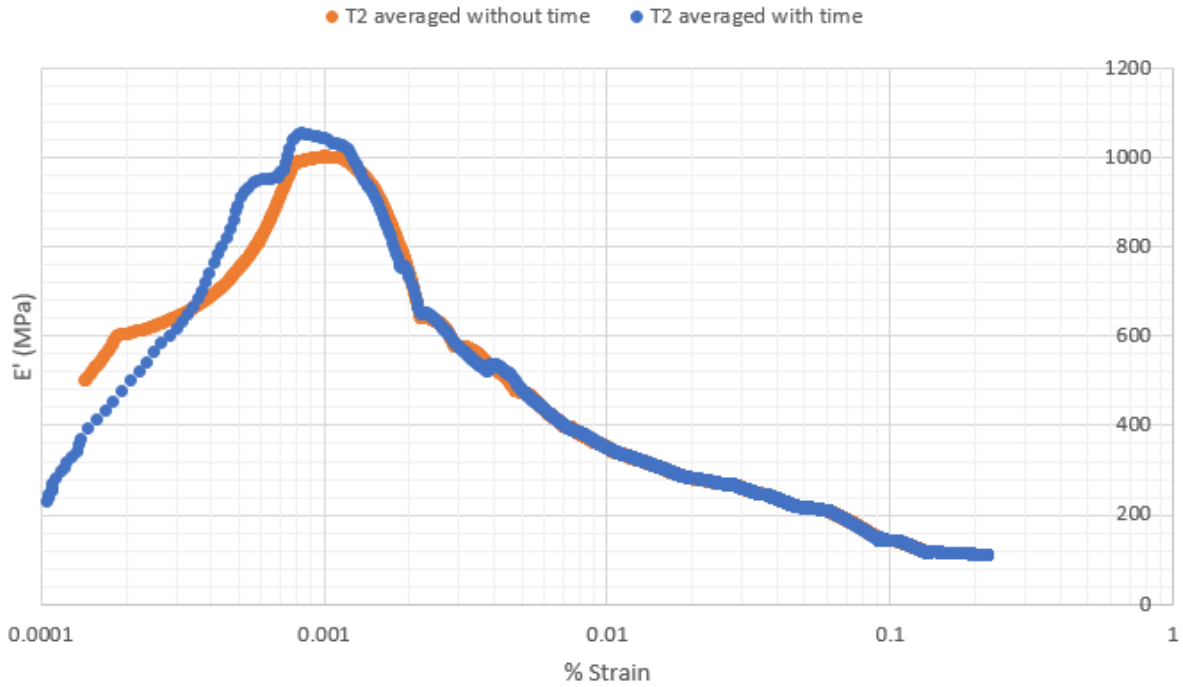

Figure 196: London clay Unit A2 unnormalised

When comparing T1, T2 and T3 normalised with p' (Figure 197), behaviour of the three specimens is similar. Between 0.001-0.05%, T2 and T3 have similar degradations of normalised stiffness. Between 0.05-0.2% T1 and T2 degrade similarly. This suggests that

UMB and London Clay have similar engineering behaviour. Interestingly, in Chapter 6 one of the conclusions is that for large strains behaviour of the clays is similar too.

The differences are at very small strains where T2 increases in stiffness and T3 has relatively constant stiffness followed by a sharp rise and then fall. This is likely to be caused by the different soil compositions. T2 contained sand while T3 has a high proportion of clay. It is interesting that two materials of different depositional environments (marine and fluvial), different mineralogy and different compositions of clay, silt and sand can act so similarly when normalised by average insitu effective stress. This data when combined with the conclusions of Chapter 6 suggest that insitu stress and stress history may be more important for OC clays than any other factor. However, due to only a small number of triaxial samples for which there is small strain data further testing is needed to confirm this.

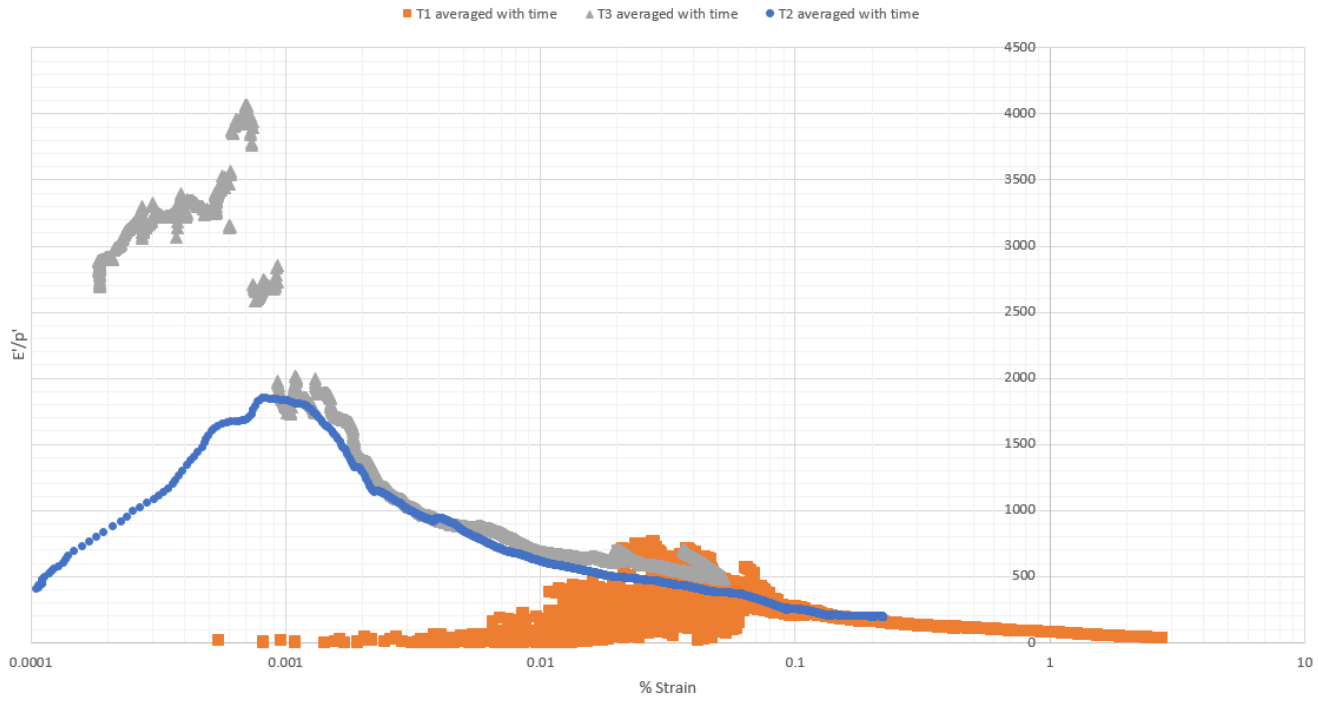

Figure 197: Normalised T1, T2 and T3 compared

When UMB and LC unit A2 data are superimposed onto Crossrail data, Figures 198 and 199, it is clear that the drained 38mm triaxial data sits between undrained data for UMB, LMB and LC Unit A2, and within the bounds found by Hight et al (2007). This is interesting as one would expect the drained stiffness to be slightly less than undrained stiffness but as the data have a naturally large range it is difficult to make a real comparison.

Further comparisons may be drawn from sample size as 38mm diameter triaxial samples were used in this thesis. The Crossrail data would likely come from rotary core samples which would make the likely size 70mm diameter; however, the size of samples is not stated. Either way, one conclusion from this may be that block sample and rotary core specimens have similar amounts of sample disturbance as the results are similar.

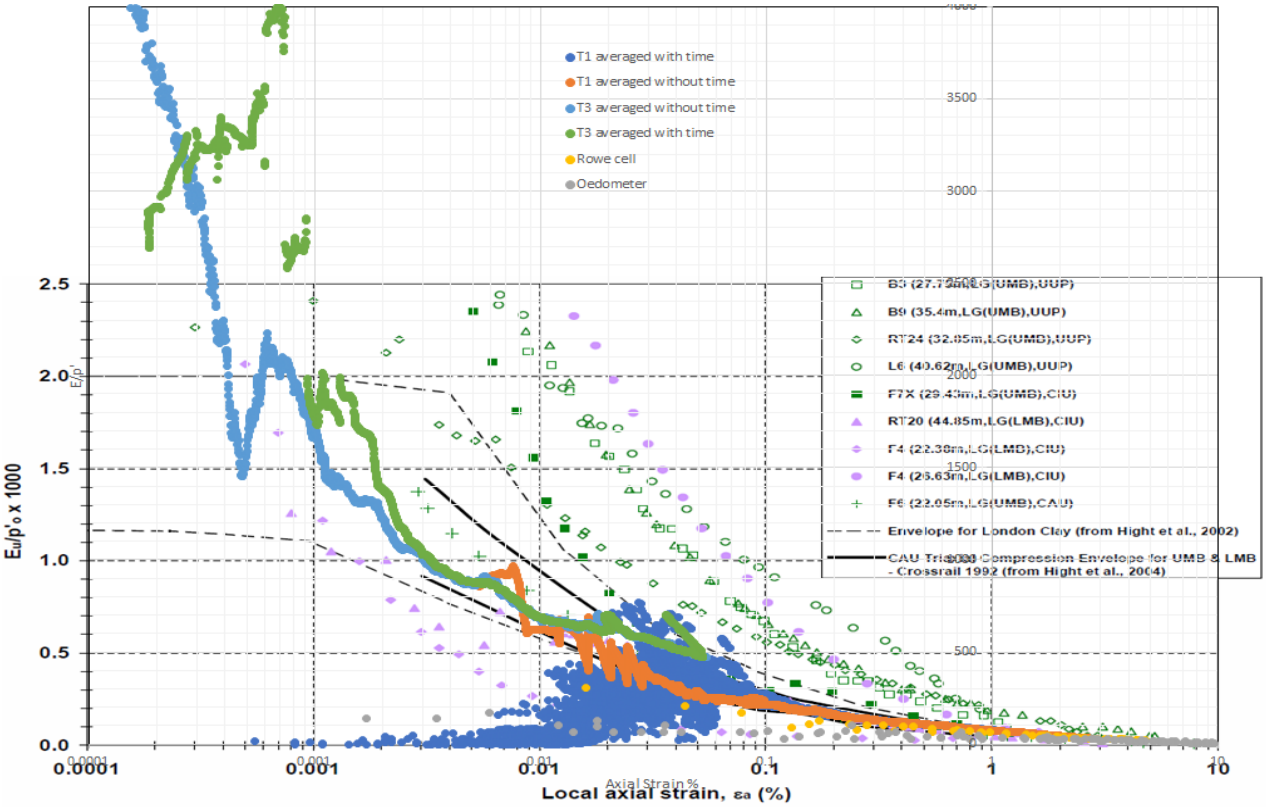

Figure 198: UMB data superimposed onto Crossrail undrained triaxial tests on UMB

7.2.1. Bender element waves

Bender element tests were conducted on all triaxial samples with benders mounted in the top and bottom of each sample at a range of stresses. This was done methodically by using a function built into CLISP studio which automatically sent a wave through the sample at a set time interval up to a maximum of 25 waves. Therefore, this was set to send a wave every hour for the duration of all the tests.

To obtain the value of the shear modulus, Equation 2.3 is used. To obtain the time between the sent and received wave some analysis of the data are needed. A raw bender element data wave can be seen in Figure 200. This wave shows that very little oscillation exists with the receiver wave. This is partly due to the frequency chosen which gave the clearest wave relative to the background noise. Background noise was significant so lower frequencies did

not give good receiver waves. Furthermore, when analysing a bender element receiver wave, there are multiple points which can be used to obtain the shear modulus. In this thesis the peak-peak method was initially used (Bonal, et al., 2012).

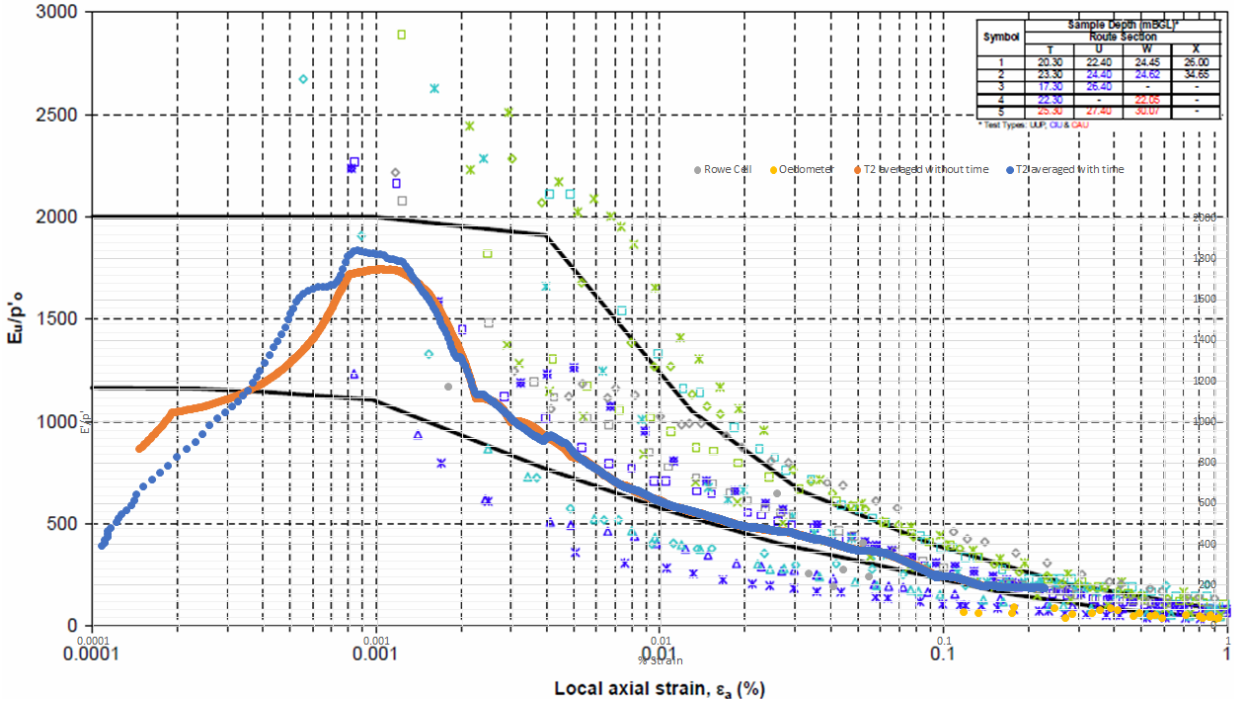

Figure 199: A2 data superimposed onto Crossrail undrained triaxial tests on A2

Unfortunately, due to a software malfunction the data for numerous tests including T1 and some of T2 were corrupted and only a backup of the data were left which did not have the necessary accuracy of information to obtain an accurate shear modulus, shown in Figure 201. Each data point is only accurate to 1.s.f so finding an accurate peak to peak time is not possible. However, an attempt was made for waves sent during T1 at frequency 20Hz. The results were a shear modulus between 547-565MPa at insitu effective stress.

In Figure 202, a single recovered test at a strain of approximately 1% on T1 shows waves which translate to a shear modulus between 509-533MPa. Note: the strain of around 1% is estimated based on the timestamp. Further tests were completed on London Clay Unit A2 and UMB but only data for test T3 has a range of stress values while the others are at insitu stresses.

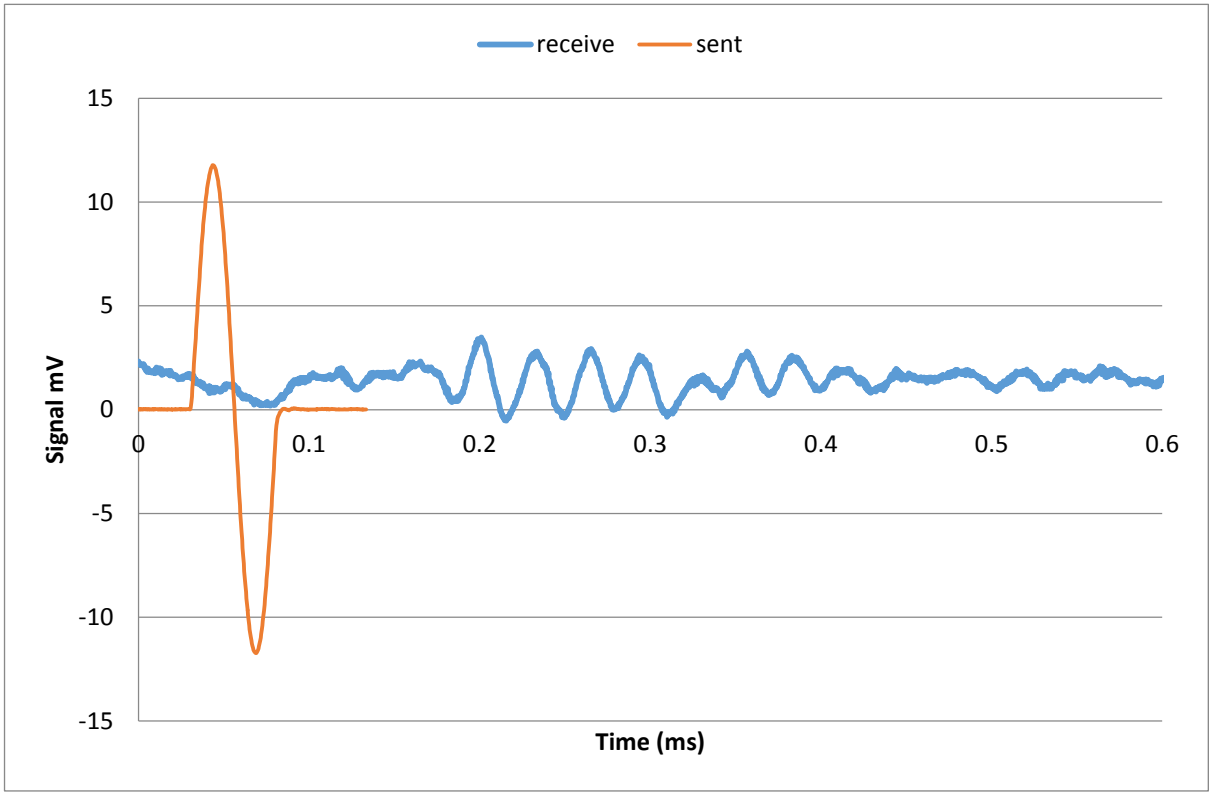

Figure 200: Example of bender element sent and receive wave

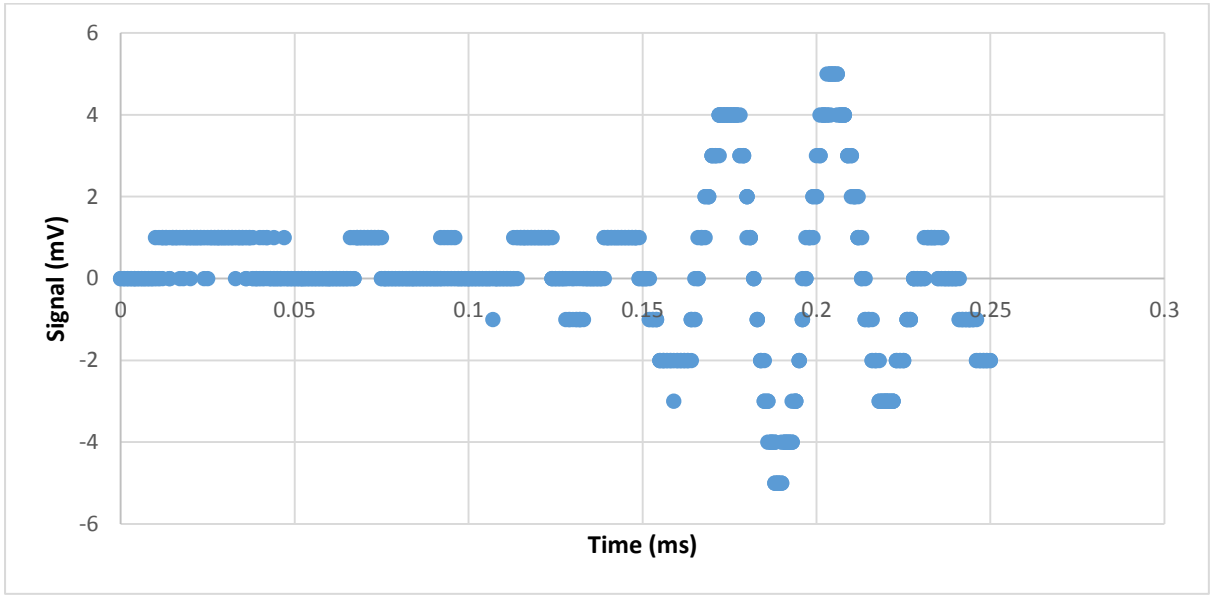

Figure 201: Data from the back up file

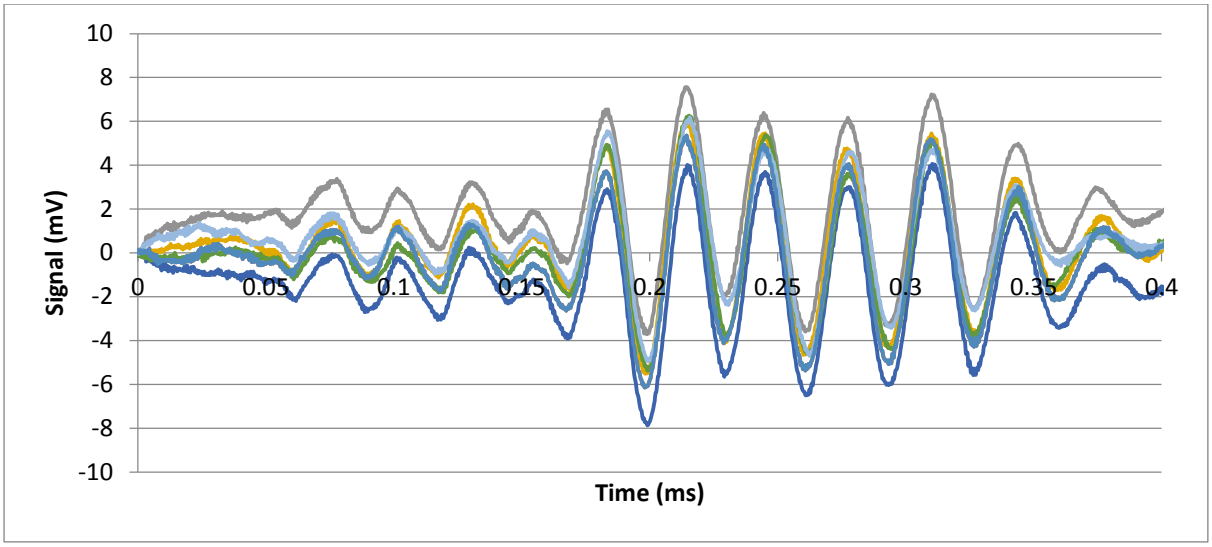

Figure 202: UMB - frequency 25Hz effective stress 600kPa at ~1% strain – shows a set of waves sent and received

Results showing receiver signals for two frequencies sent while at insitu effective stress at the start of test T2 are given in Figures 203 and 204. These waves translate to a shear modulus of 488-491MPa for 20Hz and 472-487MPa for 25Hz.

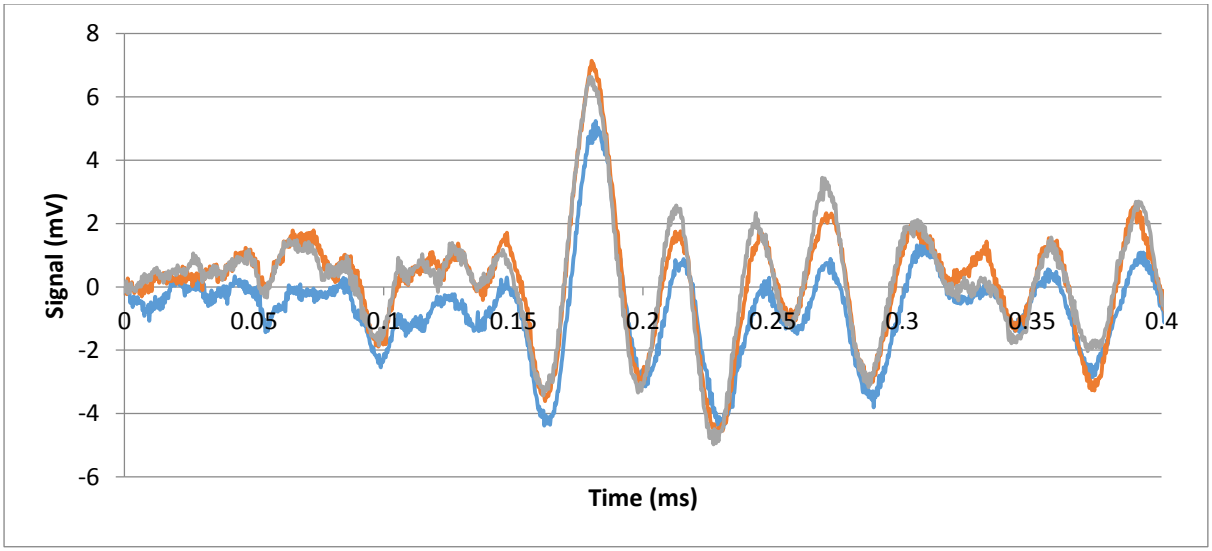

Figure 203: London Clay Unit A2 - frequency 20Hz effective stress 570kPa at 0.0001% strain - shows a set of waves sent and received

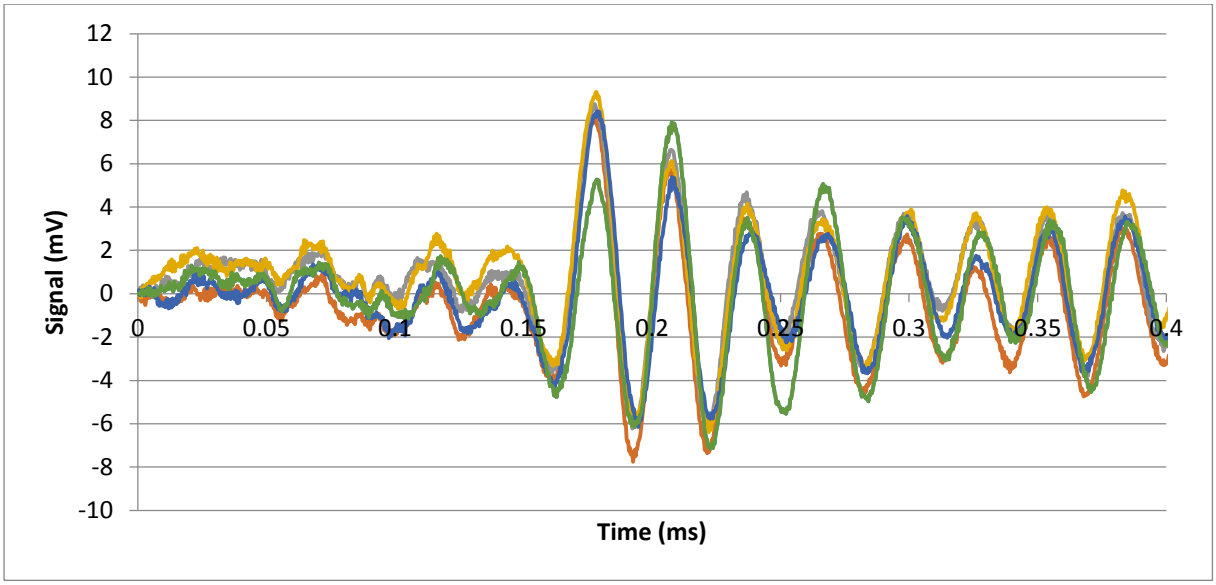

Figure 204: London Clay Unit A2 - frequency 25Hz effective stress 570kPa at 0.0001% strain - shows a set of waves sent and received

In Figure 205, three waves at 25Hz are compared from T3. Each wave is at a different confining stress. It is obvious at a time below 0.1ms that the receiver signal is picking up background noise as each wave is oscillating differently but, after 0.1ms a pattern starts to form and although the period of each wave differs slightly, the peaks begin to align. On Figure 205, arrows have been placed where potential peaks are for the receiver signal. It is the belief of the author that third peak is actually the first of the true receiver signal but it is not clear.

Due to the difficulty in interpreting peak-peak bender waves, the cross-correlation method was introduced to better analyse the data, shown in Figure 206. The cross-correlation method can be seen to give an altered wave which works by correlating the receiver signal and source signal (Viggiani & Atkinson, 1995 (a)). The results from the cross-correlation method are given in Table 21.

Table 21: Cross Correlation results

Confining stress (kPa)	Signal (Tcc)	Shear Modulus (kPa)
1000	0.1549	796
600	0.1552	789
100	0.1686	669

Results from small strain testing are given in Table 22 and show that the bender element test results complement the Young's moduli found when plotting stiffness vs strain. For T2, Poisson's ratio can be estimated at 0.04 using Equation 2.6 which is very low and less than the values found and/or used in the case histories elsewhere. For T3 the relationship between the shear modulus and the drained modulus is more common with the Poisson's ratio estimated at 0.14.

Table 22: Tabulated results for stiffness parameters at insitu effective stress

Test	$E'_{v,\ drained}$	G_{hv}	Poisson ratio estimate	Bulk modulus
T1	Unsure	510-570MPa	0.1 (assumed)	504MPa (Est)
T2	900-1100MPa	470-490MPa	0.04	326-398MPa
T3	1800MPa	789MPa	0.14	834MPa

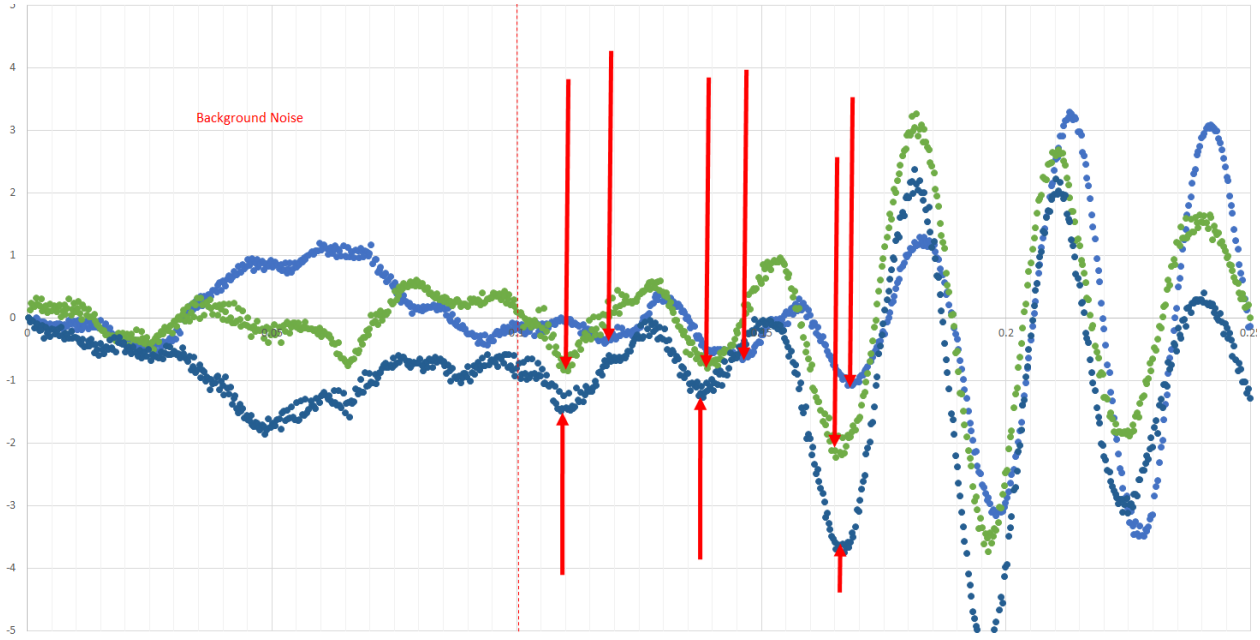

Figure 205: Analysing raw bender element data from T3, for data from three different confining stresses

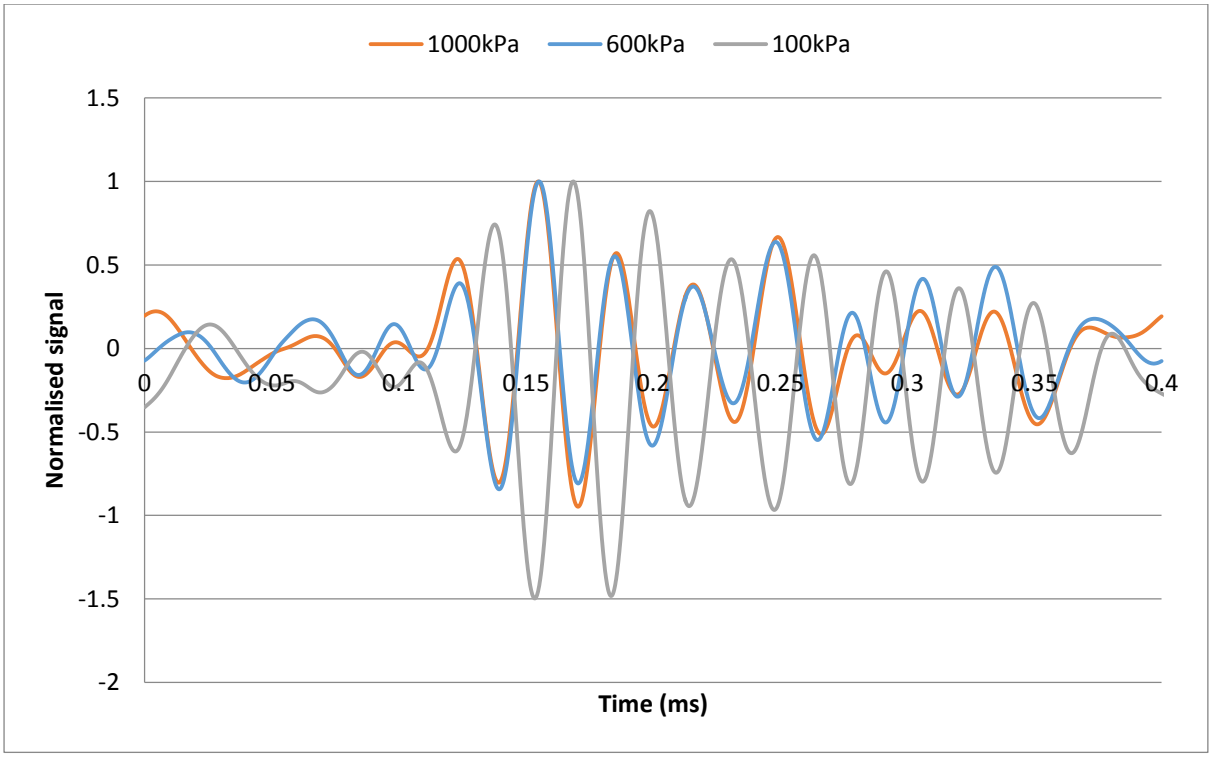

Figure 206: Cross-correlated bender element data for confining stresses 100kPa, 600kPa and 1000kPa

7.2.2. Comparison with strain ranges found at VSU

When comparing the strain ranges for heave found in Chapter 4 with the data in Chapters 6 and 7 the following statistics can be drawn from the data sets. Firstly, the average strain of 0.03% found between magnets at VSU leads to a stiffness (Young's modulus) reduction of between 72-76%. This is significant as relatively small ground movements occurred for a large reduction in stiffness.

Secondly, the clay would not be expected to surpass the second yield locus Y2 and therefore, would not be expected to fail in the horizontal plane (Gasparre, 2005). If confirmed, this would suggest that heave can be reduced further by keeping strains below the Y2 yield point. This may be a significant target to aim for in basement design.

8. CONCLUSIONS

8.1. Reflection

This thesis reflects the embodiment of the EngD programme and research has been influenced by opportunities only available due to the involvement of the industrial sponsor Mott Macdonald.

8.2. Conclusions

8.2.1. Victoria Station Upgrade (VSU) fieldwork

Field instrumentation was installed at VSU to analyse the effect of casting a ground-contacting basement slab on an expansive soil. Earth and water pressures, strains in the slab and vertical ground movements were measured over a two-year period.

The evidence at VSU suggests that small ground movements can be achieved behind and in front of the basement wall, using a combination of mitigating measures, such as: construction sequence; a ground-contacting basement slab supported by large plunge columns/piles at close spacings and using a hard-hard secant wall. In particular, the ground contacting basement slab supported by large piles effectively reduces heave when combined with the other measures; at least in the 'short-term'. This was confirmed both during excavation and shortly after a ground-contacting basement slab was cast.

When compared to other basement case histories in the literature the amount of heave measured by the magnet extensometers at VSU is low if using excavation depth as a predictor for heave. However, the concept of effective depth was explored in 4.3.6 and found that $0.25\%D_E$ (effective depth) gives a good estimation of short-term heave at the base of a deep excavation into overconsolidated clay.

Contact pressures were measured beneath the ground-contacting basement slab in several locations. The pressure increase was greater at the mid-point of a group of piles connected to the slab rather than closer to an individual pile. This suggests the relationship between swell strain and swell pressure is close; and both immediately next to and equidistant between tension piles, heave and the swell pressure that results from that heave was restricted. Slab deflection was found to have a negligible effect as bending strains in the slab were likely very small, although difficult to interpret as ambient temperature changes had a large effect on the results.

Both deep and shallow piezometers were installed to measure the response of pore water pressures during and after excavation. It was found earth pressures equalise quicker than expected if using the bulk permeability of the clay as a guide. Pore pressures gradually rose from the start of monitoring which suggests unloading of the ground prior to bulk excavation taking place although the mechanism causing the initially low pore water pressure has proved difficult to explain.

8.2.2. Laboratory testing - small and large strain

Oedometer and Rowe cell tests were carried out to determine the stiffness on unloading of stiff overconsolidated clay materials taken from intact block samples obtained from depth in large excavations in London. Unloading was found to *generally* be slightly non-linear in semi-logarithmic space (e -log σ' or v – log σ'). What has been observed is that behaviour can be clearly divided into categories as follows:

- Strains below 0.1% - Stiffness decreases dramatically up to this strain and appears non-linear in degradation; swelling/strain indices are highly non-linear. % unload below 6%
- Strains 0.1-0.5% - Stiffness degradation begins to change from non-linear to linear - % unload 6-35%
- Strains 0.5-1% - Stiffness degradation appears linear (approximately consistent values of swelling/strain indices are reached) - % unload 20-45%
- Strains 1-3% - Stiffness degradation appears linear but at a decreased rate - % unload 35-90%
- Strains 3-6% - specimens trend towards a non-linear degradation of stiffness - % unload 65-100%
- Strains greater than 6% - Stiffness degradation is minimal but all specimens appear to degrade non-linearly towards a critical stiffness - % unload 85-100%

It was found that using larger specimen sizes increases the measured stiffness and that although mineralogy differed between materials, the dominant influence on behaviour was the stress path taken. The stress path suggested by T. O'Brien (2009) proved to be effective at reducing hysteresis effects and appeared to minimise sample destructuring on saturation. If the stress path was standardised, the stiffness was found to be broadly similar for both UMB and different lithological units of London Clay when normalising using insitu effective stresses; this is confirmed at large strain using oedometers and using a more limited set of

triaxial test data at small strains. Due to the larger specimens, small strain testing is possible using a Rowe cell but there are numerous issues with saturation and stress paths on clays that are taken at great depth. The use of the Rowe cell for testing larger samples of stiff overconsolidated clay needs further investigation.

When comparing triaxial data normalised with average insitu effective stress, behaviour of the three tested specimens is similar. Both UMB and London Clay Unit A2 degrade similarly after 0.001% strain and appear to have similar engineering behaviour. At very small strains London Clay Unit A2 and UMB behave differently; this is likely to be caused by the different soil compositions. When all laboratory testing was analysed across all strain ranges, it is found that insitu stress and stress history may be more important for overconsolidated clays than any other factor.

Finally, using data from Crossrail, it was found that there is not any real difference between the results of samples taken from rotary core and those from block samples at greater depths

8.3. Future work

Further investigation is needed into the behaviour of pore pressures when creating open pile bores into over-consolidated clay. A 3D finite element model of the interaction of the pile with the clay during its construction would help to explain the lateral unloading theory discussed in 4.3.6.

A continuation of monitoring at VSU would be beneficial to analyse the effectiveness of the aforementioned heave mitigation measures long-term. It would be interesting to see if significant movement occurs in the ground-contacting basement slab as pore pressures reach pre-excavation levels.

More testing is needed to analyse the Y2 yield surface in extension to see whether it is a reasonable target for heave mitigations measures to aim for as a maximum allowable short-term ground movement.

Further work is needed to establish whether the Rowe cell is an effective apparatus for unloading overconsolidated clays from insitu effective stress as the large sample size may obtain stiffness values that are more relatable to those measured insitu.

More data are needed to establish whether the stiffness behaviour of overconsolidated clays can be effectively normalised using the mean insitu effective stress.

APPENDIX

A1 Constitutive models for small-strains

The Jardine model

This model, proposed by Jardine et al. (1986), uses a periodic logarithmic function to project the non-linear relationship between the undrained secant Young's modulus, E_u, and axial strain, ε_a, in undrained triaxial tests. The simple function mathematically represents stiffness degradation relatively accurately and can be modified using constants:A_1; A_2; A_3; A_4; and A_5, found empirically, as given in Equation A.1.

$$\frac{E_u}{c_u} = A_1 + A_2 cos\left\{A_3\left[\log_{10}\left(\frac{\varepsilon_a}{A_4}\right)\right]^{A_5}\right\} \quad (A.1)$$

where the secant modulus is normalised with the undrained shear strength c_u. This has been converted into shear and bulk moduli by Potts and Zdravkovic (1999) and is given in Equations A.2-A.3, and the tangent values are given in Equations A.5-A.6.

$$\frac{G_s}{p'} = B_1 + B_2 cos\left\{B_3\left[\log_{10}\left(\frac{\Omega_d}{\sqrt{3B_4}}\right)\right]^{B_5}\right\} \quad (A.2)$$

$$\frac{K_s}{p'} = B_6 + B_7 cos\left\{B_8\left[\log_{10}\left(\frac{\varepsilon_p}{B_9}\right)\right]^{B_{10}}\right\} \quad (A.3)$$

$$\Omega_d = \frac{2}{\sqrt{6}}\sqrt{\left(\varepsilon_{xx} - \varepsilon_{yy}\right)^2 + \left(\varepsilon_{yy} - \varepsilon_{zz}\right)^2 + (\varepsilon_{xx} - \varepsilon_{zz})^2} \quad (A.4)$$

$$\frac{3G_t}{p'} = B_1 + B_2(\cos B_3){\Omega_1}^{B_5} - \frac{B_2 B_3 B_5 {\Omega_1}^{B_5-1}}{2.303}(\sin B_3){\Omega_1}^{B_5} \quad (A.5)$$

$$\frac{K_t}{p'} = B_6 + B_7(\cos B_8){\Omega_2}^{B_{10}} - \frac{B_7 B_8 B_{10} {\Omega_2}^{B_{10}-1}}{2.303}(\sin B_8){\Omega_2}^{B_{10}} \quad (A.6)$$

$$\Omega_1 = \log_{10}\left(\frac{\Omega_d}{\sqrt{3B_4}}\right) \quad (A.7)$$

$$\Omega_2 = \log_{10}\frac{\left|\varepsilon_{xx} + \varepsilon_{yy} + \varepsilon_{zz}\right|}{B_9} \quad (A.8)$$

Where B_1; B_2; B_3; B_4;B_5; B_6; B_7; B_8;B_9; and B_{10} are material constants; $\varepsilon_p = \varepsilon_{xx} + \varepsilon_{yy} + \varepsilon_{zz}$= the volumetric strain; and p' is the mean effective stress. The visual translation of

Equation A.5 is given in the Figure 207; this shows that the equation only models the small strain region which includes the majority of stiffness degradation. This leaves the very small and large strain region to be modelled in another way.

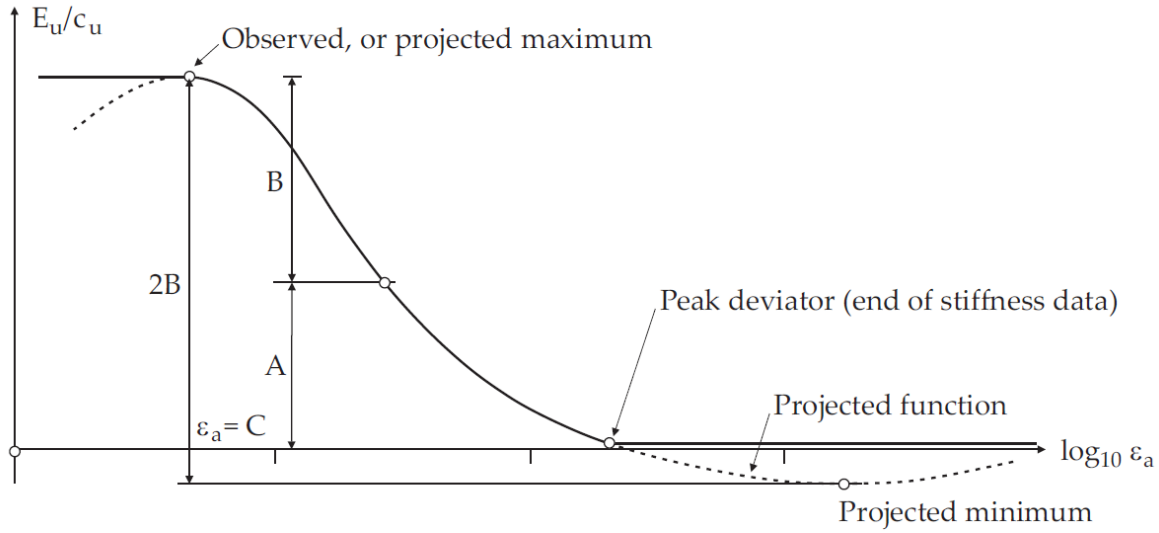

Figure 207: The Jardine model – A trigonometric function used to model the stiffness degradation in the small strain region (Benz, 2007).

Non-linear settlement (NLS) method

The method relies on three considerations: the magnitude and distribution of stresses set up in the soil mass by the loading/unloading, the immediate and long-term stress-strain properties of the soil mass in both depth and lateral extent and the linking of these two considerations to calculate strains (O'Brien & Sharp, 2001a).

The total settlement/heave is found with a modified version of the one-dimensional method:

$$\delta_{Ti} = m_{v_i} \Delta\sigma_{v_i}' H_i \qquad \text{(A.9)}$$

Where m_{v_i}= coefficient of volume compressibility for vertical direction for layer i; H_i= height of layer i and δ_{Ti}= total settlement/heave for layer i.

Also, from Henkel (1971):

$$m_{v_i} = {k_i}/{E_i'} \qquad \text{(A.10)}$$

Where, k_i= constant that depends on the degree of stiffness and E_i'= drained elastic modulus for layer i. Rearranging A.9 and A.10 gives:

$$\varepsilon_{v_i} = \frac{k_i(\Delta\sigma_{v_i} - \Delta u_i)}{E_i'} \tag{A.11}$$

Where, ε_{v_i}= vertical strain for layer i. Then, summing all layers gives:

$$\delta_T = \sum_{i=1}^{i=n} (\varepsilon_{v_i}' H_i) \tag{A.12}$$

Also, the drained secant modulus must be modified for use with average effective stress during loading/unloading. Equation A.13 is derived in O'Brien & Sharp (2001a):

$$p_a' = p_o' + \frac{(1 + v')}{6(1 - v')}\Delta\sigma_{v_i}' \tag{A.13}$$

Where, p_a'= average mean effective stress; p_o'= initial mean effective stress and v'= drained Poisson's ratio. This equation can then be substituted into Equation A.14 to convert the initial drained elastic modulus,E_{o_i}', into the corrected drained elastic modulus, E_{c_i}':

$$E_{c_i}' = E_{o_i}' \left(\frac{p_{a_i}'}{p_{o_i}'}\right) \tag{A.14}$$

These values can be found with depth and then iterated to find a suitable strain. The process depends on a known relative stiffness vs. vertical strain relationship so the result depends on the quality of the relationship, or having appropriate data.

An example of relative stiffness vs. vertical strain for clay can be seen in Figure 208. A linear relationship is assumed between known data points.

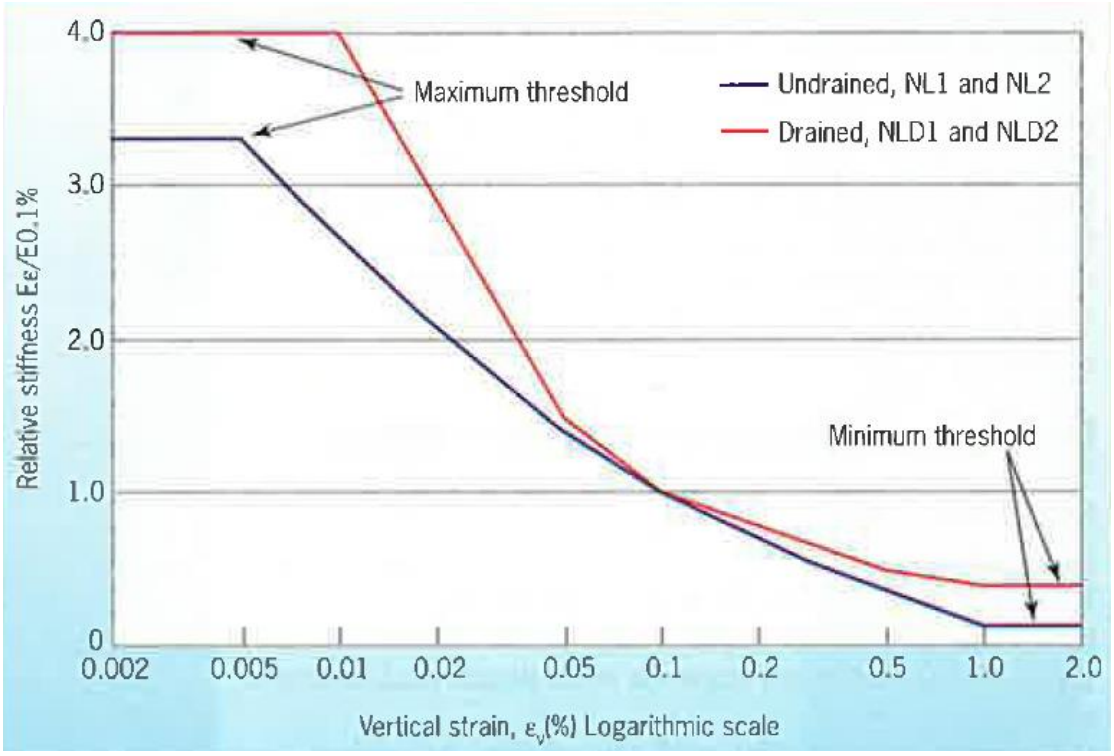

Figure 208: Relative stiffness vs. vertical strain (log scale) for drained and undrained secant Young's modulus. Data based on laboratory tests for London Clay (O'Brien & Sharp, 2001a).

A* Method

The A* method (used by Mott Macdonald) is an evolution from the Jardine Model which uses the mean effective stress and constants derived in the laboratory at small strain. This is unreliable as the mean effective stress is often an estimation, due to the difficulty and expense of obtaining, and small strain testing can be highly variable. This has led to underestimated stiffness predictions.

The A* method uses Equation 2.2 from section 2.2.2 and has less dependence on the mean effective stress as it is taken to the power 0.6. In addition, the values of the shear modulus can be much more reliably estimated using bender element tests and geophysics. As previously mentioned, Equation 2.1 is based on the work by Viggiani and Atkinson (a) (1995) and it gives good approximation to test data.

$$G_{sec,0} = A_0^* p'^{0.6} \qquad \text{(A.15)}$$

A2 Calibration Sheets

GEOSENSE QUALITY FORM
FORM No G/QF/123
ISS. 5
DATE : JUNE 14
SIG. GC

VW TOTAL PRESSURE CELL

Model	VWTPC-4000	Cal date	29-Jul-14	DPI No.	52001702
Serial	TP2040	Baro	1004.0	Readout No.	VR0601
Works ID	81 9 8	Temp °C	20	R/O Cal. date	15/07/2014

Applied pressure		Readings [digit]			Calculated Pressure		Error % fso	
psi	kPa	1 up	1 down	avg.[digit]	lin.[kPa]	polyn.[kPa]	linear	polynomial
0.000	0.000	8885.1	8885.1	8885.1	-0.66	-0.14	-0.19%	-0.04%
10.007	69.000	8189.8	8189.8	8189.8	69.42	69.32	0.12%	0.09%
20.015	138.000	7506.3	7506.3	7506.3	138.31	137.90	0.09%	-0.03%
30.022	207.000	6822.5	6822.5	6822.5	207.24	206.83	0.07%	-0.05%
40.029	276.000	6138.5	6138.5	6138.5	276.18	276.08	0.05%	0.02%
50.036	345.000	5460.7	5460.7	5460.7	344.50	345.01	-0.15%	0.00%

Calibration of master DPI valid from 25 February 2014. UKAS Certificate of Calibration 16499 issued by Chamois Metrology (UKAS Accredited Calibration Laboratory 0822)

CALIBRATION FACTORS

Linear factor (k)

kPa per digit	psi per digit	mH_2O per digit
-0.100792421	-0.014618	-0.010278

Polynomial factors

	kPa	psi	mH_2O
A	3.29113E-07	4.77321E-08	3.3560E-08
B	-0.10551323	-0.015303	-0.010759
C	911.370402	132.1784484	92.933917

Note: Digits are $Hz^2 \times 10^{-3}$ units.

(please consult the User Manuals for conversion of alternative reading units)

Polynomial calculation [kPa] = A * (Reading)^2 + B * (Reading) + C

Linear calculation [kPa] = k (kPa) * (Current Reading - Site Zero Reading)

CALIBRATED TO UKAS TRACEABLE STANDARDS
GEOSENSE CERTIFIED ISO 9001:2008

THIS CERTIFICATE IS VALID ONLY WHEN CARRYING THE OFFICIAL ORIGINAL STAMP OF GEOSENSE BELOW

Nova House, Rougham Industrial Estate, Rougham, Bury St Edmunds, Suffolk, IP30 9ND, England
t +44 (0)1359 270457 f +44 (0)1359 272860 e info@geosense.co.uk www.geosense.co.uk
Geosense Ltd Registered in England 8445199

Figure 209: Geosense total pressure cell calibration sheet

BS EN ISO 9001:2008
FM 553710

itmsoil

Bell Lane, Uckfield, East Sussex
TN22 1QL United Kingdom

t: +44 (0) 1825 765044
f: +44 (0) 1825 744398

e: info@itmsoil.com
w: www.itmsoil.com

itmsoil Group Ltd. Registered in England. Number: 4239206. Registered Office: Bell Lane, Uckfield, East Sussex TN22 1QL.

VIBRATING WIRE INSTRUMENTS CALIBRATION CERTIFICATE

Instrument Type : W4 Vibrating Wire Piezometer
Serial No. : 048566

Instrument Range : 0.00 to 300.0 kPa
Calibration Date : 04/07/2013

Gauge Factors in kPa
Ambient Temperature : 23°C

Period Gauge Factor (K): 1342.7950000
Barometric Pressure : 1018 mbar

Linear Gauge Factor (G): (kPa/digit)0.1342800
Calibration Technician : Halmar Harding

Polynomial Gauge Factor A: 0.000000147336800
Calibration Equipment:
Mensor APC 600

Polynomial Gauge Factor B: -0.1358634000
AVW200 Data Logger

Polynomial Gauge Factor C:** 875.880600
Regression Zero : 6491.7

Applied (kPa)	Reading (Period)	Reading F²/1000	Calculated (Linear)	Error %FS (Linear)	Linear Increment	Calculated (Polynomial)	Error %FS (Polynomial)
0.00	3924.6	6492.5	-0.109	-0.04	0.0	-0.002	0.00
30.00	3994.1	6268.6	29.956	-0.01	-223.9	29.997	0.00
60.00	4067.4	6044.6	60.034	0.01	-224.0	60.024	0.01
90.00	4144.7	5821.1	90.046	0.02	-223.5	89.999	0.00
120.00	4226.6	5597.8	120.030	0.01	-223.3	119.961	-0.01
150.00	4313.7	5374.0	150.082	0.03	-223.8	150.006	0.00
180.00	4406.2	5150.8	180.053	0.02	-223.2	179.984	-0.01
210.00	4505.1	4927.1	210.091	0.03	-223.7	210.045	0.02
240.00	4610.6	4704.1	240.035	0.01	-223.0	240.026	0.01
270.00	4723.7	4481.7	269.899	-0.03	-222.4	269.941	-0.02
300.00	4846.0	4258.2	299.910	-0.03	-223.5	300.019	0.01

Formulae: Linear* $E = G(R0 - R1)$
Polynomial** $E = AR1^3 + BR1 + C$

* The zero reading should be established on site by the user on installation.
** The site value of C must be calculated using the formula $C = -(AR0^2 + BR0)$

The instrument detailed hereon has, as applicable, been tested and calibrated in accordance with procedures, which are part of our ISO 9001:2008 Quality Management System, and unless otherwise indicated, performs within ± 0.10% (Polynomial) as specified. Thus, the instrument conforms in all respects to our relevant specifications and drawings.

Certified: ..... itmsoil INSTRUMENTS ... Line MANAGER

Figure 210: itmsoil vibrating wire piezometer calibration sheet

GEOSENSE

GEOSENSE QUALITY FORM
FORM No G/QF/126
ISS. 3
DATE May-14
SIG. GC

VIBRATING WIRE REBAR STRAIN METER CALIBRATION

Model	VWS-4000
Serial	405485
Works ID	1
Rebar Dia.	16mm
Readout No.	VR0602
R/O Cal. date	30/07/2014

Cal date	31 July 2014
Master	FMSL3522
Temp °C	20
Batch	64
Cable m	25M

Applied Load	Reading $Hz^2 * 10^{-3}$			Indicated Load	Error
kN	1 up	1 down	mean	kN	% FSO
0.00	8623	8629	8626.0	0.03	0.00%
5.00	9115	9157	9136.0	4.96	-0.18%
10.00	9630	9685	9657.5	9.99	-0.02%
15.00	10152	10205	10178.5	15.03	0.11%
20.00	10671	10714	10692.5	19.99	-0.02%
25.00	11204	11217	11210.5	25.00	-0.01%

Calibration of master FMSL valid from 17 May 2014. UKAS Certificate of Calibration 14058025 issued by Element Materials Technology (UKAS Accredited Calibration Laboratory 0157)

CALIBRATION FACTORS

Linear factor (s) (strain units)

microstrain / digit
0.560123663

Linear calculation [με] = s * (Current Reading - Site Zero Reading)

Linear factor (k) (load units)

kN / digit
0.009661489

Linear calculation [kN] = k * (Current Reading - Site Zero Reading)

Users are advised to establish site zero base readings for calculation purposes

Note: Readings are taken in frequency squared units.
Please refer to User Manuals if reading in period or frequency units

THIS CERTIFICATE IS VALID ONLY WHEN CARRYING THE OFFICIAL ORIGINAL STAMP OF GEOSENSE BELOW

CALIBRATED TO UKAS TRACEABLE STANDARD
GEOSENSE CERTIFIED ISO 9001:2008

Nova House, Rougham Industrial Estate, Rougham, Bury St Edmunds, Suffolk, IP30 9ND, England
t +44 (0)1359 270457 f +44 (0)1359 272860 e info@geosense.co.uk www.geosense.co.uk
Geosense Ltd Registered in England 8445199

Figure 211: Geosense strain gauge calibration sheet

A3 Zero Readings

Table 23: Zero Readings E1 and E2

	Bay 1															
	Set 1		Set 2		Set 3		Set 4		Set 5		Average			Current Distance from Datum's		
Zero Reading	Top Beep (m)	Bottom Beep (m)	Top Beep (m)	Bottom Beep (m)	Top Beep (m)	Bottom Beep (m)	Top Beep (m)	Bottom Beep (m)	Top Beep (m)	Bottom Beep (m)	Top Beep (m)	Bottom Beep (m)	Difference (m)	Top (m)	Bottom (m)	
1	12.134	N/A	12.134	12.165	12.134	12.164	12.134	12.164	12.134	12.165	12.13409	12.1645	0.030412	34.374	34.376	34.375
2	14.114	N/A	14.116	14.146	14.116	14.146	14.116	14.147	14.117	14.147	14.11589	14.1465	0.030612	32.392	32.394	32.393
3	18.047	N/A	18.048	18.084	18.047	18.083	18.049	18.084	18.048	18.084	18.04789	18.08375	0.035862	28.460	28.457	28.458
4	18.083	N/A	18.084	18.156	18.083	18.155	18.084	18.155	18.084	18.155	18.08369	18.15525	0.071562	28.424	28.385	28.405
5	20.171	N/A	20.173	20.208	20.173	20.208	20.174	20.208	20.174	20.208	20.17309	20.208	0.034912	26.335	26.333	26.334
6	24.678	N/A	24.678	24.713	24.677	24.712	24.678	24.714	24.678	24.713	24.67789	24.713	0.035112	21.830	21.828	21.829
7	31.272	N/A	31.272	31.308	31.270	31.307	31.272	31.308	31.272	31.308	31.27169	31.30775	0.036062	15.236	15.233	15.235
8	36.234	N/A	36.234	36.266	36.233	36.264	36.235	36.266	36.235	36.266	36.23429	36.2655	0.031212	10.274	10.275	10.274
Base	46.506	46.539	46.507	46.539	46.506	46.538	46.506	46.539	46.507	46.539	46.50649	46.5388	0.032312	0.000	0.000	0.000

	Bay 2															
	Set 1		Set 2		Set 3		Set 4			Average				Datum's		
Zero Reading	Top Beep (m)	Bottom Beep (m)	Top Beep (m)	Bottom Beep (m)	Top Beep (m)	Bottom Beep (m)	Top Beep (m)	Bottom Beep (m)		Top Beep (m)	Bottom Beep (m)	Difference (m)	Top (m)	Bottom (m)	Average
1	11.093	11.128	11.092	11.127	11.093	11.127	11.092	11.127		11.0925	11.12725	0.03475	37.920	37.918	37.919
2	12.162	12.197	12.161	12.196	12.161	12.196	12.161	12.196		12.16125	12.19625	0.035	36.851	36.849	36.850
3	14.132	14.168	14.132	14.168	14.132	14.1675	14.131	14.167		14.13175	14.16763	0.035875	34.881	34.878	34.879
4	16.152	16.187	16.152	16.187	16.152	16.187	16.151	16.186		16.15175	16.18675	0.035	32.861	32.859	32.860
5	18.128	18.163	18.127	18.162	18.1275	18.162	18.127	18.1615		18.12738	18.16213	0.03475	30.885	30.883	30.884
6	20.421	20.456	20.421	20.456	20.421	20.456	20.421	20.455		20.421	20.45575	0.03475	28.591	28.590	28.591
7	24.983	25.013	24.982	25.013	24.983	25.013	24.982	25.013		24.9825	25.013	0.0305	24.030	24.033	24.031
8	31.204	31.239	31.203	31.238	31.204	31.238	31.203	31.237		31.2035	31.238	0.0345	17.809	17.808	17.808
9	38.048	38.077	38.048	38.077	38.048	38.077	38.047	38.077		38.04775	38.077	0.02925	10.965	10.969	10.967
Base	49.012	49.046	49.012	49.045	49.013	49.046	49.012	49.045		49.01225	49.0455	0.03325	0.000	0.000	0.000

A4 XRD analysis

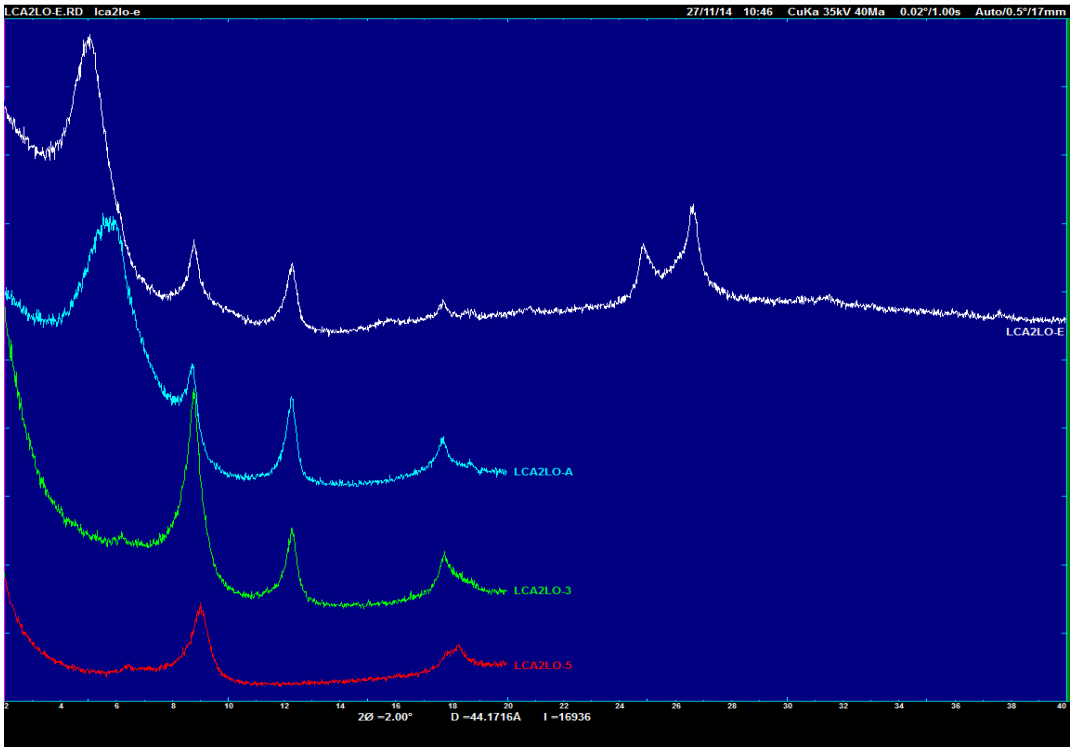

Figure 212: London Clay Unit A2(1): XRD analysis

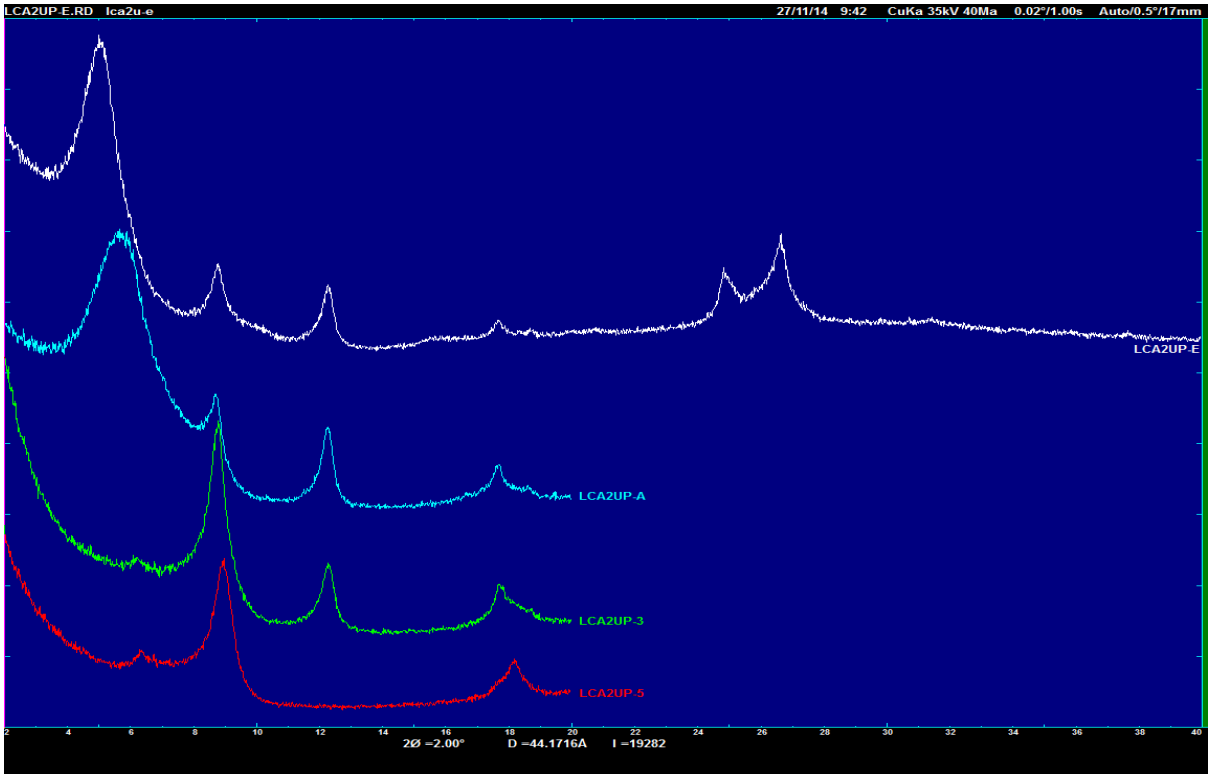

Figure 213: London Clay Unit A2(2): XRD analysis

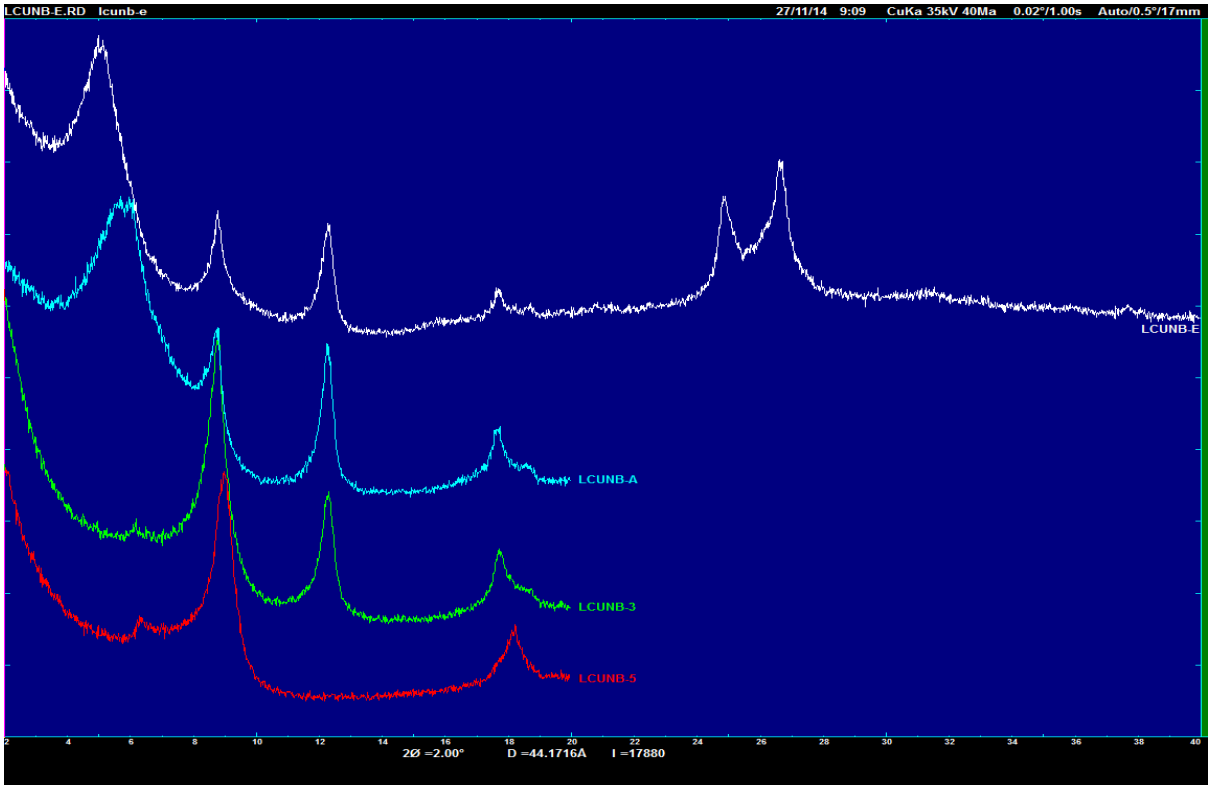

Figure 214: London Clay Unit B: XRD analysis

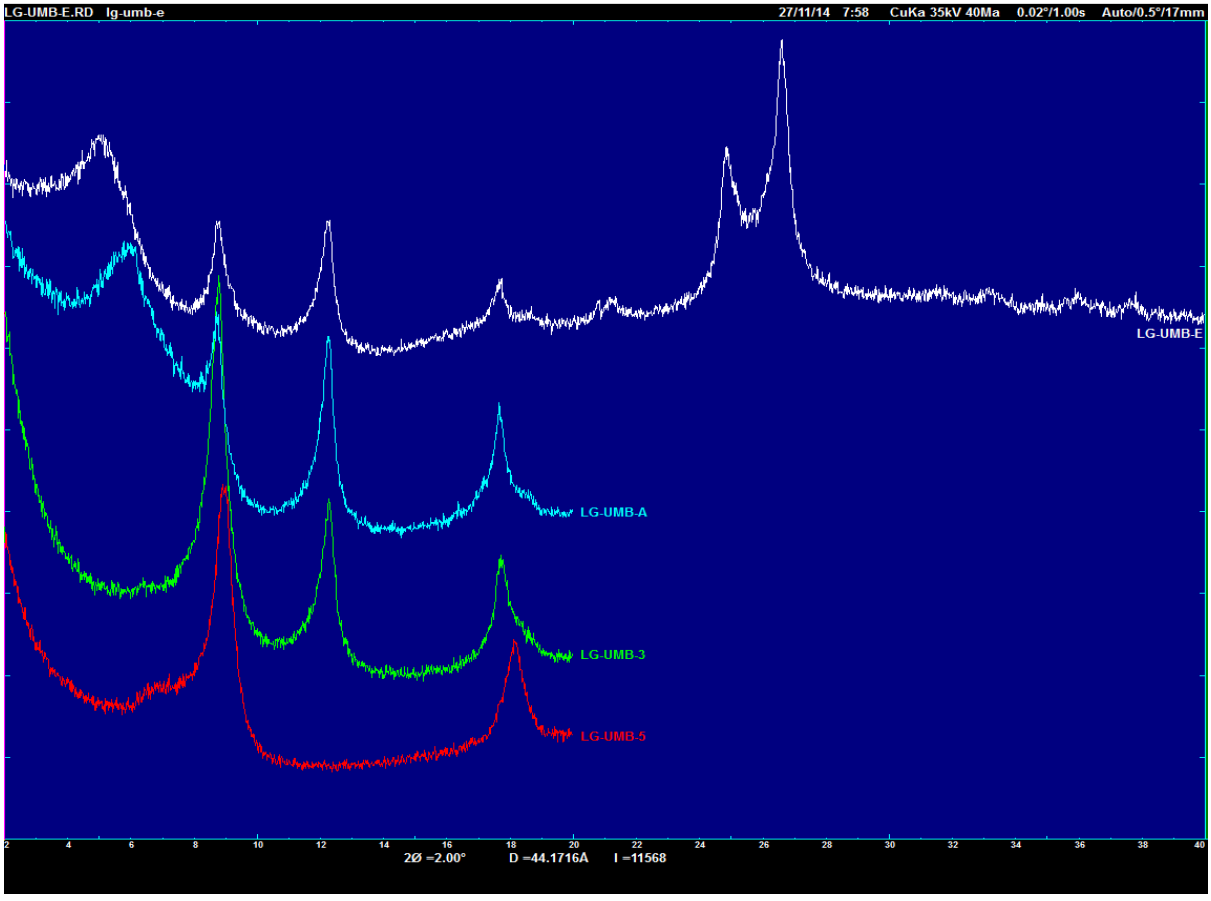

Figure 215: Lambeth Group UMB: XRD analysis

A5 Particle Size Distributions

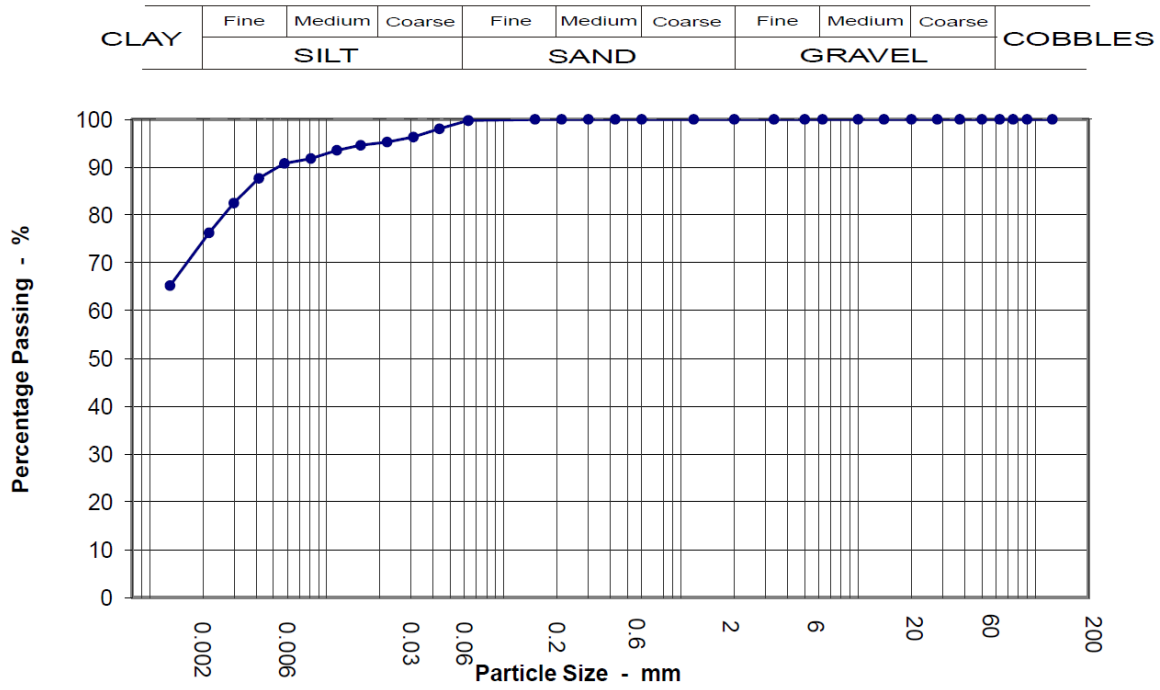

Figure 216: Particle size distribution - sedimentation by hydrometer method. Conducted by K4 soils – UMB

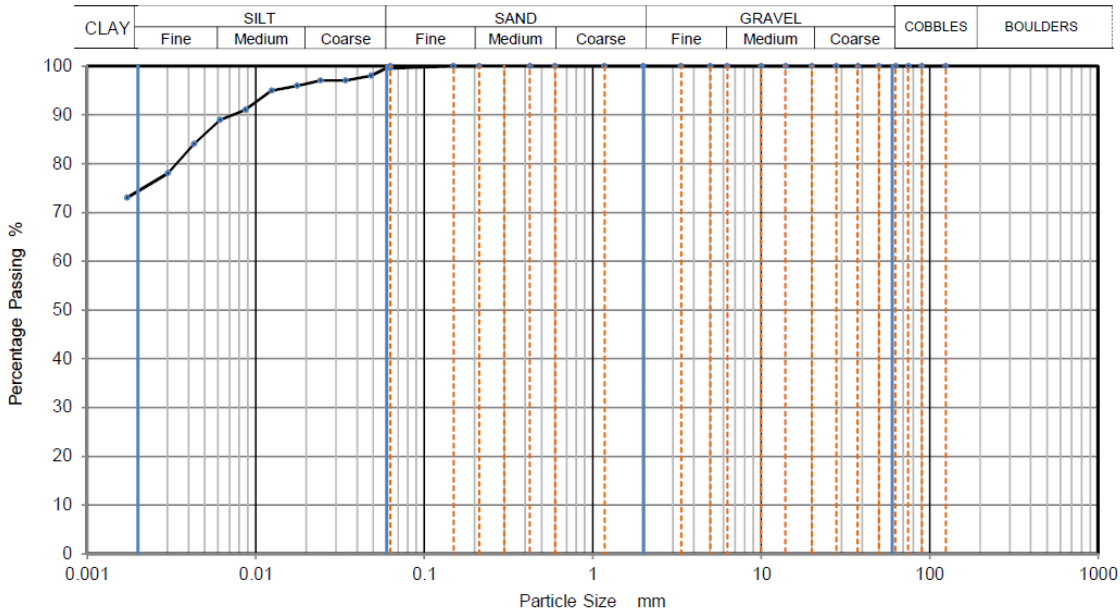

Figure 217: Particle size distribution - sedimentation by hydrometer method. Conducted by K4 soils. UMB test 2

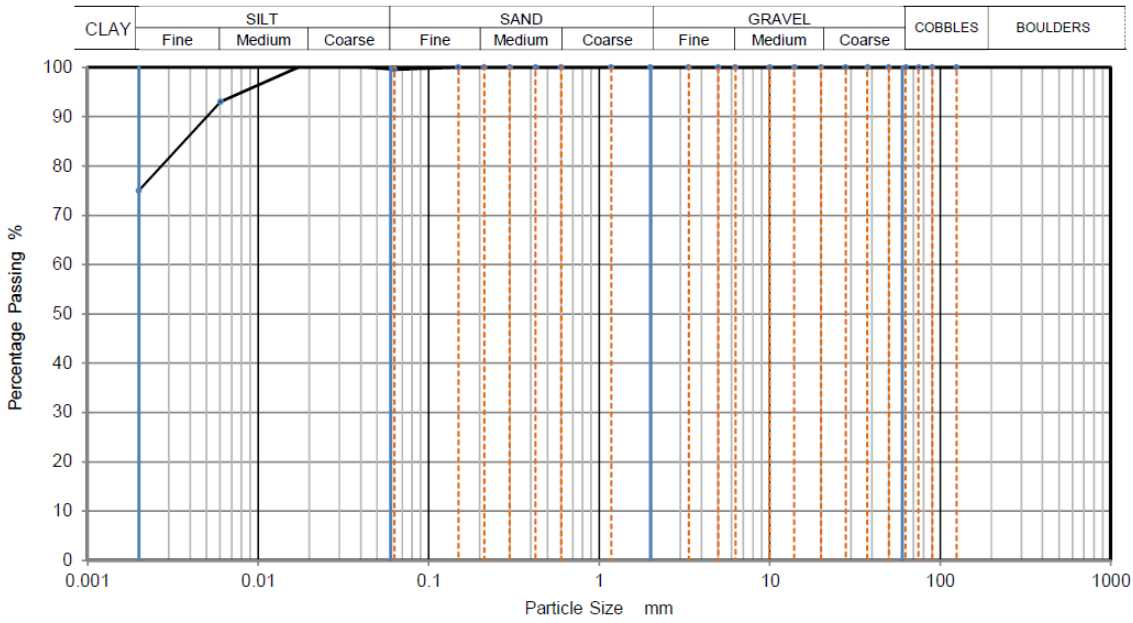

Figure 218: Particle size distribution - sedimentation by pipette method. Conducted by K4 soils. UMB

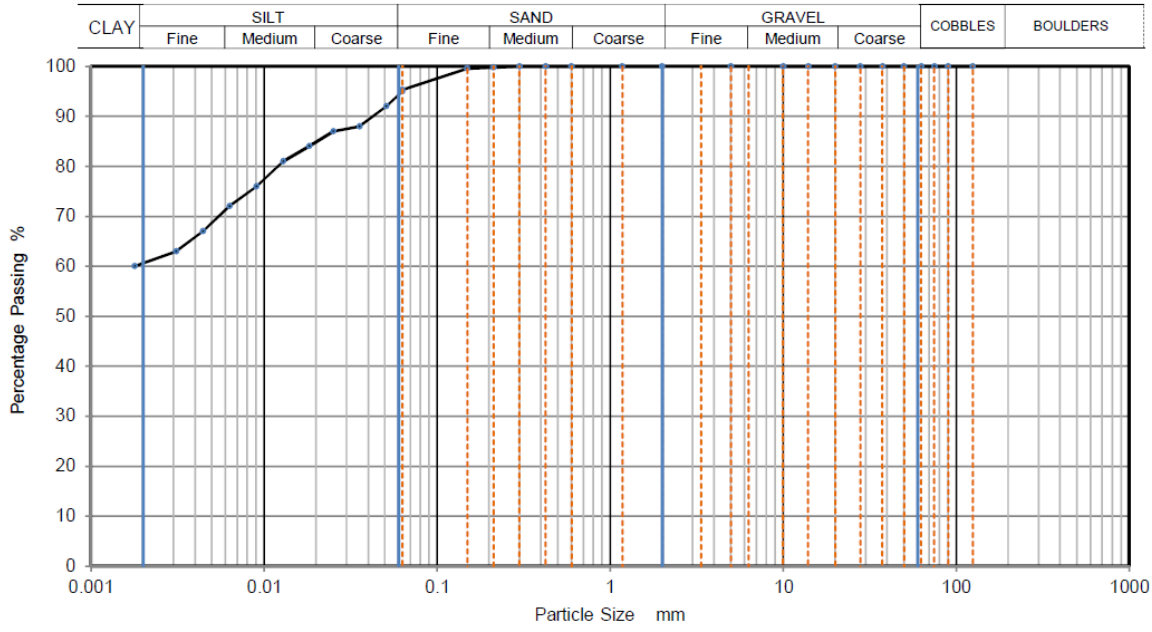

Figure 219: Particle size distribution - sedimentation by hydrometer method. Conducted by K4 soils. London Clay Unit B2

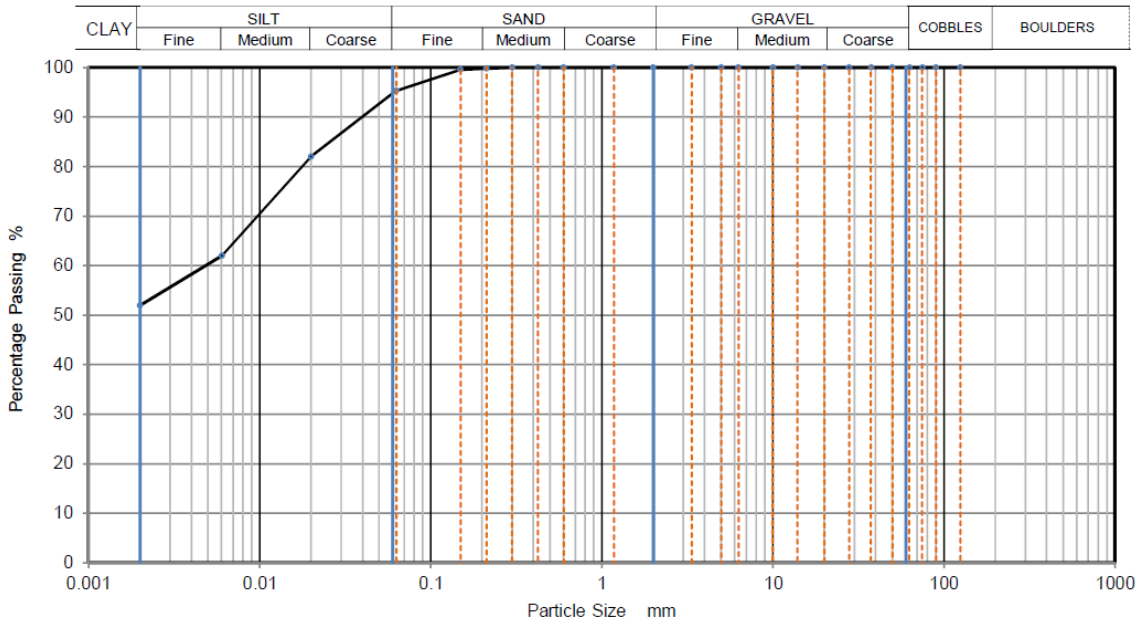

Figure 220: Particle size distribution - sedimentation by pipette method. Conducted by K4 soils. London Clay Unit B2

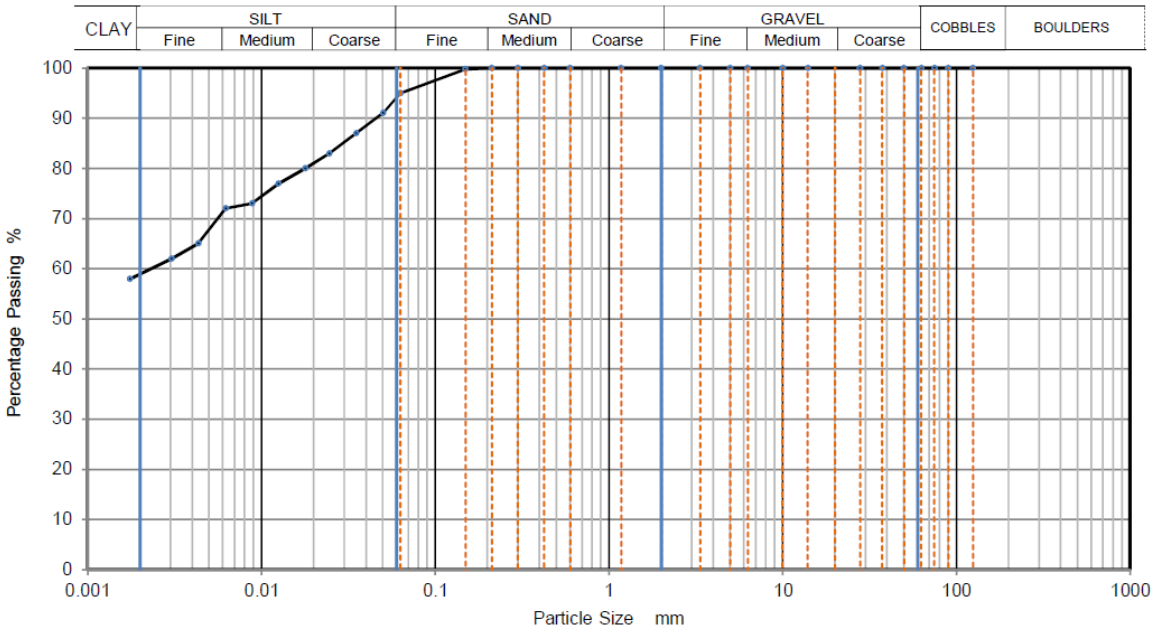

Figure 221: Particle size distribution - sedimentation by hydrometer method. Conducted by K4 soils. London Clay Unit A2(1)

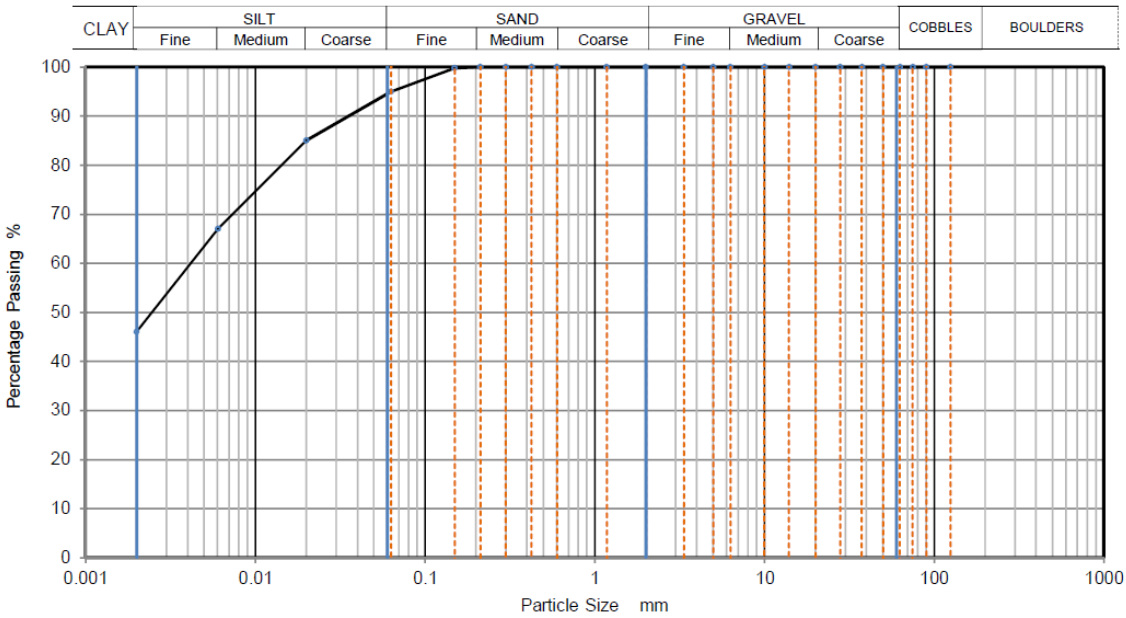

Figure 222: Particle size distribution - sedimentation by pipette method. Conducted by K4 soils. London Clay Unit A2(1)

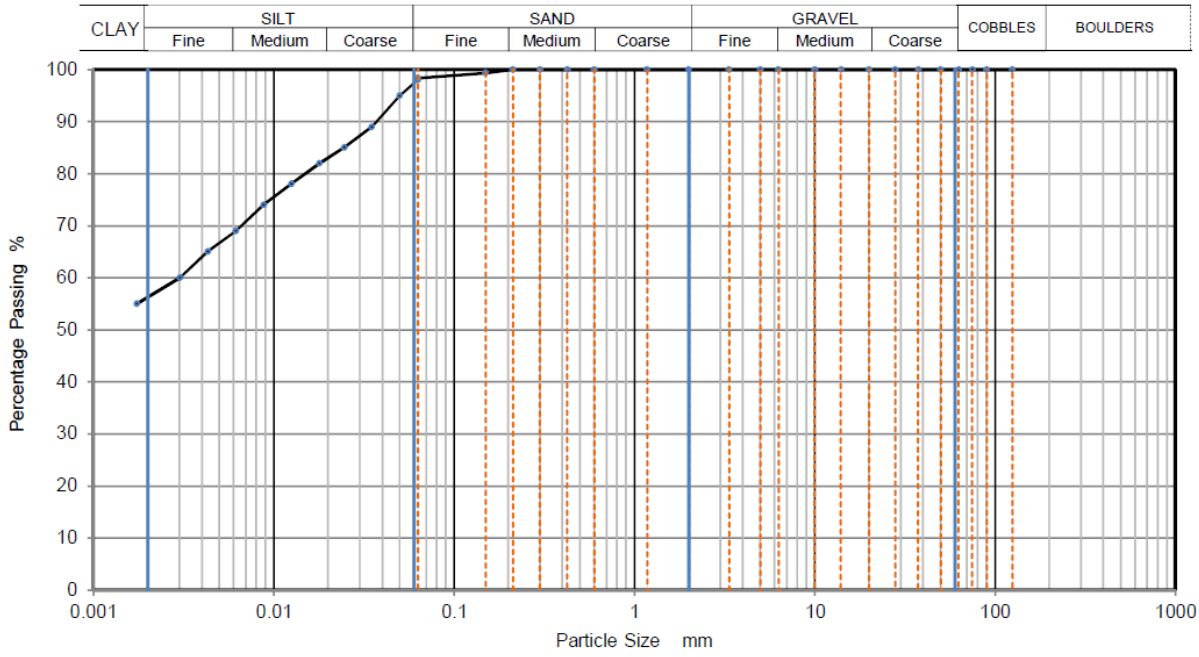

Figure 223: Particle size distribution - sedimentation by hydrometer method. Conducted by K4 soils. London Clay Unit A2(2)

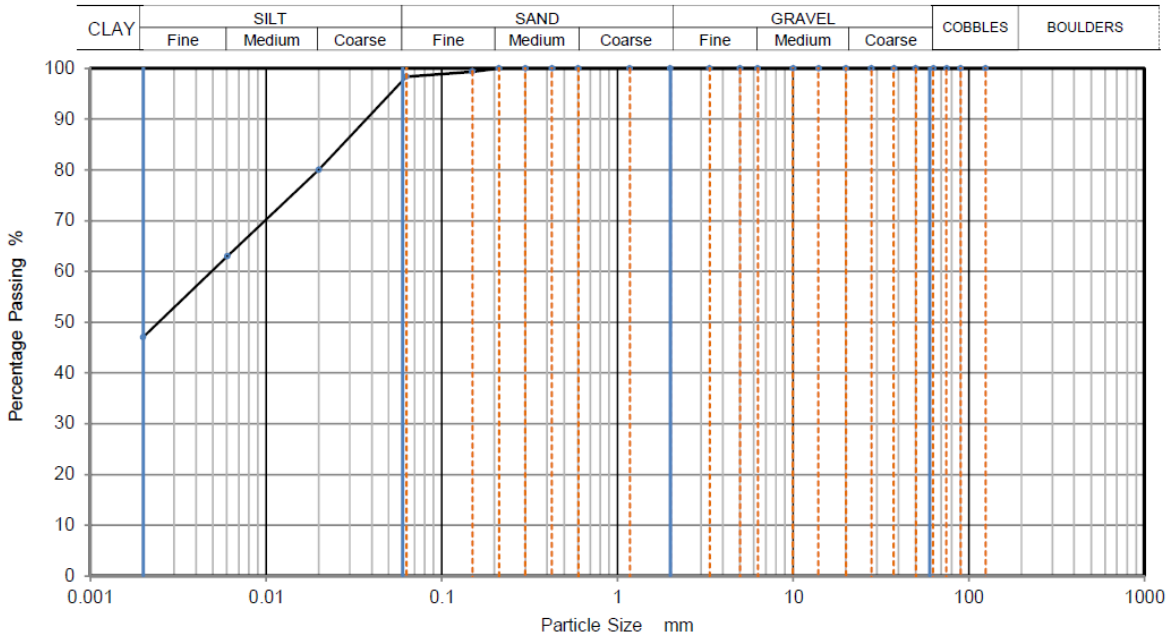

Figure 224: Particle size distribution - sedimentation by pipette method. Conducted by K4 soils. London Clay Unit A2(2)

REFERENCES

Al Tabbaa, A. & Muir Wood, D. M., 1989. An experimentally based bubble model for clay. *Numerical methods in Geomechanics NUMOG III, Elsevier Applied Science,* pp. 91-99.

Atkinson, J., 2000. Non-linear soil stiffness in routine design. *Geotechnique,* pp. 487-508.

Atkinson, J., 2007. Peak strength of overconsolidated clays. *Geotechnique,* 57(2), pp. 127-135.

Atkinson, J., Richardson, D. & Stallebrass, S., 1990. Effect of stress history on the stiffness of overconsolidated soil. *Geotechnique 40 (4),* pp. 531-540.

Banglasdesh University, 2002. [Online]
Available at: http://teacher.buet.ac.bd/sid/download/CE341/lecture12_4on1.pdf
[Accessed 2015].

Barmpopoulos, I., 2008. *Victoria Station Upgrade 231074/STH/00/101/E01,* Croydon: Mott Macdonald.

Benz, T., 2007. *Small-strain stiffness of soils and its numerical consequences,* Stuttgart, Germany: University Stuttgart.

Biscaye, P., 1965. Mineralogy and sedimentation of recent deep-sea clay in the Atlantic Ocean and adjacent seas and oceans. *GSA Bulletin ,* 76(7), pp. 803-832.

Bishop, A., 1955. *The principle of effective stress.* s.l., s.n.

Bishop, A. W., 1966. The strength of soils as engineering materials. *Geotechnique,* 16(2), pp. 91-130.

Bishop, A. W., Webb, D. L. & Lewin, P. I., 1965. Undisturbed samples of London clay from Ashford Common shaft: strength - effective stress relationship. *Geotechnique,* 15(1), pp. 1-31.

Black, M., 2009. *Geotechnical Sectional Interpretative Report 1&2 Royal Oak to Liverpool Street REPORT NO. 1D0101-G0G00-00550,* London: s.n.

Bonal, J., Donohue, S. & McNally, C., 2012. Wavelet analysis of bender element signals. *Getechnique,* 62(3), pp. 243-252.

British Standard Institution, 1990. *Methods of test for soils for civil engineering purposes BS1377,* London: British Standard Institution.

Burford, D., 1988. heave of tunnels beneath the Shell Centre, London, 1959-1986. *Geotechnique,* 38(1), pp. 135-137.

Burland, J. B., 1990. On the compressibility ad shear strength of natural soils. *Geotechnique,* 40(3), pp. 329-378.

Burland, J. B. & Hancock, R. J. R., 1977. Underground car park at the House of Commons, London: Geotechnical aspects. *The Structural Engineer,* 55(2), pp. 87-100.

Burland, J. B. & Kalra, J. C., 1986. Queen Elizabeth II COnference Centre: Geotechnical aspects. *ICE Proceedings,* 80(6), pp. 1479-1503.

Burland, J. B., Rampello, S., Georgiannou, V. N. & Calabresi, G., 1996. A laboratory study of the strength of four stiff clays. *Geotechnique,* 46(3), pp. 491-514.

Burland, J. B., Simpson, B. & St John, H. D., 1979. *British state of the art report on movements around deep excavations.* Brighton, Proc. 7th Eur. Conf. Soil Mech. Found. Engng..

C.W.W.Ng, Bolton, M. & Dasari, G., 1995. The small strain stiffness of a carbonate stiff clay. *Soils and Foundations.*

Carder, D., Barker, K., Cole, G. & Stephen, M., 2004. *The long term performance of the propped diaphragm walls at Aldershot Road underpass,* s.l.: TRL .

Carder, D. R. & Darley, P., 1998. The long term performance of embedded retaining walls. *TRL,* Volume Report 381.

Carder, D. R., Press, D. J., Morley, C. H. & Alderman, G. H., 1997. Behaviour During Construction of a Propped Diaphram Wall founded in London Clay. *TRL,* p. 239.

Chandler, R. J., 2000. Clay sediments in Depositional Basin: the Geotechnical cycle. *Quarterly Journal of Engineering Geology and Hydrogeology,* Volume 33, pp. 7-39.

Chapman, D., 1913. A contribution to the theory of electrocapillarity. *Philosophical Magazine Vol 25 (6),* pp. 475-481.

Chapman, T., 1999. *Horseferry Road basement, long term heave data,* s.l.: Arup Geoguid 1999-10 TC.

Chipera, S. J. & Bish, D. L., 2002. FULLPAT: a full-pattern quantitative analysis program fro xray powder diffraction using measured and calculated patterns. *Journal of applied crystallography,* Volume 35, pp. 744-749.

Clarke, S. D. & Hird, C. C., 2013. Modelling viscous effects during and after construction in London Clay. *Geotechincal Engineering Journal of the SEAGS & AGSSEA ,* 44(2).

Clark, J., 2006. *Performance of a propped retaining wall at the CTRL, Ashford,* s.l.: University of Southampton, School of Civil Engineering and the Environment, Doctoral Thesis.

Clayton, C. & Heymann, G., 2001. Stiffness of geomaterial at very small strains. *Geotechnique 51 (3),* pp. 245-255.

Clayton, C. R. I., Hight, D. W. & Hopper, a. R. J., 1992. Progressive destructuring of Bothkennar clay. implications for sampling and reconsolidation procedures. *Geotechnique,* 42(2), pp. 219-239.

Collins, I. F., 2005. The concept of stored plastic work or frozen elastic energy. *Geotechnique,* 55(5), pp. 373-382.

Coop, M. R., Atkinson, J. H. & Taylor, R. N., 1995. Strength yielding and stiffness of structured and unstructured soils. *Proc. 11th ECSMFE, Copenhagen,* Volume 1, pp. 55-62.

Cotecchia, F., 1996. *The effects of structure on the properties of an Italian Pleistocene clay.* PhD Thesis ed. s.l.:University of London.

Cotecchia, F., 1996. The effects of structure on the properties of an Italian Pleistogene clay. *PhD Thesis,* Volume University of London.

Cotecchia, F. & Chandler, R. J., 2000. A general framework for the mechanical behaviour of clay. *Geotechnique,* 50(4), pp. 431-447.

Cragg, A. & Nicol, M., 2011. *Non-linear numerical modelling - interpretation of geotechnical parameters* , London: Crossrail Ltd.

Cruttenden, P., 2014. *C138-MMD-C2-DDB-C101_Z-10200 Geologocal Longitudinal Section CC502,* s.l.: s.n.

D.R.Carder, 1997. Behaviour During Construction of a Propped Diaphram Wall founded in London CLay. *TRL,* p. 239.

Das, B. M., 2008. *Advanced soil mechanics.* Third ed. New York: Taylor and Francis.

Day, P., 2013. *Magnetic extensometer installation manual.* [Online]
Available at: http://www.itmsoilsupport.com/manuals/Man007_Magnetic_Extensometer.pdf
[Accessed 04 June 2014].

De Freitas, M. H. & Mannion, W. G., 2007. A biostratigraphy for the London Clay in London. *Ge´otechnique,* 57(1), pp. 91-99.

Eberl, D., 2003. *User's guide to RockJock - A program for determining quantitative mineralogy from powder X-ray diffraction data,* s.l.: US Geological Survey Open-File Report.

Ellison, R. A. et al., 2004. *Geology of London. Special memoir for 1:50 000 geological sheets 256 (North london), (Romford), 270 (South London) and 271,* Keyworth, Nottingham: British geological Survey.

Entwisle, D. C. et al., 2013. *Engineering Geology of British Rocks and Soils - Lambeth Group,* Keyworth, Nottingham: British Geological Survey.

Environment Agency, 2018. *Management of the London Basin Chalk Aquifer,* London: s.n.

Fjaer, E. et al., 1992. *Petroleum related Rock mechanics.* s.l.:Elsevier.

Forster, A. et al., 1995. *Engineering Geology of British rocks and soils: Gault Clay,* Keyworth, Nottingham: BGS Engineering Geology and Geophysics Group, Technical Report WN/94/31.

Fredlund, D. G., Rahardjo, H. & Fredlund, M. D., 2012. *Unsaturated soil mechanics in engineering practice.* s.l.:John Wiley & Sons.

G.Mesri, Ullrich, C. & Choi, Y., 1978. The rate of swelling of overconsolidated clays subjected to unloading. *Geotechnique 28 (3),* pp. 281-307.

Gasparre, A., 2005. *Advanced Laboratory Characterisation of London Clay.* London: Imperial College London.

Gasparre, A., Hight, D. W., Coop, M. R. & Jardine, R. J., 2014. The laboratory measurement and interpretation of the small-strain stiffness of stiff clays. *Ge´otechnique,* 64(12), p. 942–953.

Gasparre, A., Nishimura, S., Coop, M. R. & Jardine, R. J., 2007. The influence of structure on the behaviour of London Clay. *Geotechnique,* 57(1), pp. 19-31.

Gasparre, A. et al., 2007. The stiffness of natural London Clay. *Geotechnique 57 (1),* pp. 33-47.

Georgiannou, V. N., 1988. *The behaviour of clayey sands under monotonic and cyclic loading,* University of London: PhD Thesis.

Geosense, 2015. [Online]
Available at:
http://www.geosense.co.uk/media/ProductDatasheet/6/file/VWPiezometersVWP3000V1.2.pdf

Gilkes , R. J., 1969. Clay mineral provinces in the Tertiary sediments of the Hampshire Basin. *Clay minerals,* Volume 7, pp. 351-361.

Gouy, G., 1910. Sur la constitution de la charge electrique a la surface d'un electrolyte. *Annales de Physique (Paris). Serie 4.9.,* pp. 457-468.

Haigh, S. K., Vardanega, P. J. & Bolton, M. D., 2013. The plastic limit of clays. *Geotechnique,* 63(6), pp. 435-440.

Hardin, B. O., 1978. *The nature of stress-strain behaviour for soils,* New York: American Society of Civil Engineers.

Henkel, 1971. *The relevance of laboratory measured parameters in field studies.* Cambridge, Foulis, pp. 669-675.

Higgins, K. G., Potts, D. M. & Symons, I. F., 1989. *COmparison of predicted and measured performance of the retaining walls of the Bell Common tunnel,* Crowthorne: TRL.

Hight, D. W. et al., 2007. Characteristics of the London Clay from the Terminal 5 site at Heathrow Airport. *Geotechnique,* 57(1), pp. 3-18.

Hubbard, H. W., Potts, D. M., Miller, D. & Burland, J. B., 1984. Design of the retaining walls for the M25 cut and cover tunnel at Bell Common. *Geotechnique,* 34(4), pp. 493-512.

Huggett, J. M. & Knox, R. W., 2006. Clay mineralogy of the Tertiary onshore and offshore strata of the British Isles. *Clay Minerals,* Volume 41, pp. 5-46.

I.F.Symons & Tedd, P., 1989. Behaviour of a propped embedded retaining wall at Bell Common Tunnel in the longer term. *Geotechnique 39 (4),* pp. 701-710.

Isik, N. S., 2009. Estimation of swell index of fine grained soils using regression equations and artificaial neural neworks. *Scientific Research and Essay 4 (10),* pp. 1047-1056.

itmsoil, 2014. *Instrumentation and monitoring.* [Online]
Available at: http://www.itmsoil.com/pages/geotechnical+structural+instruments
[Accessed 04 June 2014].

Jaky, J., 1944. The coefficient of Earth Pressure at rest. *Journal for the society of Hungarian Architects and Engineers,* Volume October, pp. 355-358.

Jardine, R., 1992. Some observations on the kinematic nature of soil stiffness. *Soil and Foundations vol 32 (2),* pp. 111-124.

Jardine, R. J., 1985. *Investigation of pile-soil behaviour with special reference to the foundations of offshore structures, PhD Thesis,* s.l.: University of London.

Jardine, R. J., 1995. One perspective of the pre-failure deformation charcteristics of some geomaterials. *Proc. of the Int. conference on the pre-failure deformation charcteristics of geomaterials, Hokkaido, Japan,* Volume 2, pp. 855-885.

Jardine, R. J., Gens, A., Hight, D. W. & Coop , M. R., 2004. Development in understanding soil behaviour. In: *Advances in Geotechnical Engineering: The Skempton Conference. Jardine, R.J., Potts, D.M. & Higgins, K.G. eds.,.* London: Thomas Telford, pp. 103-206.

Jardine, R. J., Potts, D. M., Fourie, A. B. & Burland, J. B., 1986. Studies of the influence of non-linear stress-strain characteristics in soil-stucture interaction. *Geotechnique,* 36(3), pp. 377-396.

Jones, L. D. & Terrington, R., 2011. Modelling volume change potential in the London Clay. *Quarterly Journal of Engineering Geology and Hydrogeology v44,* pp. 109-122.

Jovicic, V. & Coop, M. R., 1998. The measurement of stiffness anistropy in clays with bender element tests in the triaxial apparatus. *Geotechincal testing journal,* 21(1), pp. 3-10.

K.Terzaghi, 1931. *The influence of elasticity and permeability on the swelling of two-phase systems.* New York: s.n.

Keller, W., 1962. Diagenesis of clay minerals - A review. *Clay and CLay minerals vol 11 (1),* pp. 136-157.

King, C., 1981. The Stratigraphy of the London Clay and Associated Deposits. *Tertiary Research (Special Paper),* Volume 6, pp. 3-158.

Kuwano, R., 1999. *The stiffness and yielding anisotropy of sand,* University of London: PhD thesis.

Lam, S. S. Y., 2010. *Ground Movements due to excavation in clay: physical and analytical models,* Cambridge: Churchill College .

Lings, M., 2001. DDrained and undrained anisotropic elastic stiffness parameters. *Geotechnique 51 (6),* pp. 555-565.

Lings, M., Pennington, D. & Nash, D., 2000. Anisotropic stiffness parameters and their measurement in a stiff natural clay. *Geotechnique 50 (2),* pp. 109-125.

Long, M., 2001. Database for retaining wall and ground movements due to deep excavations. *Journal of Geotechnical and Geoenvironmental Engineering,* 127(3).

Mayne, P. W. & Kulhawy, F. H., 1982. K0– OCR relationship in soil. *J. Geotech. Eng. Div., Am. Soc. Civ. Eng.,* 108(6), p. 851–872.

Measor, E. O. & Williams, G. J. M., 1962. Features in the design and construction of the shell centre, London. *ICE Proceedings,* 21(3), pp. 475-502.

Mesri, G., Ullrich, C. R. & Choi, Y. K., 1978. The rate of swelling of overconsolidated clays subjected to unloading. *Geotechnique,* 28(3), pp. 281-307.

Mitaritonna, G., Amorosi, A. & Cotecchia, F., 2014. Experimental investigation of the evolution of elastic stiffness anisotropy in a clayey soil. *Geotechnique,* 64(6), pp. 463-475.

Mott MacDonald , 2008. *Victoria Station Upgrade MDC2 MMD-V047-1159-GEO-50-006 Rev E10 Geotechnical Interpretative Report,* Croydon: s.n.

Mott MacDonald Limited, 2008. *Victoria Station Upgrade MDC2 MMD-V047-1159-GEO-50-006 Rev E01 Geotechnical Interpretative Report,* London: s.n.

Ng, C. W., 2004. *A short course in soil-structure engineering of deep foundations, excavations and tunnels.* London: Thomas Telford.

Ng, C. W. W., Simpson, B., Lings, M. L. & Nash, D. F. T., 1998. Numerical analysis of a multipropped excavation in stiff clay. *Canadian Geotechnical,* Volume 35, pp. 115-130.

Nishimura, S., 2005. *Laboratory study on anisotropy of natural London Clay,* London: Imperial College.

O'Brien, A. & Sharp, P., 2001a. Settlement and heave of overconsolidated clays part 1. *Ground Engineering October,* pp. 28-32.

O'Brien, A. & Sharp, P., 2001b. Settlement and heave of overconsolidated clays part 2. *Ground Engineering November.*

O'Brien, A. S. & Newman, R. L., 1990. Self boring pressuremeter testing in London Clay. *Geological Society, London, Engineering Geology Special Publications,* 6(1), pp. 39-53.

O'Rourke, T. D., 1993. Base stability and ground movement prediction for excavations in soft clay. In: *Retaining structures.* London: Thomas Telford, pp. 131-139.

Osman, A. & Bolton, M., 2006. Ground movement predictions for braced excavations in undrained clay. *Journal of Geotechnical and Geoenvironmental Engineering 132. 10.1061/(ASCE)1090-0241.*

Owsianka, A., 1988. Discussion on Paper 9138 by Burland, J. B. and Kalra, J. C. *Proceedings of the Institution of Civil Engineers - Part 1,* 84(Feb), pp. 111-114.

Pantelidou, H. & Simpson, B., 2007. Geotechnical variation of London Clay across central London. *Geotechnique,* 57(1), pp. 101-112.

Pearce, R., 2014. *Clay mineralogy analysis.* Southampton: s.n.

Pender, M., Kikkawa, N. & Liu, P., 2009. Macro-void structure and permeability of Auckland residual clay. *Geotechnique,* 59(9), pp. 773-778.

Pennington, D., Nash, D. & Lings, M., 1997. Anisotropy of G0 shear stiffness in Gault Clay. *Geotechnique 47 (3),* pp. 391-398.

Potts, D. M. & Zdravkovic, L., 1999. *Finite element analysis in geotechnical engineering.* Vol 1 ed. s.l.:Thomas Telford Limited.

Poulos, H. & Davis, E., 1974. *Elastic solutions for soil and rock mechanics.* s.l.:John Wiley & Sons.

Procter, M., 2014. *Photo taken during block sampling at Moorgate Station.* s.l.:s.n.

Raison, C. A., 1988. Discussion on Paper 9138 by Burland, J. B. and Kalra, J. C.. *Proceedings of the Institution of Civil Engineers - Part 1,* 84(Feb), pp. 114-117.

Ratananikom, W., Litkitlersuang, S. & Yimsiri, S., 2013. An investigation of anisotropic elastic parameters of Bangkok Clay from vertical and horizontal cut specimens. *Geomechanics and Geoengineering: An International Journal,* 8(1), pp. 15-27.

Redshaw, P. G., 2015. *A Geomorphological and Geotechnical Investigation of the Roughlands Landslide Complex, Southwest Isle of Wight, UK,* s.l.: Univeristy of Southampton.

Rees, S., 2013. *Intrduction to triaxial testing.* [Online]
Available at:
http://www.gdsinstruments.com/__assets__/pagepdf/000037/Part%201%20Introduction%20to%20triaxial%20testing.pdf

Richards, D. J., Clark, J., Powrie, W. & Heymann, G., 2007. Performance of push-in pressure cells in overconsolidated clay. *Geotechnical engineering,* 160(January GE1), pp. 31-41.

Ryley, M. D. & Carder, D. R., 1995. The performance of push-in spade cells installed in stiff clay. *Geotechnique,* 45(3), pp. 533-539.

Samuels, S. G., 1975. Some properties of the Gault Clay from the Ely-Ouse Essex water tunnel. *Geotechnique,* Volume 25, pp. 239-264.

Schadlich, B. & Schweiger, H. F., 2013. Influence of anisotropic small strin stiffness on the deformation behaviour of geotechnical structures. *International Journal od Geomechanics,* 13(6).

Schmertmann, J. H., 1969. Swell sensitivity. *Geotechnique,* 19(41), pp. 530-533.

Schmidt, B., 1966. Earth pressure at rest related to stress history. *Can. Geotech.,* 3(4), pp. 239-242.

Serota, S. & Jennings, R. A., 1959. The elestic heave at the bottom of excavations. *Geotechnique,* 9(2), pp. 62-70.

Simpson, B., 1992. *Development and application of a new soil model for prediction of ground movements.* Oxford, s.n., pp. 628-643.

Simpson, B., 2010. Engineering in stiff sedimentary clays. *Geotechnique 60 (12),* pp. 903-911.

Simpson, B., O'Riordan, N. & Croft, D., 1979. A computer model for the analysis of ground movements in London Clay. *Geotechnique 29 (2),* pp. 149-175.

Simpson, B. & Tatsuoka, F., 2008. Geotechnics: the next 60 years. *Geotechnique 58, No. 5,* pp. 357-368.

Simpson, B. & Vardanega, P. J., 2014. Results of monitoring at the British Library excavation. *ICE Proceedings,* Issue Ahead of Print.

Skipper, J. A., 1999. *The Stratigraphy of the Lambeth Group (Palaeocene) of south east England,* s.l.: PhD thesis University of London.

Smethurst, J. A. & Powrie, W., 2007. Monitoring and analysis of the bending behaviour of discrete piles used to stabilise a railway embankment. *Geotechnique,* 57(8), pp. 663-677.

Smith, P., Jardine, R. J. & Hight, D. W., 1992. the yielding behaviour of Bothkennar clay. *Geotechnique,* 42(2), pp. 257-274.

Smith, P. R., 1992. *The behaviour of natural high compessibility clays with special reference to consolidation on soft ground.* PhD Thesis: University of London.

Spinola, D. N. et al., 2017. Origin of clay minerals in Early Eocene volcanic paleosols on King George Island, Maritime Antarctica. *Nature* , Scientific Reports volume 7, Article number: 6368(https://www.nature.com/articles/s41598-017-06617-x).

Stallebrass, S. E. & Taylor, R. N., 1997. The development and evaluation of a constitutive model for the prediction of ground movements in overconsolidated clay. *Geotechnique,* 47(2), pp. 235-253.

Standing, J. R., 2018. Identification and implications of the London Clay Formation divisions from an engineering perspective. *Proceedings of the Geologists Association,* pp. ISSN 0016-7878.

Standing, J. R. & Burland, J. B., 2006. Unexpected tunneling volume losses in the Westminister area, London. *Geotechnique,* 56(1), pp. 11-26.

Stroud, M. A., 1989. The Standard Penetration Test - It's application and interpretation. In: I. o. C. Engineers, ed. *Penetration testing in the UK.* London: Thomas Telford, pp. 29-49.

Symons, I. F. & Tedd, P., 1989. Behaviour of a propped embedded retaining wall at Bell Common Tunnel in the longer term. *Geotechnique,* 39(4), pp. 701-710.

Takahashi, A., Fung, D. & Jardine, R., 2005. *Swelling effects on mechanical behaviour of natural London Clay.* Rotterdam , Millpress Science Publishers, pp. 443-446 .

Takahashi, M., 1981. *Transient and cyclic behaviour of a sandy clay.* PhD Thesis ed. s.l.:University of London.

Tatsouka, F. et al., 1998. *Some new aspects of time effects on the stress-strain behaviour of stiff geomaterials.* Napoli, 2HSSR.

Tedd, P., Chard, B., Charles, J. & Symons, I., 1984. Behaviour of a propped embedded retaining wa;; in stiff clay at Bell Common Tunnel. *Geotechnique.*

Tedd, P. & Charles, J. A., 1981. In situ measurement of horizontal stress in overconsolidated clay using push-in spade-shaped pressure cells. *Geotechnique,* 31(4), pp. 554-558.

Teng, F., Ou, C. & Hsieh, P., 2014. Measurements and Numerical Simulations of Inherent Stiffness Anisotropy in Soft Taipei Clay. *Journal of Geotechnical and Geoenvironmental Engineering*, 140(1).

Terzaghi, K., 1936. *Stability of slopes of natural clays.* Cambridge, Massachusetts, s.n., pp. 161-165.

Terzaghi, K., Peck, R. & Mesri, G., 1996. *Soil mechanics in engineering practice (3rd edition).* New York: John Wiley & Sons.

Vargas, M., 1955. Foundation of structures on over-consolidated clay layers in Sao Paulo. *Geotechnique,* 5(3), pp. 253-266.

Viggiani, G. & Atkinson, J. H., 1995 (a). Interpretation of bender element tests. *Geotechnique,* 45(1), pp. 149-154.

Viggiani, G. & Atkinson, J. H., 1995 (b). Stiffness of fine-grained soils at very small strains. *Geotechnique,* 45(2), pp. 249-265.

Vitone, C. & Cotecchia, F., 2011. The influence of intense fissuring on the mechanical behaviour of clays. *Geotechnique 61 (12),* pp. 1003-1018.

VJtech, 2015. [Online]
Available at: (http://www.vjtech.co.uk/products/soil-rock-testing/triaxial-test-automated-triaxial-testing-triaxial-load-frames/triaxial-cells-and-accessories/bender-element-sets/bender-elements-in-100-mm-top-cap-base-pedestal-set-for-tc100)
[Accessed 2015].

W.W.Ng, C., 2004. *Soil-structure Engineering.* London: Thomas Telford Publishing.

Ward, W. H., 1962. *Discussion on Paper No. 6596 - Proc. Instn civ. Engrs, vol. 21 (March 1962). pp. 475-502,* s.l.: ICE.

Watabe, Y., Lebihan, J. & Leroueil, S., 2006. Probabilistic modelling of saturated/unsaturated hydraulic conductivity for compacted glacial tills. *Geotechnique,* 56(4), pp. 274-284.

West, I., 2013. [Online]
Available at: http://www.southampton.ac.uk/~imw/jpg/3AB-Reduction-patch.jpg
[Accessed 2015].

Wood, L. A., 1990. The performance of a raft foundation in London Clay. In: *Ggeotechnical Instrumentation in Practice.* London: Thomas Telford, pp. 323-340.

Wood, L. A., 2000. Soil-Structure interaction in design. In: J. A. Hemsley, ed. *Design applications of raft foundations.* London: Thomas Telford, pp. 205-242.

Wykeham Farrance, 2015. *User Manual.* s.l.:s.n.

Yao, Y., Gao, Z., Zhao, J. & Wan, Z., 2012. Modified UH model: Constitutive modelling of overconsolidated clays based on a parabolic Hvorslev envelope. *Journal of Geotechnical and Geoenvironmental Engineering,* 138(7), pp. 860-868.

Yimsiri, S. & Soga, K., 2011. Cross-anisotropic elastic parameters of two natural stiff clays. *Geotechnique 61 (9),* pp. 809-814.

Yukselen-Aksoy, Y. & Kaya, A., 2013. Specific surface area effect on compressibility behaviour of clayey soils. *ICE proceedings,* 166(GE1), pp. 76-87.